

2
**TECHNICAL LIBRARY
REFERENCE COPY**

240
AD-682714

TECHNICAL REPORT NO. 10276 (Final)

Fracture Mechanics Technology For
Combined Loading
and
Low-To-Intermediate Strength Metals



Final Technical Report

November 18, 1968

Distribution of This Document is Unlimited

----- by W.K. Wilson, W.G. Clark, Jr. & E.T. Wessel

Westinghouse Research Laboratories
Pittsburgh, Pa.
Contract DAAE 07-67-C-4021

TACOM

VEHICULAR COMPONENTS & MATERIALS LABORATORY

U.S. ARMY TANK AUTOMOTIVE COMMAND Warren, Michigan

20040204002

obligatory

The findings in this report are not to be construed
as an official Department of the Army position,
unless so designated by other authorized documents.

Destroy this report when no longer needed.
Do not return it to the originator.

**Fracture Mechanics Technology For
Combined Loading and Low-To-
Intermediate Strength Metals**

Final Technical Report

by

W. K. Wilson, W. G. Clark, Jr., and E. T. Wessel

November 18, 1968

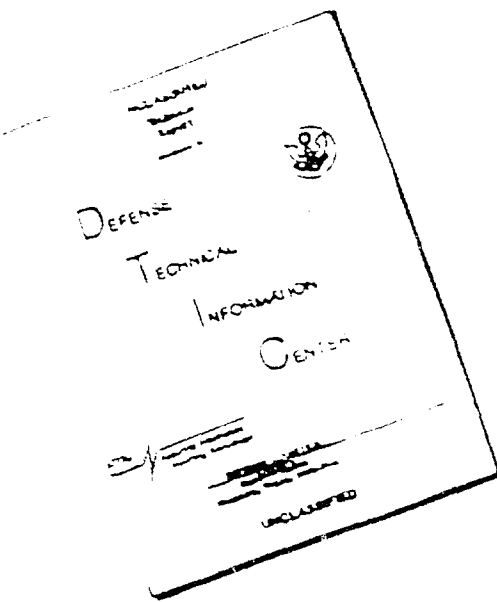
**Contract No. DAAE 07-67-C-4021
Department of the Army, Project No. 1 G 024 401 A 105
Vehicular Components and Materials Laboratory
U. S. Army, Tank Automotive Command
Warren, Michigan 48090**

Distribution of this document is unlimited.

**Westinghouse Research Laboratories
Pittsburgh, Pennsylvania 15235**



DISCLAIMER NOTICE



THIS DOCUMENT IS BEST
QUALITY AVAILABLE. THE COPY
FURNISHED TO DTIC CONTAINED
A SIGNIFICANT NUMBER OF
PAGES WHICH DO NOT
REPRODUCE LEGIBLY.

ABSTRACT

An exploratory program was conducted to determine the feasibility of extending the usefulness of fracture mechanics technology in two areas of practical interest: (1) situations of crack instability under combined crack-tip loading conditions, (2) characterization of the fracture behavior to low-to-intermediate strength materials.

In the area of combined loading, calibrations of the crack-tip stress intensity factors were developed for combined modes I-II and modes I-III types of loading. Experimental determinations of the critical crack-tip conditions for fracture were obtained for various ratios of K_I/K_{II} and K_I/K_{III} loading using 7178-T651 and 7075-T651 aluminum alloys. The feasibility of developing an engineering fracture criteria for combined mode loading under plane-strain conditions is demonstrated.

In the area of low-to-intermediate strength materials, established fracture mechanics tests for K_{Ic} fracture toughness and fatigue crack growth rates (da/dN versus ΔK_I) were conducted for AISI 1020, 1045, 1144 and 4140 steels and 7039-T6 aluminum. Existing linear-elastic fracture mechanics technology was found to be directly applicable to all of the materials, except AISI 1020 steel, for the temperature range of 0 to 75°F and the 4 inch section size and metallurgical conditions investigated. Example problems are provided to demonstrate the engineering application of the technology. Existing elastic-plastic analysis were applied to the AISI 1020 steel test data which represented a non plane-strain behavior. The results indicate that the elastic-plastic analysis approach has a good potential for developing an engineering fracture criteria applicable to non-plane-strain fracture conditions.

FOREWORD

The work described in this report was authorized by the Vehicular Components and Materials Laboratory, U.S. Army Tank Automotive Command, Warren, Michigan under Contract No. DAAE 07-67-C-4021, Department of the Army, Project No. 1G024401A105. This project is a portion of an overall program to affect more efficient and effective utilization of materials, and to minimize brittle failure potential in the use of these materials.

In this program the work was conducted simultaneously in two independent phases. Phase I is concerned with crack instability for conditions of combined loading under linear-elastic conditions. Phase II involves an investigation of the applicability of the current linear-elastic fracture mechanics technology to low-to-intermediate strength metals. W. K. Wilson was the principal investigator for Phase I and W. G. Clark, Jr. was principal investigator for Phase II. Technical coordination and program management was the responsibility of E. T. Wessel.

For the convenience of the reader the body of this report has been divided into two independent sections dealing with the two phases of activity, Phase I (Section 6) and Phase II (Section 7). Each of these sections is essentially a self-contained unit. The preceding sections involve a general description of the overall program. This method of presentation is intended to make it convenient for the reader to focus his attention to that portion of the report which is of particular interest to him.

The authors are indebted to the sponsor of this program for having made this research possible, and to the representatives of the Vehicular Components and Materials Laboratory, Messrs. C. J. Kropf, V. H. Pagano and A. Rofe, who served as technical contacts during the course of this work. Appreciation is also expressed to the authors' associates who contributed to various portions of this program; namely

Messrs. L. J. Ceschini, A. J. Bush, L. M. Piraja, R. B. Stouffer, J. A. Fratangelo, J. Malley, and T. Clements of the Materials Testing and Evaluation Laboratory, and Messrs. R. R. Hovan and W. H. Pyle of the Mechanics Department. The valuable comments and suggestions of P. R. Toolin, E. A. Davis, and members of the Analytic Mechanics Section are also acknowledged.

TABLE OF CONTENTS

	Page
Section 1. Introduction.....	1
Section 2. Object.....	4
Section 3. Summary.....	6
Section 4. Conclusions.....	10
Section 5. Recommendations.....	12
Section 6. Combined loading investigation (for detailed table of contents for this section see page 14).....	21
Section 7. Low-to-intermediate strength materials investi- gation (for detailed table of contents for this section see page 151).....	156
Distribution List.....	235
DD Form 1473.....	238

LIST OF ILLUSTRATIONS

A detailed list of illustrations is provided at the beginning of each pertinent section.

	Page
Section 6. Combined loading.....	17
Section 7. Low-to-intermediate strength materials	153

Note: Illustrations, tables, appendices, and references are provided within the pertinent sections (6 and 7).

Section 1

INTRODUCTION

During the past few years there have been rapid advancements in the development and application of linear-elastic (plane-strain) fracture mechanics technology.⁽¹⁻³⁾ Originally much of the work on this technology was focused on the relatively brittle, high-strength materials.⁽³⁻⁶⁾ As a result of this work it has now been generally accepted that the technology, when properly employed, can be a useful engineering tool for the prevention of brittle failures in high-strength metals.

However, the usefulness of the technology is limited to those loading, defect and geometry conditions for which appropriate fracture mechanics expressions have been developed, and to those materials which are sufficiently brittle in the section sizes of practical interest to fracture under essentially plane-strain conditions.

To broaden the practical usefulness of the fracture mechanics technology, a program was undertaken to determine the feasibility of developing modifications and extending the technology in two areas; namely, Phase I, crack tip instability and appropriate expressions for combined or mixed-mode loading, and Phase II, application of linear-elastic fracture mechanics testing techniques and technology to the lower and intermediate strength materials. Both of these areas of investigation are important from the viewpoint of making more practical use of the technology.

Real defects in real structures are often subjected to combined loading conditions such that the mode of crack surface displacements become more complex than the simple displacement modes for

which stress-intensity solutions and experimental verification currently exist. Hence, solutions and associated experimental data for mixed mode conditions are necessary to extend the usefulness of the technology to more practical situations.

Many structures made of low-to-intermediate strength materials are known to be subject to brittle failure. While most of the current experience with linear-elastic fracture mechanics technology has been confined to the higher-strength materials, there are no obvious technical reasons why the technology would not be equally applicable to the lower strength materials when employed in structures having sufficient thickness and other restraints to provide essentially plane-strain conditions.⁽⁷⁾ It has been recently demonstrated that the technology could be applied to very heavy sections of intermediate strength steels.^(8,9) Thus in an attempt to further broaden the range of materials for which the technology may be applicable, established plane-strain testing techniques were applied to several common structural materials of low-to-intermediate strengths and the results were analyzed using existing linear-elastic and elastic-plastic fracture mechanics technology.

In Phase I, both analytical and experimental studies of various combined mode crack-tip loading conditions were conducted using aluminum alloys 7178-T651 and 7075-T651. In the area of low-to-intermediate strength materials, plane-strain fracture toughness and sub-critical crack growth rate tests were conducted on AISI 1020, 1144, 1045 and 4140 steels, and 7039T6 aluminum alloys. This report describes the work conducted and results obtained in each of the above areas of investigation which are directed toward extending the practical usefulness of fracture mechanics technology.

Section 1 References

1. "Fracture Toughness Testing and Its Applications," ASTM, S.T.P. 381 (1965).
2. "Plane-Strain Crack Toughness Testing of High Strength Metallic Materials," ASTM, S.T.P. 410 (1967).
3. E. T. Wessel, W. G. Clark, Jr. and W. K. Wilson, "Engineering Methods for the Design and Selection of Materials Against Fracture," Final Technical Report, Contract DA-30-069-AMC-602(T) June 1966. Available through Defense Documentation Center, Cameron Station, Alexandria, Va., #AD 801005. To be published by John Wiley and Sons.
4. "The Slow Growth and Rapid Propagation of Cracks," Materials Research and Standards, Vol. 1, 1961, p. 389.
5. "Progress In Measuring Fracture Toughness and Using Fracture Mechanics," Materials Research and Standards, Vol. 4, 1964, p. 107.
6. G. R. Irwin, J. M. Krafft, P. C. Paris and A. A. Wells, "Basic Aspects of Crack Growth and Fracture," NRL Report 6598, Nov. 1967.
7. E. T. Wessel, "State-of-the-Art of the WOL Specimen For K_{Ic} Fracture Toughness Testing," Engineering Fracture Mechanics, Vol. 1, No. 1 1968, p. 77.
8. H. D. Greenberg, E. T. Wessel and W. H. Pyle, "Fracture Toughness of Turbine-Generator Rotor forgings," Presented at 2nd National Symposium on Fracture Mechanics, Lehigh University, June 1968. To be published in Engineering Fracture Mechanics 1969.
9. E.T. Wessel, W. G.Clark, and W. H. Pyle, "Fracture Mechanics Technology Applied to Heavy Section Steel Structures," To be published in preprints of Second International Conference on Fracture, Brighton, England, April 1969.

Section 2

OBJECT

The overall objective of the program was to explore the feasibility of extending the practical usefulness of fracture mechanics technology in the following areas:

1. Plane-strain crack instability under combined or mixed mode loading conditions.
2. Applicability of linear-elastic (plane-strain) technology to low-to-intermediate strength materials in moderately thick sections.

Each of these two major objectives have associated sub-objectives as follows:

Phase I Combined Loading

1. Review available analytical solutions and experimental data.
2. Design and develop appropriate test specimens, and associated analytical solutions for the stress intensity factors, for studying the effects of combined modes of crack-tip loading on fracture behavior.
3. Experimentally study fracture behavior under combined modes of crack-tip loading.
4. Evaluate the practical potential of any future work, and if applicable, develop an appropriate program with the ultimate objective of applying the technology to practical situations.

Phase II Low-to-Intermediate Strength Metals

1. Conduct plane-strain (linear-elastic) types of fracture mechanics tests (both fracture toughness and crack growth rate) using established procedures and several commonly employed low-to-intermediate strength materials.
2. Analyze the test results using established linear-elastic procedures.
3. For those results which indicate a non plane-strain behavior, analyze the data using any available analytic elastic-plastic crack-tip solutions.
4. Evaluate the potential of developing an elastic-plastic fracture criteria, and if applicable, develop an appropriate program with the ultimate objective of providing an engineering fracture criteria for a non plane-strain (elastic-plastic) type of brittle fracture.

Section 3

SUMMARY

3.1 General

In order to broaden the practical usefulness of fracture mechanics technology, exploratory investigations were conducted to determine the feasibility of extending the technology to (1) situations of crack instability under combined mode crack-tip loading conditions, and (2) characterizing the fracture behavior of low-to-intermediate strength materials to determine the applicability of linear-elastic fracture mechanics technology to this class of materials.

3.2 Phase I. Combined Loading

Stress intensity calibration curves (K expressions) were developed for combined modes I-II, and modes I-III, types of loading situations. The respective geometries were a center slant cracked plate subjected to tension loading, and circumferentially notched cracked round bar subjected to combined tension (mode I) and torsional (mode III) loading.

Fracture toughness tests to determine combined mode crack instability conditions for various degrees of combined loading were conducted using these two geometries. In the center slant cracked plate various degrees of combined mode I-II were achieved by varying the orientation of the center crack with respect to the uniform stress field. Hence a wide range of K_I/K_{II} ratios were investigated. Aluminum alloy 7178-T651 was used for these tests. The resulting data reported in a K_{Ic} versus K_{IIC} plot indicated an initial gradual increase in K_{Ic} as the K_{IIC} component was increased and then a rapid decline as the pure mode II condition was approached. The plane-strain pure mode I fracture toughness

was 18 ksi $\sqrt{\text{in.}}$. The pure mode II value could not be determined. An analysis of the data in terms of the ratio of the nominal stress at fracture to the yield strength, and the appearance of the load-deflection records, indicated that crack instability occurred under conditions of plane-strain for all K_{Ic}/K_{IIc} ratios investigated. The fracture surfaces were essentially flat and the direction of fracture propagation was approximately normal to the direction of the uniform stress field. This observation suggests that once an instability had occurred under combined mode I-II conditions, the resulting propagation was controlled by mode I. The experiments provided apparent plane-strain $K_{Ic}-K_{IIc}$ crack instability (critical) conditions for the 7178-T651 aluminum alloy studied.

A complete range of K_I/K_{III} conditions were investigated in 7075-T651 aluminum using the circumferentially notched round bar by varying the relative amounts of tension and torsional loads applied. In a K_{Ic} versus K_{IIIc} type of plot, K_{Ic} is essentially constant as the mode III component increases. When the mode III component became appreciable a rapid drop in K_{Ic} was observed. The relative values for pure mode I and mode III were 30 ksi $\sqrt{\text{in.}}$ and 25 ksi $\sqrt{\text{in.}}$ respectively. Based on an analysis of the load-deflection records and the fracture appearance for the specimens tested at various K_I/K_{III} ratios, it appears that the instability values obtained at K_I/K_{III} ratios less than about 0.9 do not represent plane-strain conditions. As the K_I/K_{III} ratio decreased progressively more non-linearity appeared in the load-deflection records with corresponding changes in the appearance of the fracture surfaces. This is indicative of a non plane-strain behavior (excessive plasticity prior to fracture). Hence, the results obtained for most of the K_{Ic}/K_{III} ratios are not entirely geometry independent (plane-strain) toughness values. Larger specimens will be required to obtain plane-strain conditions.

A boundary collocation procedure was used to obtain the stress intensity calibration curve for the center slant crack specimens. The stress intensity calibration curve for the mode III component of the circumferentially cracked round bar specimen was determined by a finite element method. Also a slant edge cracked plate geometry was analyzed

as a possible candidate for a combined mode I-II test specimen by use of a boundary collocation method. The analysis indicated that a specimen of this geometry would not be practical. Hence no experimental tests were conducted using this geometry.

In view of the progress and encouraging results that were made in this exploratory phase of investigation, it appears feasible to determine critical crack instability conditions, analogous to K_{Ic} toughness, for mixed mode loading conditions. An appropriate program to develop such information for practical use was prepared and submitted to the sponsoring agency.*

3.3 Phase II. Low-to-intermediate Strength Metals

In order to assess the applicability of linear-elastic fracture mechanics technology to low-to-intermediate strength metals, plane-strain fracture toughness tests were conducted using an established test method on 4" thick specimens of AISI 1020, 1045, 1144 and 4140 steels, and 7039-T6 aluminum alloy. The range of yield strengths encompassed in these materials was 38 to 78 ksi. For the particular metallurgical conditions and thickness investigated, all of these materials except AISI 1020 steel exhibited a plane-strain fracture behavior within the temperature range of 0 to 75°F. Valid K_{Ic} fracture toughness values were determined. Hence linear elastic fracture mechanics technology is applicable to these materials (except AISI 1020 steel).

In order to fully utilize fracture mechanics technology in cyclic loaded applications, it is also necessary to establish the crack growth rate characteristics of the materials so that appropriate considerations can be applied to the growth of defects from a sub-critical to a critical size. The crack growth rate characteristics of the 5 materials cited above were determined in terms of da/dN vs ΔK_I for a wider range ΔK_I using 4" thick specimens. The applicability of linear-elastic fracture mechanics

*Westinghouse Research Laboratories unsolicited proposal No. 8M307 (Aug. 1968) "Development of Fracture Mechanics Technology for Low-to Intermediate Strength Materials and Combined Loading."

technology to these materials (excluding AISI 1020 steel) is demonstrated in example problems which use the K_{Ic} and crack growth rate data generated in this investigation. Two different applications are treated; a structural beam member loaded in bending, and an internally loaded pressure vessel.

For applications involving materials (such as AISI 1020 steel) which do not exhibit a linear-elastic fracture behavior in the section size, metallurgical condition, and at the temperature of interest, an elastic-plastic failure criteria must be developed to provide quantitative design information. As a first approximation towards determining the feasibility of developing an elastic-plastic fracture criteria, the AISI 1020 steel test results were compared with an existing finite element elastic-plastic stress-strain analysis. It was shown that the elastic plastic analysis can accurately predict the displacements in the 1020 steel specimen subjected to non plane-strain loading. Since the displacements are directly related to the local crack-tip stresses and strains, which in turn control fracture, this technique has the potential for development of an engineering criteria for fracture under non plane-strain (elastic-plastic) conditions. An appropriate program to further develop this potential, and ultimately develop an elastic-plastic fracture criteria was prepared and submitted to the sponsoring agency.*

*Westinghouse Research Laboratories unsolicited proposal No. 8M307 (Aug. 1968) "Development of Fracture Mechanics Technology for Low-to-Intermediate Strength Materials and Combined Loading."

Section 4

CONCLUSIONS

4.1 Phase I. Combined Loading

Specimens and appropriate stress intensity calibration curves were developed to study crack instability conditions under combined modes of crack-tip loading. Experimental determinations were made of the critical conditions for crack instability under various K_I/K_{II} and K_I/K_{III} loading conditions. Plane-strain behavior, hence geometry independent values for various K_I/K_{II} instability conditions are believed to have been determined for 7178-T651 aluminum. For most of the K_I/K_{III} ratios investigated using 7075-T651 aluminum, it is believed that the test specimens were too small to provide suitable plane-strain, geometry-independent values of crack toughness. Based on the results of this exploratory investigation it is concluded that it is feasible to determine critical crack tip instability conditions, analogous to K_{Ic} fracture toughness, for various conditions of combined loading, and such information, when properly developed, will be of practical engineering value for structures involving combined loading. It is further concluded that the analytical methods that were developed to obtain the stress intensity calibration of the combined mode specimens utilized in this program are generally applicable to other geometries and other combined modes of crack loading. A more detailed description of these conclusions may be found in Section 6.1.4.

4.2 Phase II. Applicability of Linear-Elastic Fracture Mechanics Technology for Low-to-Intermediate Strength Metals

Established linear-elastic (plane-strain) fracture toughness tests were conducted on 5 low-to-intermediate strength materials, AISI 1020, 1045, 1144 and 4140 steels and a 7039-T6 aluminum alloy. Both

K_{Ic} fracture toughness and fatigue crack growth rate (da/dN versus ΔK_I) tests were conducted to characterize the fracture behavior of these 5 materials using 4 inch thick specimens. Within the temperature range of 0 to 75°F all of the materials except AISI 1020 steel exhibited plane-strain behavior, hence valid K_{Ic} toughness values were obtained. The fatigue crack growth rates as a function of the applied stress-intensity range (da/dN versus ΔK_I) for all of the materials except the 7039-T6 aluminum conformed to the generalized fracture mechanics crack growth rate law where $da/dN = C_0 \Delta K^n$. The aluminum alloy did not exhibit the usual linear relationship between $\log da/dN$ and $\log \Delta K$.

In an attempt to assess the feasibility of developing an extension of fracture criteria for situations involving non plane-strain (linear-elastic) behavior, of the type observed in the toughness tests of AISI 1020 steel, an existing elastic-plastic stress-strain analysis (developed in Westinghouse programs) was applied to the 1020 steel test results. Good agreement was obtained between the crack surface displacements that were measured experimentally and those predicted from the elastic-plastic analysis. Hence the feasibility of utilizing elastic-plastic analysis for developing a fracture criteria applicable to non linear-elastic behavior was demonstrated.

It is concluded that existing linear-elastic fracture mechanics technology is directly applicable to AISI 1045, 1144, and 4140 steels and the 7039-T6 aluminum for the section size and metallurgical conditions that were investigated. It is further believed that the technology may be equally applicable to other materials in this low-to-intermediate strength category when employed in reasonably thick sections. It is further concluded that it is feasible to develop an appropriate modified fracture criteria applicable to materials and application situations where a non plane-strain behavior occurs. An elastic-plastic analyses approach to this problem appears promising. Detailed conclusions relative to the low-to-intermediate strength materials may be found in Section 7.4.

Section 5

RECOMMENDATIONS

On the basis of the results obtained and the progress demonstrated in present exploratory investigations, it is recommended that a development program be undertaken to continue developing modifications and extending fracture mechanics in the two areas of practical interest. The ultimate objectives of the continuing program are to develop engineering fracture criteria applicable to:

(1) Various combined mode crack-tip displacements under plane-strain (linear-elastic) loading conditions.

(2) Material and application conditions where the amounts of crack-tip plasticity prior to brittle fracture result in a non plane-strain behavior.

More details concerning these recommendations are given in Sections 6.1.5 and 7.5. A specific detailed program directed to accomplishing the objectives cited above has already been provided in another document.*

It is also recommended that an internal program be undertaken by TACOM to exploit the currently available linear-elastic fracture mechanics technology for use in areas such as: materials evaluation and selection, design, specifications and acceptance standards, inspection requirements, component integrity and life expectancy evaluations. The technology is sufficiently well advanced to be of considerable practical value in the above areas, and is applicable to a wide variety of

*Westinghouse Research Laboratories unsolicited proposal No. 8M307 (Aug. 1968), "Development of Fracture Mechanics Technology for Low-to-Intermediate Strength Materials and Combined Loading."

materials and applications. The technology provides a quantitative means of effectively and efficiently tailoring the material and fabrication requirements to the exact needs of the application. The information developed and supplied in the present and previous contracts (DA-30-069-AMC-602 (T)) should be useful in this regard.

TABLE OF CONTENTS

Section 6

COMBINED MODE LOADING OF CRACKS

	<u>Page</u>
6.1 INVESTIGATION OF COMBINED MODE LOADING.....	21
6.1.1 Introduction.....	21
6.1.2 Objectives.....	23
6.1.3 Summary.....	24
6.1.4 Conclusions.....	26
6.1.5 Recommendations.....	27
6.2 TEST SPECIMEN TO STUDY CRACK INSTABILITY IN METALS UNDER COMBINED MODE I AND II LOADING.....	31
6.2.1 Introduction.....	31
6.2.2 Test Specimen Geometry and Loading Conditions.....	31
6.2.3 Specimen Preparation.....	32
6.2.4 Fracture Test Procedure.....	34
6.2.5 Results and Conclusions.....	34
6.3 TEST SPECIMEN TO STUDY CRACK INSTABILITY IN METALS UNDER COMBINED MODE I AND III LOADING.....	54
6.3.1 Introduction.....	54
6.3.2 Test Specimen Geometry and Loading Conditions.....	54
6.3.3 Precracking Procedure.....	55
6.3.4 Testing Procedure.....	56
6.3.5 Results and Conclusions.....	58
6.4 COLLOCATION METHOD FOR CALCULATING STRESS INTENSITIES FOR FINITE PLATES CONTAINING AN INTERIOR THROUGH THICKNESS CRACK.....	73
6.4.1 Introduction.....	73
6.4.2 Theoretical Development.....	73
6.4.3 Application.....	77
6.4.4 Conclusions.....	78

TABLE OF CONTENTS (cont.)

	<u>Page</u>
6.5 A FINITE ELEMENT METHOD FOR DETERMINING STRESS INTENSITY FACTORS OF CIRCUMFERENTIALLY CRACKED ROUND BARS.....	88
6.5.1 Introduction.....	88
6.5.2 Finite Element Method.....	89
6.5.3 Torsional Ring Element.....	92
6.5.4 Crack Tip Element.....	96
6.5.5 Application to Circumferentially Cracked Round Bar.....	100
6.5.6 Conclusions.....	102
6.6 ANALYSIS OF EDGE SLANT CRACK SPECIMEN.....	119
6.6.1 Introduction.....	119
6.6.2 Williams Stress Function.....	119
6.6.3 Procedure.....	122
6.6.4 Study of Convergence.....	123
6.6.5 Conclusions.....	124
 APPENDIX I INTEGRATION OF COMPLEX FUNCTIONS.....	138
APPENDIX II BOUNDARY CONDITIONS OF AIRY STRESS FUNCTION FOR CENTER CRACKED PLATE.....	139
APPENDIX III METHOD OF SOLUTION OF SIMULTANEOUS LINEAR ALGEBRAIC EQUATIONS.....	140
APPENDIX IV STRAIN ENERGY OF MODE III CRACK TIP ELEMENT.....	143
APPENDIX V BOUNDARY CONDITIONS OF AIRY STRESS FUNCTION FOR EDGE CRACKED PLATE.....	145
APPENDIX VI LEAST SQUARE SOLUTION OF A SYSTEM OF SIMULTANEOUS LINEAR ALGEBRAIC EQUATIONS.....	148

LIST OF TABLES

Section 6

COMBINED MODE LOADING OF CRACKS

	<u>Page</u>
Section 6.2	
TABLE I Geometry of Center Slant Crack Specimens.....	37
TABLE II Results of $K_I - K_{II}$ Combined Mode Plate Tests.....	38
Section 6.3	
TABLE I Results of $K_I - K_{III}$ Combined Mode Round Bar Tests.....	61
Section 6.4	
TABLE I Influence of Number of Collocation Points on K_I^* and K_{II}^*	81
Section 6.5	
TABLE I Influence of Element Refinement on Calculated Stress Intensity.....	104
Section 6.6	
TABLE I Influence of M on K_*^* For 47 Boundary Stations....	127
TABLE II Influence of M on K For 55 Boundary Stations....	128

LIST OF FIGURES

Section 6

COMBINED MODE LOADING OF CRACKS

	<u>Page</u>
Section 6.1	
Figure 1. Basic modes of crack surface displacements.....	29
Figure 2. Coordinates measured from the leading edge of a crack and stress components in crack tip stress field.....	30
Section 6.2	
Figure 1. Loading condition for center slant crack specimen.....	40
Figure 2. Drawings of center slant crack specimens.....	41
Figure 3. EDM slot extending from 1/8 in. hole.....	42
Figure 4. Precracking operation for center slant crack specimen.....	43
Figure 5. Drawing of precracking geometry for center slant crack specimens.....	44
Figure 6. Fatigue precracking and fracture specimen geometries.....	45
Figure 7. Fatigue precracking of specimens.....	46
Figure 8. Fracture testing of center slant crack test specimen.....	47
Figure 9. Clip gage used to establish load deflection curves.....	48
Figure 10. Apparent combined Mode I-II critical stress intensity factors for aluminum alloy 7178-T651....	49

Figure 11. Effect of crack orientation on load-deflection curve.....	50
Figure 12. Fracture surfaces of center slant crack specimens.....	51
Figure 13. Fracture directions of center slant crack specimens.....	52
Figure 14. Angle of crack propagation.....	53

Section 6.3

Figure 1. Loading condition for circumferentially cracked round bar specimen.....	62
Figure 2. Drawing of circumferentially notched round bar specimen.....	63
Figure 3. Precracking and final test geometry of $K_I - K_{III}$ notched round bar specimen.....	64
Figure 4. Fatigue precracking rotating beam machine.....	65
Figure 5. Torsion-tension test machine and auxiliary equipment used in the testing of precracked notched round bars.....	66
Figure 6. Load cell calibration curves.....	67
Figure 7. Measuring axial and angular deflections with clip gages.....	68
Figure 8. Recorded information for $K_I - K_{III}$ round bar specimens.....	69
Figure 9. Apparent combined Mode I-III critical stress intensity factors for aluminum alloy 7075-T651...	70
Figure 10. Effect of K_I/K_{III} loading ratio on load-deflection curve for circumferentially cracked round bar specimens.....	71
Figure 11. Fracture surfaces for various K_I/K_{III} loading ratios.....	72

Section 6.4

Figure 1.	Plate with through crack.....	82
Figure 2.	Geometry and loading condition assumed for center slant crack specimen.....	83
Figure 3.	Geometry and coordinates for collocation solution of center cracked specimen.....	84
Figure 4.	K_I^* and K_{II}^* as a function of number of boundary collocation points. The boundary conditions are U and dU/dN	85
Figure 5.	$K_I - K_{II}$ curves for center slant cracked specimens.....	86
Figure 6.	K_I^* and K_{III}^* as a function of number of boundary collocation points. The boundary conditions are $\partial U / \partial n$ and $\partial U / \partial s$	87

Section 6.5

Figure 1.	Finite element representation of plane region.....	105
Figure 2.	Finite element representation of axisymmetric solid.....	106
Figure 3.	Circular ring element with triangular cross-section.....	107
Figure 4.	Linear shear surface traction on boundary surface of a boundary element.....	108
Figure 5.	Finite element representation of hollow cylinder.....	109
Figure 6.	Comparison of finite element solution with exact solution for hollow cylinder subject to torsion.....	110
Figure 7.	Circular crack tip element and first two rings of enclosing triangular element mesh.....	111
Figure 8.	Relative crack tip element coordinate and dimensions.....	112
Figure 9.	Finite element representation of circumferentially cracked round bar.....	113

Figure 10.	Crack-tip element and surrounding triangular elements.....	114
Figure 11.	K_{III}^* as a function of number of nodal points for $r_c/R_c = 0.5$	115
Figure 12.	Deflections for circumferentially cracked bar subject to torque (T) as determined by finite element method.....	116
Figure 13.	K_{III} calibration for circumferentially cracked round bar subject to torsion.....	117
Figure 14.	Finite element representation of circumferentially cracked round bar with 60° V notch.....	118

Section 6.6

Figure 1.	Loading condition for edge slant crack specimen.....	129
Figure 2.	General coordinates for plane elasticity.....	130
Figure 3.	Geometry and coordinates for collocation solution of edge slant crack specimen.....	131
Figure 4.	K_I^* as a function of number of coefficients used to satisfy boundary conditions in least square sense at 23 boundary points.....	132
Figure 5.	K_I^* as a function of number of coefficients used to satisfy boundary conditions in least square sense at 47 boundary points.....	133
Figure 6.	K_I^* and K_{II}^* as a function of number of coefficients used to satisfy boundary conditions in the least square sense at 27 boundary points.....	134
Figure 7.	K_I^* and K_{II}^* as a function of number of coefficients used to satisfy boundary conditions in the least square sense at 27 boundary points.....	135
Figure 8.	K_I-K_{II} curves for edge cracked plates subject to uniform tension.....	136
Figure 9.	K_I-K_{II} curve for edge cracked plates subject to bending.....	137

Section 6.1

COMBINE MODE LOADING OF CRACKS

6.1 INVESTIGATION OF COMBINED MODE LOADING

6.1.1 INTRODUCTION

The stress fields around crack tips can be divided into three components, each associated with a mode of crack surface displacement as shown in Figure 1. These modes are: (I) the opening mode where crack surface displacement is perpendicular to the plane of the crack; (II) the edge sliding mode where the edges slide over each other in a direction perpendicular to the leading edge of the crack; and (III) the tearing mode where the crack surfaces slide over each other in a direction parallel to the leading edge of the crack. In terms of the coordinate system shown in Figure 2, the local crack tip stress field corresponding to each mode of crack surface displacement are listed below.⁽¹⁾

Mode I:

$$\sigma_x = \frac{K_I}{(2\pi r)^{1/2}} \cos \frac{\theta}{2} \left[1 - \sin \frac{\theta}{2} \sin \frac{3\theta}{2} \right]$$

$$\sigma_y = \frac{K_I}{(2\pi r)^{1/2}} \cos \frac{\theta}{2} \left[1 + \sin \frac{\theta}{2} \sin \frac{3\theta}{2} \right]$$

$$\tau_{xy} = \frac{K_I}{(2\pi r)^{1/2}} \sin \frac{\theta}{2} \cos \frac{\theta}{2} \cos \frac{3\theta}{2}$$

$$\sigma_z = \nu (\sigma_x + \sigma_y) \quad \tau_{xz} = \tau_{yz} = 0$$

Mode II:

$$\sigma_x = - \frac{K_{II}}{(2\pi r)^{1/2}} \sin \frac{\theta}{2} \left[2 + \cos \frac{\theta}{2} \cos \frac{3\theta}{2} \right]$$

$$\sigma_y = \frac{K_{II}}{(2\pi r)^{1/2}} \sin \frac{\theta}{2} \cos \frac{\theta}{2} \cos \frac{3\theta}{2}$$

$$\tau_{xy} = \frac{K_{II}}{(2\pi r)^{1/2}} \cos \frac{\theta}{2} \left[1 - \sin \frac{\theta}{2} \sin \frac{3\theta}{2} \right]$$

$$\sigma_z = v (\sigma_x + \sigma_y) \quad \tau_{xz} = \tau_{yz} = 0$$

Mode III:

$$\tau_{xz} = - \frac{K_{III}}{(2\pi r)^{1/2}} \sin \frac{\theta}{2}$$

$$\tau_{yz} = \frac{K_{III}}{(2\pi r)^{1/2}} \cos \frac{\theta}{2}$$

$$\sigma_x = \sigma_y = \sigma_z = \tau_{xy} = 0$$

The Mode I and II stress fields given are for plane strain conditions. The stress intensity factor (K_I , K_{II} , K_{III}) associated with each mode controls the magnitude of the stress distribution for that mode.

By extending the principles of crack instability as presented by Irwin,^(2,3) it can be hypothesized that slow crack extension will begin when some functional relation $g(K_I, K_{II}, K_{III})$ of the three stress intensity components reaches a critical value. This critical value would be considered as a material property and be subject to the small scale yielding limitations associated with linear fracture mechanics. For pure Mode I crack loading conditions the validity of the critical stress intensity factor concept has been well documented.

The objective of the work to be reported in this section is to extend the critical stress intensity concept to combined mode loading conditions in metals.

Some combined mode experimental work has already been carried out on isotropic plexiglas plates by Erdogan and Sih⁽⁴⁾ and on orthotropic fiberglass plates by Wu⁽⁵⁾. In both studies combined Mode I-II conditions were investigated. For both brittle materials the combined mode $f(K_I, K_{II})$ critical stress intensity concept was found to be applicable for the plate thicknesses tested. The principal specimen geometry used in each of these investigations was a center cracked plate whose in plane dimensions were large compared to the crack length.

Nearly all fracture mechanics experimental studies have been concerned with the Mode I symmetric loading condition. While a very large majority of engineering applications of fracture mechanics to structures are of the Mode I type, a number of situations exist for which combined mode conditions are present. For example cracks in bars loaded in combined torsion and bending could be subject to all three modes of crack surface displacement. Penny shaped cracks in a uniform tension and shear field⁽⁶⁾ can be operated on by all three modes of crack tip loading. Similar situations can occur for cracks in complex stress fields similar to those around pressure vessel nozzles. Under cyclic loading a crack which may initially exist under combined mode conditions, will tend to grow into a Mode I condition. But if the crack is initially large enough, failure may occur before the pure Mode I condition is reached. For these reasons it is apparent that some preliminary investigations of combined mode crack instability should be carried out for metallic materials.

6.1.2 OBJECTIVES

The general objective of this phase of the work was to investigate two types of combine mode conditions: (a) Mode I-II and (b) Mode I-III. The specific objectives of the program are listed below.

1. Design and develop a fracture mechanics test specimen which can be used to study combined Mode I-II crack instability conditions. Obtain an analytic solution for the test specimen. Carry out preliminary experimental testing with the specimen for a metallic material.

2. Task (2) is the same as task (1) except that a combined Mode I-III specimen is to be designed, analyzed, and tested.

3. Assess the feasibility of achieving a practical combined mode fracture criteria, and if applicable, develop an appropriate program to accomplish this objective.

The development and experimental testing of a Mode I-II specimen is reported in Section 6.2. The method of analysis of the specimen is given in Section 6.4. The Mode I-III specimen development and preliminary testing is described in Section 6.3 and the corresponding analysis is presented in Section 6.5. A method of analysis which can be applied to edge cracked plates subjected to Mode I-II loading conditions is described in Section 6.6. This analysis is the result of studies carried out under task (1).

6.1.3 SUMMARY

(1) A center slant cracked plate specimen was developed for combined Mode I-II fracture testing. By varying the orientation of the center crack with respect to the uniform stress field, a wide range of the K_I/K_{II} ratio can be obtained. A precracking technique was also developed. The stress intensity calibration curve was derived by a boundary collocation method. Fourteen specimens of aluminum alloy 7178-T651 were tested. The specimens were 0.45 in. thick and 2.0 in. wide. The data reported in a K_{Ic} versus K_{IIc} plot indicated an initial increase in K_{Ic} as K_{IIc} begins to increase from zero (pure K_I condition). Also as the K_{Ic}/K_{IIc} ratio decreases, the data scatter increases. The non-linearity at fracture in the load-deflection records increased with decreasing K_{Ic}/K_{IIc} , but was never appreciable.

The ratio of the nominal stress to the yield stress at instability in all but two of the specimens was less than 0.72, indicating an absence of gross yielding. The fracture surfaces were essentially flat and the direction of crack propagation was approximately normal to the direction of the uniform stress field.

(2) A circumferentially notch cracked round bar specimen was selected for combined Mode I-III fracture testing. The specimen is subject to combined tension (Mode I) and torsion (Mode III) loading. With this specimen, a complete range of the K_I/K_{III} ratio can be investigated. The Mode III stress intensity component calibration was obtained by a finite element method. Eleven specimens of aluminum alloy 7075-T651 having an outer diameter of $D = 1.5$ in. were tested. The specimens were precracked by fatigue and load-deflection records were obtained (either tensile load-axial displacement or torque load-angular displacement). The fracture data is recorded in a K_{Ic} versus K_{IIIC} plot. The load-deflection records indicate that for the size specimens tested appreciable nonlinearity occurred just prior to fracture. This is particularly true of the tests where K_{III} was predominant. The ratio of nominal stress to yield stress for the specimens in which appreciable nonlinearity of deflection occurred were well above unity. The pure Mode III critical stress intensities measured (25 ksi $\sqrt{\text{in.}}$) were less than the pure Mode I critical intensities measured (30 ksi $\sqrt{\text{in.}}$). As the combine loading changes from a pure Mode I loading condition to a pure Mode III loading condition, the fracture surface changes from one which is nearly flat to one in which the original fatigue crack has divided into a series of cracks which all propagate out of the original crack plane. The lower the K_I/K_{III} ratio the greater is the angle at which the crack leaves the original plane.

(3) Stress intensity calibration curves were obtained for the center slant crack specimen by a boundary collocation procedure. An existing complex stress function was converted to the form of an Airy stress function. The point matching technique was carried out on the Airy stress function and its normal derivative.

(4) The Mode III stress intensity calibration curve for the circumferentially notched crack specimen was obtained by a finite element method. The method combines triangular cross section ring elements with a circular cross-section ring element which encloses the crack tip. The defined displacement pattern for the crack tip element is the classical Mode III displacement field in terms of K_{III} .

(5) An edge cracked plate was analyzed as a candidate for a combined Mode I-II test specimen. A least square point matching method involving both the even and odd terms of the Williams stress function was used. The analysis indicated a specimen of this geometry would not be practical.

6.1.4 CONCLUSIONS

(1) A combined Mode I-II test specimen has been developed. Stress intensity calibration curves have been obtained for the center slant crack test specimen. Specimens of 7178-T651 aluminum alloy, 0.45 in. plate, were tested over a wide range of K_I/K_{II} ratios. An apparent plane strain $K_{Ic} - K_{IIc}$ crack instability curve was estimated for the alloy.

(2) A circumferentially notch cracked round bar specimen subject to combine tension and torsion was selected as the specimen for combined Mode I-III fracture tests. A calibration curve for the Mode III stress intensity component was derived. Specimens of 7075-T651 aluminum alloy were tested over the complete range of the ratio K_I/K_{III} . The non-linear load-deflection records for the specimens in which the K_{III} component was predominant indicates that a significant amount of plastic flow occurred prior to fracture in the 1.5 in. outer-diameter specimens. Under these conditions the combined mode critical stress intensities cannot be considered as geometry independent.

(3) The boundary collocation method derived for the analysis of the center cracked plate specimens can also be applied to plates of arbitrary geometry and in plane loading which contain an interior through the thickness crack.

(4) The finite element method developed for the analysis of the Mode III component of the circumferentially cracked round bar specimen also has general applicability. The triangular cross-section ring elements can be used for the analysis of arbitrary bodies of revolution subject to torsion. The use of the special crack tip element can be extended to all other modes of crack loading.

(5) The boundary collocation technique applied to the edge slant cracked plates subject to uniform tension and pure bending can, in general, be applied to any edge cracked plate subject to in plane loading.

6.1.5 RECOMMENDATIONS

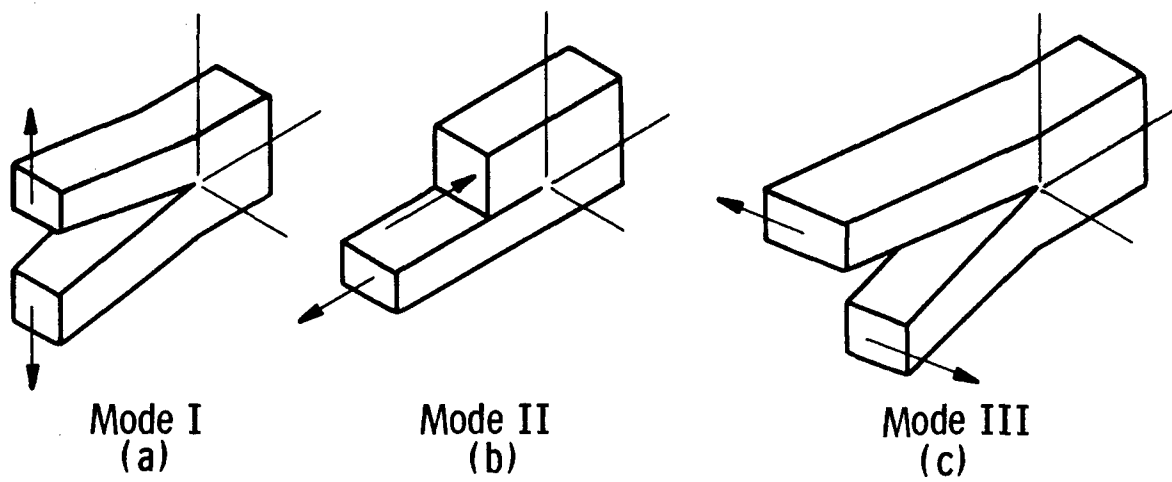
(1) It is recommended that testing continue with the Mode I-II center cracked specimen. Larger plate specimens of 7178-T651 should be tested to determine if the combined mode critical stress intensities reported here are geometry independent values. In addition the size requirements for this combined mode specimen should be established experimentally.

(2) Due to the presence of a significant amount of plastic flow in some of the combined Mode I-III round bar 7075-T651 specimens, it is recommended that larger specimens be tested. The size of the specimens tested and reported here was limited by the load capacity of the torsion-tension machine which was available. By testing larger specimens, it could be determined if a geometry independent combined Mode I-III critical stress intensity relation exists.

Section 6.1 References

1. P. C. Paris and G. C. Paris, "Stress Analysis of Cracks," ASTM Special Technical Publication No. 381.
2. G. R. Irwin, "Analysis of Stresses and Strains Near the End of a Crack Traversing a Plate," Journal of Applied Mechanics, Vol. 24, Trans. ASME, Vol. 79, 1957.
3. G. R. Irwin, "Fracture," Handbuck der Physik, Vol. 6, Springer, pp, 551-590.
4. F. Erdogan, "On the Crack Extension in Plates Under Plane Loading and Transverse Shear," Journal of Basic Engineering, December 1963.
5. E. M. C. Wu, "A Fracture Criterion for Orthotropic Plates Under the Influence of Compression and Shear," Ph.D. dissertation, University of Illinois, 1965.
6. M. K. Kassir and G. C. Sih, "Three-Dimensional Stress Distribution Around an Elliptical Crack Under Arbitrary Loading," Journal of Applied Mechanics, Sept. 1966.

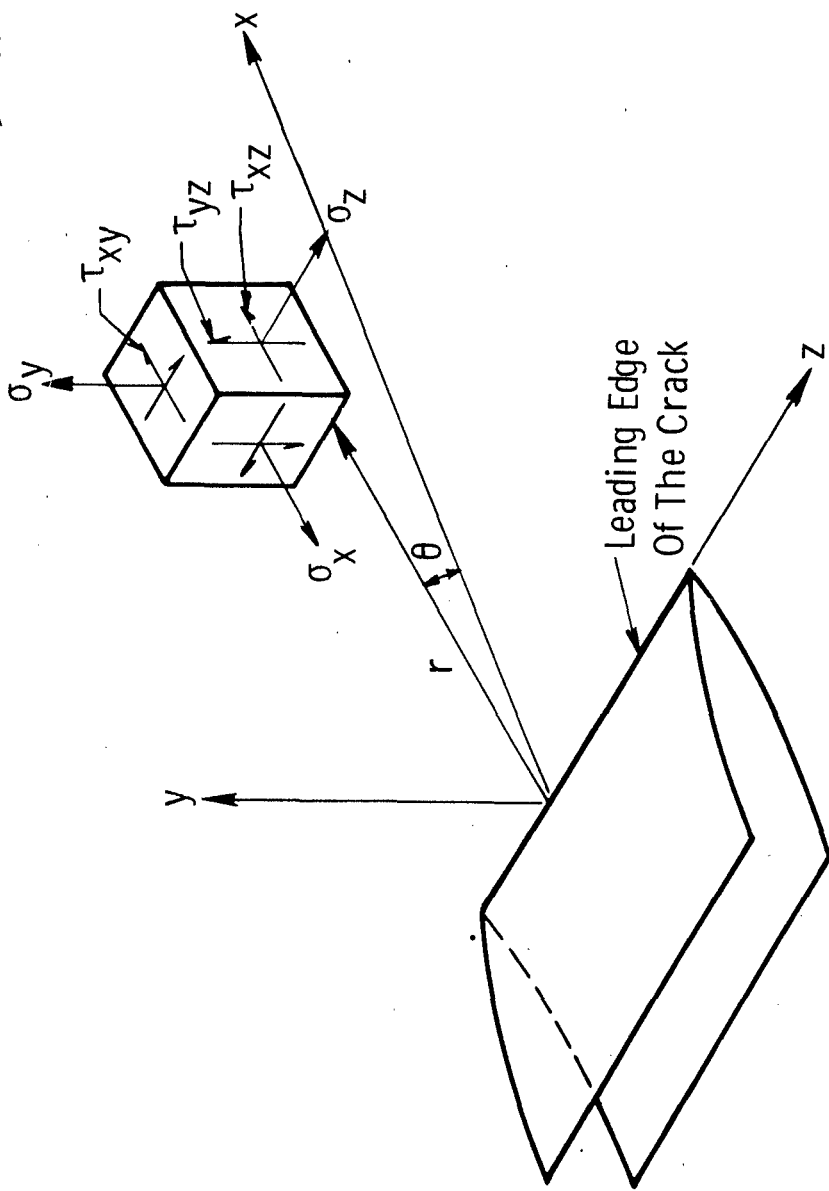
Dwg. 748A456



Sec. 6.1 Fig. 1—Basic modes of crack surface displacements

Sec. 6.1 Fig. 2—Coordinates measured from the leading edge of a crack and the stress components in the crack tip stress field

Dwg : 851A661



Section 6.2

TEST SPECIMEN TO STUDY CRACK INSTABILITY IN METALS UNDER COMBINED MODE I AND II LOADING

6.2.1 INTRODUCTION

The objective of this phase of the program was to develop a fracture mechanics test specimen which could be used to study crack instability in metals under combined Mode I-II conditions. The specific objectives undertaken were:

- (1) to design a small test specimen with low load requirements by which a wide range of K_I/K_{II} crack tip conditions can be produced,
- (2) to develop a precracking technique for this type of specimen.

6.2.2 TEST SPECIMEN GEOMETRY AND LOADING CONDITIONS

After a comprehensive study of possible geometries and loading conditions by which a wide range of K_I/K_{II} ratio's could be obtained in metals, it was concluded that the most practical type of specimen to use in the investigation is a center cracked plate specimen of finite width. The center crack is oriented at various angles (ϕ) with respect to a uniform tension field (Fig. 1) applied by pin loading. By varying the orientation of the crack, the K_I/K_{II} ratio at the crack tip can be varied as shown by the K-calibration curves presented in Fig. 5 of Section 6.4 for this loading condition. A study of these curves indicates that as ϕ approaches 90° , a pure K_{II} condition is approached but simultaneously K_{II} approaches zero. Therefore it is only practical to vary the crack angle ϕ between zero degrees and some value less than 90° . This means

that a pure K_{II} condition cannot be obtained with this specimen. But a wide range of K_I/K_{II} crack tip conditions can be investigated. This range includes many crack tip loading conditions found in structures.

A ratio of total crack length to width of $(2a/W) = 0.5$ was selected for the specimens. This is the same ratio presently recommended by ASTM for center cracked ($\phi = 0$) test specimens used in K_{Ic} testing. As shown by the calibration curve of Fig. 5 (Section 6.4) a wide K_I/K_{II} range can be obtained for this ratio with a relatively small specimen which has a low load requirement.

The material used in the initial experimental investigation of the specimen was high strength aluminum alloy 7178-T651. The 0.2% yield strength of the material is 80,000 psi. The material was purchased in a 0.5 in. plate thickness and the plate specimens tested were approximately $B = 0.45$ in. thick. Cracks were always oriented in the transverse direction of the original plate. The width (W) of the specimens tested was 2.0 in. Based on the K_{Ic} (19,300 $\text{psi}\sqrt{\text{in.}}$) for this material, $W = 2.0$ in. exceeds by almost a factor of two the width requirement recommended by ASTM⁽¹⁾ for the corresponding K_{Ic} test specimen ($\phi = 0$).

The drawings for the specimen geometries tested are shown in Fig. 2. Geometry (1) is for specimens having a large crack angle (ϕ) and having a relatively higher loading requirement whereas geometry (2) is for specimens with smaller crack angles. Specimens having crack angles of 0° , 22.5° , 45° , 67.5° , and 75° were tested. The specimen dimensions, corresponding to those defined in Fig. 2, for each crack orientation are listed in Table I.

6.2.3 SPECIMEN PREPARATION

The representative crack in each plate specimen is produced by extending fatigue cracks from each end of a 0.009" width slot cut into the plate by an electrical discharge machine. The electrical cut is made by a moving wire. A 1/8" diameter center hole is initially drilled through the specimen to provide an entry point for the wire. The hole is located at the center of the slot and its diameter is small enough such that it will not effect the stress field around the crack tips. The center hole and EDM slot are shown in Fig. 3.

The length of the EDM slot is 0.70 in. The final crack length of $2a = 1.0$ inch is then achieved by extending a fatigue crack from both ends of the slot. The fatigue crack must extend in the plane of the slot. The direction of growth of the fatigue crack created a problem. If a cyclic tensile load is produced in the direction in which the final fracture load is to be applied the fatigue crack will grow out of the plane of the slot and tend to move in a direction perpendicular to the uniaxially applied load. Therefore to extend fatigue crack in the plane of the EDM slot the sequence of operations illustrated in Fig. 4 was used in specimen preparation. The steps involved are:

- (a) Initially the 1/8 in. center hole and EDM slot are machined into a proper size plate (Fig. 4a). Also fatigue loading pin holes are placed on a line perpendicular to and bisecting the slot as shown. The loading holes are placed at a minimum distance from the slot to minimize the fatigue load need. Side slots terminated with circular holes are machined into the specimen to also reduce the required fatigue load. The size of the plate, the distance of the fatigue load pin holes from the slot, and the depth of the side slots are all minimized so that the final specimen geometry can just be cut from the plate after the fatigue crack has been extended from the EDM slot.
- (b) Fatigue cracks are initiated and grown from the slot ends by cyclic loading applied at the loading pin holes (Fig. 4b).
- (c) The final specimen geometry (Fig. 4c) is cut from the plate such that the crack is at the desired orientation with respect to the axis of the final fracture load.

The significant dimensions of the fatigue plate geometries for each crack orientation are defined in Fig. 5 and listed in Table I. The precracking specimens and the final fracture specimens are shown in Fig. 6.

The fatigue cracks were initiated at a cyclic K_{max} of approximately 0.70 K_{Ic} and grown to their final length at a cyclic K_{max} level of less than 0.50 K_{Ic} . The hydraulic cyclic fatigue machine used is shown in Fig. 7. Alignment was maintained by the loading pins and the spherical seat at the bottom of the box frame. The final crack length for each specimen is listed in Table II. The fatigue crack surfaces of the specimens can be seen in Fig. 12.

6.2.4 FRACTURE TEST PROCEDURE

After the specimens were machined to final test geometry they were loaded to failure. The loading was performed in the universal testing machine shown in Fig. 8 along with the supplementary electronic equipment used. Alignment was maintained by the loading pins and universal joints. Deflections were measured by a pair of clip gages (one on each surface) spanning the crack as shown in Fig. 9. The deflections were measured in the loading direction over a 2.0 in. gage length. Each clip gage was presprung between two small blocks which were screwed to the specimen. Load deflection records were made for each specimen.

6.2.5 RESULTS AND CONCLUSIONS

The data obtained from the 14 specimens tested are listed in Table II. The critical stress intensities are shown in Fig. 10 in a K_I versus K_{II} plot. Load deflection records for various crack orientations are presented in Fig. 11.

A study of Fig. 10 reveals a number of interesting features. As the K_{II}/K_I ratio increases the data scatter increases. Also as the K_I/K_{II} ratio increases from zero an initial increase in K_{Ic} can be observed. Similar trends can be observed in the data reported by Erdogan and Sih⁽²⁾ for large plexiglass plates. The dashed line shown in the figure represents a tentative minimum failure locus for the material tested. The curve is extrapolated toward a pure K_{II} instability condition. More data are needed to further substantiate this curve. The average $K_{Ic} = 19,300$ psi $\sqrt{\text{in.}}$ reported for $K_{II} = 0$ ($\phi=0$)

compares favorably with the 18,400 psi $\sqrt{\text{in.}}$ value reported by Kaufman and Holt⁽³⁾ for the same material.

The load deflection curves shown in Fig. 11 indicate that the higher the K_{II}/K_I ratio (or crack angle ϕ) for this specimen the greater the amount of nonlinearity at crack instability. But for all crack angles the degree of non-linearity in the curves is small. It should also be noted that at equal load levels the specimen with the smaller crack angle (ϕ) will have a greater amount of non-linearity in the load deflection curve. This is because the size of the plastic zone is larger for a smaller angle and the same load level. Also the deflection measured by the clip gage becomes less sensitive to crack tip plastic flow the larger the crack angle.

In Table II the ratio of the gross stress $\sigma_g = P/(BW)$ to the yield stress (σ_g/σ_{YS}) is given. Also listed is the ratio of nominal stress

$$\sigma_n = \frac{P}{B(W - 2a \cos \phi)}$$

to the yield stress (σ_n/σ_{YS}) where the nominal stress is based on the projected areas of the crack in the direction of loading. For all but two of the specimens $(\sigma_g/\sigma_{YS}) \leq 0.57$ and $(\sigma_n/\sigma_{YS}) \leq 0.72$. This indicates the general absence of gross yielding.

Typical fracture surfaces of the specimens are shown in Figs. 12 and 13. The surfaces are flat fractures. The direction of crack propagation is always approximately normal to the loading direction. The angle of deviation of the propagation direction from the normal to the loading direction (as defined in Fig. 14) is given in the table of Fig. 14. Also listed in the table are the corresponding angles calculated from the analysis of Ref. 2. As observed there is no agreement. The analytic method of Ref. 2 accurately predicted the propagation direction for the cracked plexiglas plates discussed in that paper. But as would be expected the analysis doesn't apply to the aluminum plates due to the presence of substantially more plastic flow at the crack tips.

The mixed mode critical stress intensities listed in Table II and shown in Fig. 10 must be considered as apparent values. At present it can't be shown that the specimens tested were large enough to give geometry independent combined mode critical stress intensities. The Mode I criteria as proposed by ASTM can be applied, but it can't be expected that this criteria will be directly applicable to the mixed condition. But it is worth noting that the dimensions of all specimens tested satisfy the criteria $a \geq 2.5 (K_e / \sigma_{YS})^2$ and $b \geq 2.5 (K_e / \sigma_{YS})^2$ where $K_e = (K_{Ic}^2 + K_{IIc}^2)^{1/2}$. The only certain way of determining whether the critical stress intensities measured are geometry independent plane strain values is to test larger specimens.

Future development of the combined Mode I-II specimen should include:

- (1) testing of larger specimens of 7178-T651 to investigate the geometry independence of the combined mode critical stress intensity factors.
- (2) testing of tougher materials than 7178-T651 under combined Mode I-II conditions.

Section 6.2 Table I

GEOMETRY OF CENTER SLANT CRACK SPECIMENS ($K_I - K_{II}$)

Specimen Number	Fracture Geometry*							Precracking Geometry**			
	ϕ°	Type*	W	H	H_1	H_2	W_1	W_2	W_3	H_3	H_4
1, 2	0	2	2.00	3.13	4.25	-	-	-	-	-	-
3, 4, 5	22.5	2	2.00	3.38	4.50	-	-	5.50	1.65	11.00	3.70
6, 7, 8, 9	45	2	2.00	3.63	5.00	-	-	9.00	2.35	9.00	2.25
10, 11, 12, 13	67.5	1	2.00	3.75	5.63	2.75	3.00	12.00	5.10	7.50	1.75
14	75	1	2.00	3.75	5.63	2.75	3.00	12.00	-	7.50	1.75

* Fig. 2

** Fig. 5

Section 6.2 Table II

RESULTS OF $K_I - K_{II}$ COMBINED MODE PLATE TESTS

Spec. No.	ϕ°	Crack Length 2a(in.)	Thickness B(in.)	Ultimate Load (lbs.)	$\frac{\sigma_g}{\sigma_{YS}}$	$\frac{\sigma_n}{\sigma_{YS}}$	K_{Ic} (psi $\sqrt{\text{in.}}$)	K_{IIc} (psi $\sqrt{\text{in.}}$)
1	0	1.07	0.45	11,300	0.16	0.32	20,000	0
2	0	1.11	0.45	11,150	0.15	0.32	20,700	0
3	22.5	1.09	0.45	13,800	0.19	0.37	21,100	7,500
4	22.5	1.11	0.45	14,000	0.20	0.38	21,900	7,800
5	22.5	1.06	0.45	13,700	0.19	0.37	20,500	7,400
6	45	1.06	0.43	22,200	0.32	0.50	20,700	18,200
7	45	1.06	0.44	25,400	0.36	0.56	23,100	20,300
8	45	1.03	0.46	23,700	0.32	0.49	20,400	18,100
9	45	1.11	0.46	24,000	0.33	0.52	21,900	19,000
10	67.5	1.07	0.44	38,125	0.54	0.68	10,400	22,200
11	67.5	1.01	0.46	40,100	0.55	0.68	10,200	22,000
12	67.5	1.06	0.45	53,200	0.74	0.93	14,100	30,300
13	67.5	1.10	0.45	41,500	0.57	0.72	11,400	24,400
14	75	1.11	0.46	57,000	0.78	0.92	7,200	23,700

$$(1) \quad \frac{\sigma_g}{\sigma_{YS}} = \frac{\text{gross stress}}{0.2\% \text{ yield stress}} \quad \text{where} \quad \sigma_g = \frac{P_{ult}}{BW} \quad \text{and} \quad \sigma_{YS} = 80,000 \text{ psi}$$

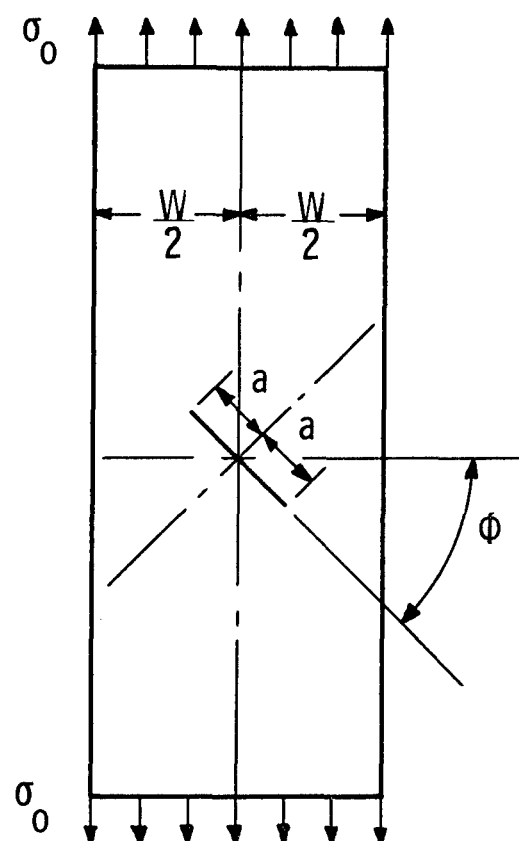
$$(2) \quad \frac{\sigma_n}{\sigma_{YS}} = \frac{\text{nominal stress}}{0.2\% \text{ yield stress}} \quad \text{where} \quad \sigma_n = \frac{P_{ult}}{B(W - 2a \cos \phi)}$$

(3) apparent critical stress intensity factors

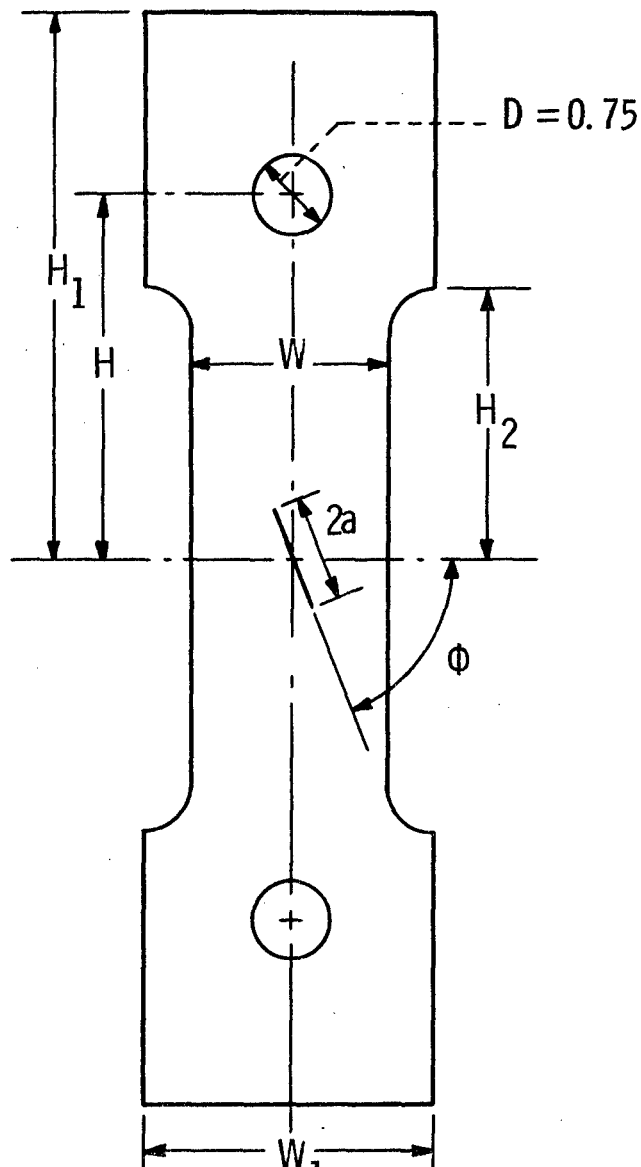
Section 6.2 References

1. W. F. Brown, Jr. and J. E. Strawley, "Plane Strain Crack Toughness Testing of High Strength Metallic Materials," ASTM Special Technical Publication No. 410.
2. F. Erdogan and G. C. Sih, "On the Crack Extension in Plates Under Plane Loading and Transverse Shear," Journal of Basic Engineering, Dec. 1963.
3. J. G. Kaufman and M. Holt, "Fracture Characteristics of Aluminum Alloys," Alcoa Research Laboratories, Technical Paper No. 18, 1965.

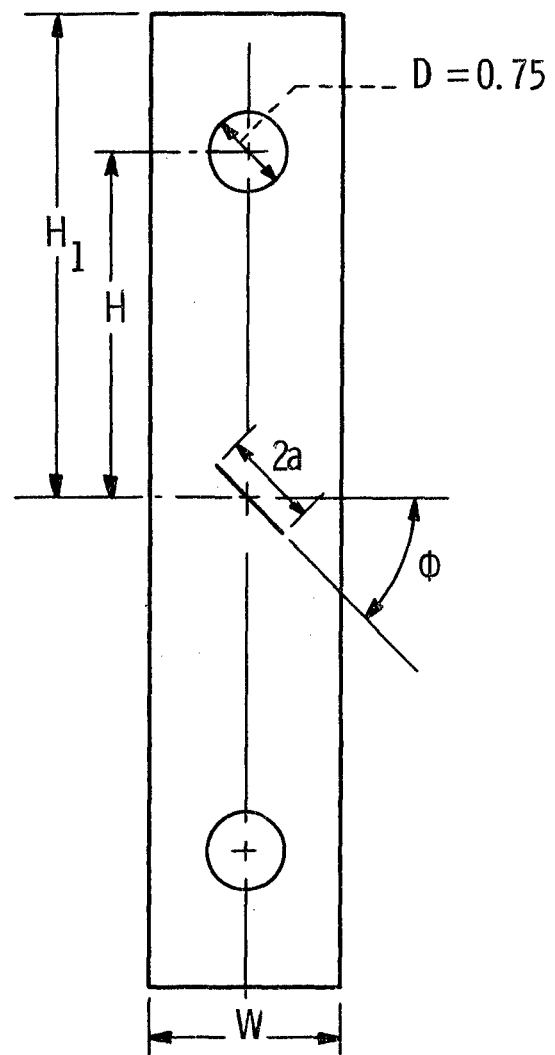
Dwg. 857A612



Sec. 6.2 Fig. 1—Loading condition for center slant crack specimen

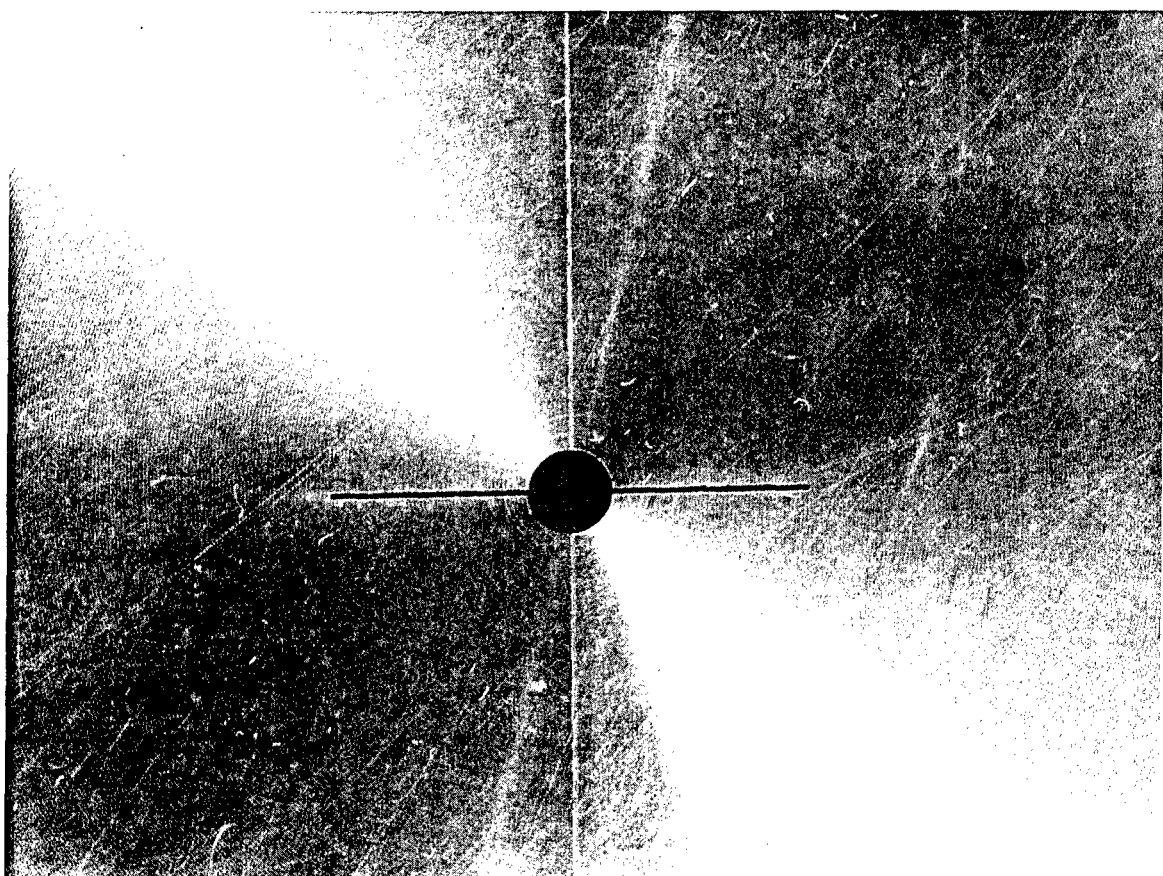


(1)

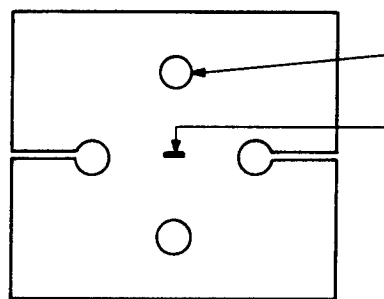


(2)

Sec. 6.2 Fig. 2—Drawings of center slant crack specimens

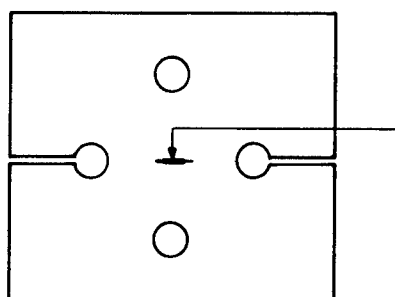


Sec. 6.2 Fig. 3—EDM slot extending from 1/8 in. hole



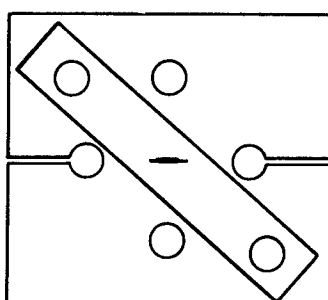
(a)

Fatigue Loading
Pin Hole
EDM Slot



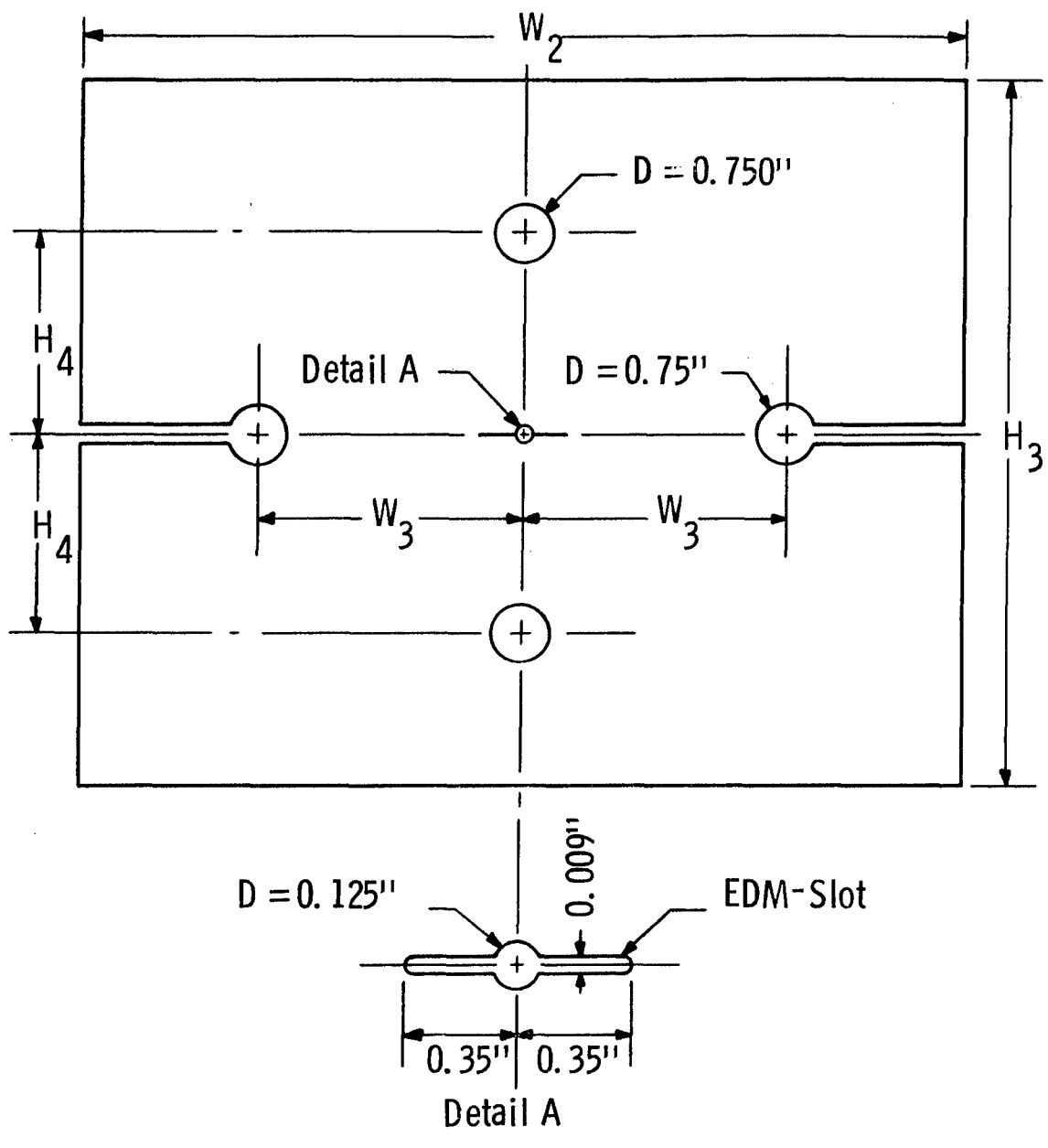
(b)

EDM Slot With
Fatigue Crack
Extension

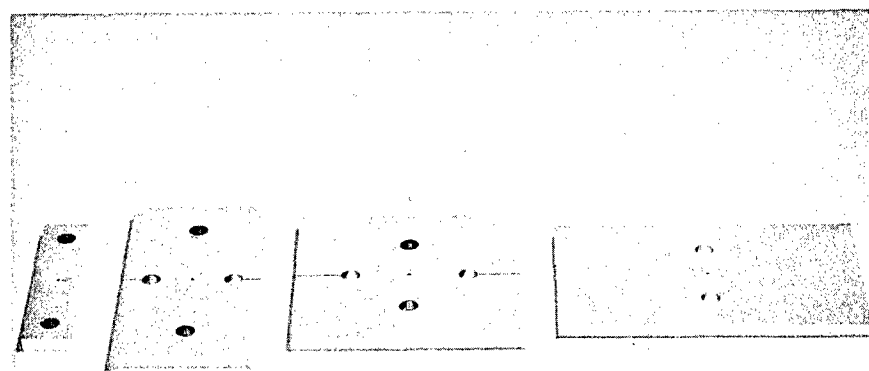


(c)

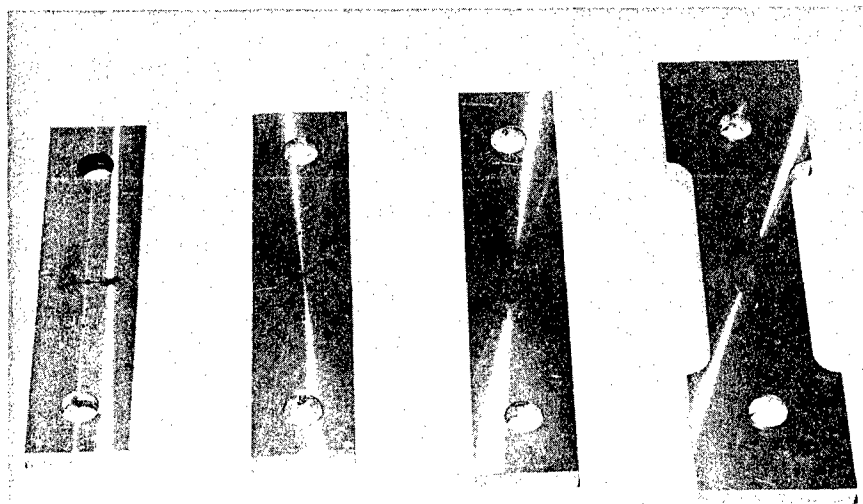
Sec. 6.2 Fig. 4—Precracking operation for center slant crack specimen



Sec. 6.2 Fig. 5 —Drawing of precracking geometry
for center slant crack specimens

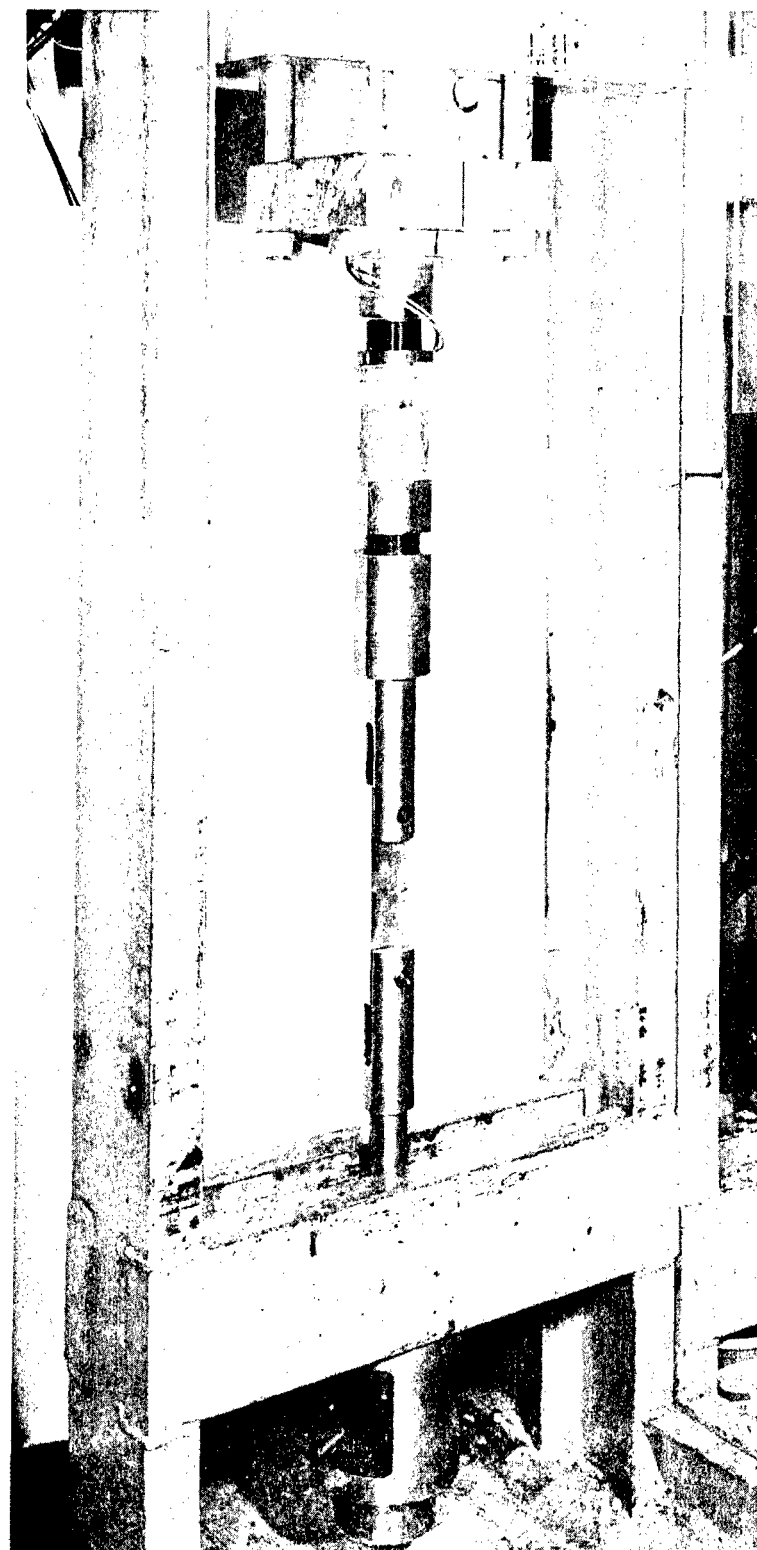


(a)

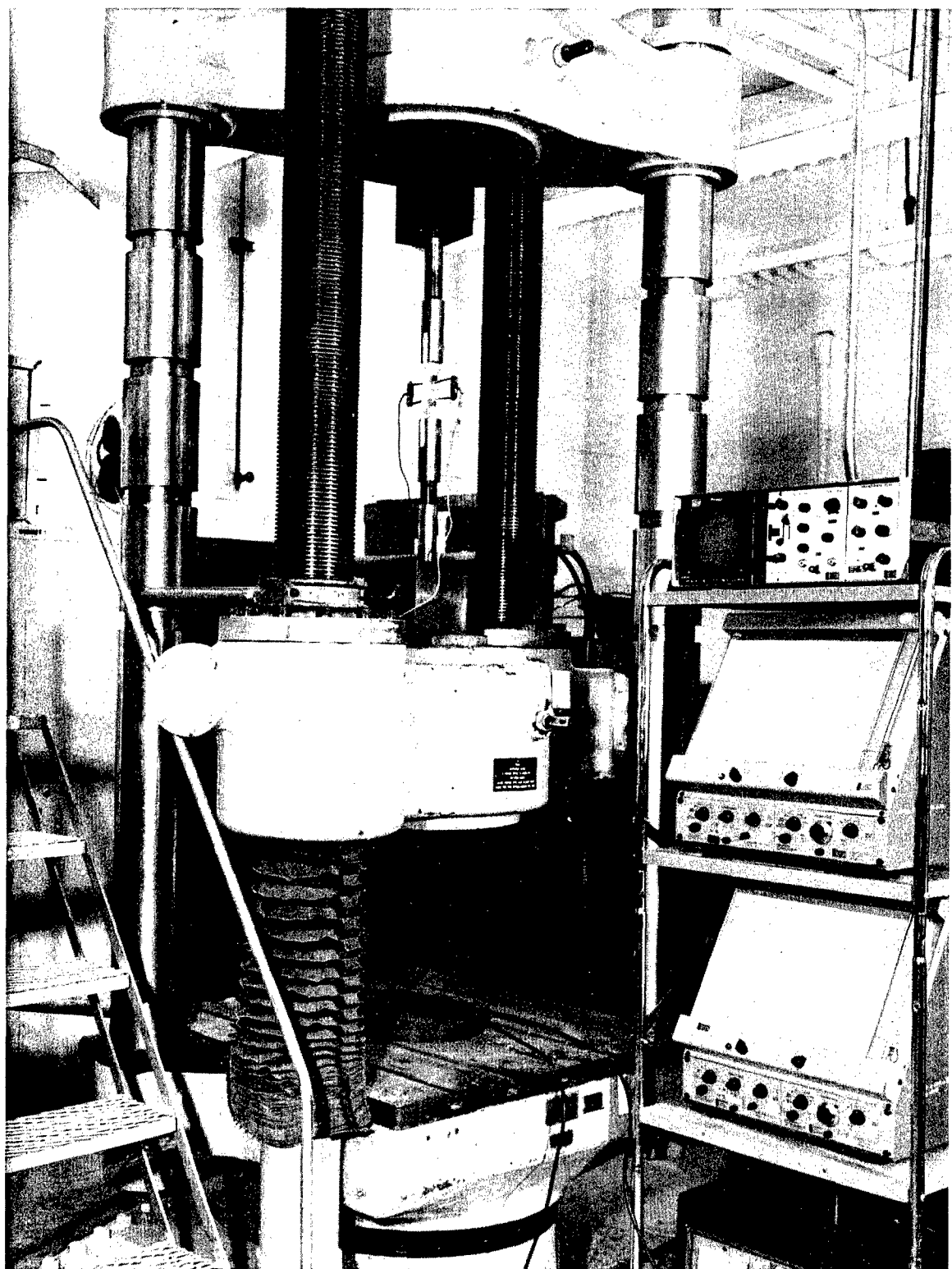


(b)

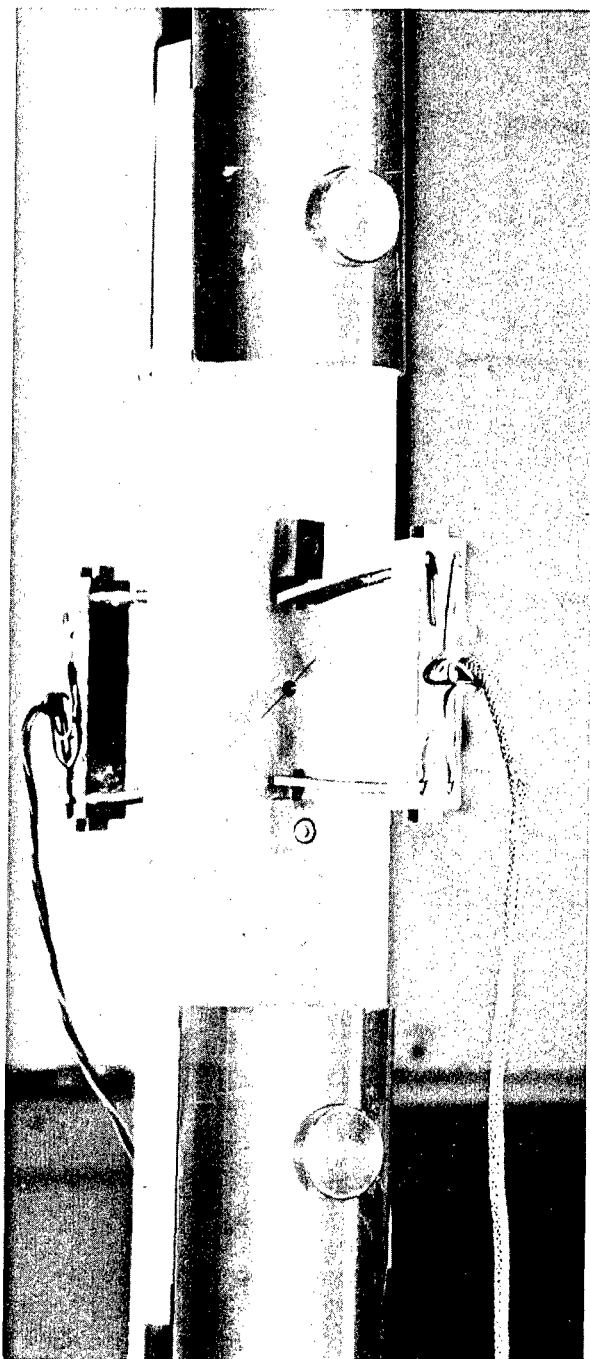
Sec. 6.2 Fig. 6—Fatigue precracking (a) and fracture (b) specimen geometries



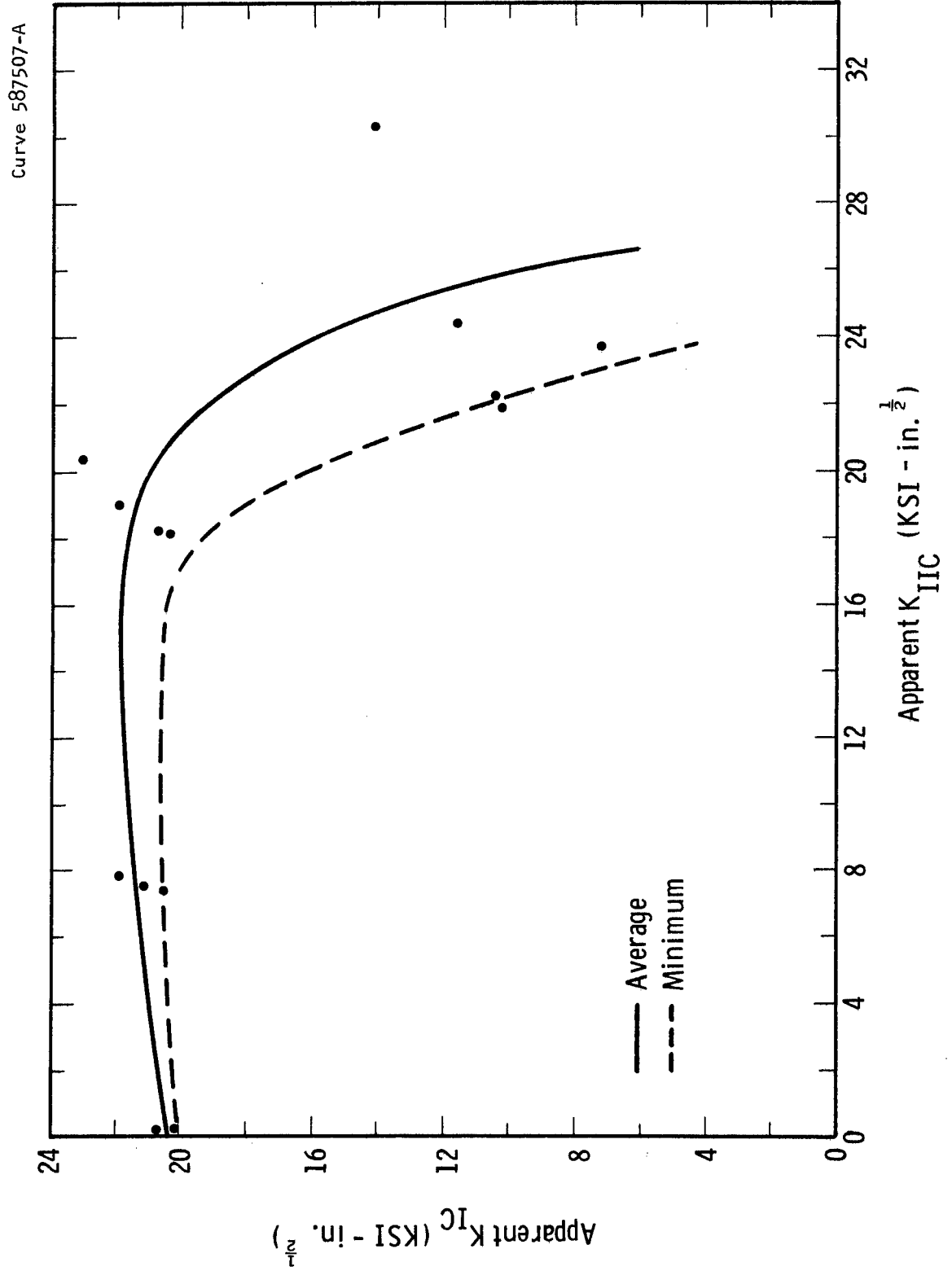
Sec. 6.2 Fig. 7—Fatigue precracking of specimen

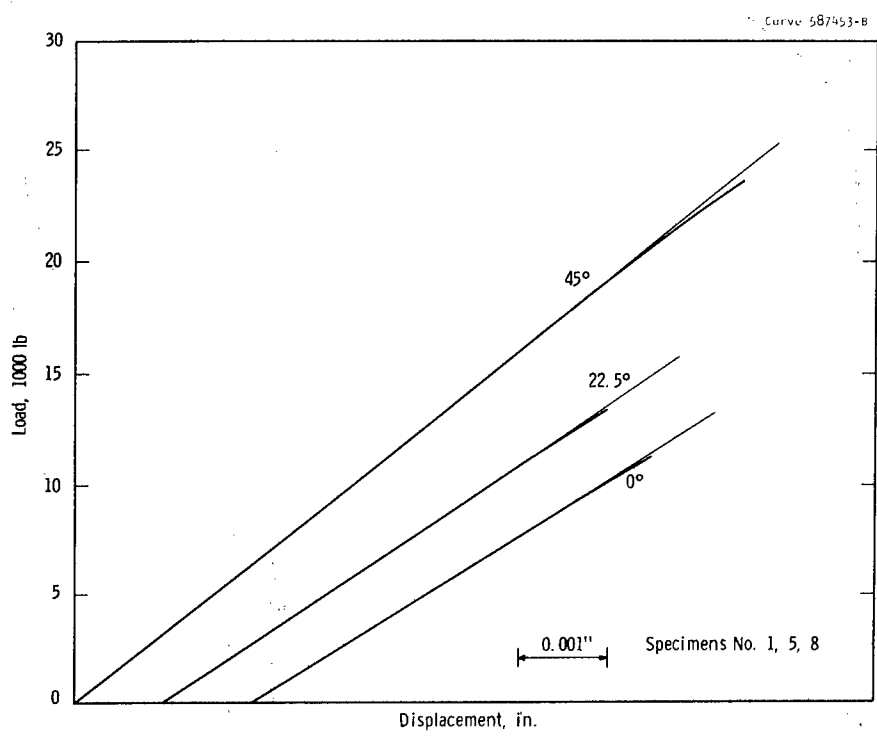
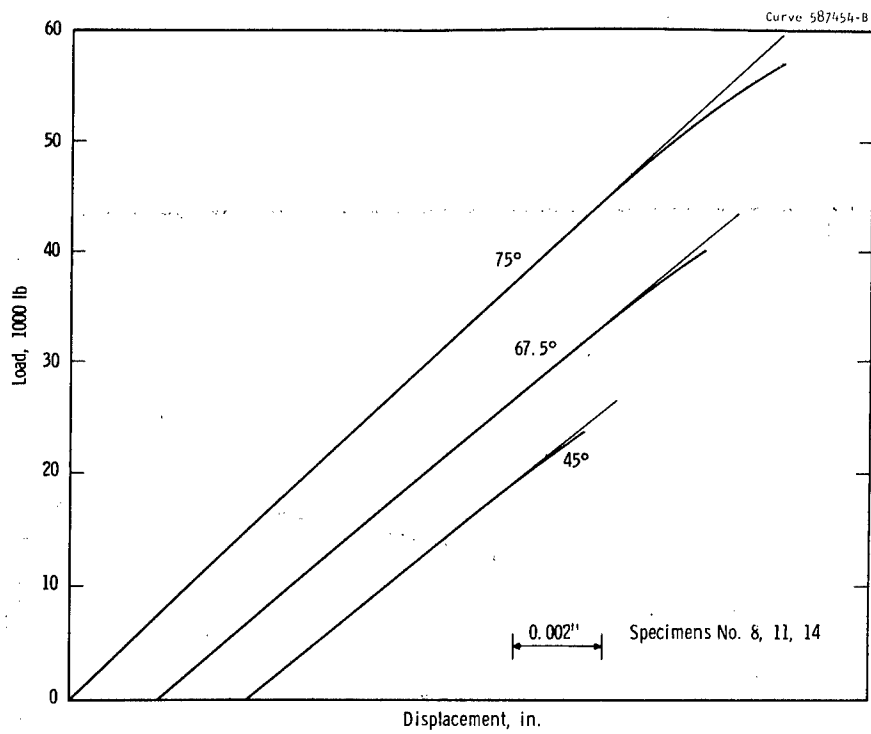


Sec. 6.2 Fig. 8—Fracture testing of center slant crack test specimen

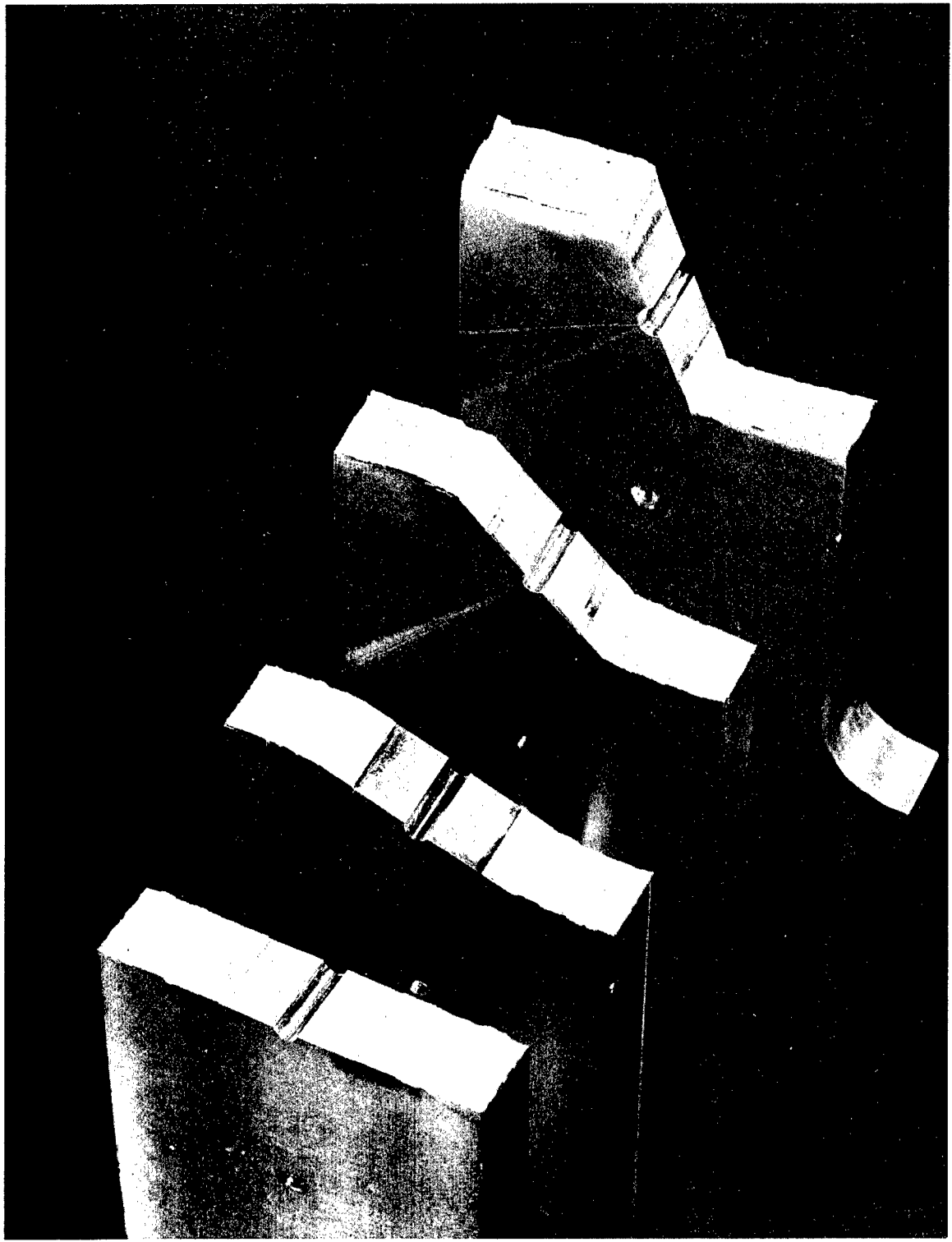


Sec. 6.2 Fig. 9—Clip gage used to establish load deflection curves

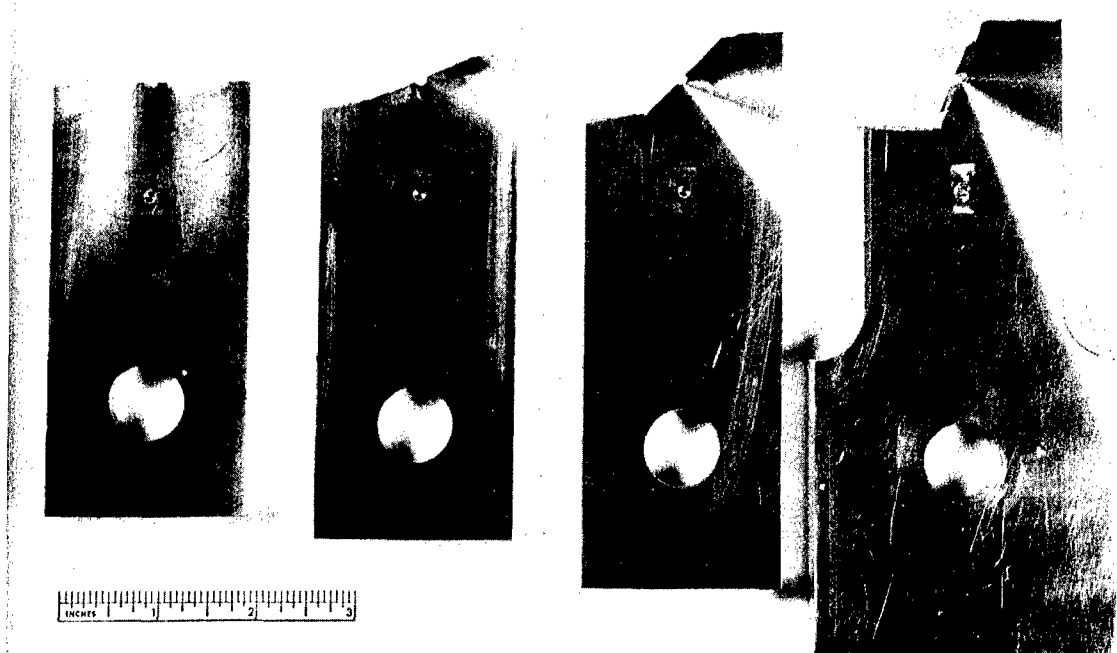




Sec. 6.2 Fig. 11—Effect of crack orientation on load-deflection curve

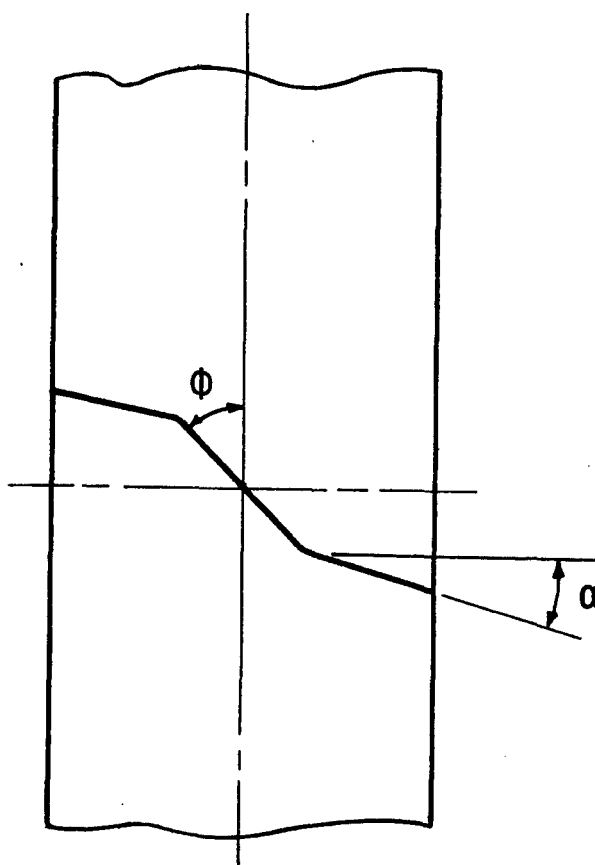


Sec. 6.2 Fig. 12—Fracture surfaces of center slant crack specimens
($\phi = 0, 22.5, 45$ and 67.5 degrees)



Sec. 6.2 Fig. 13—Fracture directions of center slant crack specimens
($\phi = 0, 22.5, 45$ and 67.5 degrees)

Dwg. 857A736



ϕ	α (Measured)	α (Ref 2)
0	0	0
22.5	11	-13.5
45	5	-8.0
67.5	0	4.5
90	0	9.5

(All Angles in Degrees)

Sec. 6.2 Fig. 14—Angle of crack propagation

Section 6.3

TEST SPECIMEN TO STUDY CRACK INSTABILITY IN METALS UNDER COMBINED MODE I AND III LOADING

6.3.1 INTRODUCTION

The object of this phase of the program was to develop a fracture test specimen by which crack instability conditions under combined Mode I-III conditions can be studied. The specific objectives of the program were:

- (1) to design a specimen with which a wide range of K_I/K_{III} crack tip loading conditions can be studied.
- (2) to develop a technique for precracking the specimen by fatigue.
- (3) to develop a method by which accurate load deflection records of the specimen can be obtained, such that slow crack growth and significant amounts of plastic flow at the crack tip can be detected.

6.3.2 TEST SPECIMEN GEOMETRY AND LOADING CONDITIONS

After a comprehensive study, a circumferentially notched precracked round bar subjected to combined torsion and tension (Figure 1) was selected as the specimen to be used for combined Mode I-III studies. The K_I crack tip component is a function of the tensile load only, and the K_{III} component is a function of the torsional load only. Therefore, it is possible to subject the crack tip to any K_I/K_{III} ratio by applying the proper ratio of tension to torsion.

The ratio of the minimum diameter d , at the cracked section, to gross diameter D was selected as $d/D = 0.5$. This is the same ratio recommended by ASTM⁽¹⁾ for a specimen of the same geometry which is used in plane strain K_{IC} testing. A 60° flank angle was also selected for the specimens.

In this initial study of K_I - K_{III} testing, high strength aluminum alloy 7075-7651 was investigated. The specimen dimensions are shown in Figure 2. The specimens were machined from $1\frac{5}{8}$ " round bar having a yield strength of 73,000 psi. An outer diameter of $D = 1.5$ in. was selected so that, based on initial estimates, the fracture loads for the specimen would be within the load capacity of the torsion-tension machine. Also based on the initially estimated K_{IC} value of the material this dimension satisfied the present ASTM recommended size requirement $D = 10(K_{IC}/\sigma_{YS})^2$ for K_{IC} testing.

To facilitate uniform crack initiation in the precracking operation the notch roots were machined to a radius of less than 0.002 in. The machined diameter at the base of the notch is $7/8$ in. By growing a fatigue crack of $1/16$ in. deep from the notch root the previously specified $d/D = 0.5$ is obtained. The extension left on one end of the specimen during the machining operation is used in the precracking rotating beam operation as a cantilever load arm. After the precracking operation this extension is removed as shown in Figure 3.

6.3.3 PRECRACKING PROCEDURE

The objective of the precracking operation is to grow a circumferential fatigue crack of uniform depth from the notch root of each specimen. A precrack of sufficient depth to remove the crack front from the influence of the starter configuration is needed. A fatigue crack depth of $1/16$ in. satisfies this requirement as demonstrated in Section 6.5.

The precracking was done in the rotating bending machine shown in Figure 4. The apparatus was designed by L. J. Ceschini of the Westinghouse Research Laboratories. The threaded end of the specimen is slipped into the hollow specimen support sleeve which is supported by

the two main bearings. The specimen is secured in the sleeve by four screws. The static cantilever load is supported on the other end of the specimen by a bearing which is slipped over the reduced end of the cantilever extension arm of the specimen. The use of the cantilever extension arm on the specimen reduces the static load required and provides a place to support the bearing for the static load. The support sleeve is rotated by a motor pulley system at approximately 300 rpm.

During the crack initiation stage the fatigue loading level was maintained at a K_{max} of 0.4 K_{IC} to allow uniform initiation. During the crack growth period K_{max} was reduced to 0.3 K_{IC} or less to avoid any influence on the final critical stress intensities. The resulting fatigue cracks were reasonably concentric. The average and the minimum diameter of the fatigue cracked notched section of each specimen tested is listed in Table I.

A minimal study was made of methods to determine the depth of the fatigue crack during the precracking operation. Both an electrical potential method and a deflection measuring method were investigated. In the short time allotted to these studies consistently meaningful results could not be obtained. Finally each specimen was cyclic loaded for a fixed number of cycles. After experience was gained, reasonable control over the depth of the cracks was obtained.

6.3.4 TESTING PROCEDURE

The test machine used to apply the combined torsional and tensile loads to the K_I - K_{III} test specimen is shown in Figure 5 along with the supplementary electronic instrumentation. The test machine was designed by E. A. Davis of these laboratories. The tensile and torsional loads can be applied independently by two variable speed motor-gear systems.

To obtain instantaneous electrical output signals proportional to the torque and tension loads one of the mechanical components of the machine in series with the test specimen was replaced by an equivalent component which was strain gaged to act as a load cell. The

equivalent component was machined from 7075-7651 aluminum alloy. Two independent four arm strain gage bridge circuits were attached to the hollow load cell component as shown in Figure 6. An experimental check shows that the linear output of the torsion bridge is independent of applied tensile load, and similarly the tension bridge output is independent of applied torque loads. The calibration curves for the two bridges are shown in Figure 6.

To detect slow crack growth or significant amounts of plastic flow at the crack tips during loading accurate measurements of relative displacements across the plane of the crack are needed. Measurements of axial deflection due to the tensile load and tangential deflection due to the torsional load are required.

The technique used to make the displacement measurements is shown in Figure 7. Two clamps are attached to the specimen; one above the notch, the other below the notch. Two clip gages are presprung between the clamps in the axial direction, Figure 7(a). This set of clip gages measures axial deflection across the crack plane over a 2.0 in. gage length. Each clamp contains diametrically opposite arms extending in the axial direction. By prespringing a set of clip gages between opposing arms of the two clamps the relative angular displacement over the 2.0 in. gauge length can be measured, Figure 7(b). For the small displacements measured it can be shown that the interaction effect of axial and angular displacements on the output of the two sets of clip gages is neglectable. The displacement signals fed into the X-Y recorders are the average deflections of each set of clip gages. The output of the clip gage bridges is linear with respect to displacement.

The type of information recorded during the testing of each specimen is displayed in Figure 8. For each test a curve (a) of the tensile and torque load was recorded. This corresponds to a recorder (b) of K_I vs K_{III} during loading. For each test the loads were applied at a rate such that the K_I/K_{III} ratio remained constant through the test. Also recorded during each test was a load deflection curve; either tensile load versus axial displacement or torsional load versus angular displacement.

6.3.5 RESULTS AND CONCLUSIONS

Eleven specimens were tested over the complete K_I/K_{III} range (1/0, 3/1, 2/1, 1/1, 1/2, 0/1). For all but one ratio two specimens were tested. The test results are reported in Table I. The calibration curve of Figure 13 Section 6.5 is used to calculate K_{III} , and the following expressions obtained from Reference 1 is used for the calculation of K_I .

$$\frac{K_I D^{3/2}}{P} = 1.72 \frac{D}{d} - 1.27$$

The listed critical stress intensities are calculated from the ultimate loads and minimum diameter d_{MIN} in the plane of the crack. These critical values are shown in the K_I-K_{III} plot of Figure 9 along with a curve through the minimum values.

The load-deflection curves obtained for various K_I/K_{III} ratios are shown in Figure 10. In Figure 10(a) the axial deflection versus tensile load curves are shown for pure K_I , $K_I/K_{III} = 2$, and $K_I/K_{III} = 1$ loading condition. In Figure 10(b) angular deflection versus torque load curves are shown for $K_I/K_{III} = 1/2$ and pure K_{III} loading conditions. As the K_I/K_{III} ratio decreases, in going from pure K_I to pure K_{III} loading, the degree of nonlinearity of the curves at fracture increases.

Assuming that no slow crack growth occurred prior to rapid fracture, this trend indicates a higher degree of plastic flow associated with the K_{III} load component as compared with the K_I component at equal stress intensity levels for the size specimen tested. This is shown in Table I where the ratio of tensile nominal stress ($\sigma_n = 4P/\pi d^2$) to tensile yield stress (σ_n/σ_{YS}) and the ratio of shear nominal stress ($\tau_n = 16T/\pi d^3$) to shear yield stress (τ_n/τ_{YS}) are presented for each specimen. For specimen number 10 tested under a pure K_{III} condition, $\tau_n/\tau_{YS} = 1.84$ at failure. This indicates that an extensive amount of plastic flow had occurred in the specimen prior to fracture.

The amount of plastic flow and nonlinearity in the deflection curves occurring in these specimens as K_I/K_{III} decreases indicates that the size of the specimens is probably not large enough to measure geometry independent combined mode critical stress intensity factors. As stated previously the size of the specimens was limited by the capacity of the tension-torsion machine used. Nevertheless the K_I-K_{III} plot of apparent critical stress intensity factors shown in Figure 9 is informative. There is little scatter in the data even though for some of the same K_I/K_{III} ratios the fracture loads differ significantly (for example specimens 1 and 2 and also specimens 10 and 11) due to the variation of d_{MIN} . The value of K_{Ic} seems to remain essentially constant as K_{III} increases from zero to approximately 20 ksi in. $^{1/2}$, and then it begins to decrease rapidly with further increase in K_{III} . Also the critical stress intensity under pure K_{III} loading is less than the critical intensity under pure K_I loading even though the K_I tests are much more linear. With a larger size specimen it would be expected that locus of critical stress intensities would move toward the origin, particularly at the pure K_{III} end of the curve.

The fracture surfaces for the various loading conditions are shown in Figure 11. As the loading progresses from pure K_I loading to pure K_{III} loading the fracture surface appearance changes from one which is almost flat to one in which the original fatigue crack has divided into a series of cracks which all propagate out of the original crack plane. The lower the K_I/K_{III} ratio the greater is the angle at which the crack leaves the original plane and also the greater is the distance it travels away from the original plane before terminating. As pure K_{III} loading is approached it appears that the series of cracks terminates in a plane parallel to the axis, that is in a plane oriented at 90° to the original crack plane. The surfaces of the pure K_{III} specimens become smeared during the fracture process as shown in Figure 11 and do not reveal any features of the fracture process.

In future work larger circumferentially cracked round bar specimens of 7075-7651 should be tested. In particular larger specimens under pure torsion (K_{III}) should be tested. Based on the present results it would appear that the size specimen needed to obtain a nearly linear load deflection curve and a geometry independent K_{IIIC} could be appreciably larger than the specimens tested here.

Section 6.3 References

1. W. F. Brown, Jr. and J. E. Strawley, "Plane Strain Crack Toughness Testing of High Strength Metallic Materials," ASTM Special Technical Publication No. 410.

Section 6.3 Table I

RESULTS OF K_I - K_{III} COMBINED MODE ROUND BAR TESTS

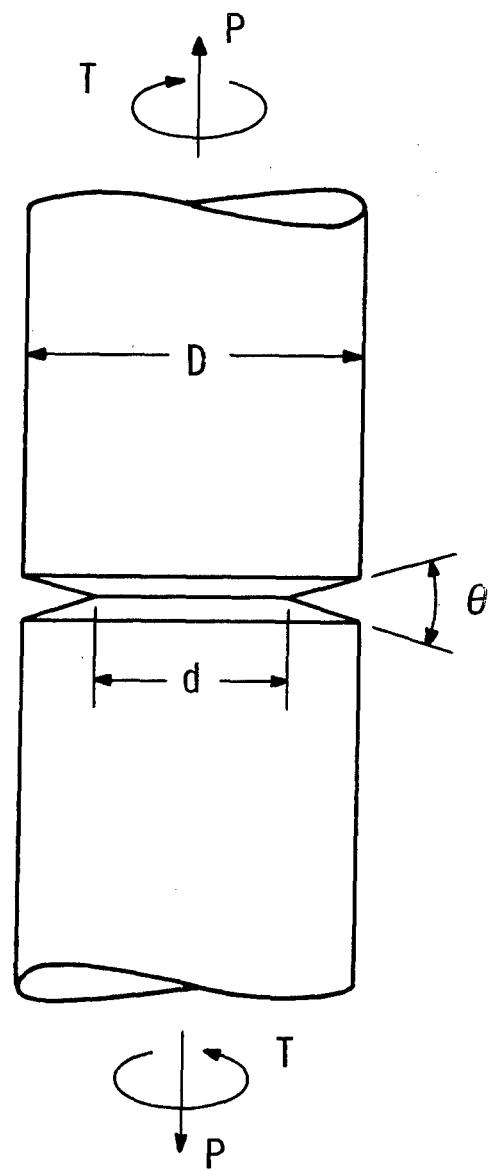
Spec. No.	K_I/K_{III} (1)	Ultimate Tensile Load P_{ULT} (lb.)	Ultimate Torque Load T_{ULT} (in. 1b.)	d_{MIN} (2) (in.)	d_{AV} (3) (in.)	$\frac{\sigma_n}{\sigma_{YS}}$ (4)	$\frac{\tau_n}{\tau_{YS}}$ (5)	K_{IC} (6) (PSI/ $\sqrt{\text{in.}}$)
1	1/0	23,300	0	0.68	0.69	0.85	0	31,900 0
	1/0	30,600	0	0.76	0.79	0.84	0	35,300 0
3	3/1	32,200	2690	0.82	0.83	0.83	0.58	32,700 10,300
	2/1	25,800	3350	0.73	0.77	0.77	0.90	31,900 17,200
4	2/1	26,800	3450	0.74	0.78	0.77	0.88	32,700 17,400
	1/1	20,625	5250	0.80	0.80	0.56	1.24	21,900 21,300
6	1/1	18,300	4720	0.75	0.77	0.54	1.25	21,600 22,700
	1/1	10,800	5500	0.77	0.78	0.31	1.43	12,200 24,600
8	1/2	11,200	5720	0.78	0.79	0.32	1.43	12,400 24,800
	1/2	0/1	0	4375	0.65	0.66	1.84	0 30,200
10	0/1	520	7000	0.83	0.83	0.01	1.48	500 25,900
11	0/1							

- (1) Approximate stress intensity ratios
 (2) Minimum diameter at plane of crack
 (3) Average diameter at plane of crack
 (outer diameter of round bar $D = 1.50$ in.)

$$(4) \frac{\sigma_n}{\sigma_{YS}} = \frac{\text{nominal tensile stress}}{0.2\% \text{ yield stress}} \text{ where } \sigma_n = \frac{4 P_{ULT}}{\pi d^2} \text{ and } \sigma_{YS} = \frac{4 P_{ULT}}{\pi d^2 \text{ av}} \text{ and } \sigma_{YS} = 73,000 \text{ psi}$$

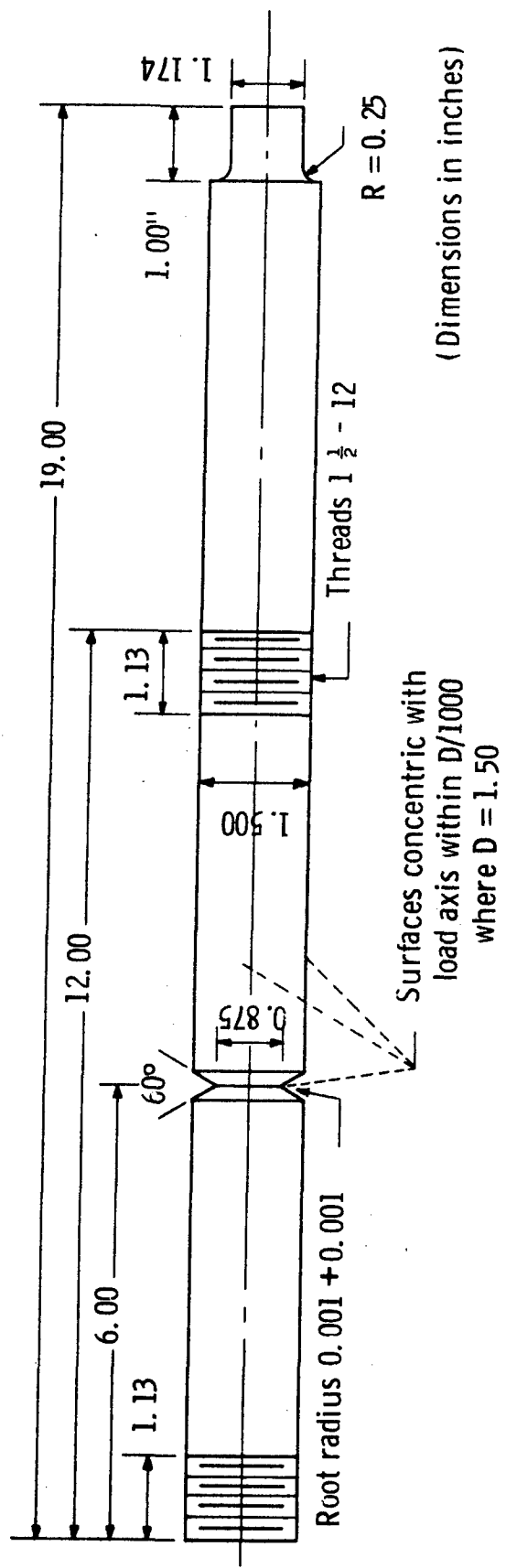
$$(5) \frac{\tau_n}{\tau_{YS}} = \frac{\text{nominal shear stress}}{\text{shear yield stress}} \text{ where } \tau_n = \frac{16 T_{ULT}}{\pi d^3} \text{ and } \tau_{YS} = \frac{16 T_{ULT}}{\pi d^3 \text{ av}} \text{ and } \tau_{YS} = 0.577 \sigma_{YS}$$

(6) Apparent critical stress intensity factors calculated
 from ultimate loads and d_{MIN} .

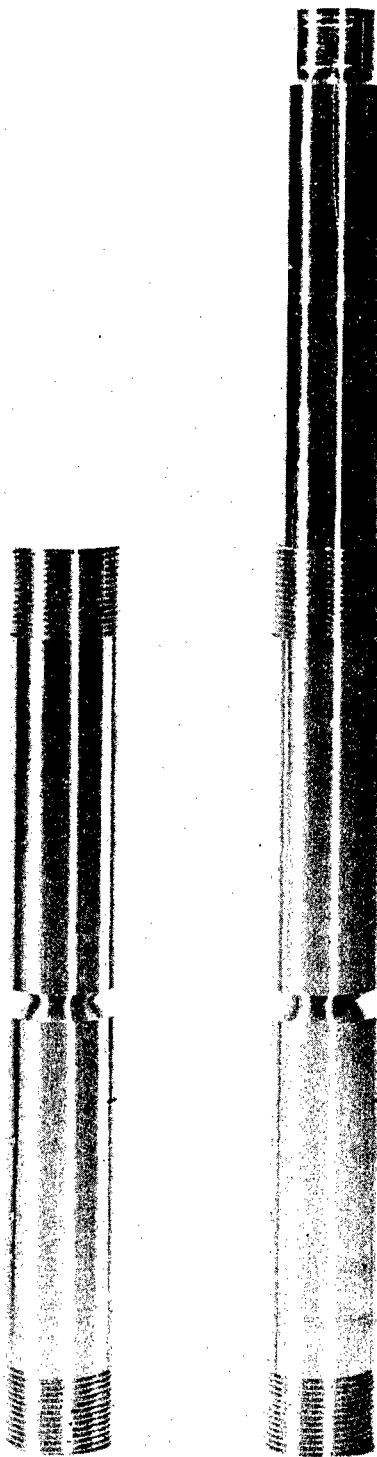


Sec. 6.3 Fig. 1—Loading conditions for circumferentially cracked round bar specimen

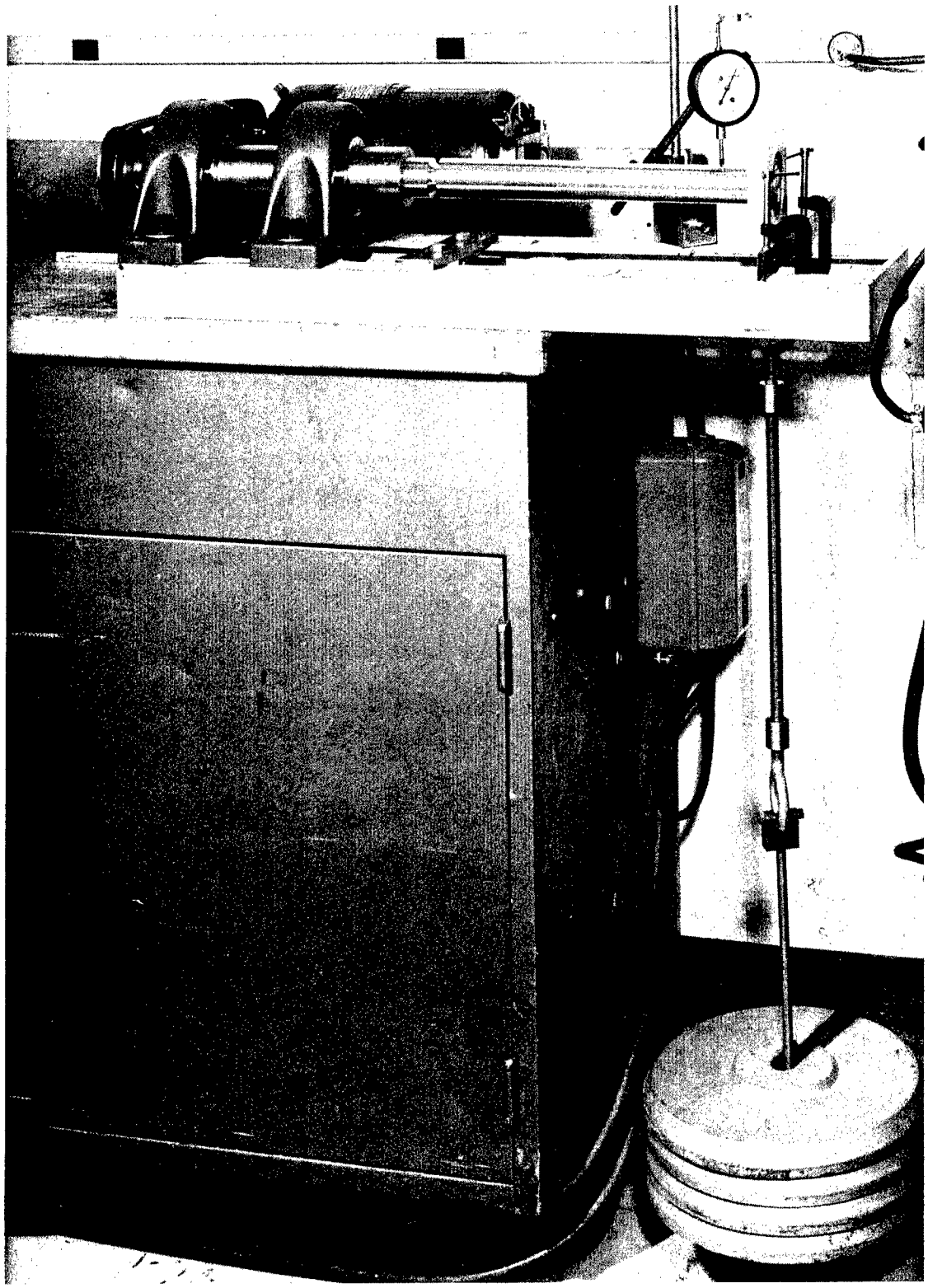
Dwg. 857A626



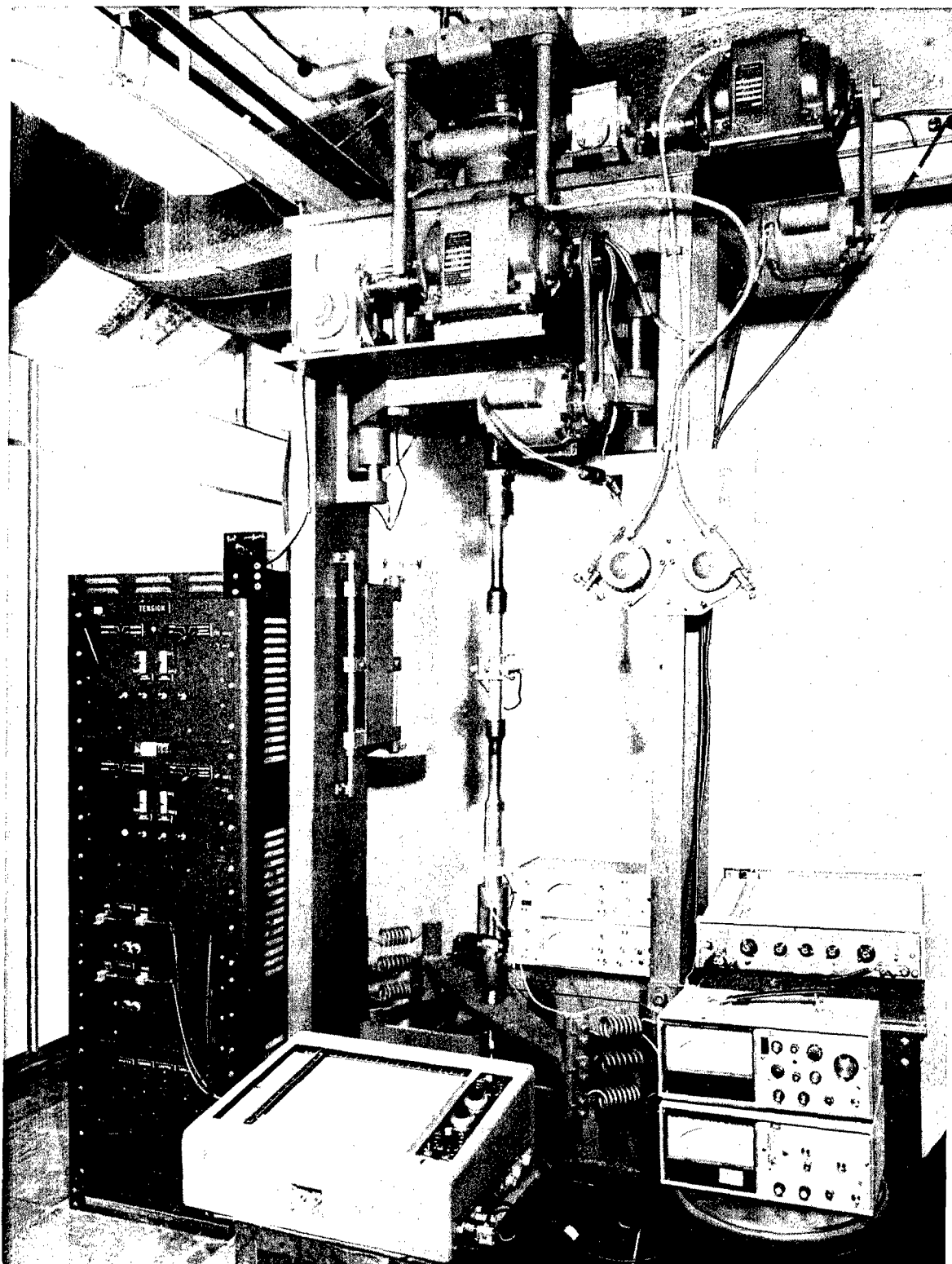
Sec. 6.3 Fig. 2—Drawing of circumferentially notched round bar specimen



Sec. 6.3 Fig. 3—Precracking and final fracture geometry of Mode I-III circumferentially crack-notched round bar specimen

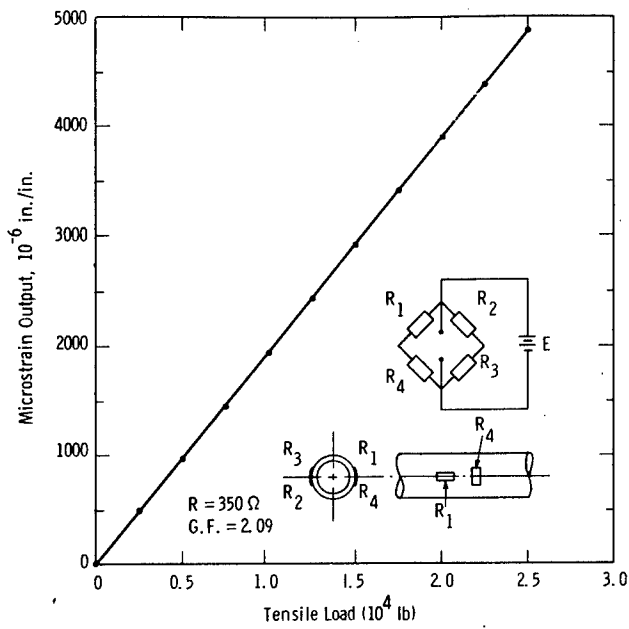


Sec. 6.3 Fig. 4—Fatigue precracking rotating beam machine



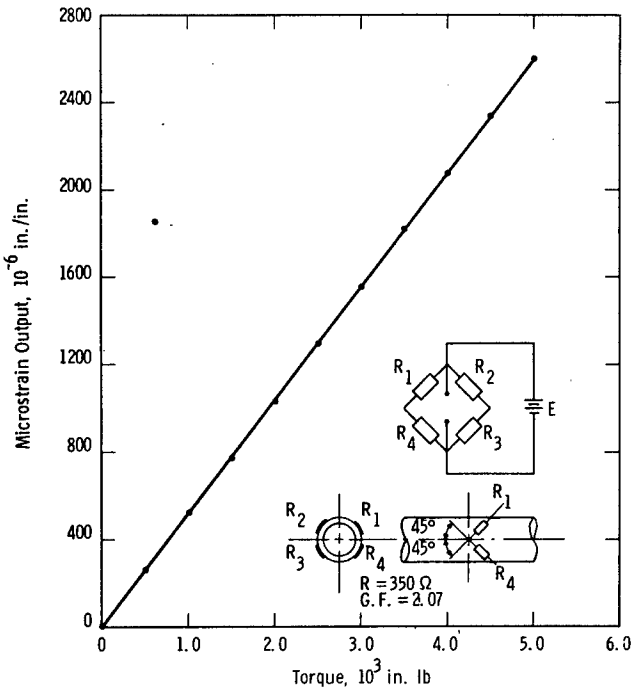
Sec. 6.3 Fig. 5—Torsion-tension test machine and auxiliary equipment used in the testing of circumferentially crack-notched round bar specimens

Curve 587387-A



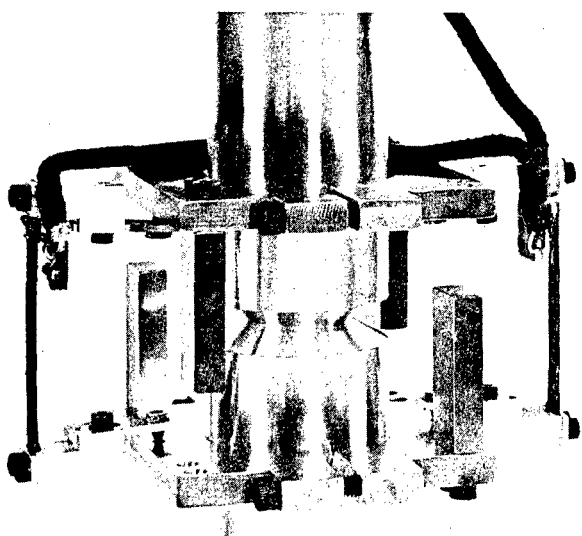
Calibration curve for tensile component of load cell

Curve 587388-A

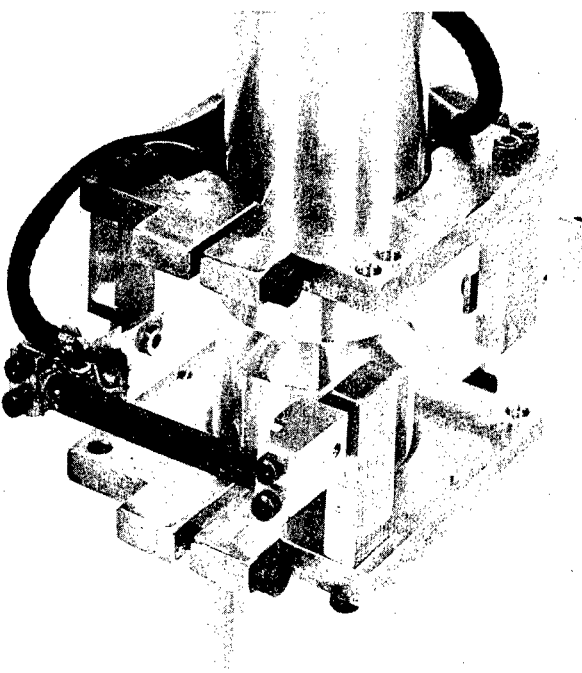


Calibration curve for torsion component of load cell

Sec. 6.3 Fig. 6—Load cell calibration curves



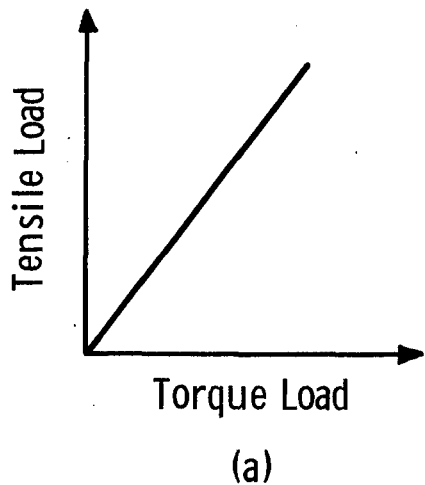
(a)



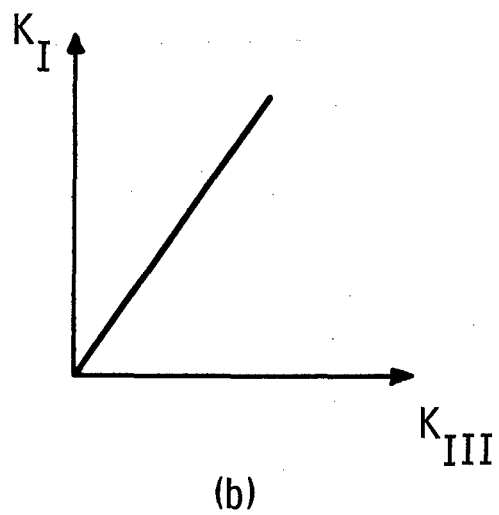
(b)

Sec. 6.3 Fig. 7—Measuring (a) axial and (b) angular deflections with clip gages

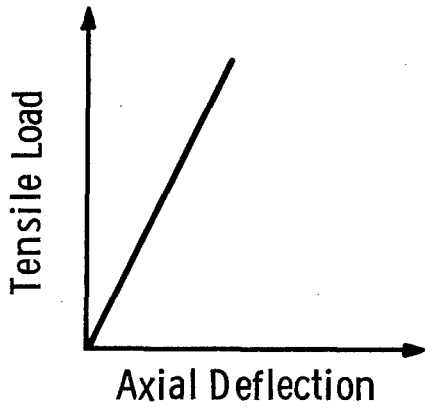
Dwg. 857A732



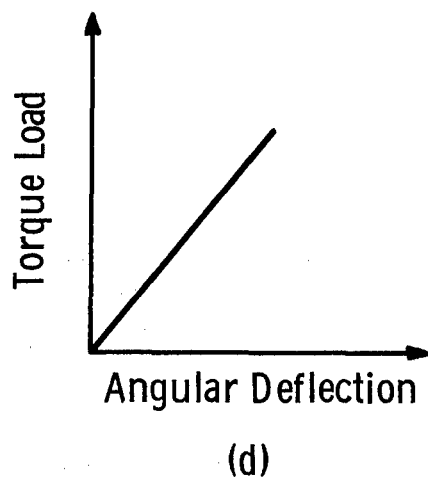
(a)



(b)



(c)

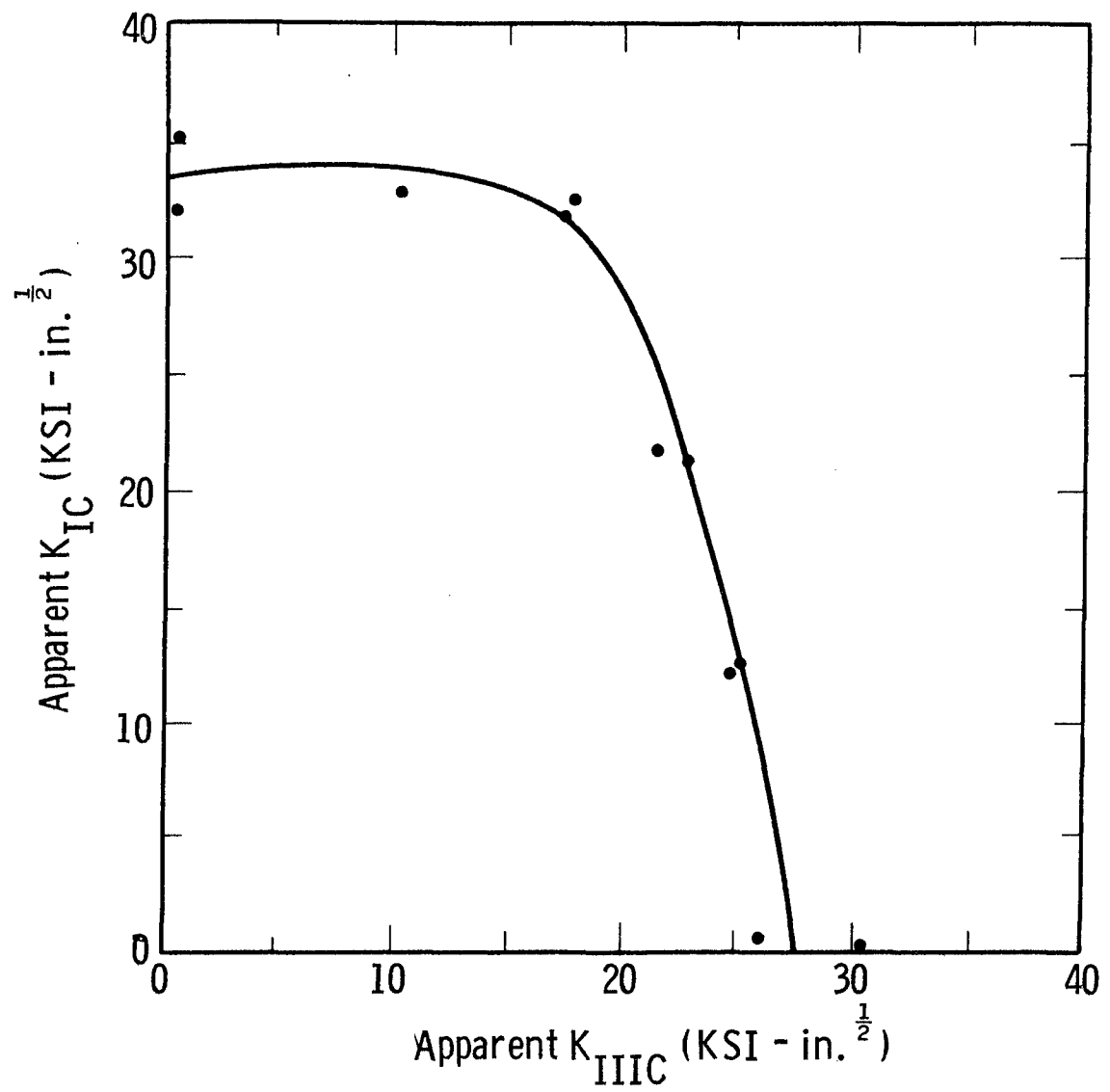


(d)

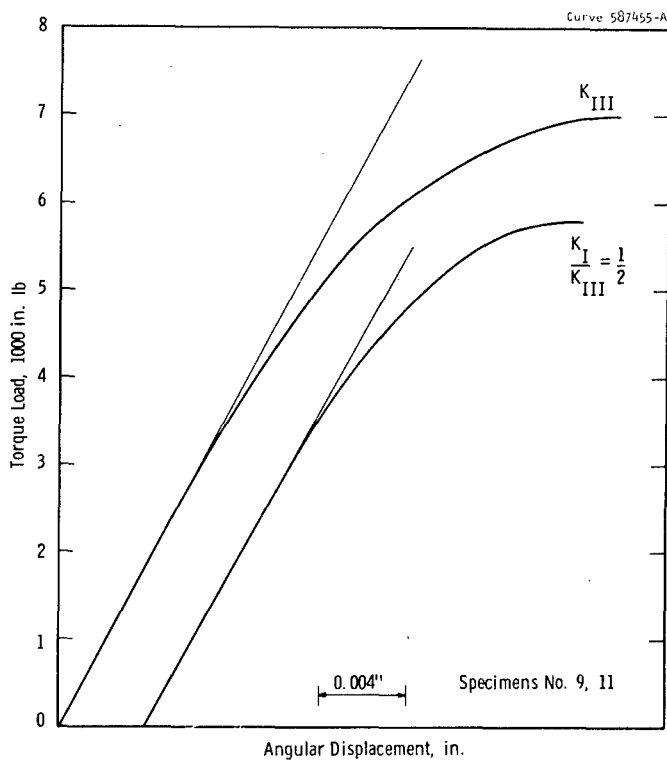
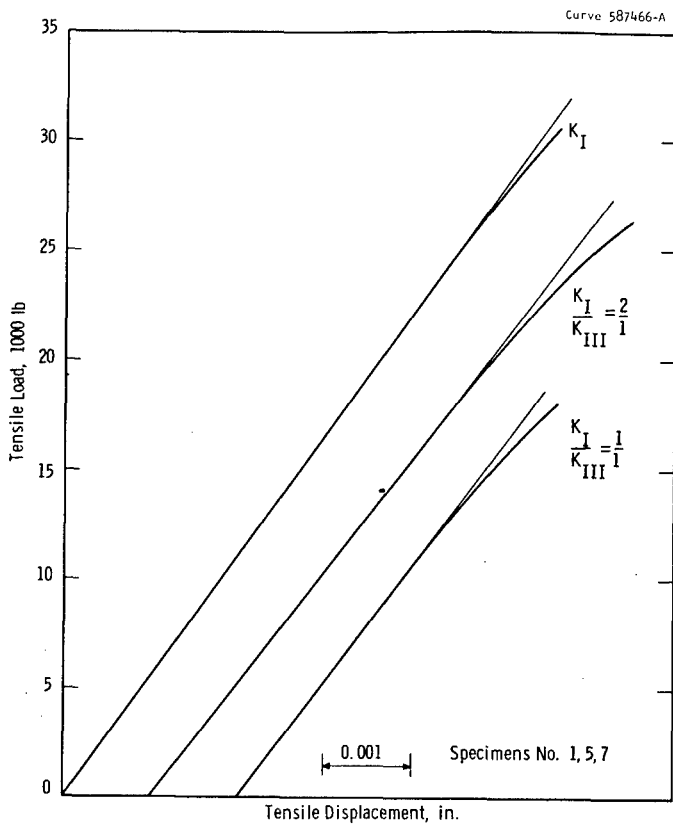
Load-Deflection Records

Sec. 6.3 Fig. 8—Recorded information for K_I - K_{III} round bar specimens

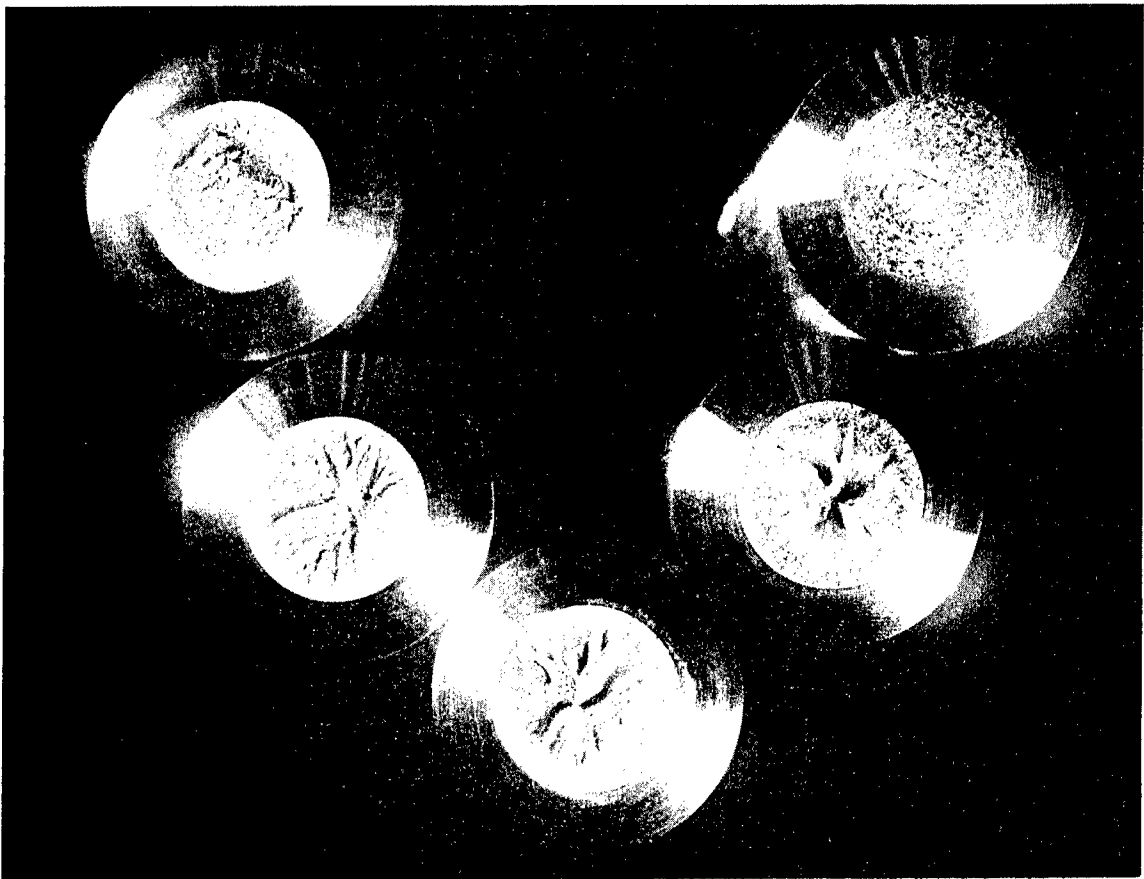
Curve 587457-A



Sec. 6.3 Fig. 9—Apparent combined mode I-III critical stress intensity factors for aluminum alloy 7075-T651



Sec. 6.3 Fig. 10—Load-deflection records from Mode I-III circumferentially crack-notched round bar specimens



Sec. 6.3 Fig. 11—Fracture surfaces for various K_I/K_{III} loading ratios (left to right: 1/0, 2/1, 1/1, 1/2 and 0/1). The far right surface was smeared during fracture

Section 6.4

COLLOCATION METHOD FOR CALCULATING STRESS INTENSITIES FOR FINITE PLATES CONTAINING AN INTERIOR THROUGH THICKNESS CRACK

6.4.1 INTRODUCTION

The stress intensity calibration curves for the center slant cracked specimens (Sec. 6.1) of finite width are obtained by use of a boundary collocation approach. The collocation method presented here and applied to the specimen geometry can also be applied to most arbitrarily shaped plates of finite dimensions subject to in-plane loading and containing an interior through thickness crack. The boundary collocation is in terms of an Airy stress function and its normal derivative. The Airy stress function used is obtained from a set of complex stress functions presented by Vooren⁽¹⁾.

6.4.2 THEORETICAL DEVELOPMENT

For a straight crack on the x-axis (Fig. 1) with crack tips at $x = a$ and $x = -b$, the stresses and displacements in the plane containing the crack can be represented by two complex stress functions $\phi(z)$ and $\Omega(z)$ as

$$\begin{aligned}\sigma_x + \sigma_y &= 2 [\phi(z) + \overline{\phi(z)}] \\ -\sigma_x + \sigma_y + 2i \tau_{xy} &= 2 [(\bar{z} - z)\phi'(z) - \phi(z) + \overline{\Omega(z)}] \quad (1) \\ 2\mu (u + iv) &= \kappa \int_0^z \phi(z) dz - \int_0^{\bar{z}} \Omega(\bar{z}) d\bar{z} - (z - \bar{z}) \overline{\phi(z)}\end{aligned}$$

where

$$\begin{aligned}\phi(z) &= F_1(z) G(z) + F_2(z) \\ \Omega(z) &= F_1(z) G(z) - F_2(z)\end{aligned}\quad (2)$$

$$F_1(z) = c_n z^n + a_{n-1} z^{n-1} + \dots + a_0$$

$$F_2(z) = d_n z^n + d_{n-1} z^{n-1} + \dots + b_0$$

$$G(z) = [(z - a)(z + b)]^{-1/2}$$

The branch of $[(z - a)(z + b)]^{-1/2}$ is used where $z[(z - a)(z + b)]^{-1/2}$ approaches one as z approaches infinity. These complex stress functions were presented by Vooren.⁽¹⁾ Functions similar to the above were used by Kobayashi et. al.,⁽²⁾ but as pointed out by Vooren they were in error. The origin of these complex functions can be traced back to Muskhelishvili⁽³⁾ and to subsequent work by Erdogan.⁽⁴⁾

The above complex functions satisfy force equilibrium, the compatibility equation and give a stress free surface on the x axis from $x = a$ to $x = -b$. To insure single valuedness of displacement in this multiply connected region the following additional condition must be satisfied.

$$\oint \phi(z) dz - \oint \Omega(\bar{z}) d\bar{z} = 0 \quad (3)$$

The stress intensity factors at the two tips of the crack can be calculated from the following equations.

$$K_I - iK_{II} = 2\sqrt{2\pi} \lim_{z \rightarrow a} (z - a)^{1/2} \phi(z) \text{ for } z = a \quad (4)$$

$$K_I - iK_{II} = 2\sqrt{2\pi} \lim_{z \rightarrow -b} (z + b)^{1/2} \phi(z) \text{ for } z = -b$$

Previously Kobayashi et. al.⁽²⁾ and Hulbert et. al.⁽⁵⁾ used complex functions similar to (2), but in error as shown,⁽¹⁾ in a boundary collocation method applied to symmetric center cracked plates. The boundary collocations were carried out on the boundary stresses. As stated⁽⁵⁾ the accuracy obtained with this type of collocation is highly dependent on the number and location of selected boundary points. Hulbert and Kanninen attempted to avoid this problem by using the least square point matching method applied to the boundary stresses. In the method presented here this problem is eliminated, as will be shown, by converting the complex stress functions to an Airy stress function $U(t,y)$ and applying boundary collocation to the Airy stress function and its normal derivative dU/dn at selected boundary points.

The relations between an Airy U stress function and its derivatives $\partial U / \partial x$ and $\partial U / \partial y$ and the Kolosoff-Mushkelishvili type complex stress functions $\phi(z)$ and $\Omega(z)$ are

$$U = R_e [\bar{z} \phi(z) + \chi(z)] \quad (5)$$

$$\frac{\partial U}{\partial x} + i \frac{\partial U}{\partial y} = \phi(z) + z \overline{\phi'(z)} + \psi(z) \quad (6)$$

where

$$\begin{aligned} \chi(z) &= \int \psi(z) dz \\ \phi(z) &= \int \phi(z) dz \end{aligned}$$

and

$$\psi(z) = \int \Psi(z) dz$$

$$\Psi(z) = \overline{\Omega}(z) - [z \phi(z)]'$$

In effect this conversion requires a single integration of $\phi(z)$ with respect to z and a double integration of $\Omega(z)$ with respect to z . Some of the less obvious relations used in carrying out these integrations are listed in Appendix I. The stress function U is in its most general form when the arbitrary linear function $Ax + By + C$ is added.

For any arbitrary loading on the outer boundaries C_o (Fig. 1), the boundary condition on C_o can be expressed as a function U and dU/dn ⁽⁶⁾

$$\begin{aligned} U &= f(s) \\ \frac{dU}{dn} &= g(s) \end{aligned} \quad \text{on } C_o \quad (7)$$

by use of the relations:

$$\sigma_{ij} n_j = T_i(s) \quad (8)$$

and

$$\sigma_{11} = U_{,22} \quad \sigma_{12} = -U_{,12} \quad \sigma_{22} = U_{,11} \quad (9)$$

where $x_1 = x$, $x_2 = y$, and $T_i(s)$ are the given boundary surface tractions. The functions $f(s)$ and $g(s)$ can be determined within an arbitrary linear function.

The boundary collocation procedure is to satisfy boundary conditions (7) at a selected number (N) of boundary points (stations) on the outer boundary C_o of the plate, and to also satisfy the single valuedness condition (3). At each boundary station two conditions are satisfied, and condition (3) represents two real conditions. Therefore, for N collocation points $2N+2$ real coefficients (i.e. $N+1$ complex coefficients) can be determined. Once these coefficients are determined by solving the appropriate set of $(2N+2)$ linear simultaneous real equations. The corresponding approximate crack tip stress intensities can be calculated from Equation (4). Normally, as the number of boundary stations is increased, the calculated stress intensities will approach the exact solution.

6.4.3 APPLICATION

The procedure described above is used to determine the stress intensity calibration curve for center slant cracked specimens considered in Sec. 6.1. The analytic model representation of the specimen is shown in Figure 2. Since the stress distribution of specimen has a period of π with respect to the plane of the crack and the center of the crack, the following complex coefficients are equal to zero

$$c_n = 0 \quad n = 0, 2, 4, \dots \quad (10)$$

$$d_n = 0 \quad n = 1, 3, 5, \dots$$

and only half of the specimen as shown in Figure 3 is analyzed.

The boundary functions $U = f(s)$ and $dU/dn = g(s)$ over the surface A-D are given in Appendix II. Due to the reduction Equations (10) the single valuedness relation (3) is automatically satisfied. For N boundary stations $2N$ conditions must be satisfied. The complex coefficients which are determined from these conditions are equally divided between the $F_1(z)$ series $F_2(z)$ series. The set of N equations corresponding to the $f(s)$ boundary condition are generated by use of Equation (5). Equation (6) along with the following relation is used to generate the N equations corresponding to the $g(s)$ boundary condition of Equation (7).

$$\frac{dU}{dn} = \frac{\partial U}{\partial x} \frac{dx}{dn} + \frac{\partial U}{\partial y} \frac{dy}{dn} \quad (9)$$

The total set of $2N$ equations was solved by an iterative elimination method developed by Wilkinson and described in Appendix III. All calculations were carried out on a CDC-6600 digital computer having 14 digit accuracy. A typical boundary collocation point distribution is shown in Figure 3. Collocation points were usually uniformly distributed over the outer boundary.

An example of the convergence of the calculated stress intensities K_I^* and K_{II}^* as a function of number of collocation points is shown in Figure 4. The same data is presented in Table I. The convergence is very good in going from 14 to 28 collocation points the change is less than 0.40%.

The stress intensity calibration curves for center slant crack specimen are given for $\phi = 0, 22.5, 45,$ and 67.5 degrees in Figure 5. The curve shown for $\phi = 0$ is in very good agreement with that given in Reference 7.

6.4.4 CONCLUSIONS

The general collocation procedure described in Section 6.4.2 can be used to obtain the crack tip stress intensities for through cracked plates of arbitrary finite geometry and subject to arbitrary in plane loading. As the application of Section 6.4.3 demonstrates very adequate convergence is obtained by the Airy stress function approach.

It is of interest to note that the boundary conditions on C_o (Figure 1) can be defined in the form⁽⁶⁾

$$\frac{\partial U}{\partial s} = h_1(s)$$

$$\frac{\partial U}{\partial n} = h_2(s) \quad \text{on } C_o$$

where $h_1(s)$ and (h_2) can be determined from the surface tractions to within an arbitrary constant term by use of Equation (8) and (9). With the boundary conditions in this form the boundary collocation procedure has also been applied to the center slant crack specimen model of Figure 3. As shown in Figure 6 convergence for this type of collocation is not good. Compared with the same case in Figure 4 where U and dU/dn were used in the collocation process, the convergence can be judged as poor. The average values for the $\partial U/\partial s$, $\partial U/\partial n$ collocation compare favorably with the converged values obtained by U , dU/dN collocation.

It is postulated that collocating on the boundary stresses for this same geometry and loading condition would result in even greater oscillations of the K^* 's if the point locations were not carefully chosen. Collocating on the stresses is in effect collocating on the second derivatives of the Airy stress function.

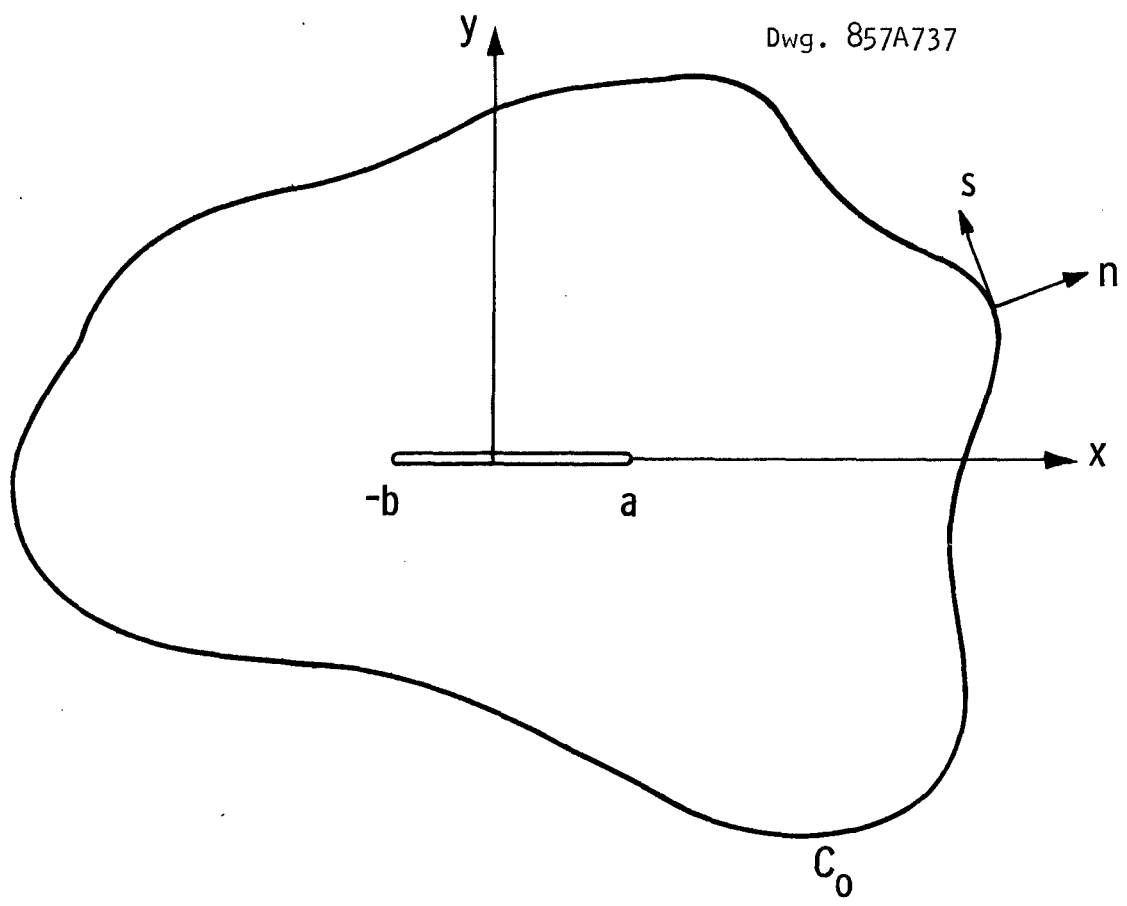
Section 6.4 References

1. J. V. D. Vooren, "Remarks on an Existing Numerical Method to Estimate the Stress Intensity Factor of a Straight Crack in a Finite Plate," *Journal of Basic Engineering*, March 1967.
2. A. S. Kobayashi, R. D. Cherepy, and W. C. Kinsel, "A Numerical Procedure for Estimating the Stress Intensity Factor of a Crack in a Finite Plate," *Journal of Basic Engineering*, Dec. 1964.
3. M. I. Muskhelishvili, "Some Basic Problems of Mathematical Theory of Elasticity," Third Edition, English translation by J. R. M. Radok, 1953, P. Noordhoff.
4. F. Erdogan, "The Stress Distribution in an Infinite Plate with Two Colinear Cracks Subject to Arbitrary Loads in its Plane," *Proceedings of the Fourth U.S. National Congress on Applied Mechanics*, June 1962, pp. 547-553.
5. G. T. Hahn, A. R. Rosenfield, L. E. Hulbert, M. F. Kanninen, "Elastic-Plastic Fracture Mechanics," Battelle Memorial Institute, Columbus Laboratories, Technical Report AFML-TR-67-143, Jan. 1968.
6. I. S. Sokolnikoff, "Mathematical Theory of Elasticity," Second Edition, 1956, McGraw-Hill.
7. W. F. Brown, Jr. and J. E. Srowley, "Plane Strain Crack Toughness Testing of High Strength Metallic Materials," *ASTM Special Technical Publication No. 410*.

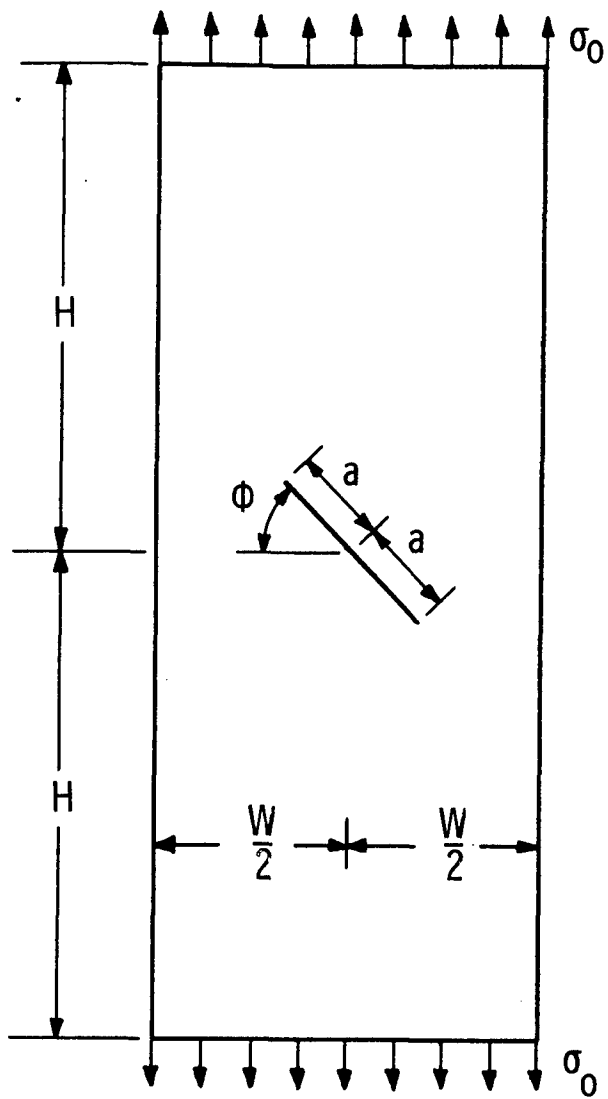
Section 6.4 Table I

INFLUENCE OF NUMBER OF
COLLOCATION POINTS ON K_I^* AND K_{II}^*

Collo. Pts.	$\frac{K_I^*}{\sigma(\pi a)^{1/2}}$	$\frac{-K_{II}^*}{\sigma(\pi a)^{1/2}}$
14	1.0857	0.9621
18	1.0836	0.9689
18	1.0838	0.9672
23	1.0844	0.9668
28	1.0842	0.9657

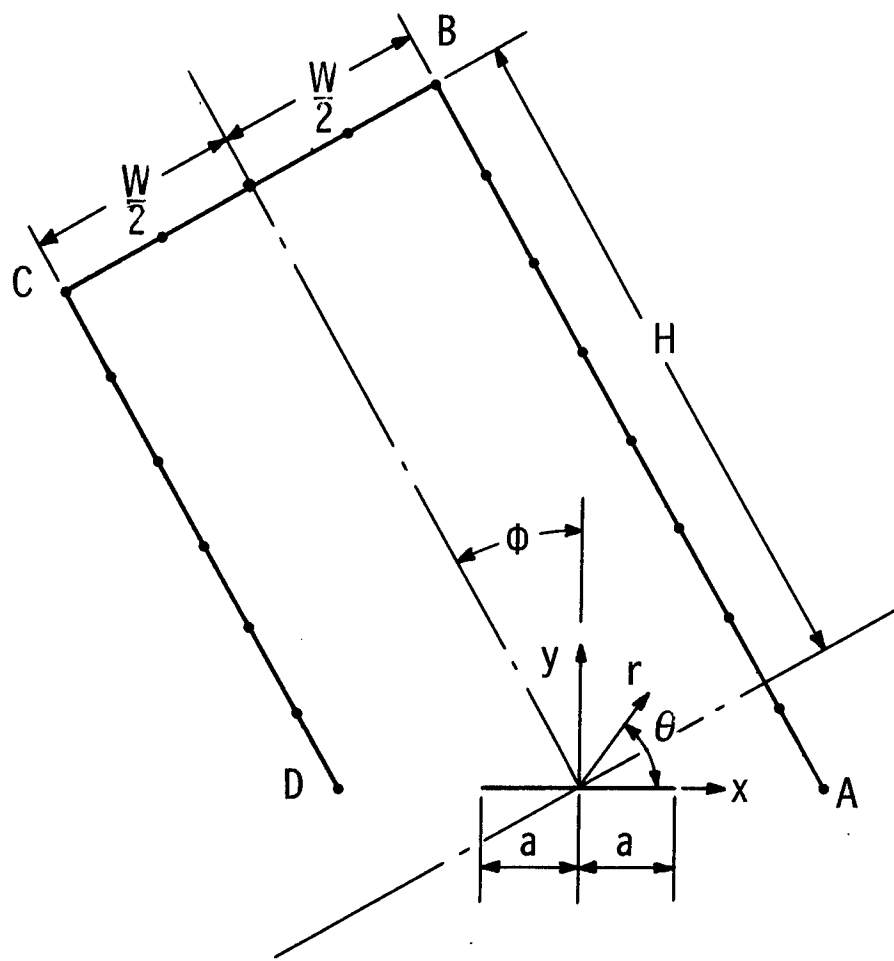


Sec. 6.4 Fig. 1—Plate with through thickness crack



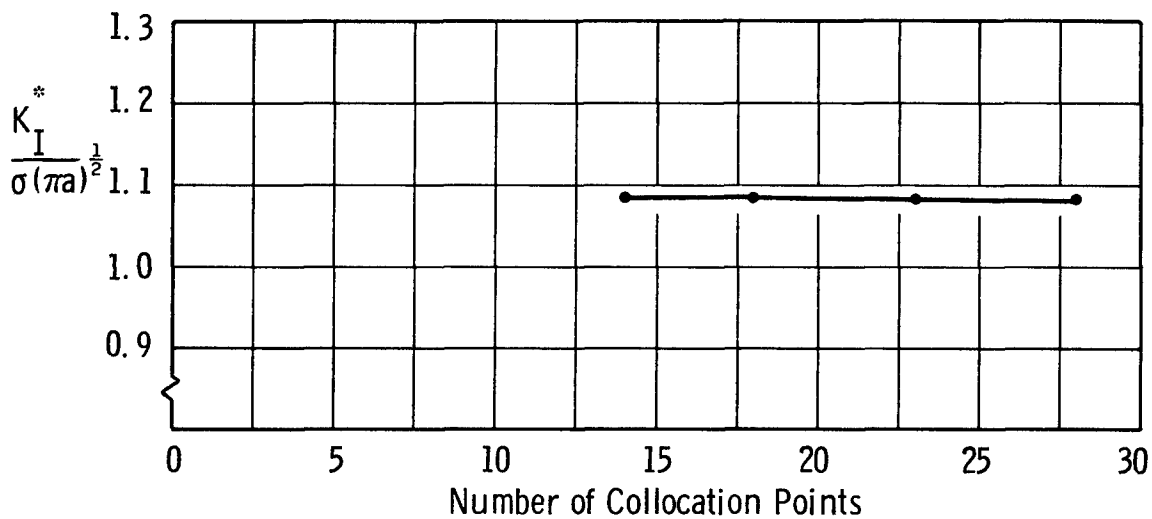
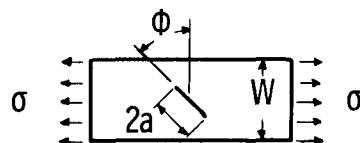
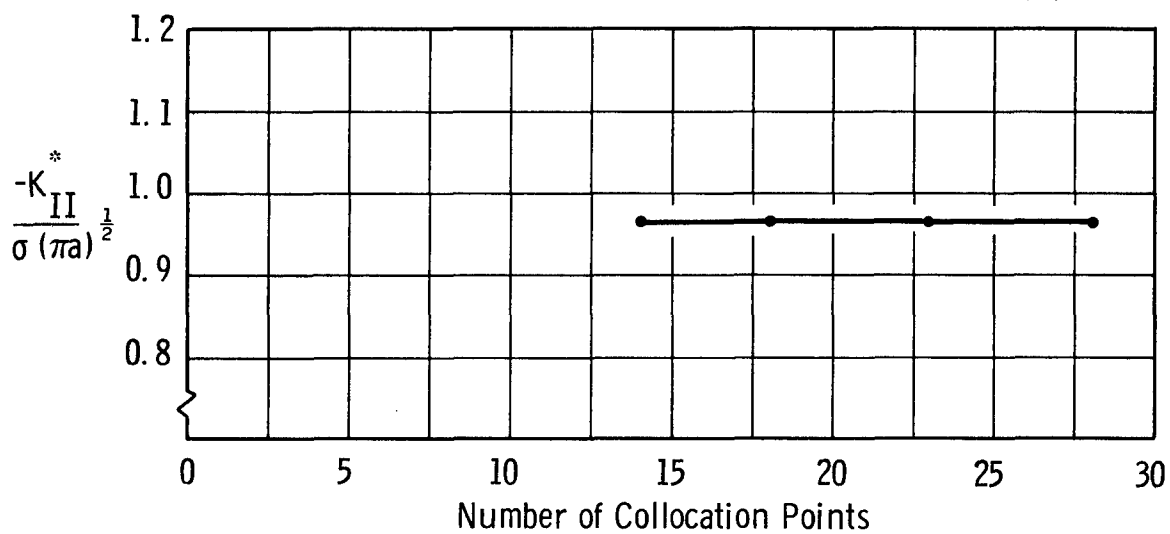
Sec. 6.4 Fig. 2—Geometry and loading condition assumed for center slant crack specimen

Dwg. 857A625

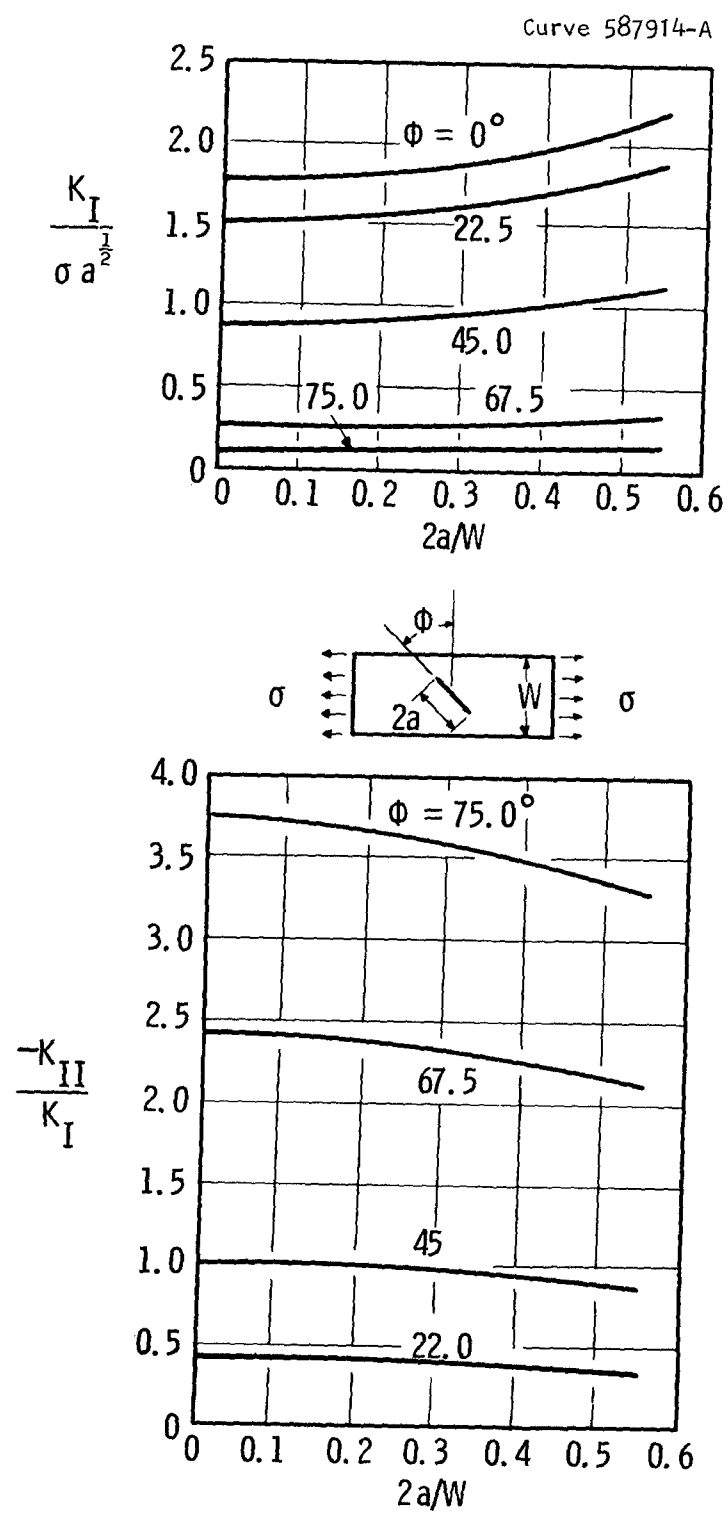


Sec. 6.4 Fig. 3—Geometry and coordinates for collocation solution of center slant crack specimen

$\Phi = 45^\circ$, $2a/W = 0.5$, $H/W = 1.25$ Curve 587460-A



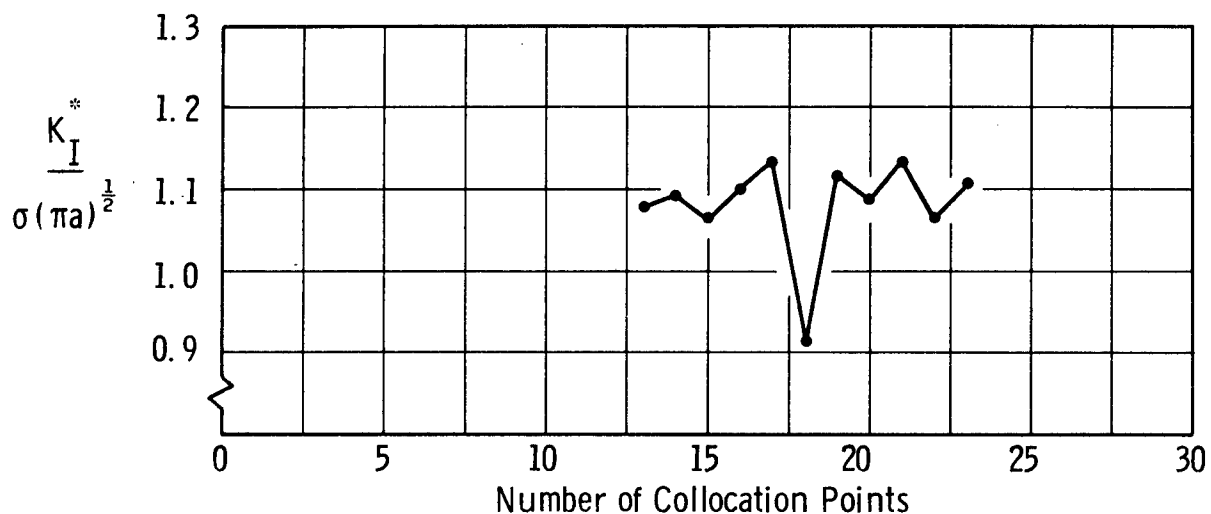
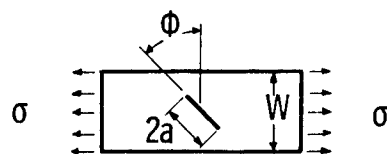
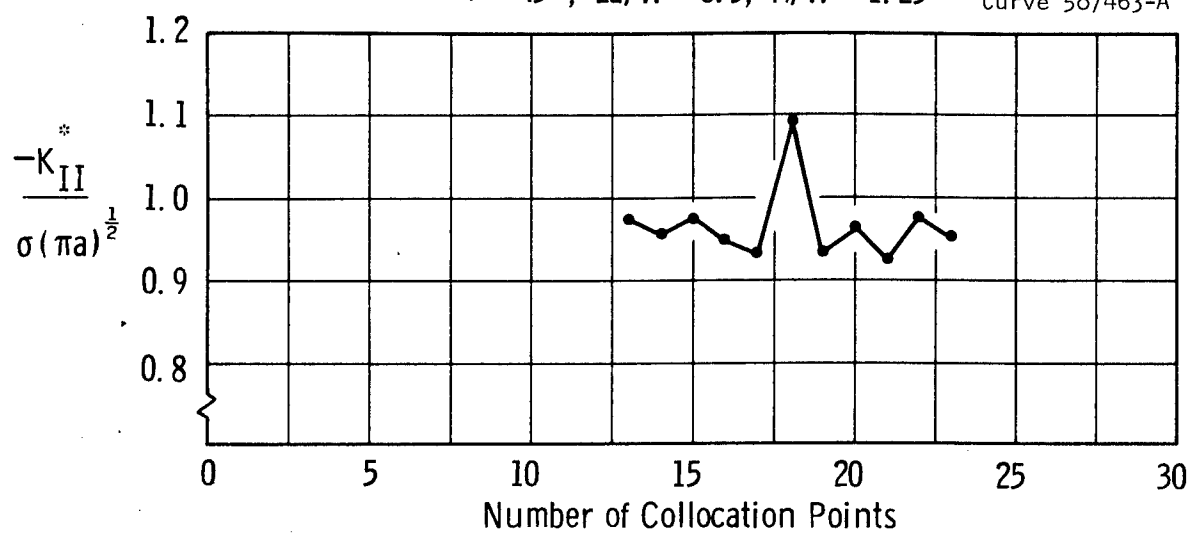
Sec. 6.4 Fig. 4— K_I^* and K_{II}^* as a function of number of boundary collocation points. The boundary conditions are U and $\partial U/\partial n$



Sec. 6.4 Fig. 5—Stress intensity calibration
for center slant cracked plate

$\phi = 45^\circ$, $2a/W = 0.5$, $H/W = 1.25$

Curve 587463-A



Sec. 6.4 Fig. 6— K_I^* and K_{II}^* as a function of number of boundary collocation points. The boundary conditions are $\partial U/\partial n$ and $\partial U/\partial s$

Section 6.5

A FINITE ELEMENT METHOD FOR DETERMINING STRESS INTENSITY FACTOR OF CIRCUMFERENTIALLY CRACKED ROUND BARS

6.5.1 INTRODUCTION

A numerical finite element method is used to determine the Mode III crack-tip stress intensity factors for circumferentially cracked round bars subject to torsion. The method of solution presented here involves an extension of the finite element method to axisymmetric bodies subject to torsional loading. Ring elements with triangular cross sections and a linear displacement field are combined with a single ring element of circular cross section which encloses the crack tip and has a Mode III type displacement field.

In addition to solving the problem at hand the developments presented here are applicable to the solutions of other related problems. The torsional triangular element presented can be used to determine the displacements and stresses in arbitrary bodies of revolution subject to torsion. The use of a crack-tip element combined with more conventional triangular elements can also be used to determine the crack tip stress intensity factors for Modes I and II loading conditions in plane or axisymmetric bodies.

The method of solution will be presented in three stages. First the general finite element method of solution of elasticity problems will be presented in summary form. Next using these basic principles a triangular torsion element which can be applied to arbitrary bodies of revolution will be developed. Finally the concept of the crack tip element will be presented and applied to circumferentially cracked round bars.

6.5.2 FINITE ELEMENT METHOD

For most complex structures it is extremely difficult, if not nearly impossible, to obtain the exact solution to the representative elasticity boundary value problem. Therefore, the stress distributions for such structures are normally determined by experimental methods or by approximate numerical techniques. With the rapid development of digital computers in the last fifteen years the sophistication and use of numerical techniques in stress analysis has accelerated. One of the most applicable methods to result from the extensive development of numerical techniques is the finite element method.^(1,2,3) The method is based on the stationary total potential energy principle, using a modified Ritz procedure for solving the stationary value problem.

In brief the method consists of dividing the structure of interest into a finite number of small closed regions (elements) as shown in Figure 1 for a plane region and prescribing a displacement function in terms of discrete parameters for each region such that there is displacement continuity at the interface of neighboring elements. These discrete parameters are normally the displacements at specific points on the boundary of the element (nodal points) as shown in Figure 1. The best solution that can be obtained for the prescribed displacement representation is that which will minimize the potential energy of the system under the constraints imposed.

The general finite element method for a linear elastic solid in absence of thermal and body forces will now be formulated. The potential energy for such a body is

$$V = \iiint_V \frac{1}{2} \{\sigma\}\{\varepsilon\} dv - \iint_S \{u\}^T \{X\} ds \quad (1)$$

where the vectors $\{\sigma\}$, $\{\varepsilon\}$, $\{u\}$, and $\{X\}$ represent the stress, strain, displacement, and surface traction vectors respectively. The first integral is carried out over the volume V of the body and the second over the bounding surface S . Since the state of displacement throughout the solid is defined element by element, the total potential energy may

be considered as the sum of the potential energies of individual elements. The potential energy of the n th element is now considered. The state of displacement defined for the element can be expressed in matrix form as:

$$\{u\} = [N] \{\delta_e\} \quad (2)$$

where the column vector $\{\delta_e\}$ represents the m discrete parameters (nodal point displacements) of the element $\{\delta_e\}^T = \{\delta_1 \ \delta_2 \dots \ \delta_m\}$. The matrix $[N]$ is a function of the spacial coordinate system and describes the defined displacement pattern of the element. Using strain-displacement relations, the strain can be expressed as a function of the displacement in the matrix form

$$\{\epsilon\} = [C] \{u\} \quad (3)$$

The elastic stress-strain relations are

$$\{\sigma\} = [D] \{\epsilon\} \quad (4)$$

where $[D]$ is a function of the elastic properties of the material. If the relations (2) to (4) are substituted into Equation (1), the potential energy for an element becomes

$$V_e = \iiint_{V_e} \frac{1}{2} \{\delta_e\}^T [N]^T [C]^T [D]^T [C] [N] \{\delta_e\} dV - \iint_{S_e} \{\delta_e\}^T [N]^T \{X\} ds \quad (5)$$

where V_e is the volume of the element and S_e is that part of the surface area of the element which coincides with the surface area of the solid. Since the nodal point parameters $\{\delta_e\}$ of the element are not a function of the spacial coordinates the potential energy of each element may be written as

$$V_e = \{\delta_e\}^T \left[\iiint_{V_e} \frac{1}{2} [N]^T [C]^T [D]^T [C] [N] dV \right] \{\delta_e\} - \{\delta_e\}^T \left[\iint_{S_e} [N]^T \{X\} ds \right] \quad (6)$$

The best values that can be obtained for all (n) nodal point displacements of the finite element representation of the body will be those that minimize the total potential energy of the body under the constraints imposed. That is the best values of δ_i ($i = 1, 2, \dots, n$) are those that satisfy the system of equations:

$$\frac{\partial V}{\partial (\delta_i)} = 0 \quad i = 1, 2, \dots, n \quad (7)$$

In forming this system of equations it is convenient to have an expression for the partial derivatives of the potential energy of each element with respect to its own nodal point displacements $\{\delta_e\}$; that is $\partial V_e / \partial \{\delta_e\}$. By use of Equation (6) this expression can be obtained.

$$\frac{\partial V_e}{\partial \{\delta_e\}} = \left[\iiint_{V_e} [N]^T [C]^T [D]^T [C] [N] dV \right] \{\delta_e\} - \left[\iint_{S_e} [N]^T \{X\} dS \right] \quad (8)$$

where

$$\frac{\partial V_e}{\partial \{\delta_e\}} = \begin{bmatrix} \frac{\partial V_e}{\partial \delta_1} & \frac{\partial V_e}{\partial \delta_2} & \dots & \frac{\partial V_e}{\partial \delta_m} \end{bmatrix}$$

The terms in the first and second brackets are normally defined as the element stiffness matrix $[k_e]$ and the element generalized nodal point force vector $\{\bar{V}\}$ respectively.

$$[k]_e = \iiint_{V_e} [N]^T [C]^T [D]^T [C] [N] dV \quad (9)$$

$$\{\bar{V}\} = \iint_{S_e} [N]^T \{X\} dS \quad (10)$$

By properly combining the submatrices (Equation (8)) obtained for each element the matrix equation representing Equation (7) can be obtained and then solved for the nodal point displacements. Once the

nodal point displacements are obtained the corresponding stresses for the defined displacement pattern can be calculated from Equations (2), (3) and (4).

6.5.3 TORSIONAL RING ELEMENT

For an axisymmetrical body subject to torsion, a finite element analysis can be carried out by representing the body by a finite number of ring elements of triangular cross section (Figure 2). The only displacement component for such a body is the displacement w in the angular direction (Figure 3). The discrete parameters used for each element displacement pattern are the displacements at the three nodal points located at the vertices of each triangular cross section as shown in Figure 3.

$$\{\delta_e\} = \begin{Bmatrix} w_i \\ w_j \\ w_m \end{Bmatrix} \quad (11)$$

The defined displacement pattern for each element is a linear variation with respect to the coordinates r and z .

$$w = \frac{1}{2A} \left[(a_i + b_i r + c_i z) w_i + (a_j + b_j r + c_j z) w_j + (a_m + b_m r + c_m z) w_m \right] \quad (12)$$

where

$$a_i = r_j z_m - r_m z_j$$

$$b_i = z_j - z_m$$

$$c_i = r_m - r_j$$

A is the area of the triangular cross section, and r_i and z_i are the coordinates of nodal points. This can be expressed in the previous notation as

$$\{u\} = [N] \{\delta_e\} \quad (13)$$

where

$$[N] = [N_i, N_j, N_m] \quad (14)$$

and

$$N_i = (a_i + b_i r + c_i z) \quad (15)$$

This displacement pattern insures continuity of displacements at the interface of neighboring elements. For an axisymmetric body subject to torsion the strain vector is

$$\{\epsilon\} = \begin{Bmatrix} \gamma_{r\theta} \\ \gamma_{\theta z} \end{Bmatrix} \quad (16)$$

The strain-displacement relations are

$$\begin{Bmatrix} \gamma_{r\theta} \\ \gamma_{\theta z} \end{Bmatrix} = \begin{Bmatrix} \frac{\partial w}{\partial r} - \frac{w}{r} \\ \frac{\partial w}{\partial z} \end{Bmatrix} \quad (17)$$

or

$$\{\epsilon\} = [C] \{u\} \quad (18)$$

where

$$[C] = \begin{bmatrix} \frac{\partial}{\partial r} - \frac{1}{r} \\ \frac{\partial}{\partial z} \end{bmatrix} \quad (19)$$

The stress-strain matrix equation is

$$\begin{Bmatrix} \tau_{r\theta} \\ \tau_{\theta z} \end{Bmatrix} = \begin{bmatrix} G & 0 \\ 0 & G \end{bmatrix} \begin{Bmatrix} \gamma_{r\theta} \\ \gamma_{\theta z} \end{Bmatrix} \quad (20)$$

where G is the shear modulus.

From Equation (4) it follows that

$$[D] = G \begin{bmatrix} 1 & 0 \\ 0 & 1 \end{bmatrix} = G I \quad (21)$$

If Equation (11) through (21) are substituted into Equation (9), and the volume increment is taken as $dV = (2\pi r)dr dz$, then the element stiffness matrix (9) for the torsional element takes the form

$$[k]_e = 2\pi G \iint_A [B]^T [B] r dr dz \quad (22)$$

where

$$[B] = [B_i \ B_j \ B_m] \quad (23)$$

and

$$[B_i] = \frac{1}{2A} \begin{bmatrix} -\frac{a_i}{r} - c_i \frac{z}{r} \\ c_i \end{bmatrix}$$

The integration is over the area A of the cross section of each ring element.

It is assumed that the surface traction over any element side making up the outer surface S of the axisymmetric body varies linearly between the two nodal points (i, j) as shown in Figure 4. That is

$$\tau = \frac{1}{2A} [(a_i + b_i r + c_i z) \tau_i + (a_j + b_j r + c_j z) \tau_j] \quad (24)$$

or

$$\{X\} = [B_i \ B_j] \ \{\tau_i\} \quad (25)$$

where $\tau = (\tau_{r\theta}^2 + \tau_{\theta z}^2)^{1/2}$. For this traction distribution the element generalized nodal point force vector (10) becomes

$$\{\bar{V}\} = [E] \ \{\bar{\tau}\} \quad (26)$$

where

$$\{\bar{V}\} = \begin{Bmatrix} V_i \\ V_j \end{Bmatrix} \quad \{\bar{\tau}\} = \begin{Bmatrix} \tau_i \\ \tau_j \end{Bmatrix}$$

and

$$[E] = \left(\frac{\pi}{6}\right) (S) \begin{bmatrix} (3r_i + r_j) & (r_i + r_j) \\ (r_i + r_j) & (3r_j + r_i) \end{bmatrix} \quad (27)$$

$$S = \left[(r_i - r_j)^2 + (z_i - z_j)^2 \right]^{1/2}$$

The general procedure used to construct and solve the system of equations (Equation (7)) from which the n nodal point displacements can be solved for is as follows:

- (1) represent the axisymmetric solid by a finite element mesh.
- (2) generate the element stiffness matrix (Equation 22) and element generalized nodal point force vector (Equation 26) for each element in the mesh.
- (3) combine these element stiffness submatrices into the total stiffness matrix corresponding to Equation (7).
- (4) solve the system of linear equations for the nodal point displacements.

A computer program has been written which will automatically carry out steps (2) to (4) for a described finite element representation of an axisymmetric solid and for specified boundary loading or displacement conditions. The integrations required in calculating the element stiffness submatrices were performed numerically using the Gauss-Radan integration rule for triangles.^(3,4) The total stiffness matrix was solved by the Gauss-Seidel overrelation method.

To demonstrate the applicability of the use of the ring elements a simple example is considered. A hollow cylinder of the dimensions shown in Figure 5 is analyzed. The finite element representation of the cylinder is also shown. The following boundary conditions are applied to the cylinder

$$\text{at } z = 0 \quad v = 0$$

$$\text{at } z = 4.0 \quad \tau_{\theta z} = (5/4\pi)r$$

The finite element solution for these conditions is compared with the exact solution in Figure 6. The comparison is very good.

6.5.4 CRACK TIP ELEMENT

The use of finite elements to determine crack tip stress intensities has previously been investigated by Chan, Tuba, and Wilson.⁽⁵⁾ In that work the crack structures of interest were represented by a large number of triangular elements. The finite element solution for the representation was obtained and by correlating the solution near the crack tip with the classical crack tip stress and displacement equations an estimate of the stress intensity factor was made. As shown the correlation in the near vicinity of the crack broke down, but by extrapolating values obtained at larger distances from the crack tip back to the tip rather accurate estimates of the stress intensity were made.

The break down in the finite element solution around the crack is caused by the inability of the assumed element displacement patterns to adequately represent the singularity condition at the crack tip. The

finite element method to be considered here avoids this problem by using a special finite element which enclosed the crack tip and has a defined displacement field which includes the crack tip singularity condition. The tip element is then combined with the more conventional triangular elements to represent the complete structure (Figure 7).

The specific crack tip element developed here and applied to the circumferentially cracked round bar is considered as only an initial investigation of the potential of the use of crack tip elements. It is anticipated that use of crack tip elements will result in the use of fewer finite elements in an analysis, avoid the need for extrapolating and result in more accurate calculations of stress intensity factors.

The particular crack tip element used in the present analysis is a ring element of circular cross section which has a radius of R'_0 and is centered on the crack tip (Figure 8). The defined displacement pattern for the tip element is that corresponding to the Mode III type stress singularity at the crack tip.

$$w = \frac{K_{III}}{G} \left[\frac{2R'}{\pi} \right]^{1/2} \sin \frac{\theta'}{2} \quad (28)$$

where the R' , θ' polar coordinate system is fixed at the crack tip (Figure 8).

The circumferentially cracked round bar is analytically represented by the circular tip element combined with the triangular cross section rings as shown in Figures 9 and 10. The discrete parameters by which the total potential energy of the system will be minimized with respect to are K_{III} of the tip element and all of the nodal points of the triangular elements except those nodal points falling on the circumference of the tip element. The nodal points on the circumference C' of the tip element are excluded because they are taken as functions of K_{III} . Letting v_i^* represent the displacements of the nodal points on C' , these displacements are defined as

$$v_i^* = \frac{K_{III}}{G} \left[\frac{2R_i'}{\pi} \right]^{1/2} \sin \frac{\theta_i'}{2} \quad i = 1, \dots, N_1 \quad (29)$$

where R_i' , θ_i' are the R' , θ' coordinates of the nodal point and N_1 is the total number of such nodal points. The equations from which the unknown parameters can be determined are therefore

$$\frac{\partial V}{\partial v_i} = 0 \quad i = 1, \dots, N_2 \quad (30)$$

$$\frac{\partial V}{\partial K_{III}} = 0 \quad (31)$$

where N_2 is the total number of nodal points (excluding those on C').

In generating the above set of linear algebraic equations an expression for the strain energy of the crack tip element is needed. If the radius of the circular cross section of the tip element is small compared to the radius of the crack tip r_c then the stresses corresponding to the defined displacement pattern of the crack tip element are the well known Mode III stress field equations. The strain energy U_{III} of the tip element in terms of this displacement field is calculated in Appendix IV to be

$$U_{III} = \frac{\pi}{G} (r_c R_o')^2 K_{III}^2 \quad (32)$$

The most convenient method of developing the system of algebraic equations corresponding to Equations (30) and (31) is as follows. First the crack tip element is neglected, that is it is assumed that the volume of the tip element represents a void in the material and the system of equations involving all of the triangular element nodal points is developed as described in Section 6.5.3.

$$\frac{\partial V}{\partial v_i} = 0 \quad i = 1, \dots, N_2 \quad (33)$$

$$\frac{\partial V}{\partial v_i^*} = 0 \quad i = 1, \dots, N_1 \quad (34)$$

where again v_i^* represent those nodal points which lie on C' . This system of equations is modified to the desired system of Equations (30 and 31) in a two step process.

(1) The first step involves the N_2 equations of (33). For all v_i^* terms in these equations the substitution specified by Equation (29) is made.

$$v_i^* = \frac{K_{III}}{G} \left[\frac{2R_o'}{\pi} \right]^{1/2} \sin \frac{\theta_i'}{2} \quad (35)$$

With these modifications made on Equation (33) they now become equivalent to Equation (30).

(2) The second step results in the formation of Equation (31). Since the strain energy U_{III} of the crack tip element is a function of K_{III} and the v_i^* 's are functions of K_{III} it follows that

$$\frac{\partial V}{\partial K_{III}} = \frac{\partial U_{III}}{\partial K_{III}} + \sum_{i=1}^{N_1} \frac{\partial V}{\partial v_i^*} \frac{\partial v_i^*}{\partial K_{III}} \quad (36)$$

where

$$\frac{\partial U_{III}}{\partial K_{III}} = \frac{2\pi}{G} (r_c R_o') K_{III}$$

$$\frac{\partial v_i^*}{\partial K_{III}} = \frac{1}{G} \left[\frac{2R_o'}{\pi} \right]^{1/2} \sin \frac{\theta_i'}{2} \quad (37)$$

By use of Equation (36) we can form Equation (31). Expressions for $\partial V / \partial v_i^*$ are obtained from Equation (34). Again any time a v_i^* term appears in this equation it is replaced by the quantity of Equation (35).

The set of Equations (30) and (31) is then solved by the Gauss-Seidel overrelation method and the unknown quantities K_{III} and v_i ($i = 1, \dots, N_2$) are determined. The modification of Equations (33) and (34) to Equations (30) and (31) can be accomplished by adding a subroutine to the general torsional finite element program described in Section 6.5.3. The general torsional program described before will generate the coefficients of Equations (33) and (34).

The continuity of displacements at the interface between the crack tip element and the neighboring triangular elements is not rigorously satisfied. The displacement of the tip element along its outer circumference C' varies as $\sin \theta / 2$, whereas the displacement of a neighboring triangular element varies linearly between its two nodal points on C' . But, in the limit, as the number of neighboring triangular elements surrounding the tip element increases continuity is restored. As noted in Reference (1) this form of continuity in the limit allows convergence to the exact solution to be obtained in the limit as element size is decreased.

6.5.5 APPLICATION TO CIRCUMFERENTIALLY CRACKED ROUND BAR

The finite element method described in Section 6.5.4 was used to determine the crack tip stress intensity factors for circumferentially cracked round bar subject to torsion. The mode three intensities K_{III} were determined over a range of r_c/R_c values. Due to symmetry only the upper half of the bar as shown in Figure 8 was considered. The boundary conditions used were

$$\begin{aligned} w &= 0 & \text{at } z = 0 & \quad 0 \leq r \leq r_c \\ \tau_{z\theta} &= 0 & \text{at } z = 0 & \quad r_c \leq r \leq R_c \\ \tau_{r\theta} &= 0 & \text{at } r = R_c & \quad 0 \leq z \leq Z_c \\ \tau_{z\theta} &= \frac{3T}{2\pi R_c^3} r & \text{at } z = Z_c & \quad 0 \leq r \leq R_c \end{aligned}$$

where T is the torque load applied to the bar.

A computer program was written which automatically generates the finite element representation for arbitrary dimensions r_c , R_c , and Z_c . Control is maintained over crack tip element size, number of triangular elements surrounding the tip element, and general size of elements. The element generator program makes use of a general purpose element generating program written by S. E. Gabrielse.⁽⁶⁾

To investigate the convergence of this method as the number of triangular elements increase and the size of the tip element decreases, the geometry of $r_c/R_c = 0.5$ and $Z_c/R_c = 1.0$ was studied in some detail. The finite element solutions were obtained for a number of finite element representations of the bar, proceeding from a coarse representation to a fine representation. The number of nodal points and the radius R_o of the crack tip element are listed for each case in Table I. The finite element representation for Case 7 is shown in Figures 9 and 10. Also listed in Table I is the calculated stress intensity factor K_{III}^* for each case. The asterisk is used to distinguish these quantities from the final converged values of K_{III} . The quantity K_{III}^* is also shown in Figure 11 as a function of number of nodal points used. This data indicates that for practical purposes the values of K_{III}^* does converge as the element representation is refined.

Some of the displacements for Case 7 are shown in Figure 12. The linear displacements at $z = Z_c$ indicates that the $Z_c/R_c = 1.0$ ratio is equivalent to a semi-infinite bar.

Dimensionless stress intensities obtained for $r_c/R_c = 0.4$, 0.5 , and 0.6 are shown in Figure 13. Element representations similar to Case 7 in refinement were used to obtain the results for $r_c/R_c = 0.4$ and 0.6 . In this figure the finite element results are compared with an approximate solution obtained by Harris⁽⁷⁾ from the work of Neuber.⁽⁸⁾ The approximate solution is an interpolation between the shallow and deep crack limiting cases. As noted the finite element results are slightly higher than Harris's values. This difference is of approximately the same order as the difference between Harris's approximate solution and Buechner's⁽⁹⁾ solution for K_I of a circumferentially cracked round bar subject to tension.

The test specimen for which the K_{III} calibration curve of Figure 13 is applied contains a crack which emanates from a 60° starter notch. To investigate the effect of the starter notch on the crack tip stress intensity a finite element representation which included the V notch was generated (Figure 14) for the $r_c/R_c = 0.5$ case. The ratio of radius to the base of the V notch r_v to the outer radius of the bar was $r_v/R_c = 7/16$. These ratios of r_c/R_c and r_v/R_c represent the conditions aimed for in the precracking operation described in Section 6.3. The dimensionless stress intensity calculated for this element representation is $K_{III}^* r_c^{2.5}/T = 0.406$. This value is approximately 2% less than that obtained when the V notch was not included.

6.5.6 CONCLUSIONS

A finite element of triangular cross section which can be used in the analysis of arbitrary bodies of revolution subject to torsion has been developed. In addition a crack tip element whose defined displacement field included the crack tip singularity condition was also developed. The crack tip element and the more conventional triangular elements were combined to determine the stress intensity factors for circumferentially cracked round bars subject to torsion.

The concept of the finite crack tip element can be applied to many other loading conditions such as cracks in plane structures and circumferential cracks in axisymmetrically loaded bodies of revolution. The defined displacement field of the element can also include displacement terms which correspond to additional terms of an eigen-function expansion about the crack tip.

Section 6.5 References

1. O. C. Zienkiewicz and Y. K. Cheung, "The Finite Element Method in Structural and Continuum Mechanics," 1967, McGraw-Hill.
2. C. Visser and S. E. Gabrielse, "The Approximate Solution of Plane Problems of Elasticity by the Finite Element Method," Westinghouse Research Report 67-1D7-GENCO-R2, Sept. 1967.
3. S. E. Gabrielse and C. Visser, "A Finite Element Computer Program for Axisymmetric Elasticity Problems," Westinghouse Research Report 68-1D7-GENCO-R1, April 1968.
4. B. M. Irons, "Engineering Application of Numerical Integration in Stiffness Methods," AIAA Journal Technical Notes, Vol. 4, No. 11, pp. 2035-2037, Nov. 1966.
5. S. K. Chan, I. S. Tuba, and W. K. Wilson, "On the Finite Element Method in Linear Fracture Mechanics," Westinghouse Scientific Paper 68-1D7-FMPWR-P1, April 1968.
6. S. E. Gabrielse, "A Method to Generate Element and Nodal Point Data for Finite Element Computer Programs," Westinghouse Research Report 68-1D7-GENCO-R3, May 1968.
7. D. O. Harris, "Stress Intensity Factors for Hollow Circumferentially Notched Round Bars," Journal of Basic Engineering, March 1967.
8. H. Neuber, "Theory of Notch Stresses," Second Edition, United States Atomic Energy Commission Translation AEC-tr-4547.
9. H. F. Bueckner, Discussion in "Fracture Toughness Testing and Its Applications," ASTM Special Technical Publication No. 381.

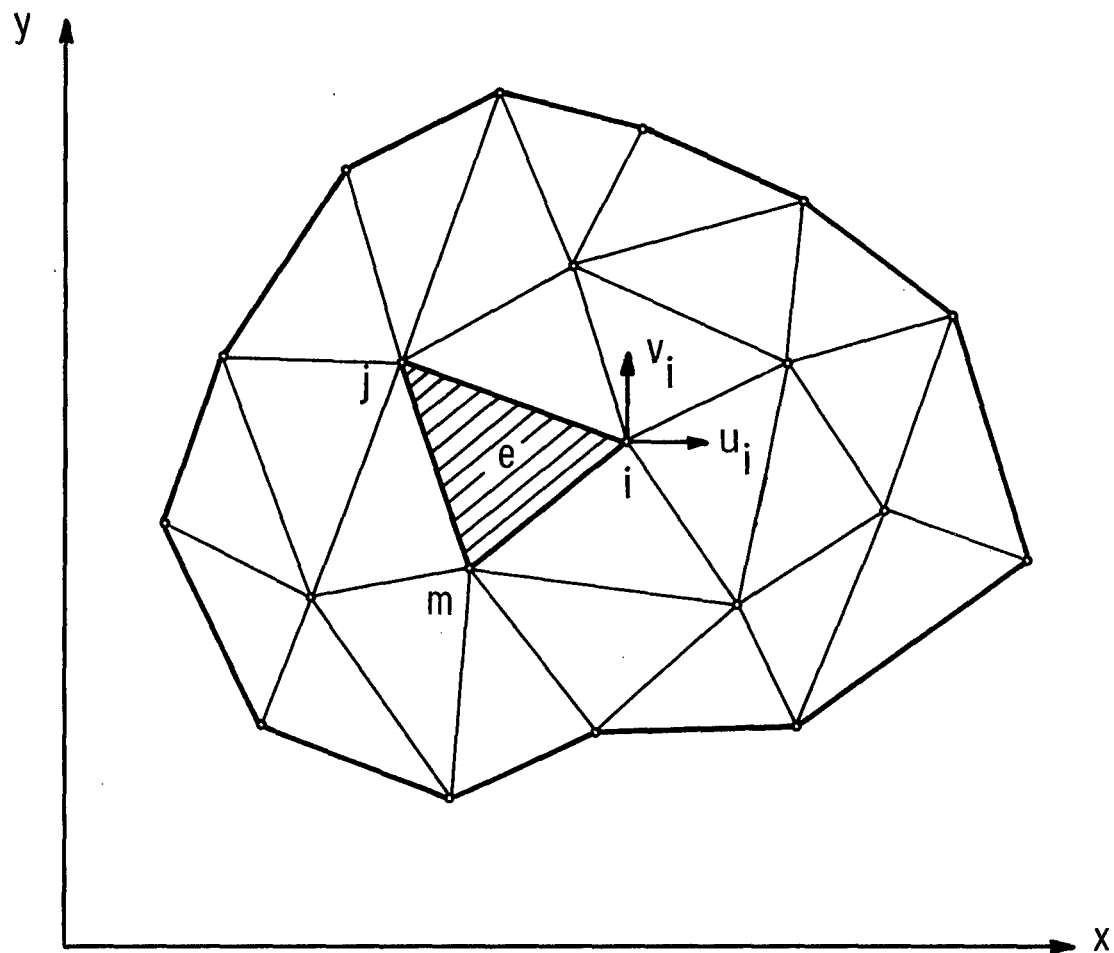
Section 6.5 Table I

INFLUENCE OF ELEMENT REFINEMENT ON CALCULATED STRESS INTENSITY

Case	Number of Nodal Pts	$\frac{R_o}{r_c}$	$\frac{K_{III} * r_c^{2.5}}{T}$
1	96	0.1000	0.376
2	221	0.1000	0.383
3	272	0.0500	0.401
4	549	0.0250	0.409
5	766	0.0250	0.410
6	766	0.0125	0.4137
7	1048	0.0125	0.4141
8	1048	0.00625	0.4156

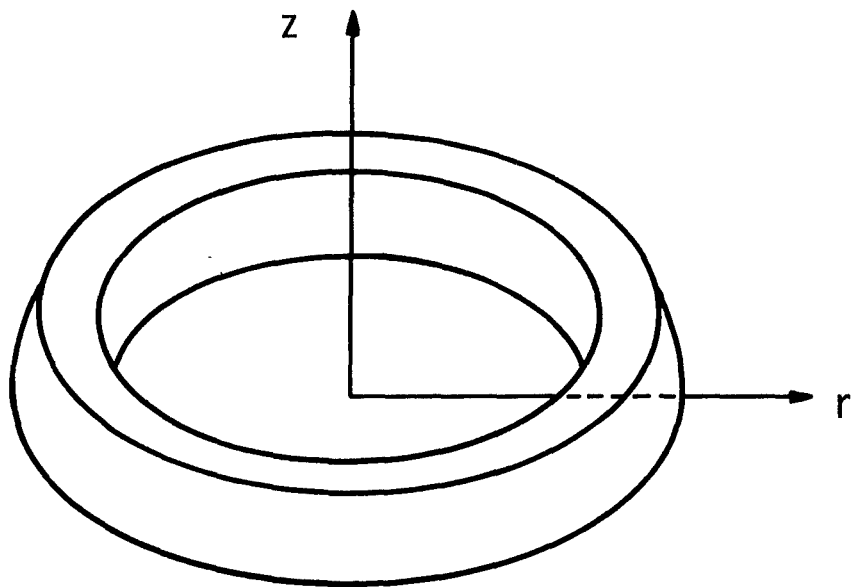
† R_o = radius of crack tip element

r_c = radius to crack tip

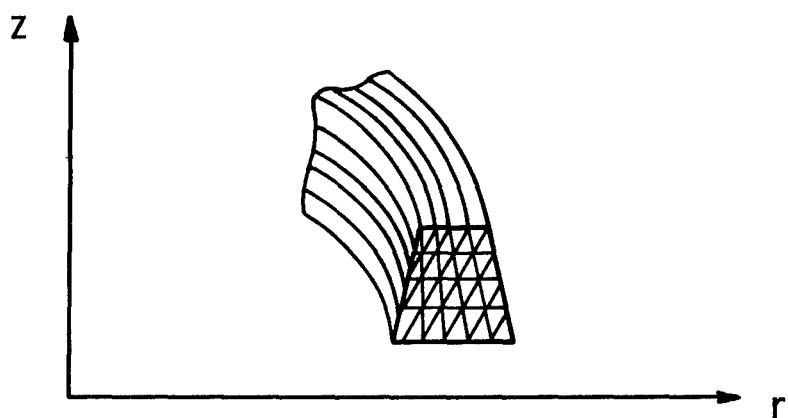


Sec. 6.5 Fig. 1—Finite element representation of plane region

Curve 587384-A

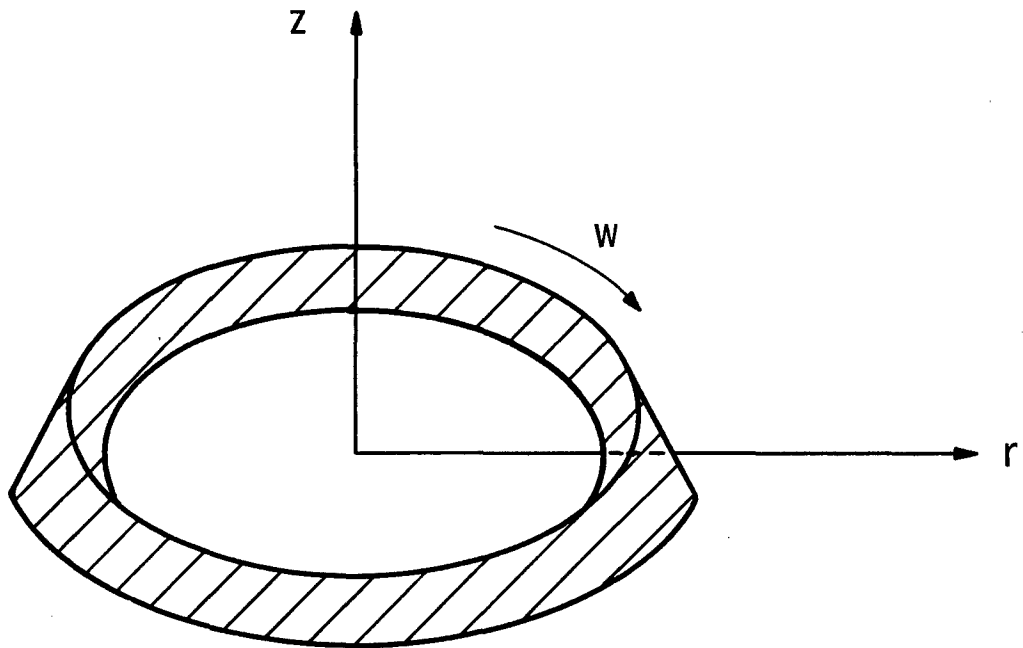


(a) Axi-Symmetric Solid

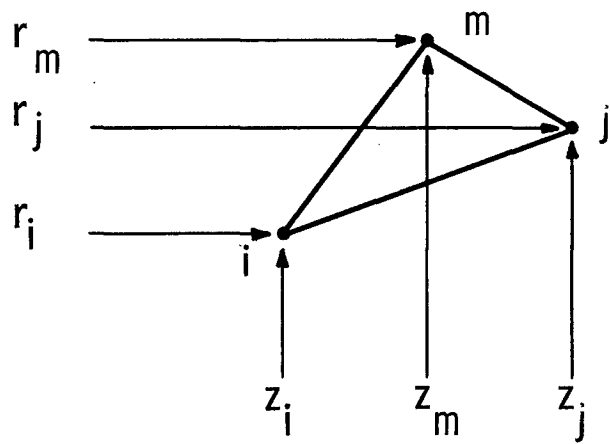


(b) Ring Element Idealization

Sec. 6.5 Fig. 2—Finite element representation
of axi-symmetric solid



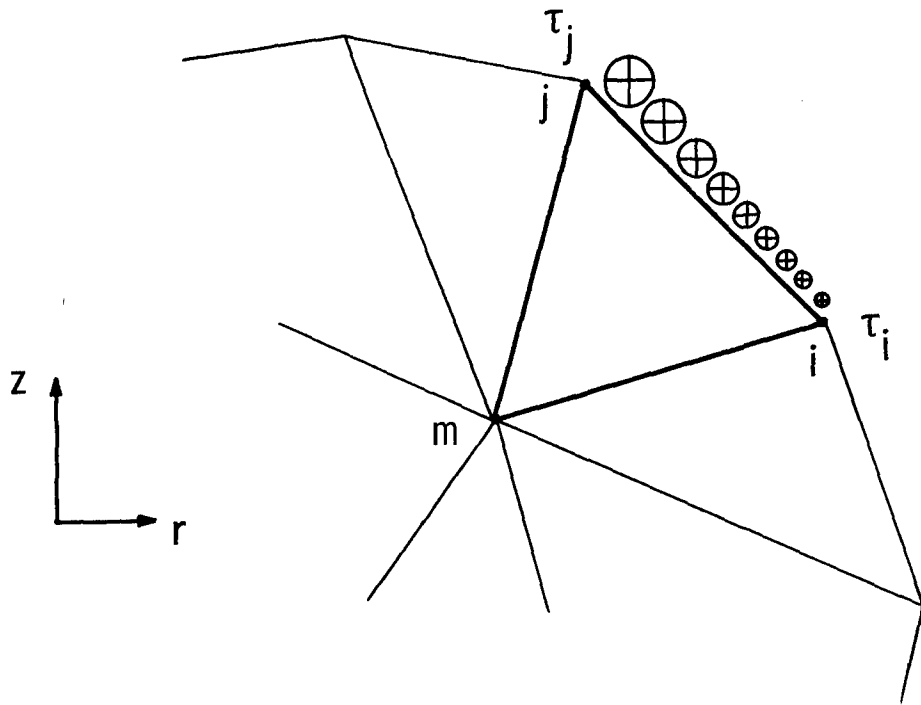
(a) Circular Ring Element



(b) Nodal Points and Coordinates of Triangular Cross-Section of Ring Element

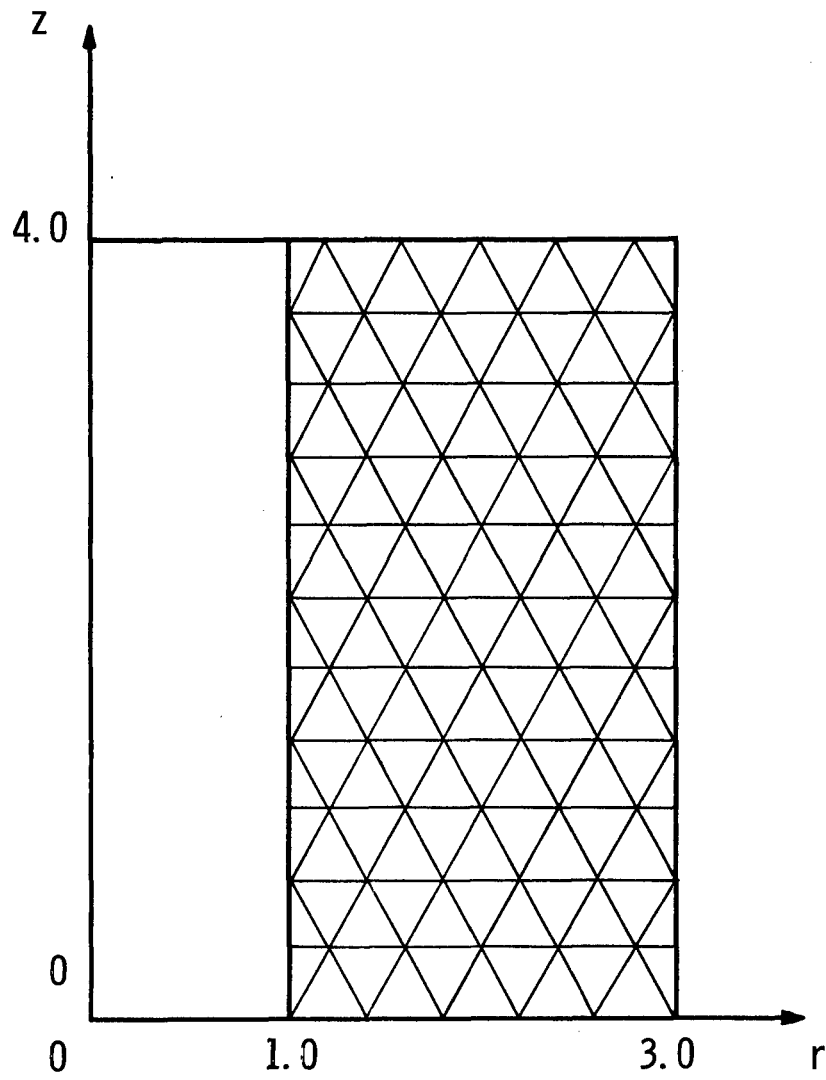
Sec. 6.5 Fig. 3—Circular ring element with triangular cross-section

Dwg. 857A610

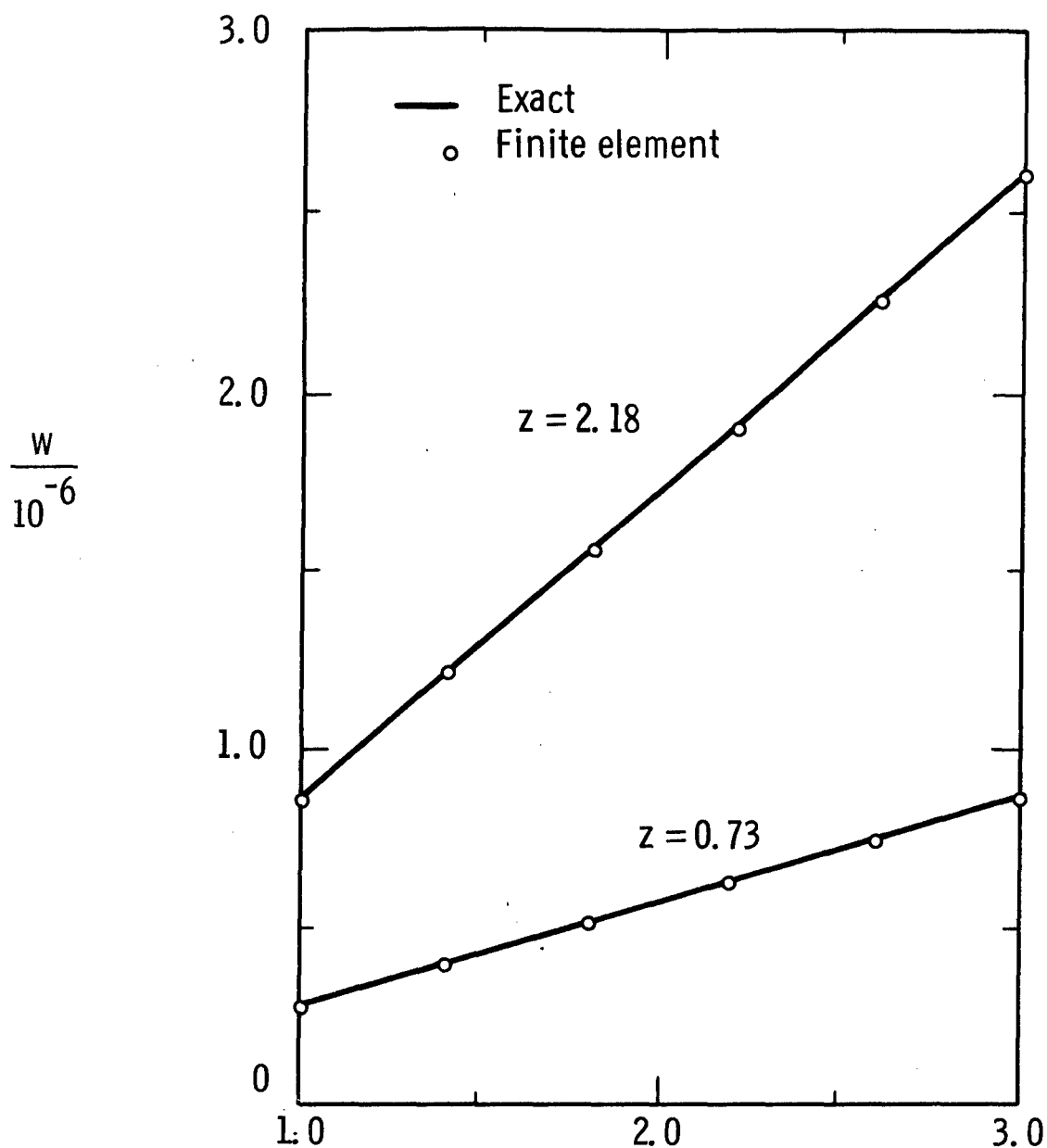


Sec. 6.5 Fig. 4—Linear shear surface traction on boundary surface of a boundary element

Dwg. 857A618

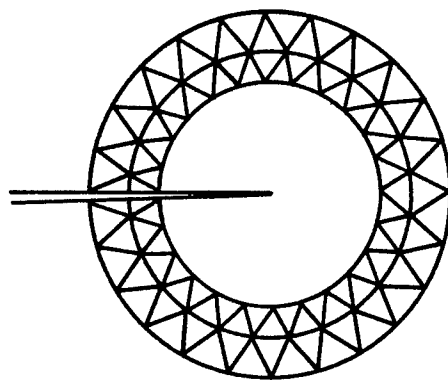


Sec. 6.5 Fig. 5—Finite element representation
of hollow cylinder

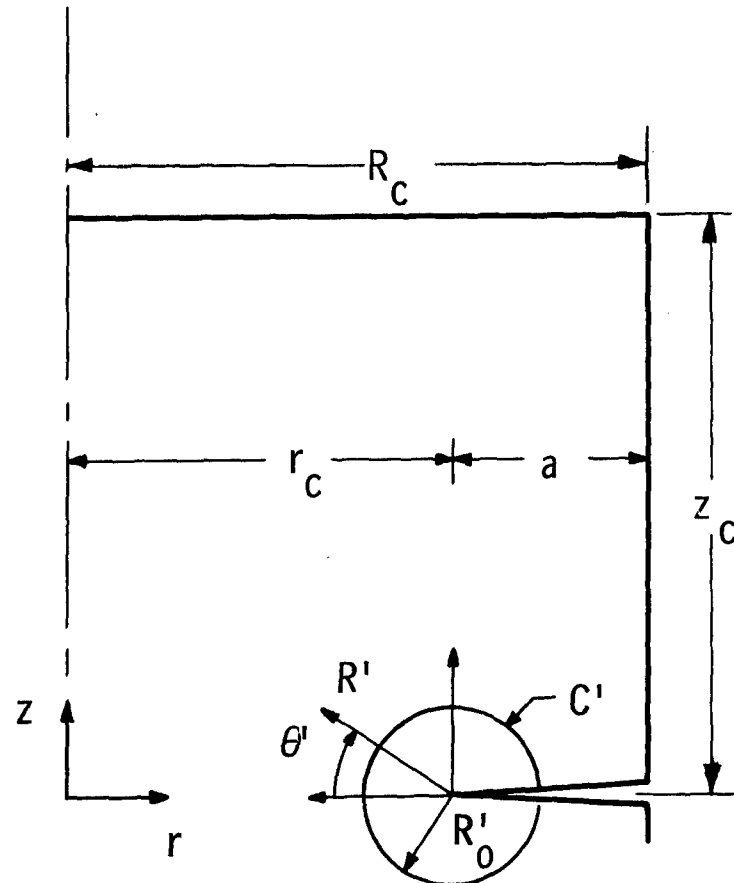


Sec. 6.5 Fig. 6—Comparison of finite element solution
with exact solution for hollow cylinder
subject to torsion

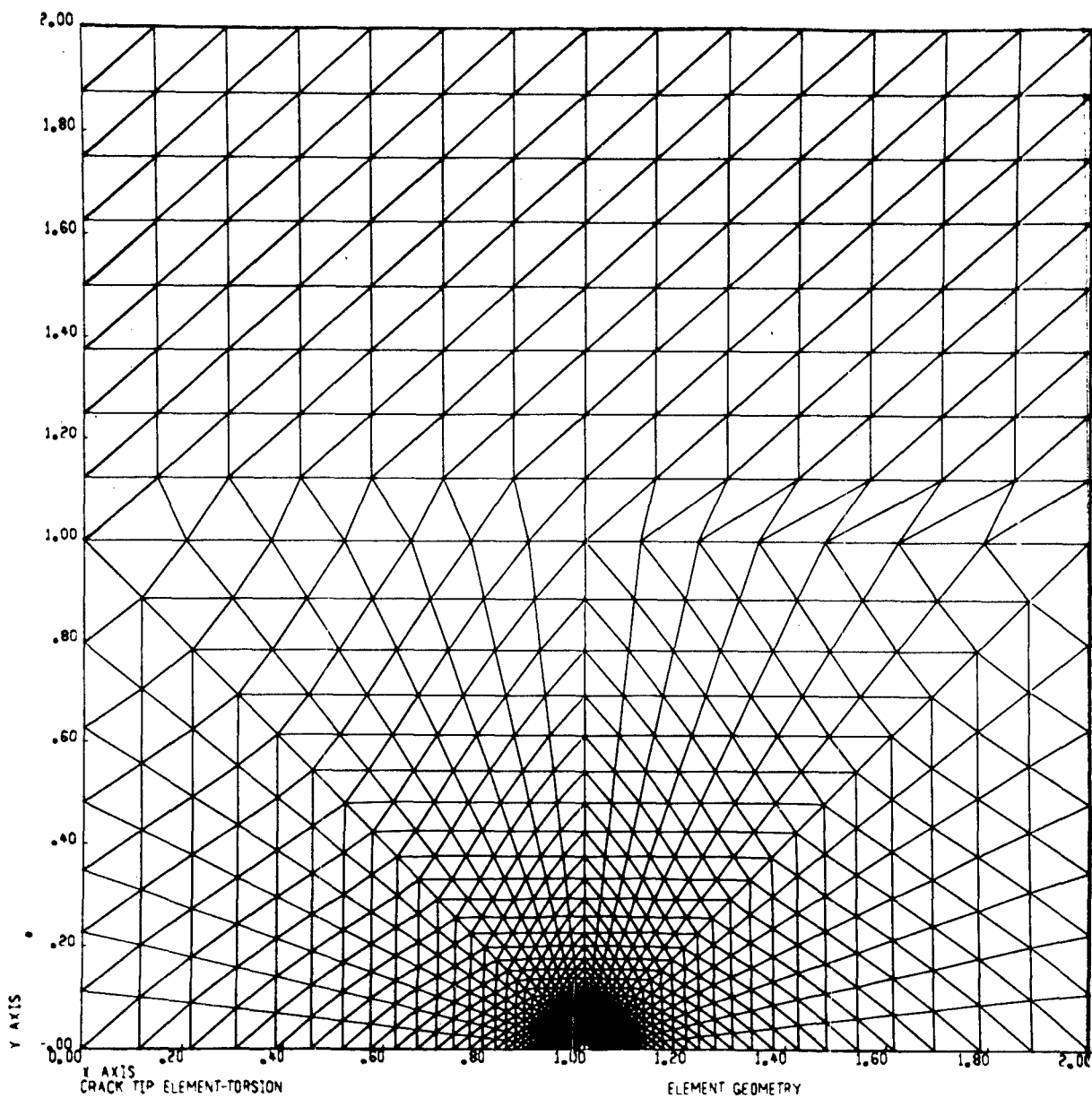
Dwg. 857A623



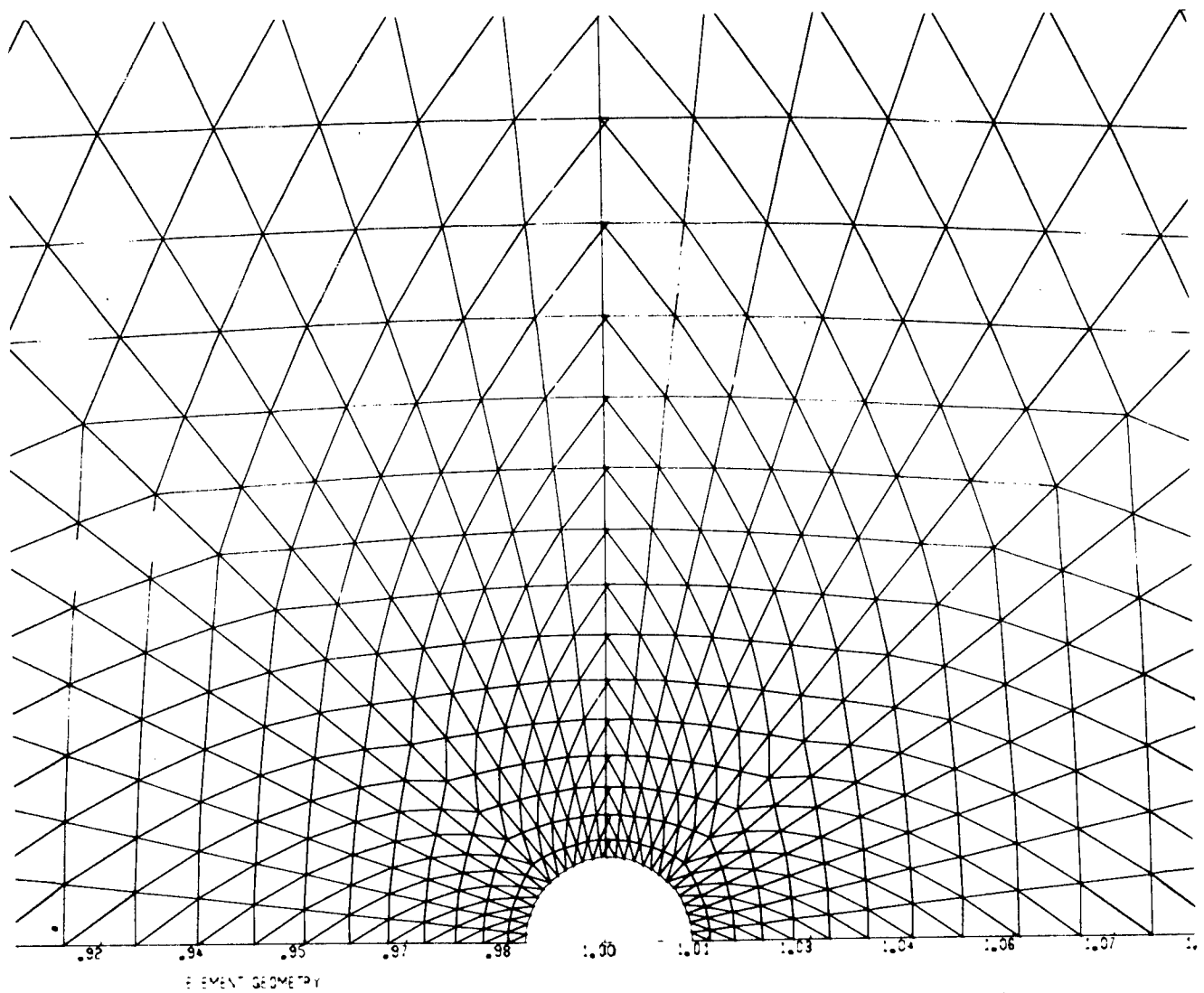
Sec. 6.5 Fig. 7—Circular crack tip element
and first two rings of inclosing
triangular element mesh



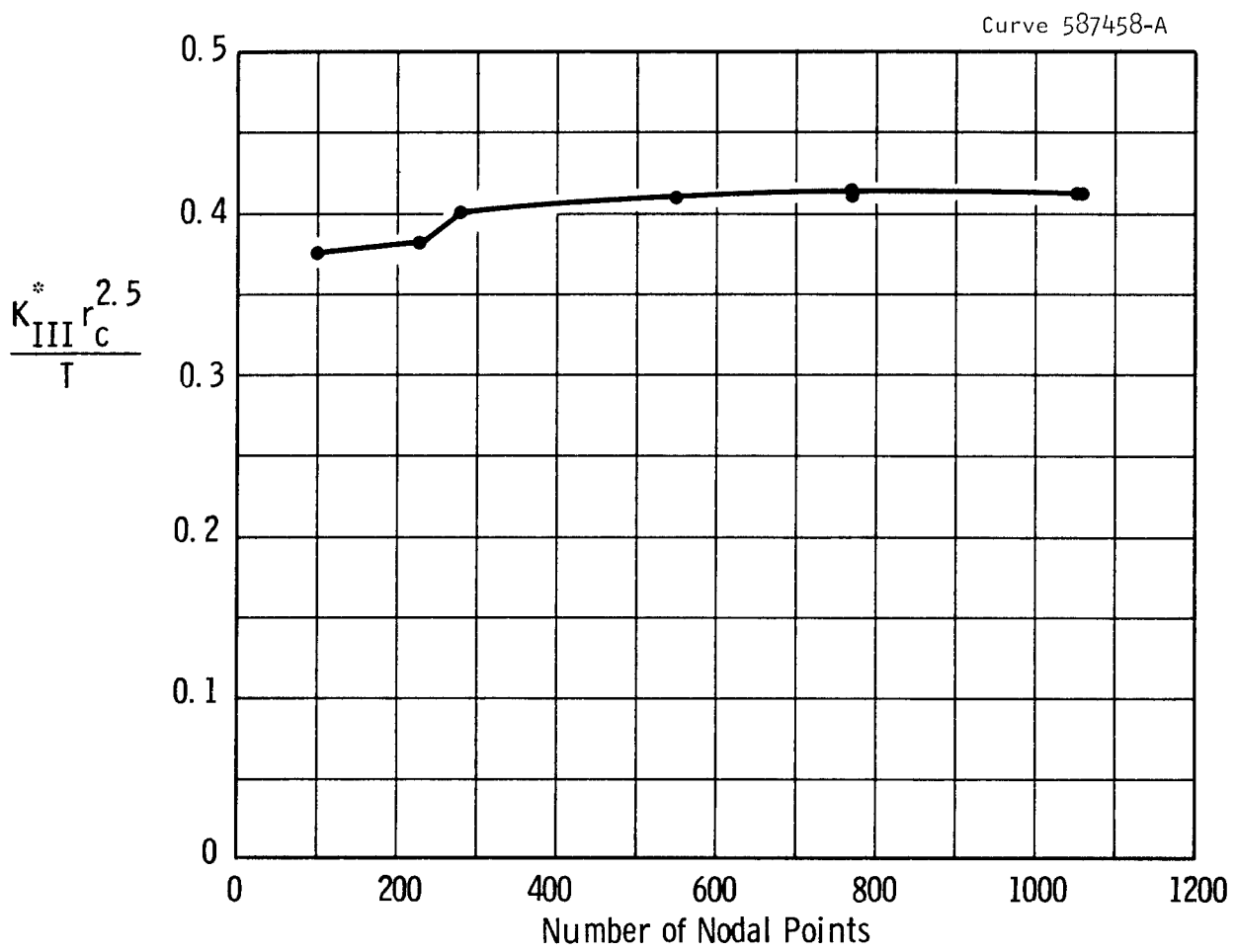
Sec. 6.5 Fig. 8 —Relative crack tip element coordinates and dimensions



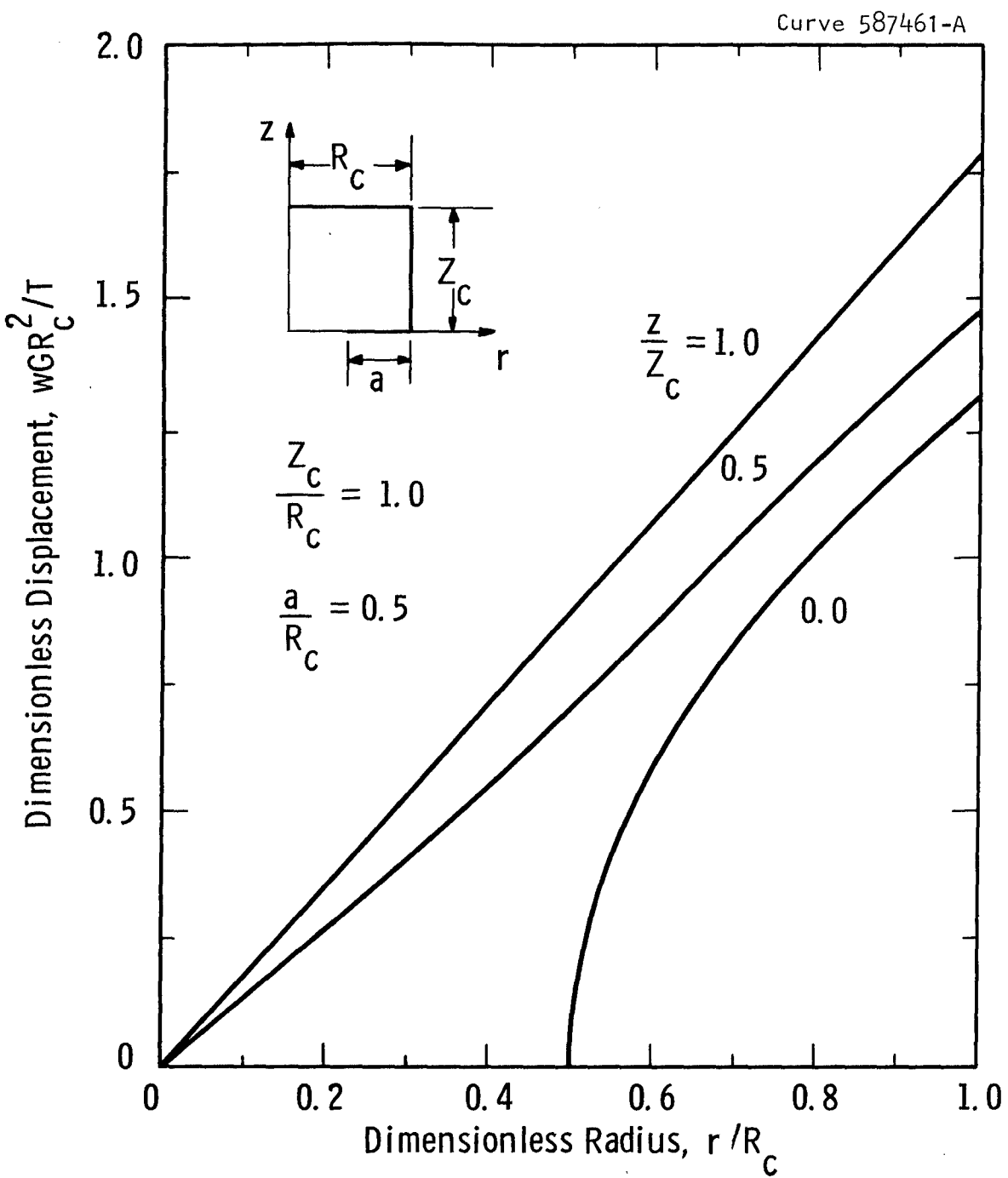
Sec. 6.5 Fig. 9—Finite element representation of circumferentially cracked round bar (Case 7)



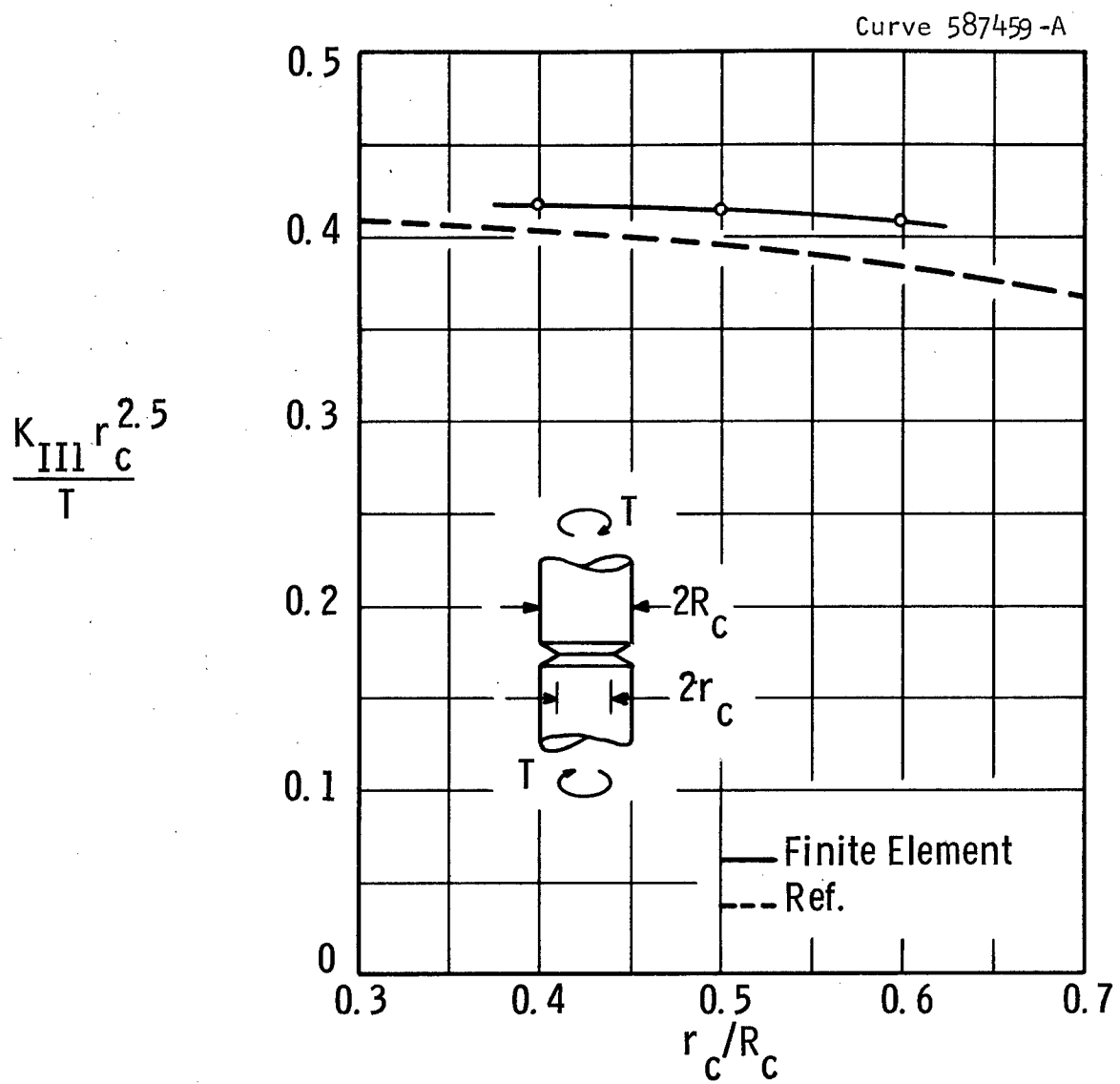
Sec. 6.5 Fig. 10—Crack tip element and surrounding triangular elements (Case 7)



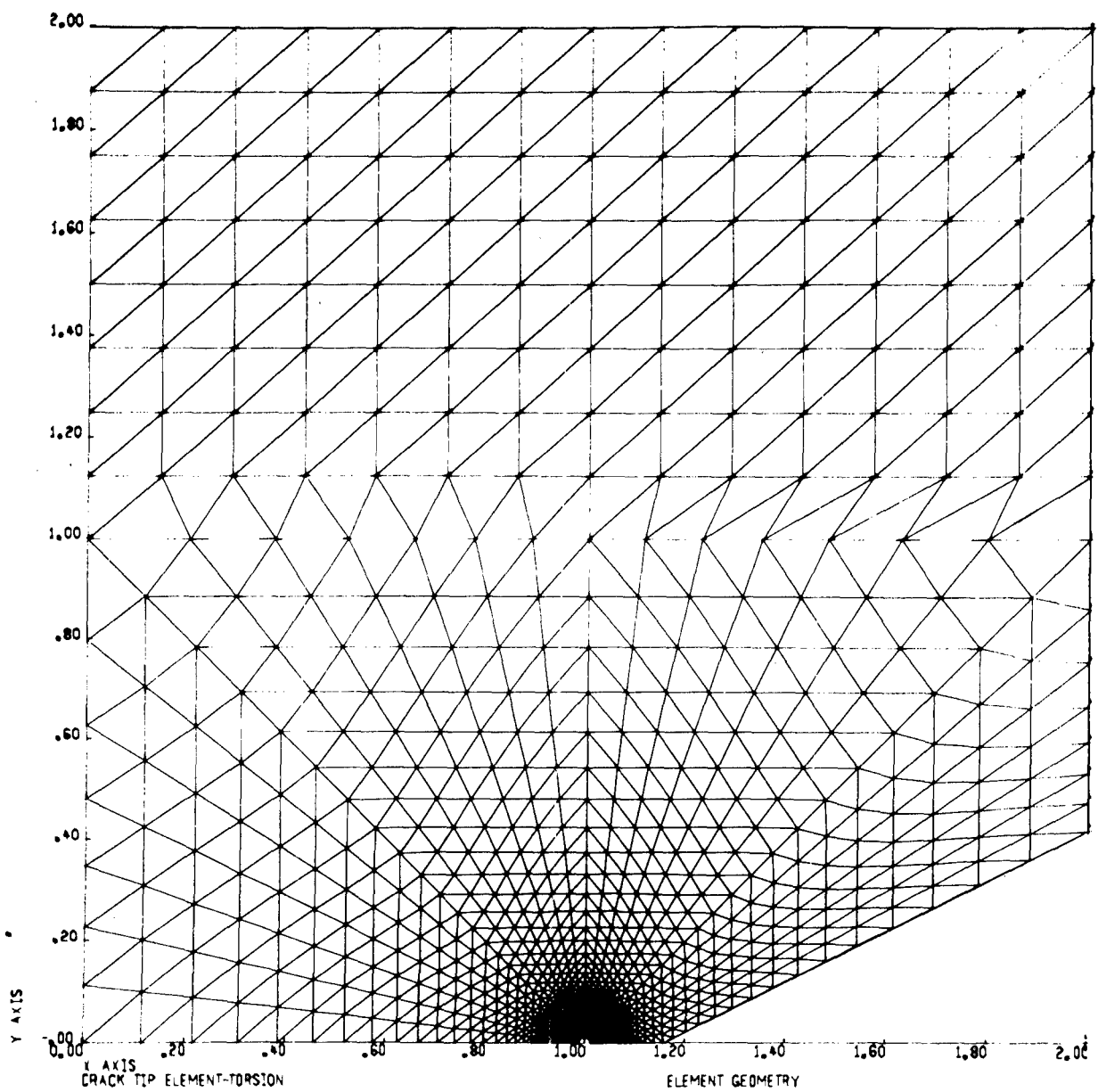
Sec. 6.5 Fig.11— K_{III}^* as a function of number of nodal points for $r_c/R_c = 0.5$



Sec. 6.5 Fig. 12—Deflections for circumferentially cracked round bar subject to torque (T) as determined by the finite element method



Sec. 6.5 Fig. 13- K_{III} for circumferentially cracked
round bar subject to torsion



Sec. 6.5 Fig. 14—Finite element representation of circumferentially cracked round bar with 60° V notch

Section 6.6

ANALYSIS OF EDGE SLANT CRACK SPECIMEN

6.6.1 INTRODUCTION

In considering the usefulness of a slant edge crack specimen in the study of K_I - K_{II} crack-tip stability, the expressions or curves for K_I and K_{II} as a function of geometry and loading conditions must be available. The boundary collocation of the Williams stress function⁽¹⁾ is used to provide this information. The geometry considered is shown in Figure 1 where the crack length "a" and the angle of crack orientation ϕ are varied. The two loading conditions, uniform tension and pure bending, are also shown in the figure.

Previously only the symmetric terms of the Williams stress function were used in the analysis of symmetrically loaded edge cracked plates.^(2,3) Now due to the non-symmetry of the geometry and loading conditions both the symmetric and anti-symmetric terms are used. The boundary collocation procedure is carried out in the least square sense.

6.6.2 WILLIAMS STRESS FUNCTION

In formulating a plane elasticity problem in terms of an Airy stress function $U(x,y)$ where

$$\begin{aligned}\sigma_{xx} &= \frac{\partial^2 U}{\partial y^2} \\ \sigma_{yy} &= \frac{\partial^2 U}{\partial x^2} \\ \tau_{xy} &= -\frac{\partial^2 U}{\partial x \partial y}\end{aligned}\tag{1}$$

the equilibrium equations (zero body forces)

$$\sigma_{ij,i} = 0 \quad (2)$$

where $x_1 = x$

$$x_2 = y$$

are automatically satisfied. The compatibility equation

$$\nabla^2 (\sigma_x + \sigma_y) = 0 \quad (3)$$

and the imposed boundary traction conditions

$$\sigma_{ij} v_j = T_i(s) \quad (4)$$

are satisfied if the stress function $U(x,y)$ satisfies the following boundary value problem

$$\nabla^4 U = 0 \quad (5)$$

$$U = f(s) \quad (6)$$

$$\frac{dU}{dn} = g(s) \quad (7)$$

where n and s are the normal and tangent coordinates on the outer boundary C_o (Fig. 2). The boundary conditions $g(s)$ and $f(s)$ are dependent on the imposed surface tractions T_i and can be evaluated from equations (1) and (4). The values of $f(s)$ and $g(s)$ are given in Appendix V for the two loading conditions being investigated (Fig. 1) in terms of the dimensions and coordinates of Fig. 3.

In obtaining solutions for single edge cracked plates of finite dimensions, the Williams stress function:^{(1)*}

*The function as initially presented in Ref. (1) was in error. The correct form was given by Williams in Ref. (4).

$$U(r, \theta) = \sum_{n=1,2,3} \left\{ b_{2n-1} r^{n+\frac{1}{2}} \left[-\cos(n - \frac{3}{2})\theta + \frac{2n-3}{2n+1} \cos(n + \frac{1}{2})\theta \right] \right. \\ \left. + b_{2n} r^{n+1} \left[-\cos(n-1)\theta + \cos(n+1)\theta \right] \right. \\ \left. + c_{2n-1} r^{n+\frac{1}{2}} \left[\sin(n - \frac{3}{2})\theta - \sin(n + \frac{1}{2})\theta \right] \right. \\ \left. + c_{2n} r^{n+1} \left[-\sin(n-1)\theta + \frac{n-1}{n+1} \sin(n+1)\theta \right] \right\} \quad (8)$$

is a very suitable function to work with. It satisfies the biharmonic equation (5). It also gives a stress free surface at $\theta = \pm \pi$ as can be shown by use of the relations

$$\sigma_y = \frac{\partial^2 U}{\partial x^2} = \frac{\partial^2 U}{\partial r^2} \cos^2 \theta - 2 \frac{\partial^2 U}{\partial \theta \partial r} \frac{\sin \theta \cos \theta}{r} + \frac{\partial U}{\partial r} \frac{\sin^2 \theta}{r} \\ + 2 \frac{\partial U}{\partial \theta} \frac{\sin \theta \cos \theta}{r^2} + \frac{\partial^2 U}{\partial \theta^2} \frac{\sin^2 \theta}{r^2}$$

$$\sigma_x = \frac{\partial^2 U}{\partial y^2} = \frac{\partial^2 U}{\partial r^2} \sin^2 \theta + 2 \frac{\partial^2 U}{\partial \theta \partial r} \frac{\sin \theta \cos \theta}{r} + \frac{\partial U}{\partial r} \frac{\cos^2 \theta}{r} \\ - 2 \frac{\partial U}{\partial \theta} \frac{\sin \theta \cos \theta}{r^2} + \frac{\partial^2 U}{\partial \theta^2} \frac{\cos^2 \theta}{r^2} \quad (9)$$

$$-\tau_{xy} = \frac{\partial U}{\partial x \partial y} = \frac{\partial^2 U}{\partial r^2} \sin \theta \cos \theta + \frac{\partial^2 U}{\partial r \partial \theta} \frac{\cos 2\theta}{r} - \frac{\partial^2 U}{\partial r \partial \theta} \frac{\sin \theta \cos \theta}{r^2} \\ - \frac{\partial U}{\partial r} \frac{\sin \theta \cos \theta}{r} - \frac{\partial U}{\partial r} \frac{\cos 2\theta}{r^2}$$

This means that the surface described by the negative x - axis of Figure 3, has zero shear and normal stress and can represent a stress free crack. The stress function also contains an unlimited number of

arbitrary constant coefficients (b_n and c_n)* which can be used to satisfy conditions (6) and (7) on the remaining outer surface (A-B-C-D-E-F) of the plate in some approximate manner, resulting in an approximate solution.

The stress intensity factors can be related to the first two coefficients of the Williams stress function. The expression for the stress in the y direction in the immediate vicinity of the crack tip is obtained from the dominate terms as

$$\sigma_y = \frac{-b_1}{\sqrt{r}} \cos \frac{\theta}{2} (1 + \sin \frac{\theta}{2} \sin \frac{3\theta}{2}) + \frac{c_1}{\sqrt{r}} \sin \frac{\theta}{2} \cos \frac{\theta}{2} \cos \frac{3\theta}{2}$$

Therefore it follows that

$$K_I = -b_1 \sqrt{2\pi} \\ K_{II} = c_1 \sqrt{2\pi} \quad (10)$$

The method used here to satisfy the remaining boundary conditions in an approximate manner is the boundary collocation method. The collocation procedure consists of using a truncated form of the Williams function to satisfy the boundary conditions (6) and (7) at a selected finite set of boundary points in the least square sense⁽⁵⁾ (Appendix VI). As the number of coefficients used in the truncated series increases, the first two coefficients b_1 and c_1 of the series will usually converge. From the converged values of b_1 and c_1 for each specific geometry and loading condition K_I and K_{II} can be calculated by use of equations (10).

6.6.3 PROCEDURE

The general procedure is to select a finite number (N) of boundary stations (collocation points) at which the corresponding (2N)

* The term corresponding to coefficient c_2 is trivial.

boundary conditions (6) and (7) will be satisfied in the least square sense. Also chosen is the number of terms (M) of the Williams stress function to be used in the least square fit ($M \leq 2N$). The corresponding $2N$ equations in terms of the M unknown series coefficients are generated and the equations solved in the least square sense. The method used to solve the final set of M equations is described in Appendix III. Once the M unknowns have been determined the approximate stress intensity factors K_I^* and K_{II}^* can then be calculated from equations (10).

All of these operations were carried out on a CDC-6600 digital computer which has an accuracy of 14 significant figures. Boundary stations were evenly distributed over each side of the plate (Fig. 3). The generation of the N linear equations corresponding to the boundary condition on U (Equation 6) is straight forward. In generating the N equations which correspond to the boundary condition on dU/dn (Equation 6) the relation

$$\frac{dU}{dn} = \left[\frac{\partial U}{\partial r} \frac{\partial r}{\partial x} + \frac{\partial U}{\partial \theta} \frac{\partial \theta}{\partial x} \right] \frac{dx}{dn} + \left[\frac{\partial U}{\partial r} \frac{\partial r}{\partial y} + \frac{\partial U}{\partial \theta} \frac{\partial \theta}{\partial y} \right] \frac{dy}{dn}$$

is used since the Williams function is expressed in terms of the r, θ coordinate system.

6.6.4 STUDY OF CONVERGENCE

As the number of boundary stations (N) increases and the number of series terms (M) used to satisfy in the least square sense the corresponding $2N$ boundary conditions also increases, a form of convergence of K_I^* and K_{II}^* is obtained. The general convergence patterns can be shown by studying a couple of examples in some detail.

For the case $\phi = 0.0$, $a/W = 0.5$, and $L/W = 2.0$, the K_I^* values as a function of M (number of coefficients) are shown in Figure 4 for $N = 23$ boundary stations. Both the uniform tension and the pure bending cases are shown. As M approaches $2N = 56$, at which point the boundary

conditions at all N stations are satisfied exactly, the K_I^* values begin to level off. The limiting value at $M = 56$ agrees very well with the values given for the corresponding cases reported in Reference 6. In Figure 5, K^* values are shown as a function of M for the same geometry, but for $N = 47$ boundary stations. This data is also listed in Table I. As shown the K^* for each loading case changes very little from $M = 40$ to $M = 94$ at which point the boundary conditions are satisfied exactly at each boundary station. The converged values agree with the $M = 2N$ values in Figure 4 and the values of Reference 6.

For the values of ϕ other than zero the variation of K_I^* and K_{II}^* as a function of M for any specified N becomes more complex and the selection of a converged value less obvious. This is shown by a study of the case $\phi = 45^\circ$, $a/W = 0.707$, and $L/W = 2.5$. The variation of the K^* 's as a function of M for $N = 27$ and $N = 55$ are shown in Figures 6 and 7 respectively, and the data for $N = 55$ is listed in Table II. For $N = 27$ the K^* 's appear to be converging between $M = 38$ and $M = 42$, but as M approaches $2N = 54$ the values begin to diverge. At $M = 55$ the values diverge so much that they can't be shown on the scale used. For the case of $N = 55$ a somewhat similar trend is noted. But now the values do converge over a range from $M = 40$ to $M = 105$. The converged values of K_I^* and K_{II}^* over this range are approximately the same values that the K^* 's were nearly converging too for $N = 27$. Again when $M = 2N = 110$ the values diverge and cannot be shown on the scale used here.

The reason for this divergence at and near $M = 2N$ is not apparent at this time. This problem will be subjected to further study. For the present a converged value of K^* over a wide range of M is accepted as the approximate stress intensity factor for the geometry and loading condition being investigated.

6.6.5 CONCLUSION

The stress intensities for a moderate range of ϕ 's and a/W 's are shown in Figures 8 and 9 for the uniform tension case and the pure bending cases respectively. A study of the curves indicates that a

wide range of the ratio K_I/K_{II} cannot be obtained with this type of geometry and these loading conditions. Therefore an edge slant crack geometry is not a candidate for a K_I-K_{II} test specimen. The collocation procedure presented here can be applied to edge cracked plates of arbitrary geometry and in plane loading conditions.

Section 6.6 References

1. M. L. Williams, "On the Stress Distribution at the Base of a Stationary Crack," *Journal of Applied Mechanics*, Vol. 24, No. 1, March 1957.
2. B. Gross, J. E. Srawley, and W. F. Brown, Jr., "Stress Intensity Factors for a Single Edge Notch Tension Specimen by Boundary Collocation," *NASA TN D-2395*, August 1964, Lewis Research Center.
3. W. K. Wilson, "Analytic Determination of Stress Intensity Factors for the Manjoine Brittle Fracture Test Specimen," *Westinghouse Research Report for AEC, WERL 0029-3*, August 1965.
4. M. L. Williams, "The Bending Stress Distribution at the Base of a Stationary Crack," *Journal of Applied Mechanics*, March 1961.
5. L. E. Hulbert, "The Numerical Solution of Two-Dimensional Problems of the Theory of Elasticity," *Bulletin 198*, Engineering Experiment Station, Ohio State University.
6. W. F. Brown, Jr., and J. E. Srawlwy, "Plane Strain Crack Toughness Testing of High Strength Metallic Materials," *ASTM Special Technical Publication No. 410*.

Section 6.6 Table I

*
INFLUENCE OF M ON K
FOR 47 BOUNDARY STATIONS ‡

($\phi = 0^\circ$, $a/W = 0.5$, $L/W = 2.0$)

M	TENSION	BENDING
	$\frac{K_I^* a^{1/2}}{\sigma W}$	$\frac{K_I^* a^{3/2}}{M_o}$
20	2.3151	3.5916
40	2.4976	3.9701
60	2.5043	3.9826
80	2.5043	3.9822
90	2.5040	3.9821
94	2.5041	3.9821

‡ 94 boundary conditions

Section 6.6 Table II

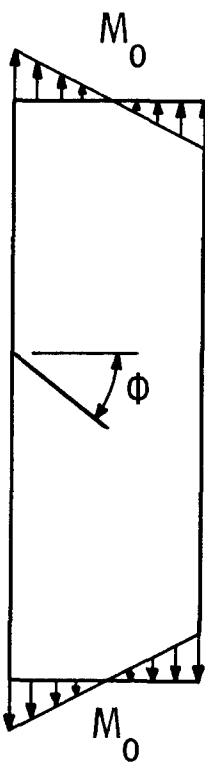
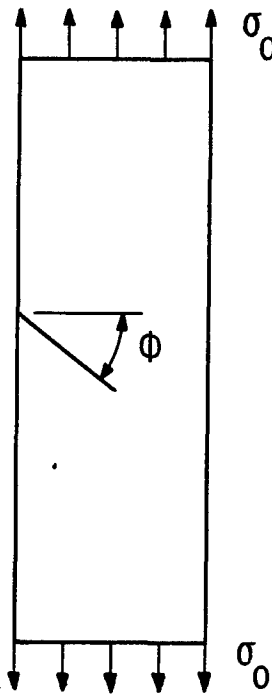
INFLUENCE OF M ON K^*
FOR 55 BOUNDARY STATIONS \dagger

($\phi = 45^\circ$, $a/W = 0.707$, $L/W = 2.5$)

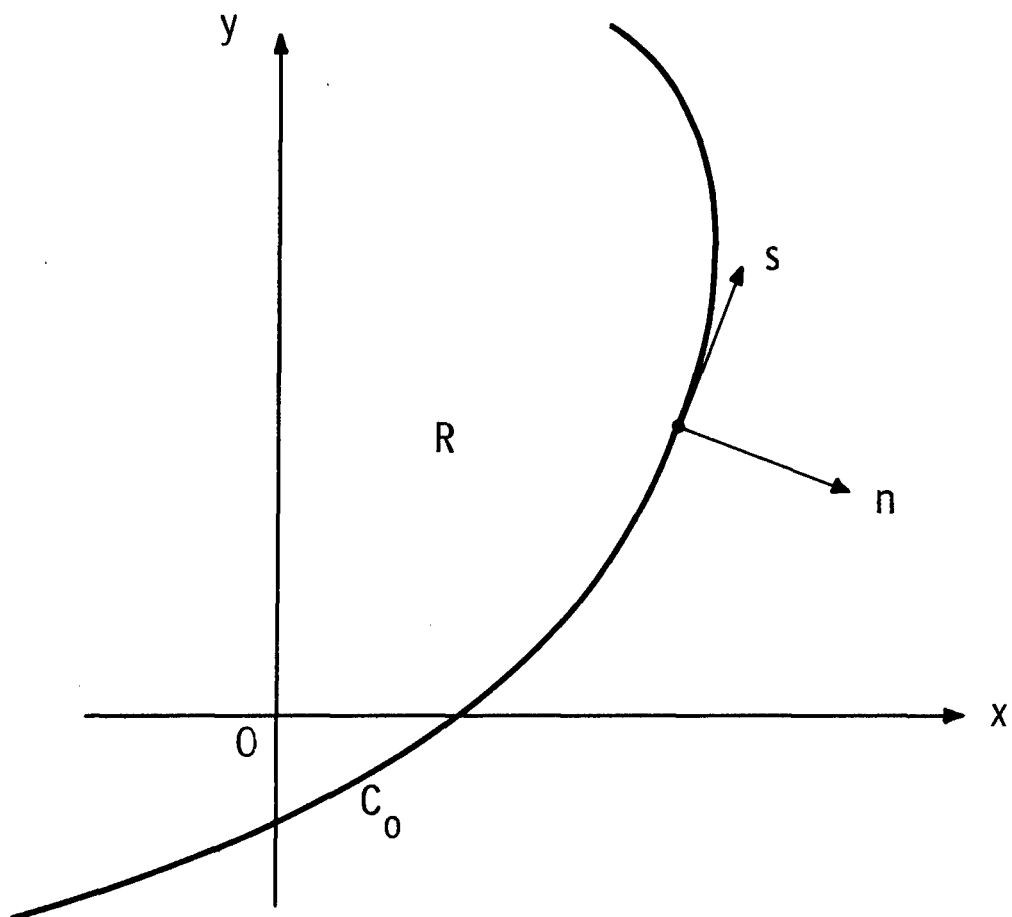
M	$\frac{K_I^* a^{1/2}}{\sigma W}$	$\frac{-K_{II}^* a^{1/2}}{\sigma W}$
20	2.0869	0.9146
40	2.3245	1.0340
60	2.3211	1.0445
74	2.3196	1.0434
80	2.3193	1.0443
100	2.3196	1.0436
105	2.3200	1.0427
110	-26.25	-48.51

\dagger 110 boundary conditions

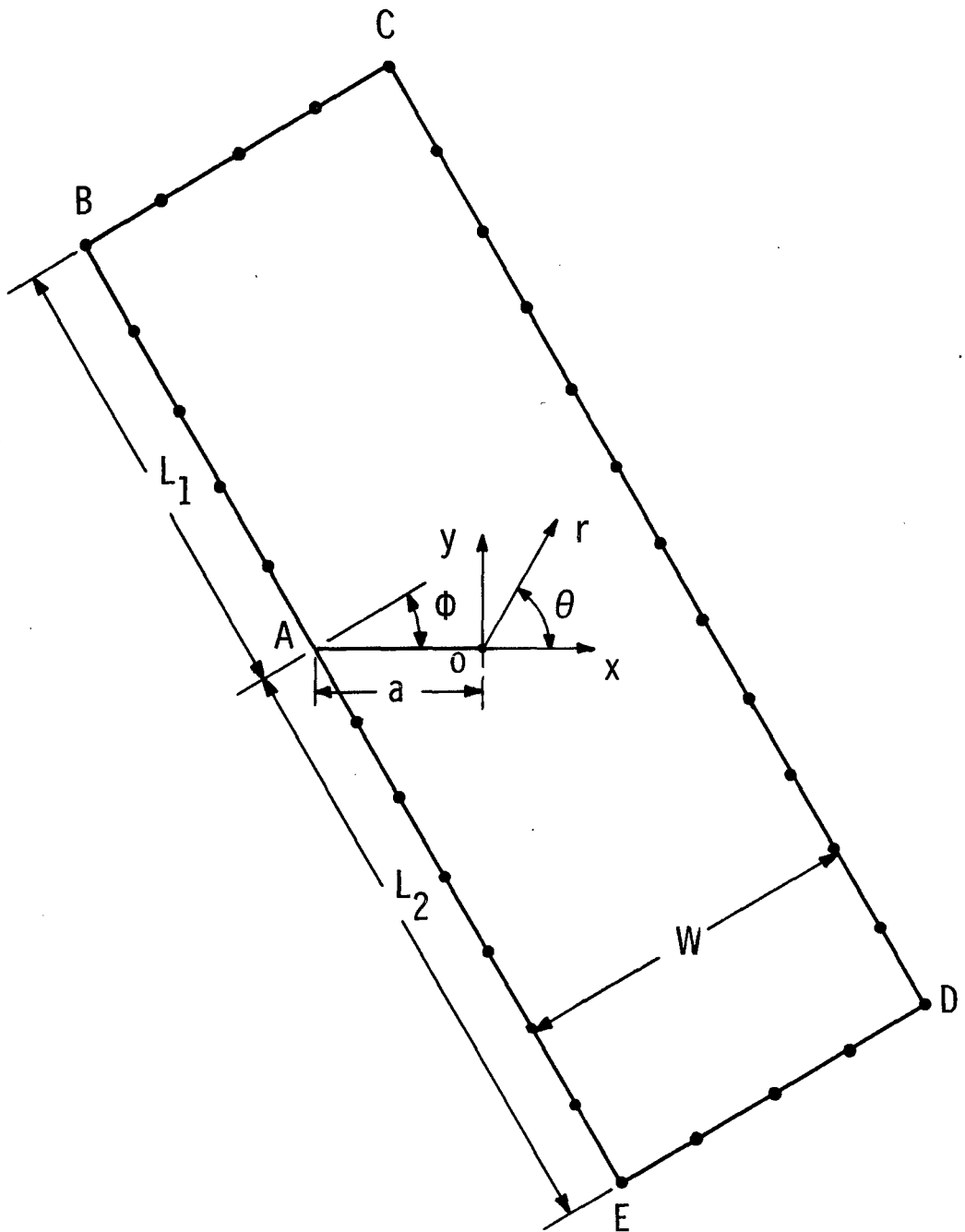
Dwg. 857A619



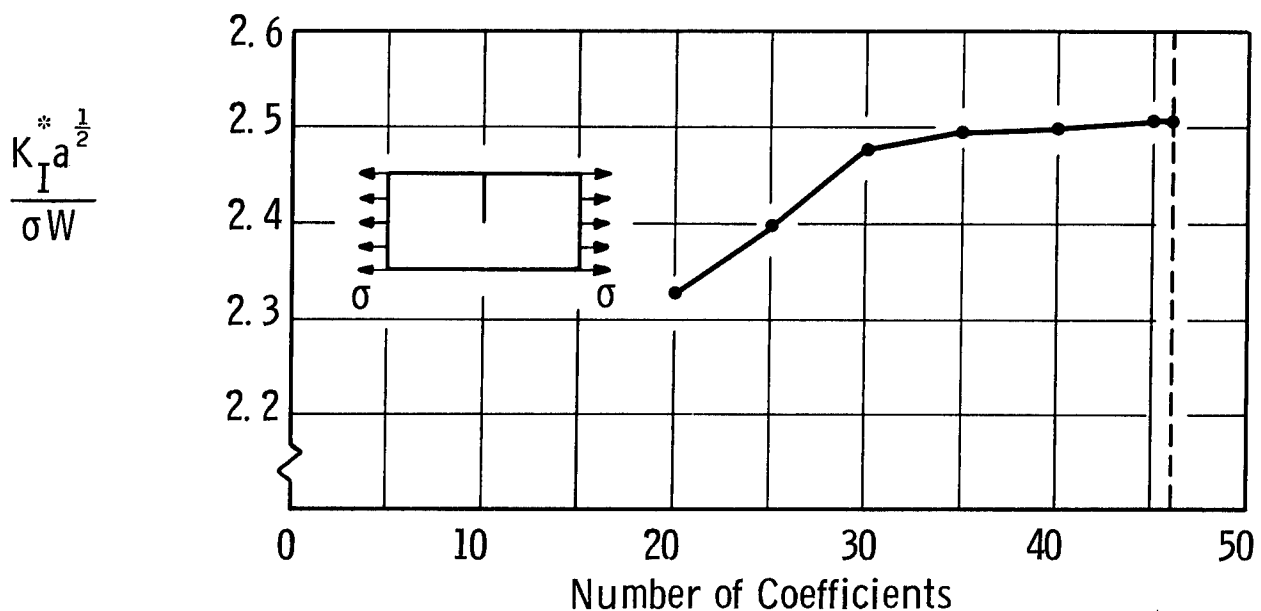
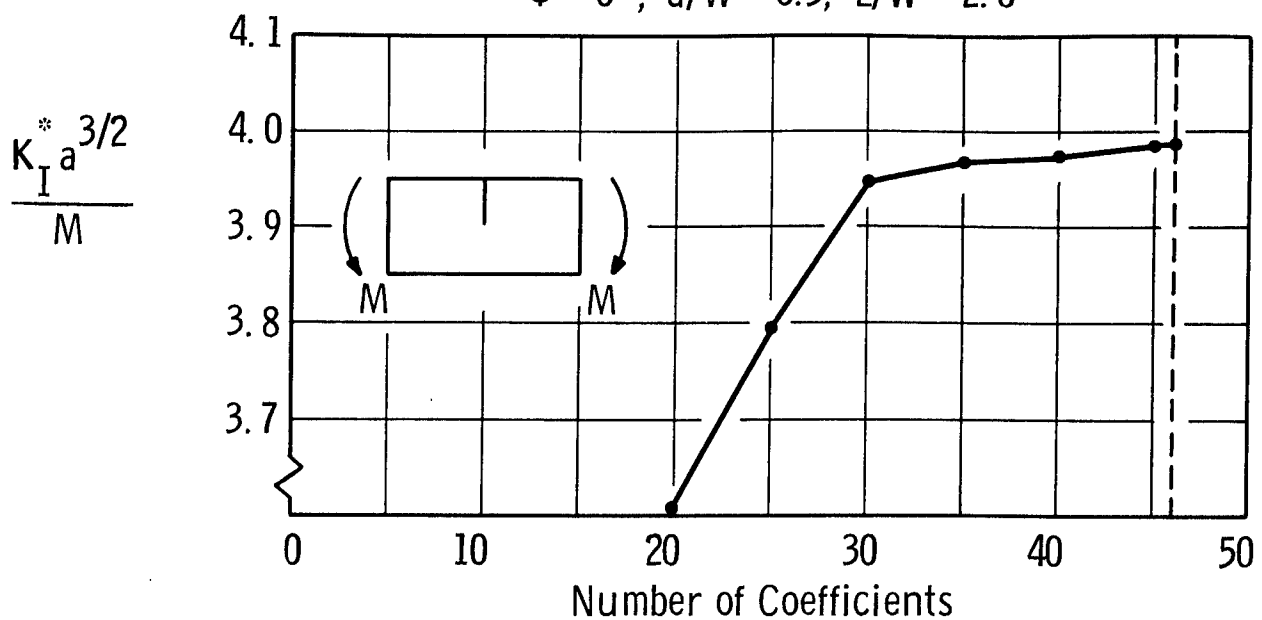
Sec. 6.6 Fig. 1—Loading conditions for
edge slant crack specimen



Sec. 6.6 Fig. 2-General coordinates for plane elasticity



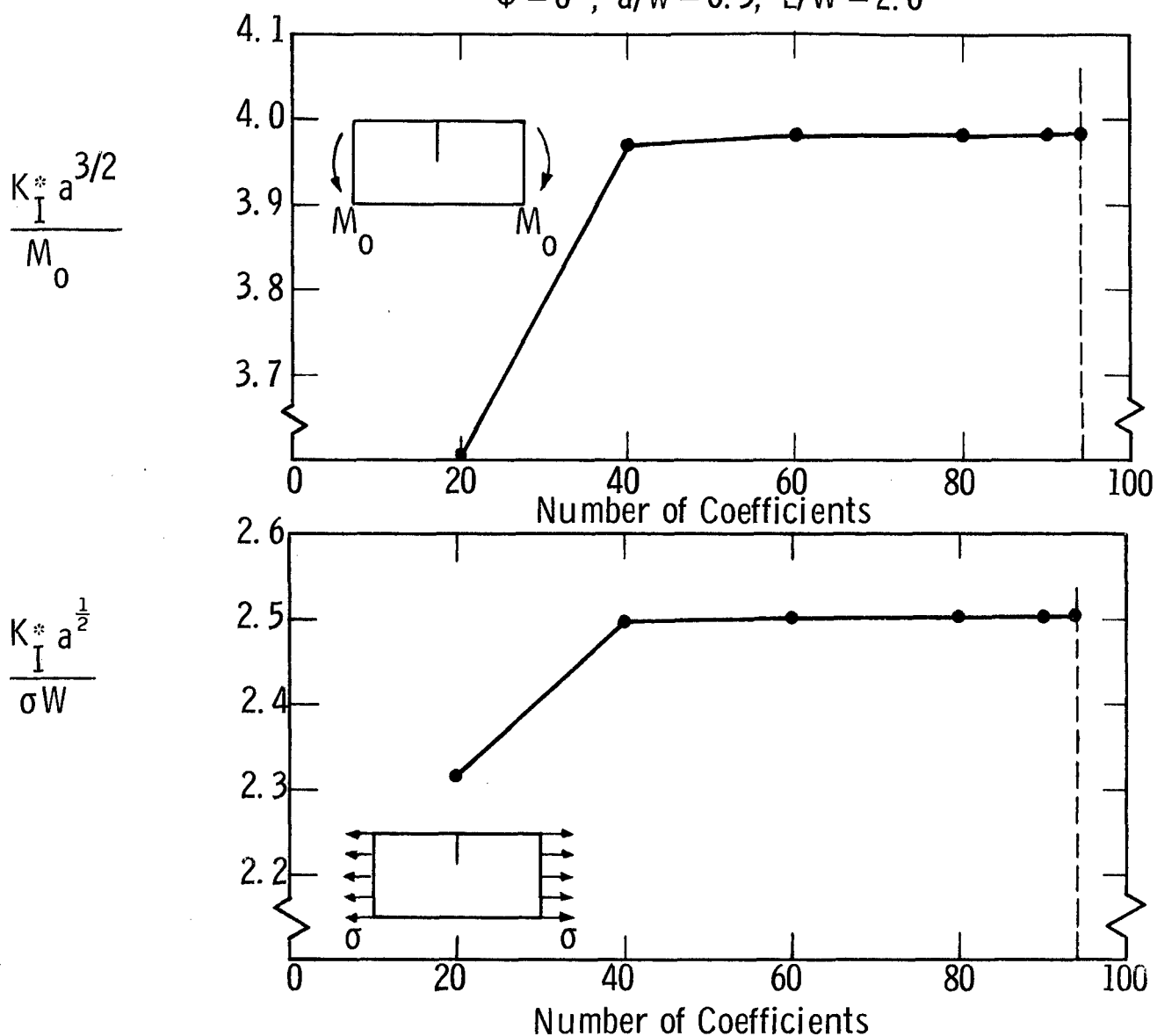
Sec. 6.6 Fig. 3—Geometry and coordinates for collocation
solution of edge slant crack specimen

$\Phi = 0^\circ, a/W = 0.5, L/W = 2.0$


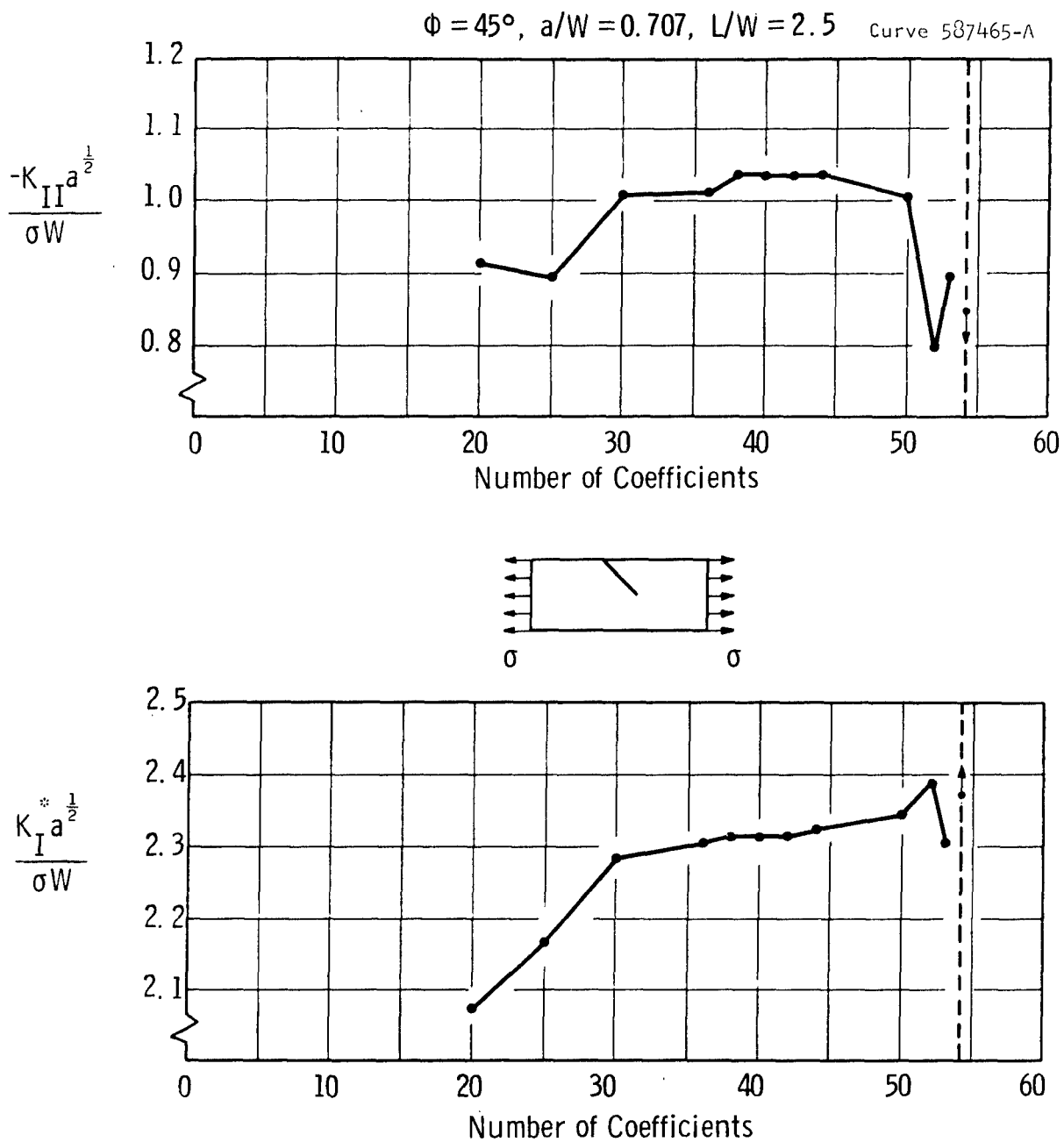
Sec. 6.6 Fig. 4- K_I^* as a function of number of coefficients used
to satisfy boundary conditions in the least square
sense at 23 boundary points (46 equations)

Curve 587527-A

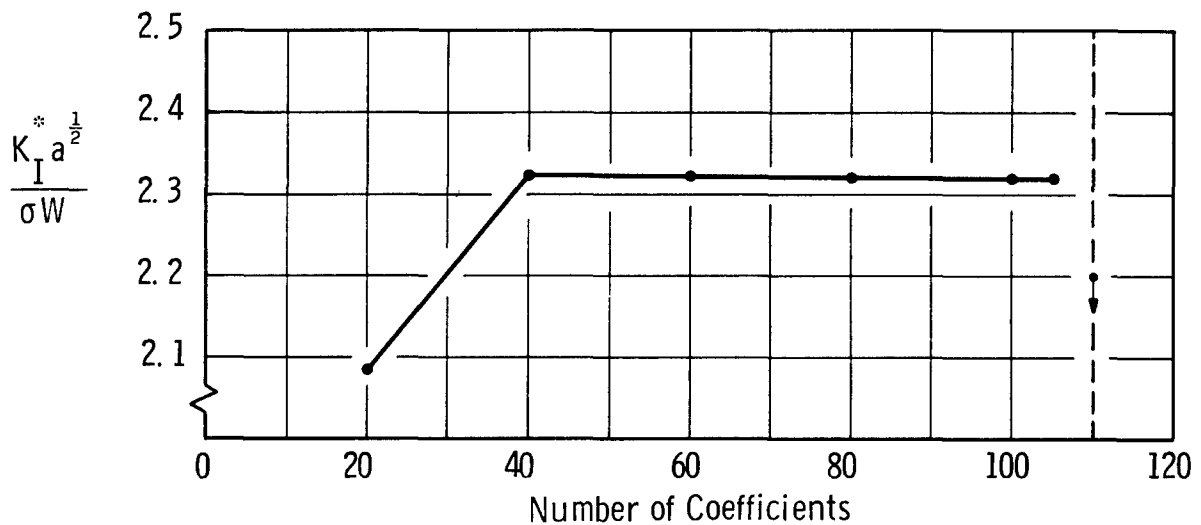
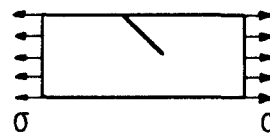
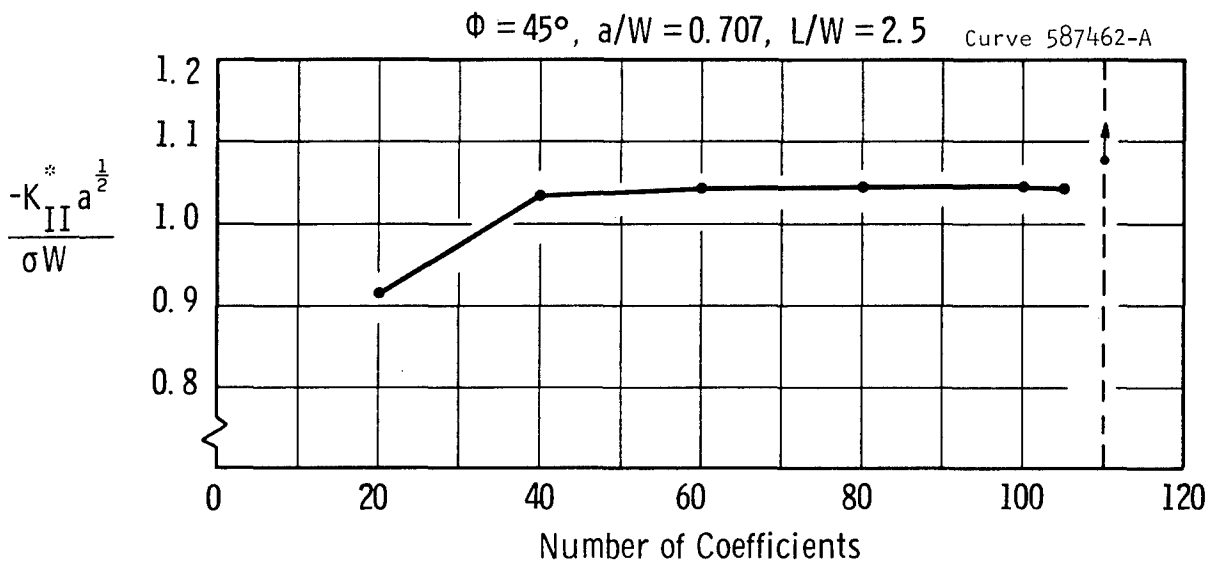
$\Phi = 0^\circ, a/w = 0.5, L/W = 2.0$



Sec. 6.6 Fig. 5— K_I^* as a function of number of coefficients used to satisfy boundary conditions in the least square sense at 47 boundary points (94 equations)

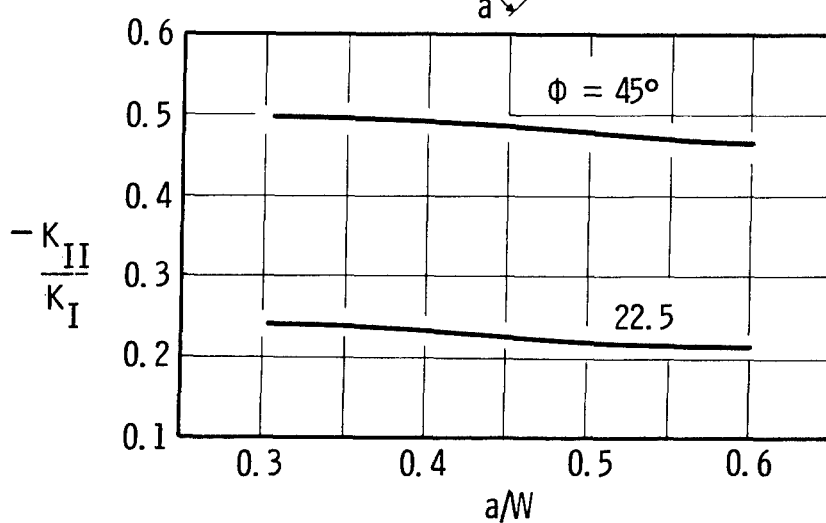
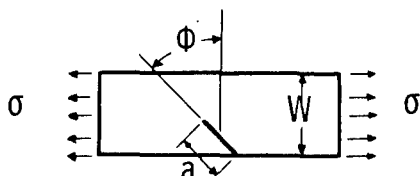
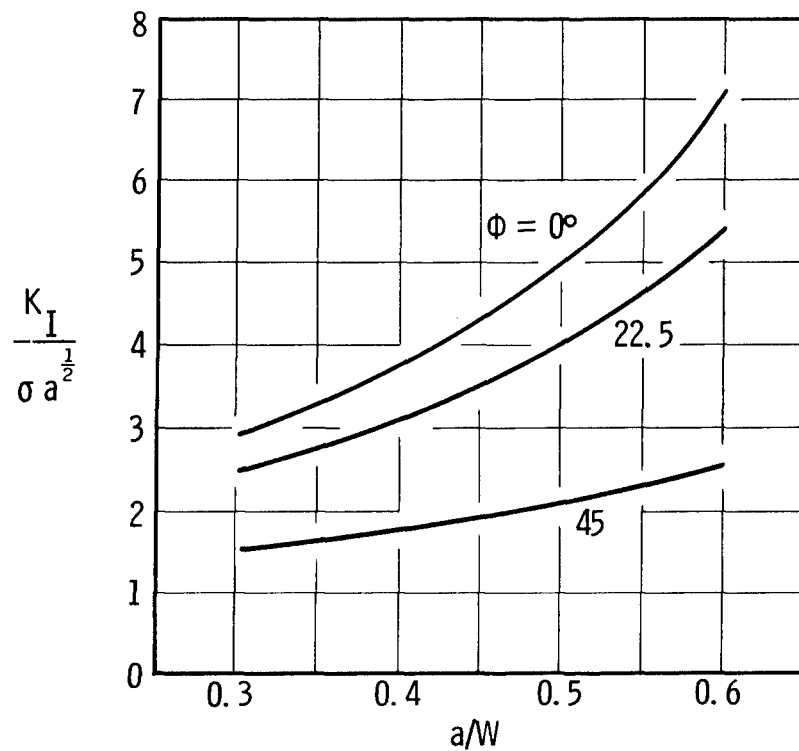


Sec. 6.6 Fig. 6- K_I^* and K_{II}^* as a function of number of coefficients used
to satisfy boundary conditions in the least square sense at 27
boundary points (54 equations)



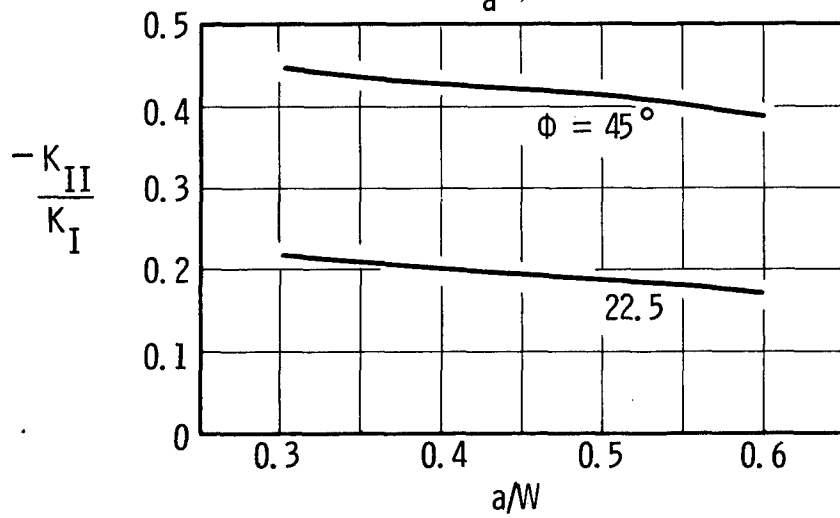
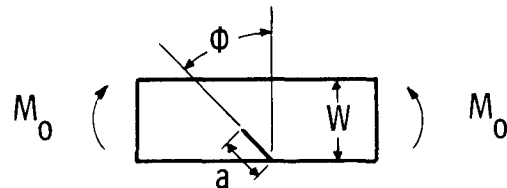
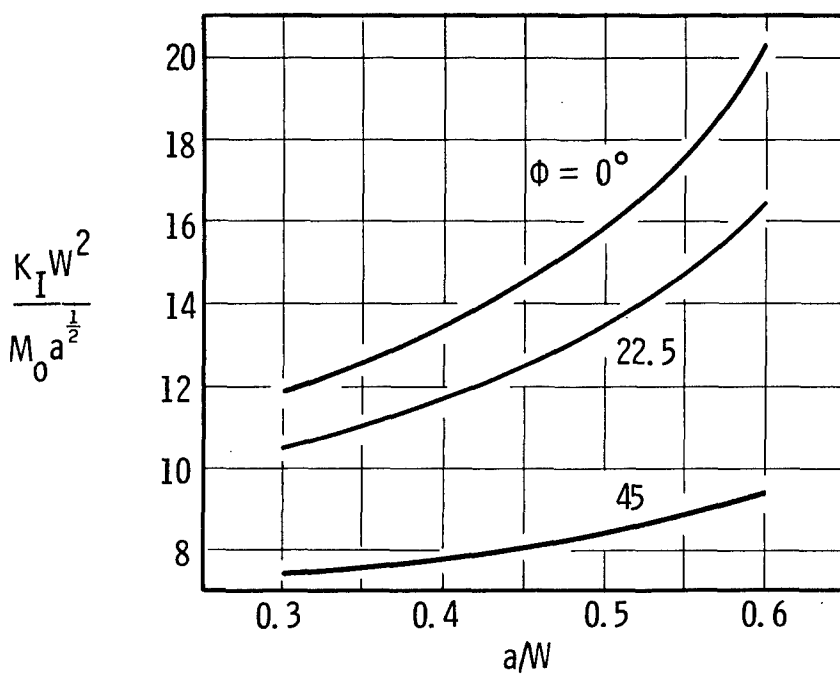
Sec. 6.6 Fig. 7 $-K_I^*$ and K_{III}^* as a function of number of coefficients used
to satisfy boundary conditions in the least square sense at
55 boundary points (110 equations)

Curve 587916-A



Sec. 6.6 Fig. 8—Stress intensity factors for edge slant cracked plate subject to uniform tension

Curve 587917-A



Sec. 6.6 Fig. 9—Stress intensity factors for edge slant cracked plate subject to pure bending

Section 6 - Appendix I

INTEGRATION OF COMPLEX FUNCTIONS

In performing the necessary integrations (Section 6.4) of the complex stress functions $\phi(z)$ and $\Omega(z)$ the following relations are useful.

A.

$$\int \frac{z^n}{(z^2-1)^{1/2}} dz = (z^2-1)^{1/2} \left\{ \begin{array}{l} \frac{1}{n} z^{n-1} + \frac{(n-1)}{n(n-2)} z^{n-3} + \dots \\ \dots + \frac{(n-1)(n-3)\dots-4}{n(n-2)\dots-3} z^2 + \frac{(n-1)(n-3)\dots-2}{n(n-2)\dots-1} \end{array} \right\} \text{ for } n \text{ odd}$$

$$\dots + \frac{(n-1)(n-3)\dots-3}{n(n-2)\dots-2} z \} + \frac{(n-1)(n-3)\dots-3}{n(n-2)\dots-2} \ln [z + (z^2-1)^{1/2}] \text{ for } n \text{ even}$$

$$= \log [z + (z^2 - 1)^{1/2}] \quad \text{for } n = 0$$

B.

$$\int z^n (z^2-1)^{1/2} dz = \frac{1}{n+1} z^{n+1} (z^2-1)^{1/2} - \int \frac{z^{n+2}}{(z^2-1)^{1/2}} dz$$

C.

$$\int \ln [z + (z^2-1)^{1/2}] dz = z \ln [z + (z^2-1)^{1/2}] - (z^2-1)^{1/2}$$

Section 6 - Appendix II

BOUNDARY CONDITIONS OF AIRY STRESS FUNCTION FOR CENTER CRACKED PLATE

The boundary functions $U = f(s)$ and $dU/dn = g(s)$ over the surface A-D of Figure 3, Section 6.4, for the loading shown in Figure 2 of the same section are listed below.

$$f(s) = \frac{1}{8} \sigma_0 (W^2) \quad \text{on A-B}$$

$$= \frac{\sigma_0}{2} [(x + H \sin \phi) \cos \phi + (y - H \cos \phi) \sin \phi]^2 \quad \text{on B-C}$$

$$= \frac{1}{8} \sigma_0 (W^2) \quad \text{on C-D}$$

$$g(s) = \frac{1}{2} \sigma_0 W \quad \text{on A-B}$$

$$= 0 \quad \text{on B-C}$$

$$= \frac{1}{2} \sigma_0 W \quad \text{on C-D}$$

Section 6 - Appendix III
METHOD OF SOLUTION OF SIMULTANEOUS LINEAR ALGEBRAIC EQUATIONS

The method used to solve large systems of linear simultaneous algebraic equations is that developed by Wilkinson⁽¹⁾ for ill-conditioned systems. Accurate solutions of simultaneous equations can be obtained by this method when the matrix of coefficients is not sparse or otherwise specialized. The method involves an iteration technique applied to a standard elimination method of solution. First the system of equations (in matrix form)

$$A \mathbf{x} = \mathbf{b} \quad (1)$$

is solved by the Crout elimination method with partial pivoting incorporated. Once the initial solution vector $\mathbf{x}^{(0)}$ is obtained by the Crout method it is substituted back into Equation (1) and the initial residual vector $\mathbf{r}^{(0)}$ is calculated.

$$\mathbf{r}^{(0)} = A \mathbf{x}^{(0)} - \mathbf{b} \quad (2)$$

The residual vector is now used as a new right hand side, and the error vector $\mathbf{e}^{(0)}$ corresponding to $\mathbf{x}^{(0)}$ is calculated by solving the matrix equation

$$A \mathbf{e}^{(0)} = \mathbf{r}^{(0)} \quad (3)$$

The improved solution vector now becomes

$$\mathbf{x}^{(1)} = \mathbf{x}^{(0)} + \mathbf{e}^{(0)} \quad (4)$$

Next the residual corresponding to the improved solution $x^{(1)}$ is calculated and so the iteration process continues as indicated below:

$$\begin{aligned} r^{(k)} &= A x^{(k)} - b \\ A e^{(k)} &= r^{(k)} \\ x^{(k+1)} &= x^{(k)} + e^{(k)} \end{aligned} \quad (5)$$

The iterations continue until a working accuracy is obtained.

As stated, systems of equations of the form $A e^{(k)} = r^{(k)}$ (initially $A x^{(0)} = b$) are solved by the Crout elimination method with partial pivoting. Crouts method triangularizes the matrix A by resolving it into the product of a lower triangular matrix L and a unit upper triangular matrix U.

$$A = LU \quad (6)$$

The method proceeds by the following three steps.

$$\begin{aligned} (1) \quad A &= LU, \quad \text{i.e.} \quad LU e^{(k)} = r^{(k)} \\ (2) \quad Ly^{(k)} &= r^{(k)} \\ (3) \quad Ux^{(k)} &= y^{(k)} \end{aligned} \quad (7)$$

That is, first the matrix A is decomposed into L and U

$$\begin{aligned} l_{ij} &= a_{ij} - \sum_{k=1}^{j-1} l_{ik} u_{kj} \quad i \geq j \\ u_{ij} &= a_{ij} - \sum_{k=1}^{i-1} l_{ik} u_{kj} \quad i < j \end{aligned} \quad (8)$$

with partial pivoting incorporated. Secondly the elements of the vector y are calculated from the matrix equation $Ly^{(k)} = r^{(k)}$

$$y_i^{(k)} = \frac{1}{l_{ii}} \left[b_i - \sum_{j=1}^{i-1} l_{ij} y_j^{(k)} \right] \quad (9)$$

Finally, the elements of the solution vector are calculated from the matrix equation $Ux = y$

$$x_i^{(k)} = y_i^{(k)} - \sum_{j=i+1}^n u_{ij} x_j^{(k)} \quad (10)$$

where n is the number of equations.

The computer program which carried out the necessary operations was written in Fortran IV and was run on a CDC-6600. All arithmetic operations were carried out in single precision (14 digits) except the calculation of the residuals $r^{(k)}$ which were carried out in double precision.

Reference:

- (1) J. H. Wilkinson, "The Solution of Ill-Conditioned Linear Equations," Mathematical Methods for Digital Computers, Volume 2, John Wiley, 1967.

Section 6 - Appendix IV

STRAIN ENERGY OF MODE III CRACK TIP ELEMENT

A cross section of the circumferentially cracked round bar along with the crack tip element circular boundary C' is shown in Figure 8 of Section 6.5. In the figure, two coordinate systems are shown: (1) the unprimed coordinates are fixed at the center of the bar and the prime coordinates are fixed at the crack tip. The define displacement pattern for the tip element is

$$w = \frac{K_{III}}{G} \left[\frac{2R'}{\pi} \right]^{1/2} \sin \frac{\theta'}{2}$$

For values of R' approaching zero the stresses corresponding to this displacement field are

$$\tau_{\theta',r'} = - \frac{K_{III}}{(2\pi R')^{1/2}} \sin \frac{\theta'}{2}$$

$$\tau_{\theta',z'} = \frac{K_{III}}{(2\pi R')^{1/2}} \cos \frac{\theta'}{2}$$

The strain energy density is

$$W = \frac{1}{2G} (\tau_{\theta',r'}^2 + \tau_{\theta',z'}^2)$$

and the strain energy of the ring element is

$$U_{III} = \int_V w \, dV$$

where V is the volume of the element. An incremental volume dV of the element can be expressed as

$$dV = 2\pi(r) [dA]$$

or

$$dV = 2\pi(r_c - R' \cos \theta') [R' dR' d\theta']$$

where r_c is the radial distance from the bar center to the crack tip.
Therefore the strain energy of the tip element is

$$U_{III} = \frac{\pi}{G} \int_0^{2\pi} \int_0^{R_o'} \frac{K_{III}^2}{(2\pi R')} \left[\left(\sin \frac{\theta'}{2} \right)^2 + \left(\cos \frac{\theta'}{2} \right)^2 \right] (r_c - R' \cos \theta') R' dR' d\theta'$$

or

$$\begin{aligned} U_{III} &= \frac{K_{III}^2}{2G} \int_0^{2\pi} \int_0^{R_o'} (r_c - R' \cos \theta') dR' d\theta' \\ &= \frac{\pi}{G} (r_c R_o') K_{III}^2 \end{aligned}$$

where R_o' is the radius of crack tip element cross section.

Section 6 - Appendix V

BOUNDARY CONDITIONS OF AIRY STRESS FUNCTION FOR EDGE CRACKED PLATE

For a boundary value problem of the first type expressed in the form of the Airy stress function $U(x,y)$, the boundary conditions $U = f(s)$ and $\frac{dU}{dn} = g(s)$ on C_0 (Figure 2, Section 6.6) can be determined from the boundary surface tractions \bar{X} and \bar{Y} within an arbitrary linear function $Ax + By + C$ from the following relations

$$\begin{aligned} -\frac{\partial U}{\partial x} &= \int \bar{Y} ds \\ \frac{\partial U}{\partial y} &= \int \bar{X} ds \end{aligned} \tag{1}$$

and

$$\frac{\partial U}{\partial n} = \frac{\partial U}{\partial x} \frac{dx}{ds} + \frac{\partial U}{\partial y} \frac{dy}{ds} \tag{2}$$

$$U = x \frac{\partial U}{\partial x} + y \frac{\partial U}{\partial y} - \int \left(x \frac{\partial U}{\partial s \partial x} + y \frac{\partial U}{\partial s \partial y} \right) ds$$

The constants of the arbitrary linear function can be specified by requiring that U , $\partial U/\partial x$, $\partial U/\partial y$ equal zero at the origin. The boundary conditions for the two loading conditions being considered are given below. The subscript T refers to the uniform tension loading case and the subscript B refers to the pure bending case (Figure 1, Section 6.6). In the following sets of equations

$$\begin{aligned} x'' &= (x - x_0) \cos \phi + (y - y_0) \sin \phi \\ y'' &= (x - x_0) \sin \phi + (y - y_0) \cos \phi \end{aligned} \tag{3}$$

where x_o and y_o are defined with each set. The coordinates and surface indentifications are shown in Figure 2 of Section 6.6

Surface 0-A-B:

$$U_T = 0$$

$$\frac{dU_T}{dn} = 0$$

$$U_B = 0$$

$$\frac{dU_B}{dn} = 0$$

Surface B-C:

$$U_T = \frac{\sigma_o}{2} (x'')^2$$

$$\frac{dU_T}{dn} = 0$$

$$U_B = M_o \left[\frac{3}{w^2} (x'')^2 - \frac{2}{w} (x'')^3 \right]$$

$$\frac{dU_B}{dn} = 0$$

where

$$x_o = -a-L_1 \sin \phi_o$$

$$y_o = L_1 \cos \phi_o$$

Surface C-D:

$$U_T = \frac{\sigma_o}{2} w^2$$

$$\frac{dU_T}{dn} = \sigma_o w$$

$$U_B = M_o$$

$$\frac{dU_B}{dn} = 0$$

Surface D-E:

$$U_T = \frac{\sigma_o}{2} [(x'')^2 + 2wx'' + w^2]$$

$$\frac{dU_T}{dn} = 0$$

$$U_B = -M_o [\frac{3}{w^2} (x'')^2 + \frac{2}{w^3} (x'')^3 - 1]$$

$$\frac{dU_B}{dn} = 0$$

where

$$x_o = -a + L_2 \sin \phi + w \cos \phi$$

$$y_o = -L_2 \cos \phi + w \sin \phi$$

Surface E-A-O:

$$U_T = 0$$

$$\frac{dU_B}{dn} = 0$$

$$U_B = 0$$

$$\frac{dU_B}{dn} = 0$$

Section 6 - Appendix VI

LEAST SQUARE SOLUTION OF A SYSTEM OF SIMULTANEOUS LINEAR ALGEBRAIC EQUATIONS

For cases in which N independent linear algebraic simultaneous equations are a function of M ($M < N$) unknown variables (x_j)

$$\sum_{j=1}^M a_{ij} x_j = b_i \quad i = 1, \dots, n \quad (1)$$

it is apparent that all n equations cannot be satisfied exactly. Under these conditions it is possible to satisfy the first N_1 equations in the least square sense and last N_2 ($N_2 < M$) equations exactly ($N = N_1 + N_2$). These conditions are mathematically formulated below. The residuals R_i of the N equations are

$$R_i = \sum_{j=1}^M a_{ij} x_j - b_i \quad i = 1, \dots, N \quad (2)$$

The sum of the squares of the residuals of the first N_1 equations is

$$S = \sum_{i=1}^{N_1} (R_i)^2 \quad (3)$$

The first N_1 equations will be satisfied in the least square sense if S is minimized with respect to the M unknowns (x_i). The last N_2 equations will be satisfied exactly if this minimization is subject to the constraining conditions.

$$R_{N_1+i} = 0 \quad i = 1, \dots, N_2 \quad (4)$$

The quantity S can be minimized under the N_2 constraining conditions of equation (4) by forming the function⁽¹⁾

$$F = S + \sum_{i=1}^{N_2} \lambda_i R_{N_1+i} \quad (5)$$

where λ_i 's are Lagrange multipliers, and satisfying the equations

$$\frac{\partial F}{\partial x_i} = 0 \quad i = 1, \dots, M \quad (6)$$

$$R_{N_1+i} = 0 \quad i = 1, \dots, N_2 \quad (7)$$

Equations (6) and (7) can be written in the more explicit form

$$\sum_{j=1}^M \left(\sum_{i=1}^{N_1} a_{ik} a_{ij} \right) x_j + \frac{1}{2} \sum_{i=1}^{N_2} a_{i+N_1,j} \lambda_i = \sum_{i=1}^{N_1} a_{ik} b_i \quad k = 1, \dots, M \quad (8)$$

$$\sum_{j=1}^M a_{ij} x_j = b_i \quad i = N_1+1, \dots, N \quad (9)$$

The above equations represent $(M+N_2)$ linear algebraic equations which are a function of a similar number of unknowns (x_i , $i = 1, \dots, M$ and λ_i , $i = 1, \dots, N_2$) and can be solved by conventional methods.

For the case where no equations are satisfied exactly and all are satisfied in the least squared sense equations (8) and (9) reduce to the form

$$\sum_{j=1}^M \left(\sum_{i=1}^N a_{ik} a_{ij} \right) x_j = \sum_{i=1}^N a_{ik} b_i \quad k = 1, \dots, M$$

In Section 6.6 all equations are satisfied in the least square sense.

Reference:

1. I. S. Sokolnikoff, R. M Redheffer, "Mathematics of Physics and Modern Engineering," McGraw-Hill, 1958.

TABLE OF CONTENTS

Section 7

FRACTURE TOUGHNESS PARAMETERS FOR LOW-STRENGTH INTERMEDIATE-TOUGHNESS METALS

	<u>Page</u>
7.1 INTRODUCTION	156
7.2 OBJECTIVES	159
7.3 SUMMARY	159
7.4 CONCLUSIONS	160
7.5 RECOMMENDATIONS	161
7.6 TEST MATERIALS	163
7.7 SPECIMEN PREPARATION	172
7.8 TEST PROCEDURE	172
7.8.1 Fracture Toughness Testing	172
7.8.2 Cyclic Loading (Fatigue) Tests	174
7.9 TEST RESULTS	175
7.9.1 Fracture Toughness Testing	175
7.9.2 Cyclic Loading Tests	186
7.10 DISCUSSION	203
7.10.1 Test Materials	203
7.10.2 Toughness Testing	204
7.10.3 Cyclic Loading (Fatigue) Tests	209
7.11 ACCURACY OF RESULTS	211
7.12 EXAMPLE PROBLEMS	211
7.12.1 Example Problem No. 1 - Beam in Bending	212
a. Operational Requirements	212
b. Initial Design Considerations	213
c. Calculation of Critical Flaw Size	213

TABLE OF CONTENTS (cont.)

	<u>Page</u>
d. Calculation of Cyclic Life	218
e. Development of Inspection Criteria and Safety Factors	226
7.12.2 Example Problem No. 2 - Thin-Walled Pressure Vessel	227
a. Operational Requirements	227
b. Initial Design Considerations	227
c. Calculation of Critical Flaw Size	227
d. Calculation of Cyclic Life	228
7.12.3 Discussion of Example Problems	231
7.13 REFERENCES	233

LIST OF TABLES

Section 7

FRACTURE TOUGHNESS PARAMETERS FOR LOW-STRENGTH INTERMEDIATE-TOUGHNESS METALS

	<u>Page</u>
TABLE 1 Chemical Compositions of Materials Investigated.....	164
TABLE 2 Heat Treatments and Room Temperature Tensile Properties of Materials Investigated.....	165
TABLE 3 Results of Rising-load Fracture Toughness Testing.....	178

LIST OF FIGURES

Figure 1. Variation in tensile properties with temperature for alloys investigated.....	166
Figure 2. Variation in Charpy V-Notch properties with temperature for AISI 1020, 1045, 1144 and 4140 steels.....	167
Figure 3. Through-the-thickness variation in room temperature tensile properties (4 inch thick plate).....	168
Figure 4. Through-the-thickness variation in room temperature Charpy impact energy (4 inch thick plate).....	169
Figure 5. Variation in through-the-thickness microstructure for AISI 1020, 1045, and 1144 alloy steels.....	170
Figure 6. Variation in through-the-thickness microstructures for AISI 4140 steel and 7039-T6 aluminum.....	171
Figure 7. "4T" type wedge opening loading fracture toughness specimen and test instrumentation.....	173

LIST OF FIGURES (Cont.)

	<u>Page</u>
Figure 8. Schematic representation of the ultrasonic technique used to measure subcritical crack growth.....	176
Figure 9. Test fixture used to monitor crack growth in the WOL type toughness specimen.....	177
Figure 10. Influence of temperature on toughness and yield strength for alloys investigated.....	180
Figure 11. Room temperature rising load fracture appearance of AISI 1020 steel (4T WOL specimen).....	181
Figure 12. Room temperature rising load fracture appearance of AISI 1045 steel (4T WOL specimen).....	182
Figure 13. Room temperature rising load fracture appearance of AISI 1144 steel (4T WOL specimen).....	183
Figure 14. Room temperature rising load fracture appearance of AISI 4140 steel (4T WOL specimen).....	184
Figure 15. Room temperature rising load fracture appearance of 7039-T6 aluminum (4T WOL specimen).....	185
Figure 16. Fatigue crack growth behavior observed for various ferrous alloys.....	187
Figure 17. Comparison of the fatigue crack growth behavior observed for AISI 1020, 1144, and 4140 steels.....	188
Figure 18. Room temperature fatigue fracture appearance of AISI 1020 steel (4T WOL specimen).....	189
Figure 19. Room temperature fatigue fracture appearance of AISI 1045 steel (4T WOL specimen).....	190
Figure 20. Room temperature fatigue fracture appearance of AISI 1144 steel (4T WOL specimen).....	191
Figure 21. Room temperature fatigue fracture appearance of AISI 4140 steel (4T WOL specimen).....	192
Figure 22. Room temperature fatigue fracture appearance of 7039-T6 aluminum (4T WOL specimen).....	193

LIST OF FIGURES (Cont.)

	<u>Page</u>
Figure 23. Effect of test specimen locations on the fatigue behavior observed for 7039-T6 aluminum.....	195
Figure 24. Fatigue crack growth rate versus stress intensity factor range for AISI 1020 steel.....	197
Figure 25. Fatigue crack growth rate versus stress intensity factor range for AISI 1045 steel.....	198
Figure 26. Fatigue crack growth rate versus stress intensity factor range for AISI 1144 steel.....	199
Figure 27. Fatigue crack growth rate versus stress intensity factor range for AISI 4140 steel.....	200
Figure 28. Fatigue crack growth rate versus stress intensity factor range for AISI 7039-T6 aluminum.....	201
Figure 29. Comparison of da/dN vs ΔK for AISI 1020, 1045, 1144 and 4140 steels.....	202
Figure 30. Analytical and experimental load-displacement curves for AISI 1020 steel.....	208
Figure 31. Loading conditions for example problem No. 1.....	214
Figure 32. Notch bend specimens (four point loaded).....	216
Figure 33. K calibrations for bend specimens.....	217
Figure 34. K calibrations for 4 point loaded notched bend specimen.....	219
Figure 35. Crack growth behavior computed for example problem.....	224
Figure 36. Initial flaw size versus cycles to failure for example problem.....	225
Figure 37. Flaw shape parameter curve for surface and internal cracks.....	229

Section 7

FRACTURE TOUGHNESS PARAMETERS FOR LOW-STRENGTH INTERMEDIATE-TOUGHNESS METALS

7.1 INTRODUCTION

Fracture mechanics or "fracture toughness" technology provides a unique structural design concept which yields a quantitative relationship between applied stress, flaw size and material properties. From the proper consideration of fracture mechanics data for both the slow growth and rapid propagation phases of fracture it is possible to:

- 1) design and select materials to provide the desired reliability against fracture.
- 2) develop a quantitative evaluation of the brittle fracture potential of components in specific situations.
- 3) predict the useful life expectancy of components under sustained and/or cyclic loading conditions.
- 4) establish realistic material selection and nondestructive inspection specifications that will assure the desired degree of immunity from brittle failure for the required life of the structure.

Unfortunately however, existing fracture mechanics technology is limited to the analysis of linear elastic loading conditions (plane strain) where the amount of material at the crack tip which undergoes plastic yielding prior to catastrophic failure is very small.⁽¹⁾ In order to insure suitable plane strain conditions and ultimately, to establish useful fracture toughness data, test specimens of sufficient size are required such that a triaxial state of stress exists near the crack which prevents relaxation of the localized stresses due to plastic yielding. The higher the relative toughness of a given material

the greater the extent of crack tip plasticity prior to failure and the larger the test specimen required to develop plane strain data. Existing criteria for selecting fracture toughness specimens of sufficient size require that the specimen thickness B (and the other dimensions expressed relative to the thickness) be equal to or greater than 2.5 times the ratio of the apparent toughness (K_Q) to yield strength (σ_{YS}) quantity squared [$B \geq 2.5 (K_Q / \sigma_{YS})^2$]^(1,2). Having satisfied this criterion as well as other requirements listed in references 1 and 2, the apparent toughness measured in a given test, K_Q , is reported as the plane strain critical stress intensity factor or fracture toughness (K_{Ic}) for the material.

The above specimen size requirement can also be interpreted as a criterion for determining the applicability of linear elastic fracture mechanics technology to a particular design situation. Specifically, if the K_{Ic} and yield strength of a given material are known, one need only establish the thickness which satisfies $B = 2.5 (K_{Ic} / \sigma_{YS})^2$ to determine the minimum thickness of the material for which plane strain fracture mechanics concepts are applicable. If the proposed application involves using the material in a section size less than the minimum thickness required for plane strain conditions, existing fracture mechanics concepts cannot be used to establish fracture criteria. As demonstrated in Section 6 of this report, such a design situation requires the use of a fracture criterion based upon elastic-plastic analysis.

In an application involving sufficient mechanical restraint, a brittle plane strain state-of-stress can be developed in a component which does not satisfy the above section size requirements. Under these conditions, the actual plane strain fracture toughness measured with specimens of sufficient thickness must be used for realistic design considerations.

In view of the above size criteria, it immediately becomes apparent that materials of relatively high toughness (expressed as the ratio of K_{Ic} to σ_{YS}) require large fracture toughness specimens to measure K_{Ic} . In addition, the resulting K_{Ic} data are applicable only

to design considerations involving sufficiently large section sizes to yield plane strain loading conditions. Consequently, the majority of available fracture toughness data are limited to high-strength alloys which characteristically exhibit low-toughness and can conveniently be tested with relatively small specimens. As a result, questions exist regarding the applicability and practicability of linear elastic fracture mechanics concepts and test techniques to low-strength, intermediate to high-toughness materials.

Questions concerning the applicability of existing fracture mechanics concepts to intermediate and high-toughness materials can only be answered by conducting tests under those conditions necessary to satisfy the existing criteria for plane strain primarily, specimens of sufficient thickness. In addition, if a test technique is to be developed for predicting plane strain behavior from subsize specimens, data from tests conducted under actual plane strain conditions must be available for comparison and evaluation of the technique.

If existing fracture mechanics concepts are found to be applicable to high toughness materials provided specimens of sufficient size are tested, the practicality of conducting such tests will depend upon the specific design situation involved. For example, many applications of low-strength, intermediate to high-toughness materials involve very large section sizes where it is realistic to assume that plane strain conditions exist. For such design situations, there is no question as to the value and practicability of conducting large toughness tests to establish the brittle fracture potential of the structure.

Wessel and others have demonstrated that the existing concepts of linear elastic fracture mechanics are applicable to some intermediate-strength alloy steels.^(3,4) However, additional evidence is required to extend the range of applicability to commonly used low-strength structural alloys. The primary goal of this portion of the investigation was to develop further evidence to substantiate existing data which indicate that linear elastic fracture mechanics concepts are applicable to low-strength, intermediate to high-toughness materials. The

experimental portion of the investigation involved generating both rising load fracture toughness and fatigue crack growth rate data for four low to intermediate-strength steels and an intermediate-strength aluminum alloy.

7.2 OBJECTIVES

The specific objectives of this phase of the investigation were; (1) to explore the possibility of obtaining linear elastic fracture mechanics material parameters for low-strength structural alloys and if applicable, to acquire the necessary K_{Ic} fracture toughness and cyclic crack growth rate data and (2) if linear elastic principles are found not to be applicable; explore the feasibility of developing an appropriate elastic-plastic fracture criterion using currently available elastic-plastic technology.

7.3 SUMMARY

This investigation has demonstrated that existing linear elastic fracture mechanics concepts (based primarily on results obtained with low-toughness, high-strength alloys) are applicable to commonly used high-toughness, low-strength materials. Specifically, it has been shown that AISI 1045, 1144 and 4140 steel and 7039-T6 aluminum alloys with yield strengths ranging from 38 to 78 ksi are subject to brittle plane strain failures under specific loading conditions within the temperature range of 0 to 75°F. Consequently, the brittle fracture potential and ultimately, a quantitative design criteria for these materials under the appropriate loading conditions can be established with fracture mechanics concepts. For those applications where these materials do not exhibit plane strain behavior, elastic-plastic failure criteria must be developed to provide quantitative design information. As a first approach towards determining the feasibility of developing an elastic-plastic fracture criteria, it has been shown that an existing finite element stress analysis procedure can accurately predict the displacements in the vicinity of a crack like defect

subjected to non-plane strain loading. Since these displacements are directly related to the localized crack tip stresses which in turn, control failure; this technique has potential for the development of quantitative elastic-plastic fracture criteria. An appropriate program to further develop this potential, and ultimately develop an elastic-plastic fracture criteria was prepared and submitted to the sponsoring group.

The fatigue crack growth rate properties for the alloys mentioned above as well as AISI 1020 steel were also measured and interpreted in terms of fracture mechanics parameters. These results show that the ferrous alloys studied exhibit fatigue crack growth rate properties which conform to the generalized growth rate law established for more brittle alloys. Therefore, existing techniques for predicting the useful life expectancy of these alloys under cyclic loading conditions are applicable.

Two example problems selected to demonstrate the use of fracture mechanics data in design are included and the pertinent areas of consideration described in detail.

7.4 CONCLUSIONS

1. Existing linear elastic fracture mechanics concepts were found to be applicable to the AISI 1045, 1144 and 4140 steel and 7039-T6 aluminum alloys investigated within the temperature range of 0 to 75°F and for the metallurgical conditions employed.

2. The room temperature fracture toughness of the 1144 and 4140 steels and the 7039-T6 aluminum alloy were found to be 62, 56 and 18 ksi $\sqrt{\text{in.}}$, respectively. These toughness values indicate that room temperature plane strain failure is possible with the 1144 and 4140 steel and 7039-T6 aluminum alloys when used in section sizes of at least 1.48, 1.72 and 0.27 inch thick, respectively.

* Westinghouse Research Laboratories Unsolicited proposal #8M307 (Aug. 1968), "Development of Fracture Mechanics Technology for Low-to-Intermediate Strength Materials and Combined Loading".

3. The highest temperature for which plane strain toughness data were obtained for 4 inch thick specimens of the AISI 1045 steel was 25°F. The fracture toughness at this temperature was 46 ksi $\sqrt{\text{in.}}$ and the corresponding minimum thickness for plane strain loading is 1.8 inches.

4. Although plane strain fracture toughness data were not obtained for the 1020 steel tested in 4 inch sections, the results indicate that a 7.5 inch thick section of this steel is required to develop plane strain behavior under room temperature loading conditions.

5. At ΔK levels above 37 ksi $\sqrt{\text{in.}}$ the fatigue crack growth rate properties of the 1020, 1045, 1144 and 4140 steels investigated conform to the generalized fracture mechanics crack growth rate law where $da/dN = C_o \Delta K^n$.

6. Of the ferrous alloys studied, the 1144 steel showed the greatest resistance to fatigue crack propagation and the 4140 steel the least.

7. The 7039-T6 aluminum alloy did not exhibit crack propagation behavior consistent with the growth rate law; considerable deviation from a straight line relationship between $\log da/dN$ versus $\log \Delta K$ was encountered at ΔK levels above 13 ksi $\sqrt{\text{in.}}$

8. Correlation between the actual displacement across the crack starter notch in a 1020 steel specimen tested at room temperature and the displacement predicted by a finite element computer technique indicates that it may be possible to analyze the stresses associated with non-plane strain loading conditions. Consequently, this finite element technique may eventually lead to the development of elastic-plastic fracture criteria.

7.5 RECOMMENDATIONS

In view of the fact that existing linear elastic fracture mechanics concepts are applicable to low-strength, intermediate to high-toughness alloys it is apparent that such alloys are subject to brittle failure under appropriate loading conditions. Since knowledge

of a materials inherent fracture toughness permits determination of the brittle fracture potential under known loading conditions, it is obvious that such data are invaluable as a quantitative approach to design. The results presented in this investigation have shown that existing fracture toughness testing criteria and test techniques are applicable to some commonly used low-strength structure alloys. However, the limited amount of testing involved did not permit the development of sufficiently reliable design data. Further testing with a statistically accurate sampling of materials is required to establish the necessary heat-to-heat variations and ultimately, reliable design data. Therefore, we recommend that additional fracture toughness and fatigue crack growth rate testing be conducted for other heats of the alloys studied in this investigation as well as other materials where it is desirable to establish a quantitative approach to design against failure.

Many structural alloys are used for applications which do not result in the development of plane strain loading, consequently, these applications cannot be analyzed in terms of existing fracture mechanics concepts. Failure under such nonplane strain conditions is accompanied by the development of extensive crack-tip plastic yielding resulting in a stress situation which, at the present time, cannot be accurately analyzed. The development of the elastic plastic solutions necessary to permit analysis of the stress situations associated with non plane-strain failure has the potential to lead to a quantitative design approach similar to that currently available for plane strain conditions.

In view of the encouraging results obtained thus far in the development of elastic-plastic stress analyses, it is recommended that this area of investigation be continued with the ultimate objective of developing an engineering fracture criteria applicable to non plane-strain (elastic-plastic) loading conditions. An appropriate program has been prepared and submitted to TACOM.*

* Westinghouse Research Laboratories Unsolicited proposal #8M307 (Aug. 1968), "Development of Fracture Mechanics Technology for Low-to-Intermediate Strength Materials and Combined Loading".

7.6 TEST MATERIALS

The materials involved in this investigation included AISI 1020, 1045, 1144 and 4140 steels and aluminum alloy 7039-T6. All materials were supplied as either 2 ft. x 5 ft. plate or 10 in. x 12 in. forgings 4-inches thick. The materials were purchased to chemistry, heat treated conditions and approximate yield strength requirements and not to any existing material property specifications.

The 1020 and 1045 carbon steels were supplied as normalized plate representative of low-strength ferrous alloys with yield strengths of 32 and 37.5 ksi, respectively. The 4140 and 1144 oil hardening steels were supplied as quenched and tempered plate and forgings, respectively with yield strengths of 65 and 70 ksi. The 7039-T6 aluminum was supplied as solution treated and aged forgings with a yield strength of 57 ksi. The chemical compositions of the alloys studied are presented in Table 1. Table 2 presents the heat treatment and pertinent room temperature tensile properties. The variations in tensile and Charpy impact properties with temperature are illustrated graphically in Figures 1 and 2, respectively. All tensile and impact tests from plate material were conducted with longitudinal specimens (major axis of the specimen parallel to the primary rolling direction). The major axes of the specimens taken from the forgings were aligned in the 10 inch direction.

In order to thoroughly characterize the 4 inch thick sections involved in this investigation, the through-the-thickness room temperature tensile and impact properties were determined. The results are presented in Figures 3 and 4, respectively. Figures 5 and 6 show the typical variation in microstructure between near-the-surface and center-thickness portions of the "as-received" materials. Note that the AISI 1020 and 1045 carbon steels consist of pearlite and free ferrite whereas the 1144 and 4140 steels consist primarily of pearlite. Although the 1144 and 4140 steels were quenched and tempered, microstructures developed were not representative of conventionally hardened material because of factors such as mass effect (on quenching) of heavy sections, high tempering temperatures, and lengthy tempering times. The micro-structure of the 7039-T6 aluminum alloy is typical of solution treated and aged aluminum alloys.

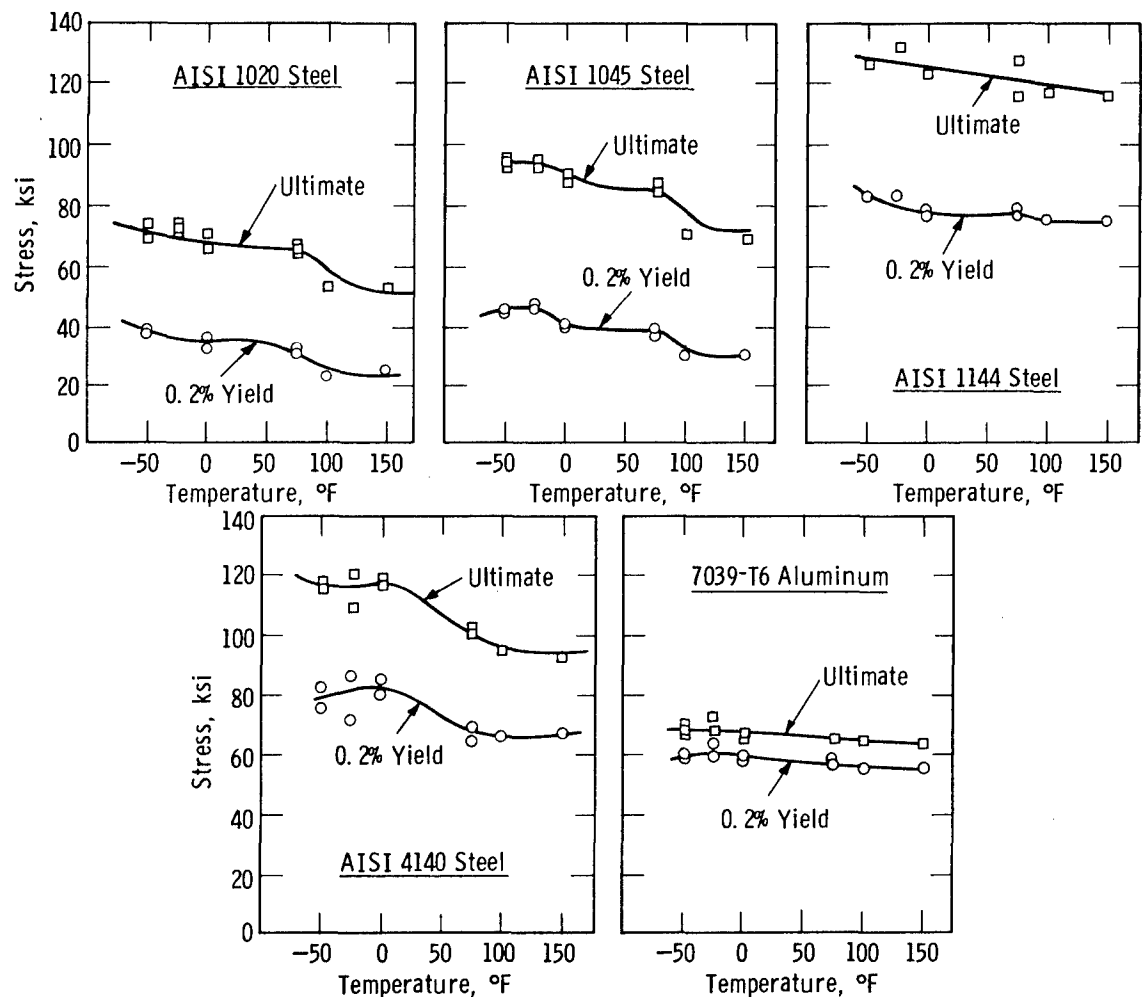
SEC. 7 TABLE I-CHEMICAL COMPOSITIONS OF MATERIALS INVESTIGATED

<u>Material</u>	Composition (weight percent)							
	<u>C</u>	<u>Mn</u>	<u>P</u>	<u>S</u>	<u>Si</u>	<u>Ni</u>	<u>Cr</u>	<u>Mo</u>
1020 Steel	0.27	0.48	0.005	0.031	0.27	0.18	0.11	0.04
1045 Steel	0.52	0.83	0.006	0.028	0.25	0.12	<0.10	0.03
1144 Steel	0.52	1.46	0.016	0.25	0.20	—	—	—
4140 Steel	0.42	0.78	0.007	0.023	0.23	0.22	0.89	0.21
	<u>Si</u>	<u>Fe</u>	<u>Cu</u>	<u>Mn</u>	<u>Mg</u>	<u>Cr</u>	<u>Zn</u>	<u>Ti</u>
Aluminum 7039-T6	0.30 Max	0.40 Max	0.10 Max	0.10 0.40	2.3 3.3	0.15 0.25	3.5 4.5	1.10 Max

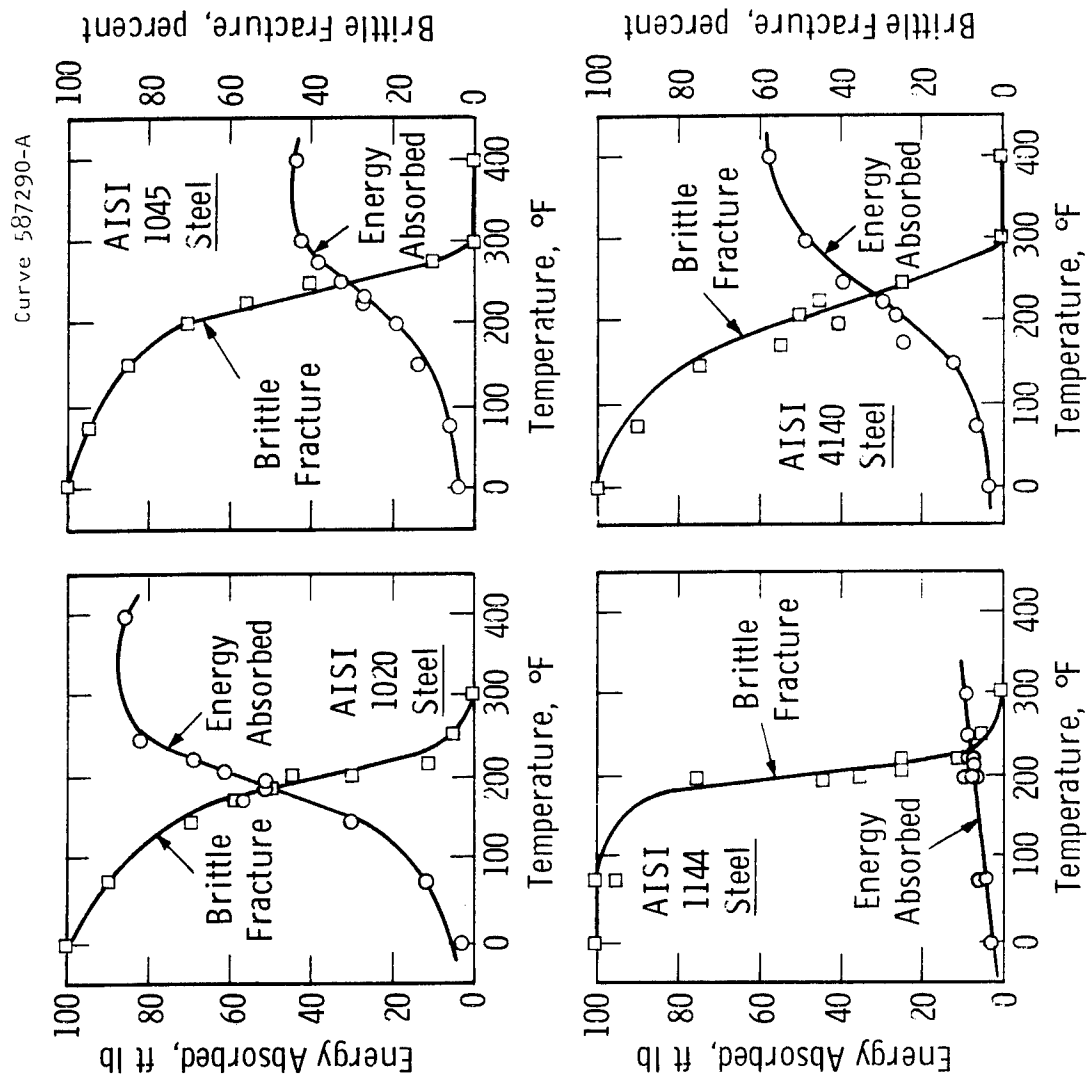
SEC. 7 TABLE 2- HEAT TREATMENTS AND ROOM TEMPERATURE TENSILE
PROPERTIES OF MATERIALS INVESTIGATED

Material	Heat Treatment	Tensile Properties			
		Yield Strength (psi)	Ultimate Strength (psi)	Elongation in 1.5 inches (percent)	Reduction in Area (percent)
1020 Steel	Normalized, Heated to 1700°F, Air-Cooled	32000	66100	35.70	55.80
1045 Steel	Normalized, Heated to 1650°F, Air-Cooled	37500	85550	24.72	38.80
1144 Steel	Oil Quenched and Tempered, Quenched From 1550°F, Tempered at 900°F (6 hr) Furnace Cooled	78000	122000	5.18	6.87
4140 Steel	Oil Quenched and Tempered, Quenched From 1550°F, Tempered at 1200°F (6 hr) Furnace Cooled	65000	100900	16.83	47.30
7039-T6 Aluminum	Solution Treated 4 hr at 850°F, Aged 18 hr at 320°F	57000	65350	12.43	35.05

Curve 587296-B

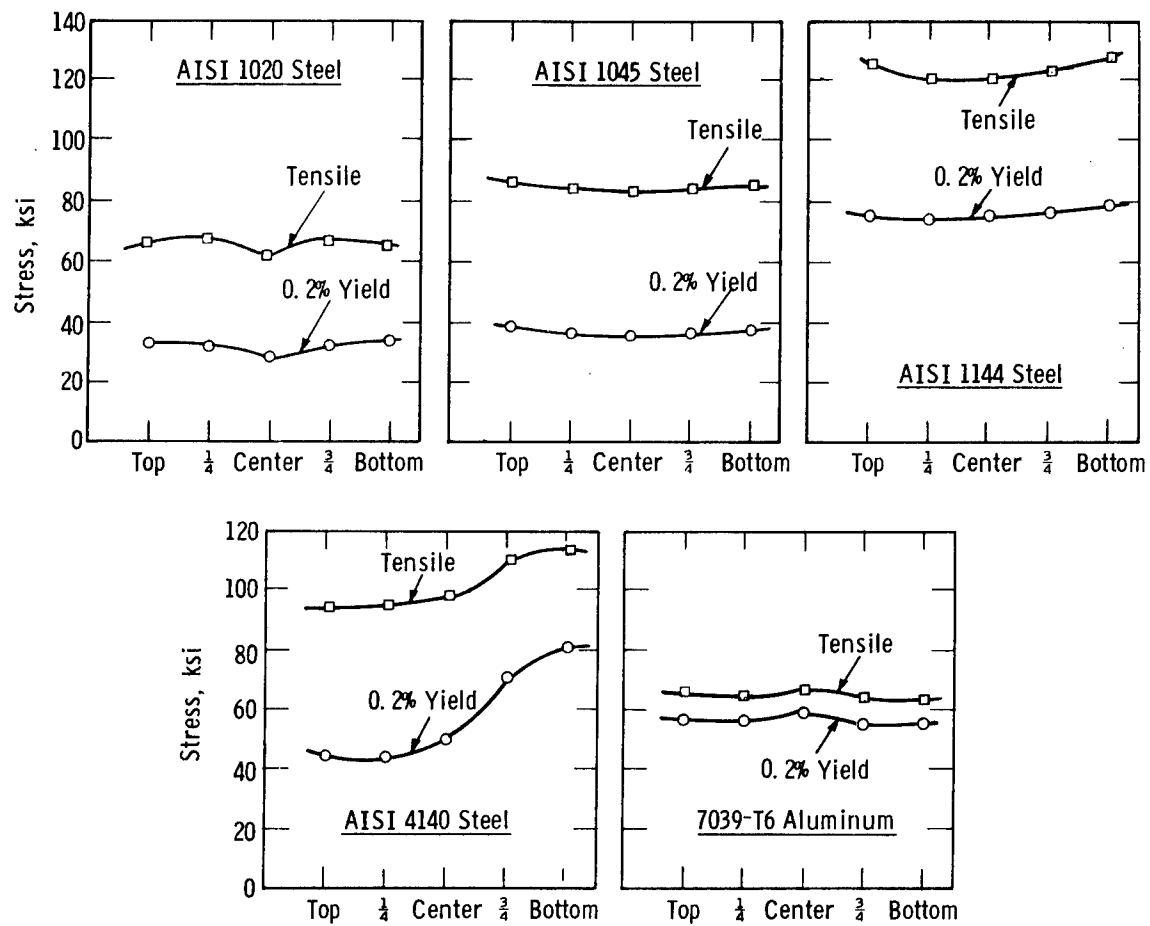


Sec. 7 Fig. 1—Variation in tensile properties with temperature for alloys investigated

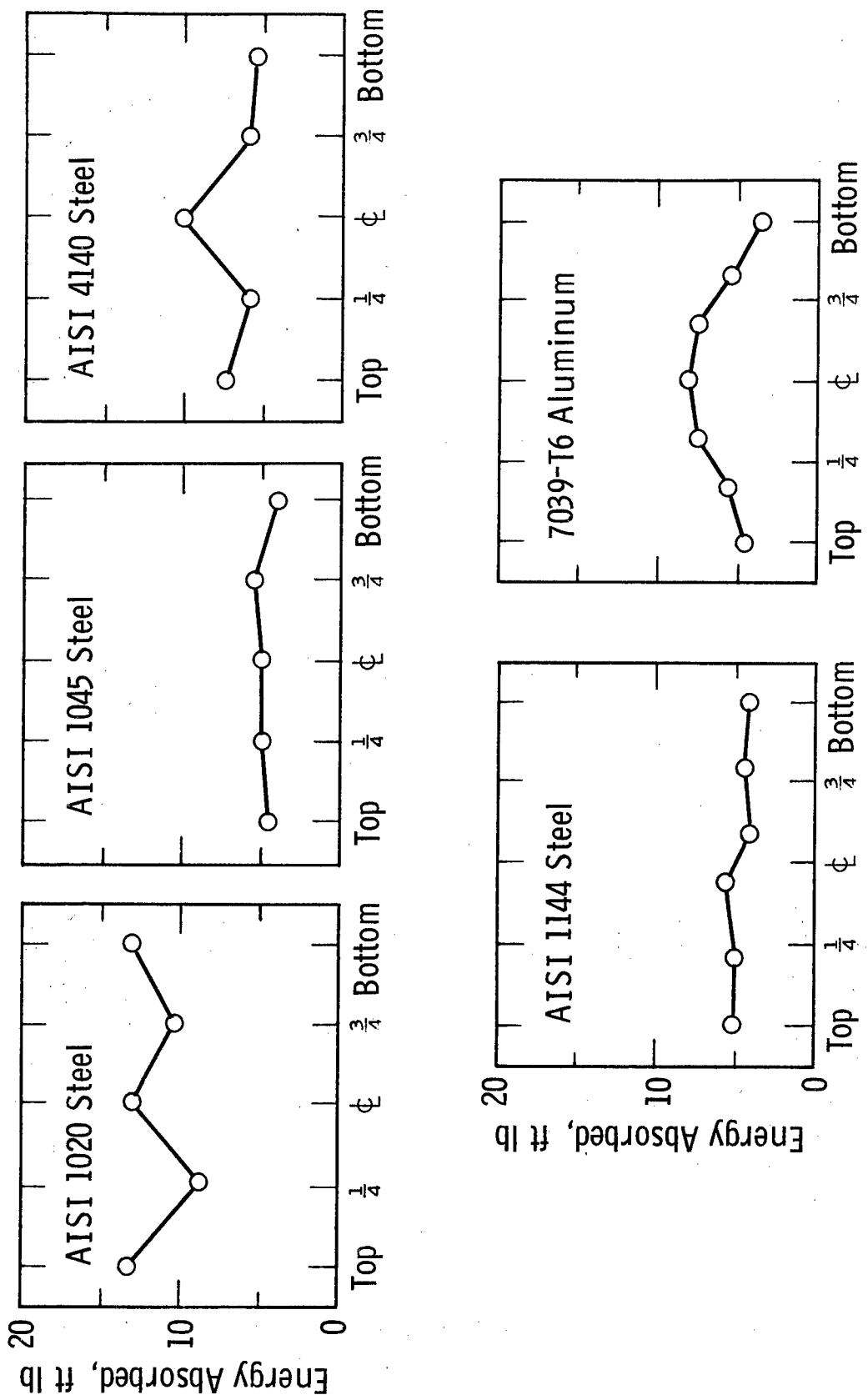


Sec. 7 Fig. 2—Variation in Charpy V-Notch properties with temperature for AISI 1020, 1045, 1144 and 4140 steels

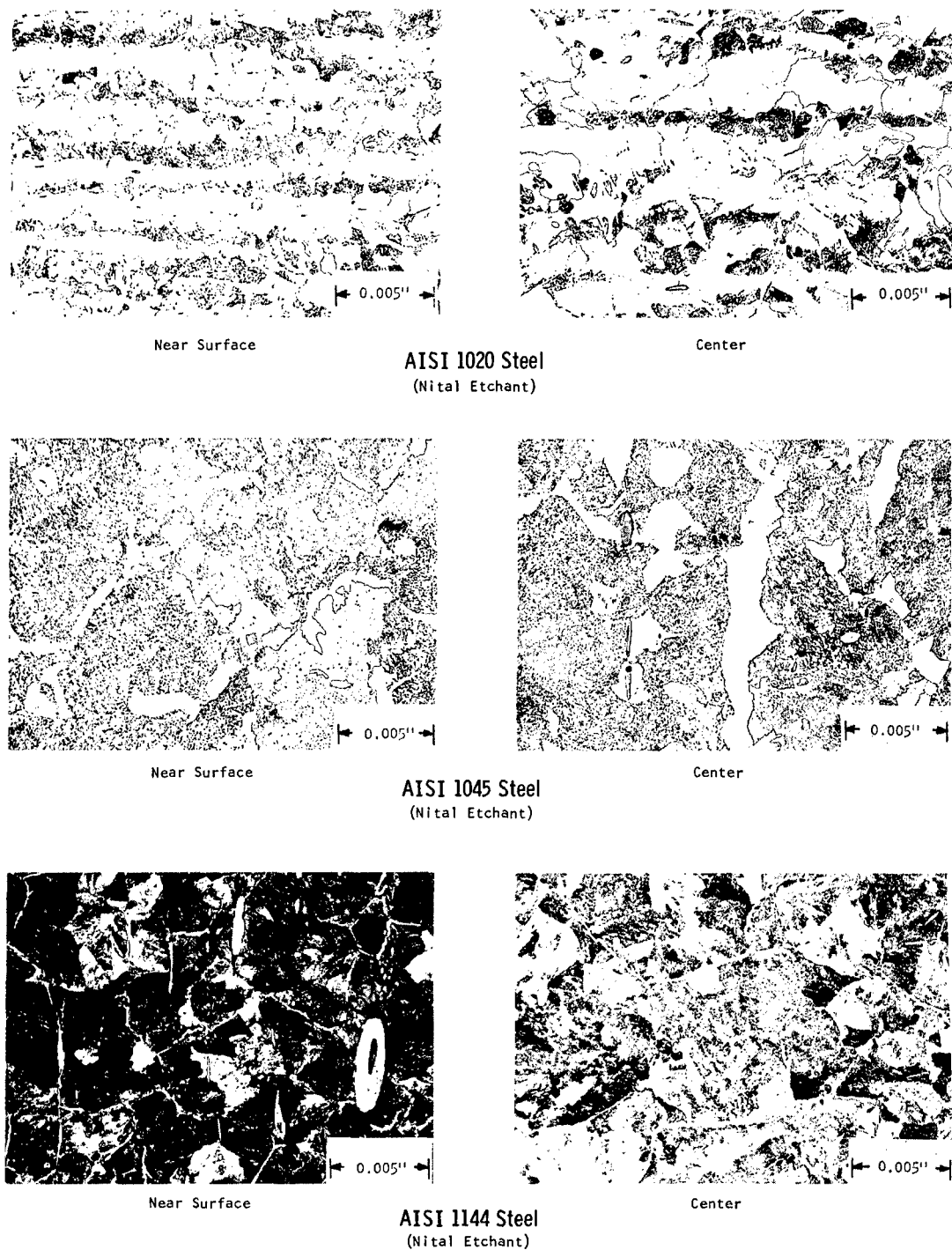
Curve 587297-B



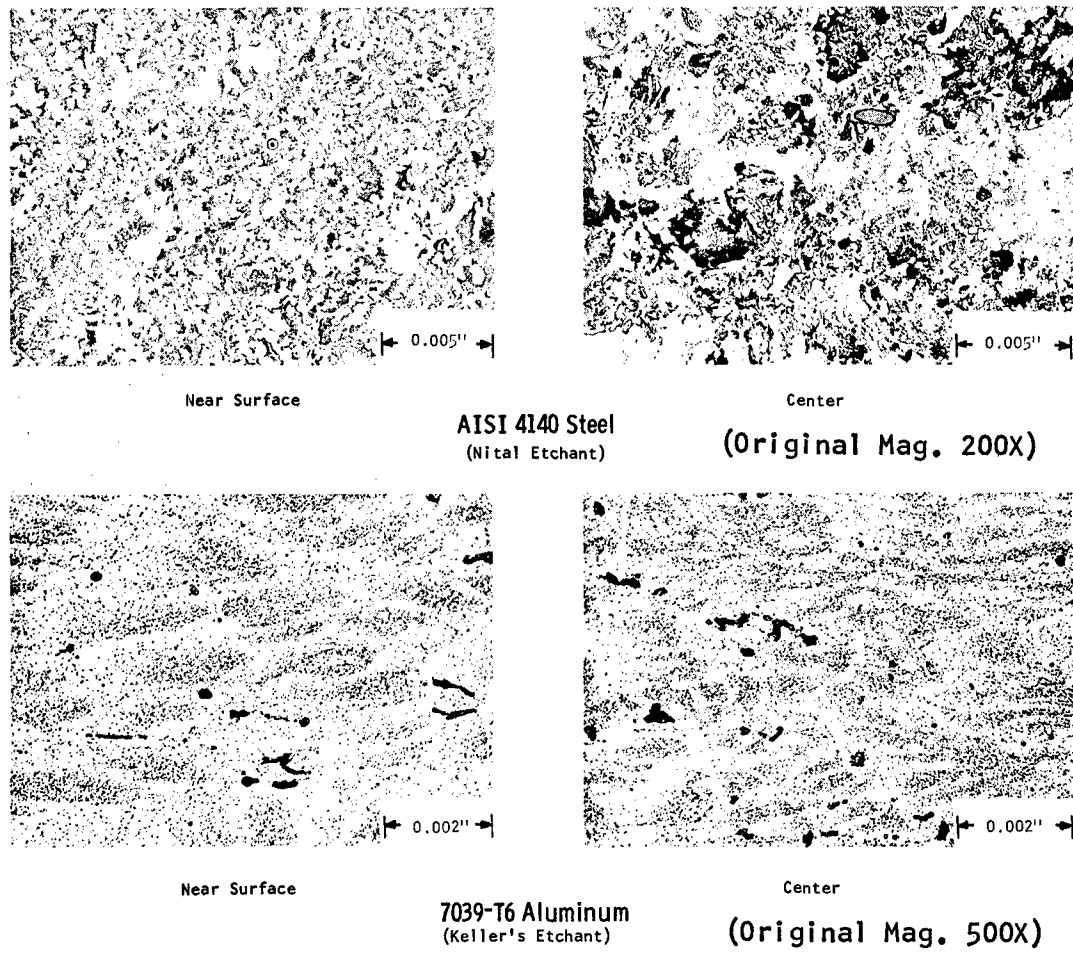
Sec. 7 Fig. 3—Through-the-thickness variation in room temperature tensile properties
(4 inch thick plate)



Sec. 7 Fig. 4-Through-the-thickness variation in room temperature
Charpy impact energy (4-inch thick plate)



Sec. 7 Fig. 5—Variation in through-the-thickness microstructure
for AISI 1020, 1045 and 1144 alloy steels
(Original Mag. 200X)



Sec. 7 Fig. 6—Variation in through-the-thickness microstructure for AISI 4140 steel and 7039-T6 aluminum

7.7 SPECIMEN PREPARATION

All rising load toughness testing involved in this investigation was conducted with 4 inch-thick wedge-opening-loading (WOL) type crack-notch fracture toughness specimens of the "4T" geometry illustrated in Figure 7.⁽³⁾ Fatigue testing was conducted with "4T" WOL specimens modified slightly (side grooved, 45° included angle, 0.010 in. root radius, 0.200 in. deep on each side) from the specimen shown in Figure 7. Side grooving was used to insure crack propagation along a plane perpendicular to the direction of loading.

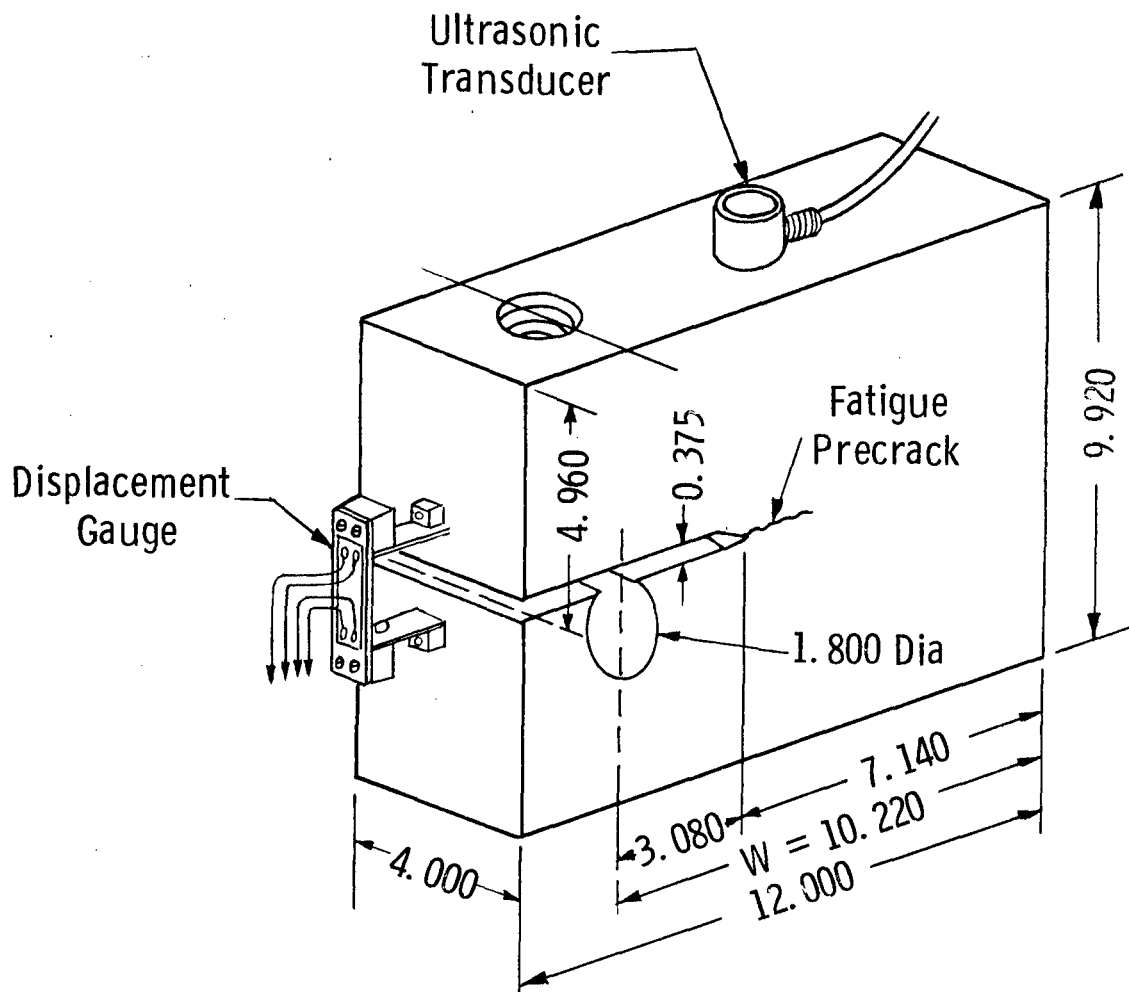
The crack-starter notches (Figure 7) were extended to fatigue crack severity by subjecting the specimens to low-stress sinusoidal cyclic loading at room temperature. The maximum stress intensity factor at the termination of precracking did not exceed 25 ksi $\sqrt{\text{in.}}$ for the steel alloys or 10 ksi $\sqrt{\text{in.}}$ for the 7039-T6 aluminum. All tests involving plate material (AISI 1020, 1045 and 4140 steels) were conducted with longitudinal specimens in which the major plane of the precrack was in the transverse direction of the as-received plate. The testing direction associated with specimens removed from the forged material (AISI 1144 steel 7039-T6 aluminum) was such that the direction of crack propagation was along the 12-inch dimension.

7.8 TEST PROCEDURE

7.8.1 FRACTURE TOUGHNESS TESTING

A total of three "4T" WOL specimens from each material were tested under rising load conditions. One test each was conducted at 75°F and 0°F and the remaining specimen tested at a temperature which served to confirm the prior results. The tests were conducted on a universal hydraulic test machine at a head motion rate of 0.04 in. per minute (K of 100 ksi $\sqrt{\text{in.}}$ per minute). A liquid nitrogen cooling chamber was used for the low temperature tests and the specimens soaked for 1 hour at temperature prior to testing. Except for the 1045 steel, the rising load tests were monitored with load-displacement and ultrasonic crack growth instrumentation as illustrated in Figure 7. Due

Dwg. 857A555



Sec. 7 Fig. 7—"4T" type wedge opening loading fracture toughness specimen and test instrumentation

to the large grains and coarse structure encountered in the 1045 steel, this material could not be monitored for crack growth using ultrasonics.

A load-displacement clip gauge calibrated to 40 micro-inches of strain per 1 mil (0.001 in.) of displacement was used to measure the relative displacement across the crack-notch during loading. A 10 MHz (megahertz) ultrasonic transducer was used to monitor crack growth behavior.⁽⁵⁾ The transducer was mounted on the test specimen surface just ahead of the tip of the precrack (Figure 7). When crack growth occurred, the scanning beam of the transducer was interrupted such that the amplitude of the back reflection signal (signal reflected from the opposite face of the specimen) decreased. Consequently, a decreasing back reflection signal could be interpreted as crack extension.

An adequate correlation between the decrease in back reflection signal and the extent of crack growth has not been established; however, the primary purpose of this technique was to detect the onset and nature of the crack growth (stable or unstable) rather than the absolute amount of extension.

The load-displacement and ultrasonic instrumentation outputs were recorded independently as a function of the applied load using X-Y recorders.

7.8.2 CYCLIC LOADING (FATIGUE) TESTS

With the exception of the 7039-T6 aluminum alloy, fatigue crack growth testing was limited to a single "4T" WOL test for each material. The fatigue tests involving 7039-T6 aluminum included two "1T" WOL specimens as well as a "4T" WOL test. The configuration of a "1T" WOL specimen is identical to the "4T" (Figure 7) except that all dimensions are reduced by a factor of four.

The fatigue crack growth rate tests were conducted on a constant-load universal hydraulic fatigue machine under sinusoidal tension-tension (0 to maximum load) loading conditions at 75°F in air.

The test frequency was 600 cycles-per-minute and the maximum alternating load was maintained constant throughout each individual test.

With the exception of the AISI 1045 steel, the extent of fatigue crack growth during cyclic loading was measured and recorded with an ultrasonic crack growth monitor developed specifically for use with the WOL specimen.⁽⁶⁾ The essence of the technique is to maintain a constant ultrasonic signal from the tip of the propagating crack by moving a transducer along the specimen surface such that crack growth can be related to transducer location. A schematic illustration of the principle involved is presented in Figure 8 where Δa is the change in crack length and ΔD is the change in transducer location. The actual test fixture is shown in Figure 9. This crack growth monitoring procedure exhibits a crack length measurement sensitivity of ± 0.010 inch and provides a continuous record of crack length versus number of elapsed cycles.

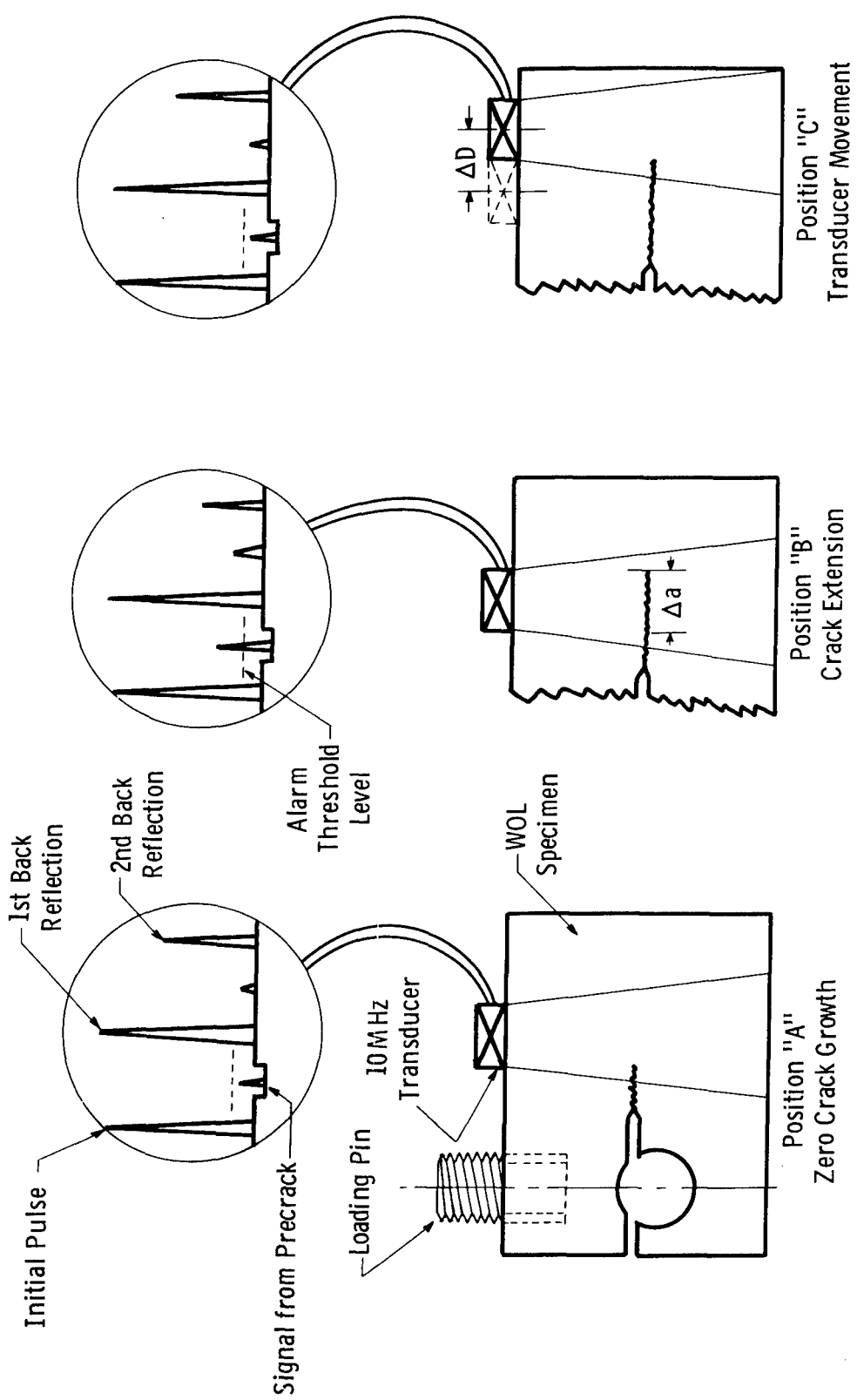
The crack growth encountered in the 1045 steel specimen was measured visually on each side of the specimen and the average crack length recorded against the elapsed cycles.

7.9 TEST RESULTS

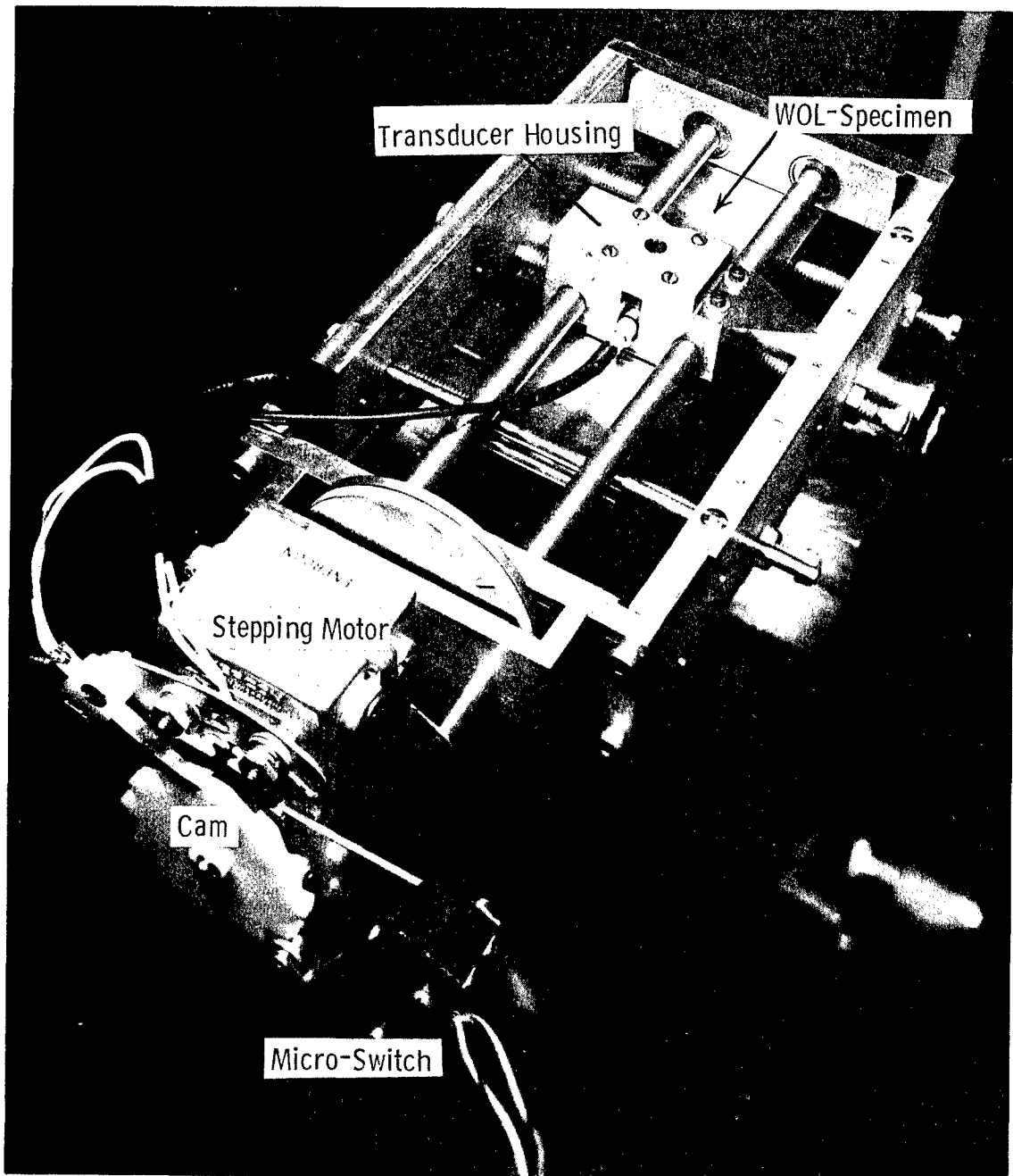
7.9.1 FRACTURE TOUGHNESS TESTING

Table 3 presents a summary of the results of the rising load fracture toughness testing for the five alloys investigated. The stress intensity factors reported as K_Q refer to the stress intensity value associated with the 5 per cent secant offset load as determined in accordance with the current ASTM recommendations for the evaluation of load-displacement behavior for plane strain fracture toughness testing.^(2,7,8)

The K_Q parameters were determined in accordance with the fracture mechanics relationship between the stress intensity factor, applied load, and crack length established for the WOL type specimen.^(3,9) This relationship is expressed as:



Sec. 7 Fig. 8—Schematic representation of the ultrasonic technique used to measure subcritical crack growth



Sec. 7 Fig. 9 —Test fixture used to monitor crack growth in the WOL type toughness specimen

SEC. 7 TABLE 3—RESULTS OF RISING-LOAD FRACTURE TOUGHNESS TESTING

<u>Material</u>	<u>Spec Ident</u>	<u>Test Temp °F</u>	<u>Yield Strength (ksi)</u>	<u>K_Q ksi$\sqrt{\text{in.}}$</u>	<u>$a_0 / \left(\frac{K_Q}{\sigma_{YS}} \right)^2$</u>	<u>$B / \left(\frac{K_Q}{\sigma_{YS}} \right)^2$</u>	<u>$a_0 / \left(\frac{K_Q}{\sigma_{YS}} \right)^2$</u>	<u>Fracture Toughness* K_{IC}, ksi$\sqrt{\text{in.}}$</u>
AISI 1020 Steel	2	75	32	55	1.35	1.43	—	—
	3	0	34	60	1.31	1.40	—	—
	4	-50	39	52	2.23	2.36	—	—
AISI 1045 Steel	2	75	37	63	1.43	1.50	—	—
	3	0	40	46	3.09	3.15	46	46
	4	25	39	46	2.95	3.27	—	—
AISI 1144 Steel	2	75	78	57	7.50	6.61	57	57
	3	0	78	52	8.88	9.22	52	52
	4	75	78	66	5.58	6.10	66	66
AISI 4140 Steel	2	0	82	52	10.04	10.03	52	52
	3	75	66	52	6.58	8.53	52	52
	4	75	66	58	5.25	6.46	58	58
7039-T6 Aluminum	2	75	57	19	35.90	52.90	19	19
	3	0	59	17	46.00	70.00	17	17
	4	75	57	Irregular Fatigue Precrack —				

* Satisfy Current Recommended Plane Strain Fracture Toughness Testing Criteria, a and $B \geq 2.5 (K_Q / \sigma_{YS})^2$

$$K_Q = Y \frac{P\sqrt{a}}{B W}$$

Where P is the applied load at the 5 per cent secant offset, "a" is the crack length measured from the centerline of loading, B is the specimen thickness, W is the specimen width measured from the centerline of loading to the back of the specimen (Figure 7) and Y is a compliance constant dependent upon crack length.

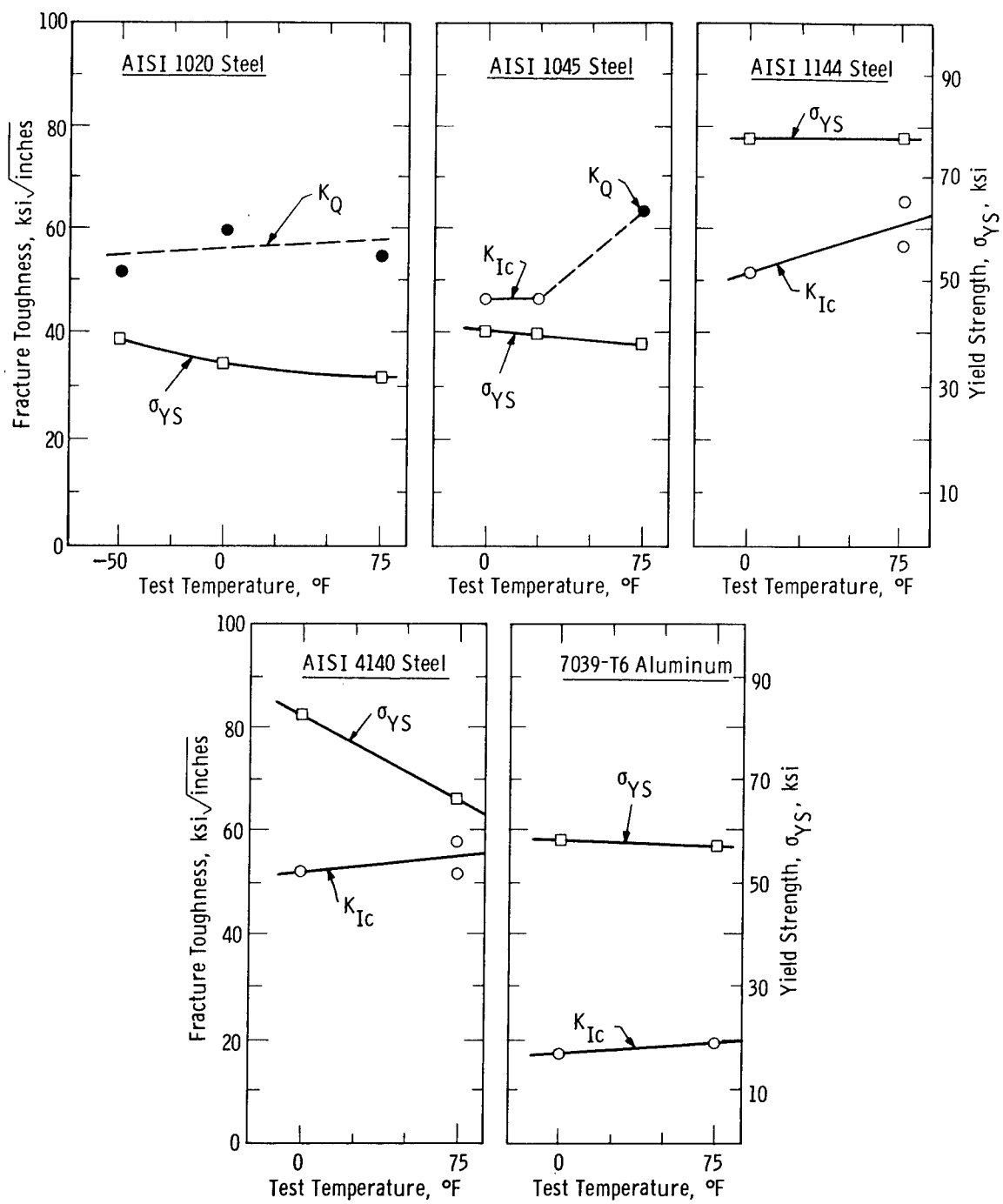
The stress intensity factors identified as K_{Ic} refer to the plane strain critical stress intensity factor and are representative of the actual inherent fracture toughness of the material. The reported K_{Ic} parameters were determined from an evaluation of the apparent toughness K_Q , in accordance with the current recommendations.^(1,2,8) Specifically, if K_Q satisfies the criteria:

$$\text{"a"} \text{ and } B \geq 2.5 \quad \left(\frac{K_Q}{\sigma_{YS}} \right)^2$$

as well as other requirements listed in references 1 and 8, K_Q is considered a valid measure of K_{Ic} . Note that for the AISI 1144 and 4140 steels and the 7039-T6 aluminum, valid K_{Ic} data were obtained at 0°F and 75°F. No valid K_{Ic} data were obtained for the AISI 1020 steel at the temperatures investigated. The tests involving AISI 1045 steel were valid at 0 and 25°F and invalid at 75°F. These observations are summarized graphically in Figure 10. The open points represent valid K_{Ic} measurements and the closed points nonvalid data. Figures 11 through 15 show the typical room temperature fracture appearances for each alloy investigated.

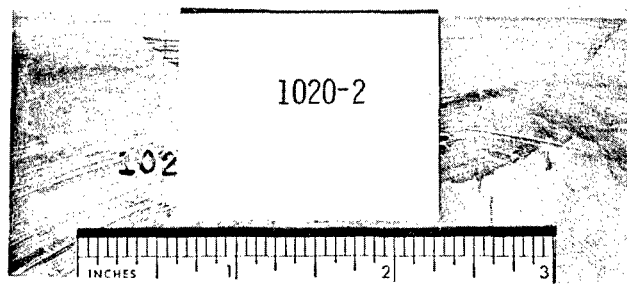
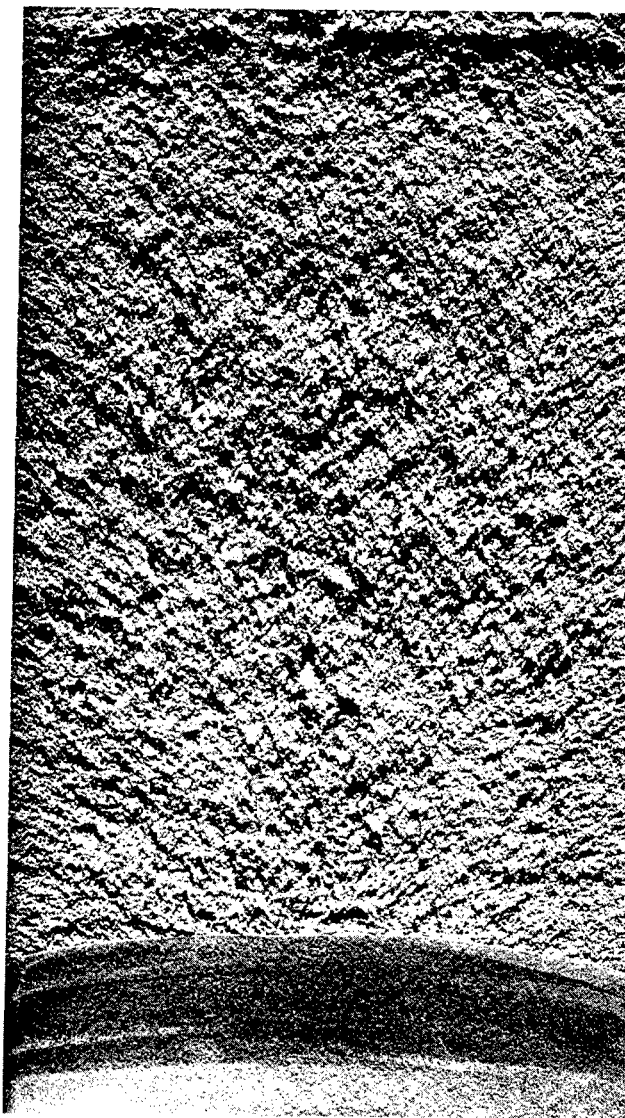
As indicated in Figures 13, 14 and 15, considerable difficulty was encountered in developing straight fatigue precracks in the AISI 1144 and 4140 steels and the 7039-T6 aluminum. Attempts were made to facilitate the development of straight fatigue precracks by extending the cracks

Curve 587298-B

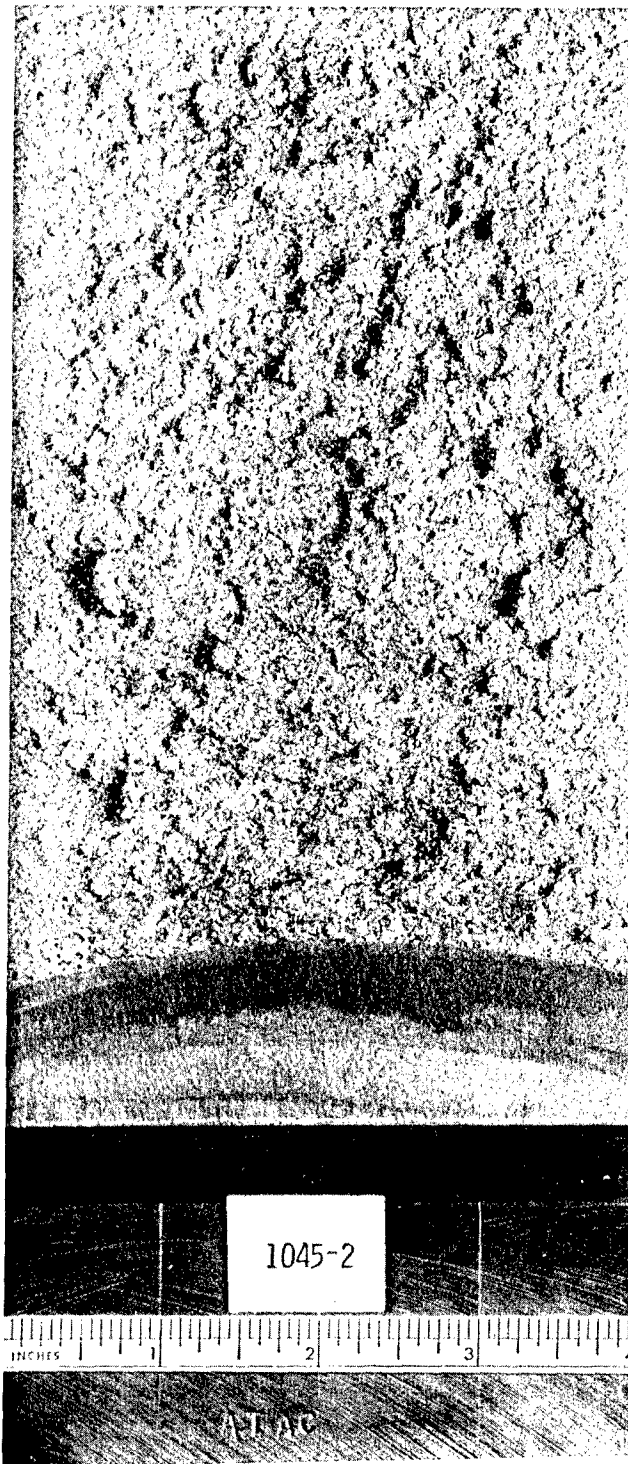


Open Points Refer to K_{IC} Values Where $a & B \geq 2.5 \left(\frac{K_Q}{\sigma_{YS}} \right)^2$
 Closed Points Refer to Apparent Toughness K_Q

Sec. 7 Fig. 10—Influence of temperature on toughness and yield strength for alloys investigated



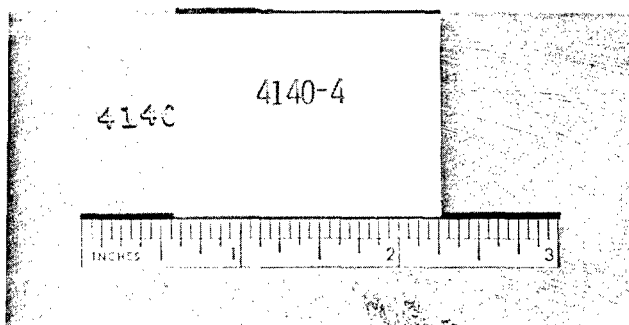
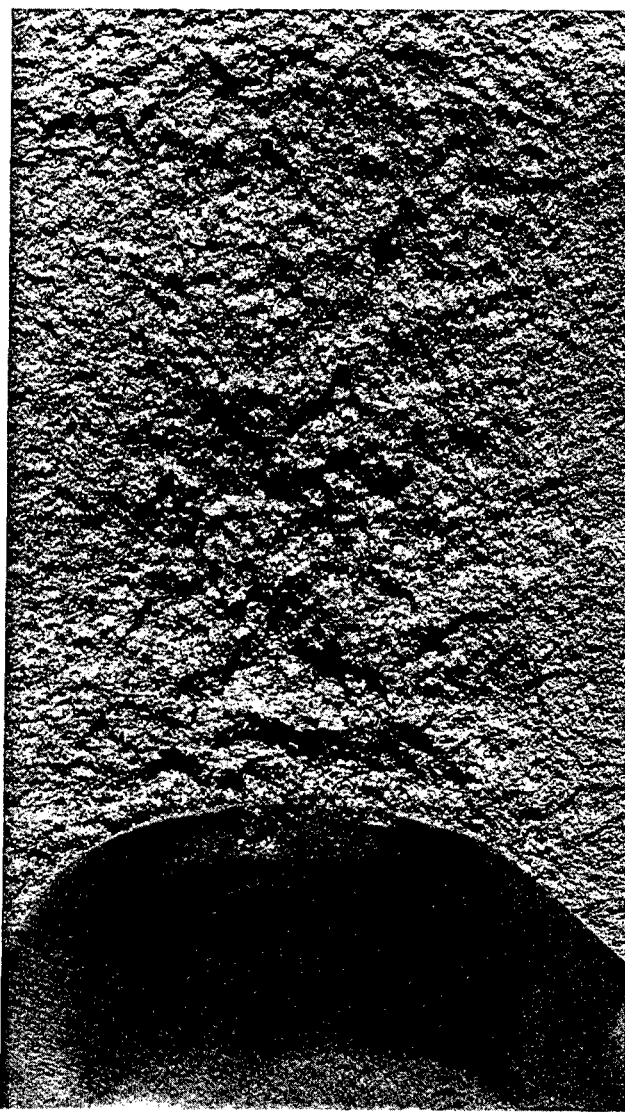
Sec. 7 Fig. 11-Room temperature rising load fracture appearance of AISI 1020 steel
(4T WOL Specimen)



Sec. 7 Fig. 12—Room temperature rising load fracture appearance of AISI 1045 steel
(4T WOL specimen)



Sec. 7 Fig. 13—Room temperature rising load fracture appearance of AISI 1144 steel
(4T WOL specimen)



Sec. 7 Fig. 14-Room temperature rising load fracture appearance of AISI 4140 steel
(4T WOL specimen)



Sec. 7 Fig. 15—Room temperature rising load fracture appearance of 7039-T6 aluminum
(4T WOL specimen)

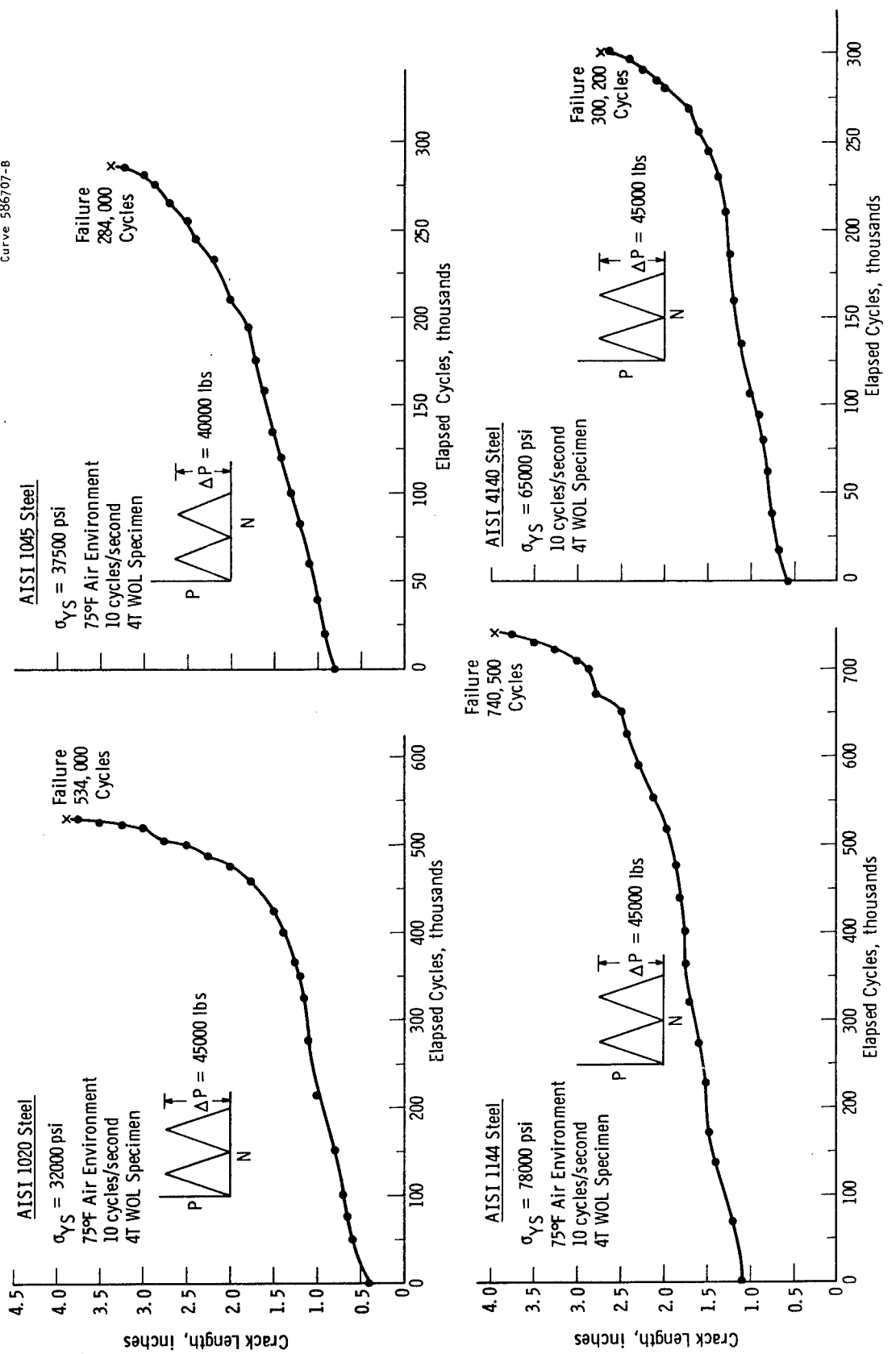
beyond the normal length requirements and also by electric-arc discharge machining the initial portion of the precrack. However, neither technique produced straight precracks. The 7039-T6 aluminum alloy was the most difficult to precrack. In fact, aluminum specimen 7039-T6-4 (Table 3) could not be precracked across the entire thickness and for this reason, the results of this test are not reported.

Examination of the ultrasonic crack growth measurement records indicated that no significant crack growth occurred prior to rapid fracture in any rising load test.

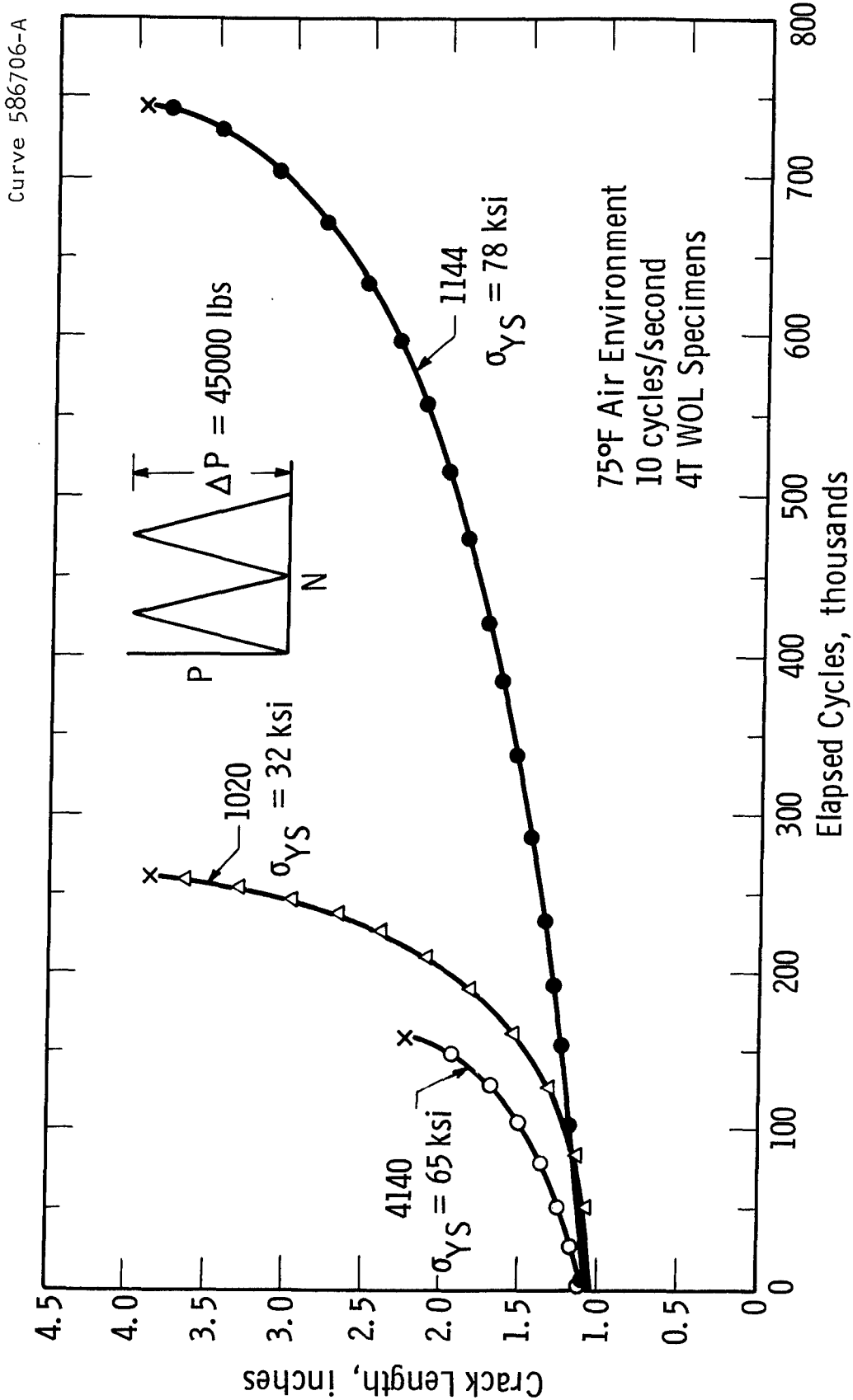
7.9.2 CYCLIC LOADING TESTS

The fatigue crack growth behavior observed for each ferrous alloy investigated is shown in Figure 16. Presented in this manner (crack length versus number of elapsed cycles), such data are comparable only if the tests were conducted under identical loading conditions. Specifically, the results to be compared must be generated with test specimens of the same size and geometry and at the same applied cyclic load. In addition, the data must be normalized to the same initial crack length. Figure 17 presents a comparison of the fatigue crack growth behavior observed for the AISI 1020, 1144 and 4140 steels normalized to an initial crack length of 1.1 in. The 1045 data are not included since testing was conducted at a cyclic load of 40,000 lbs. rather than 45,000 lbs. Note that the fatigue resistance of the AISI 1144 steel is much superior to that of the 1020 and 4140 steels. In addition, the fatigue resistance of the 1020 steel is somewhat superior to the 4140 steel. Also note that the higher relative toughnesses of the 1020 and 1144 steels over the 4140 alloy (Table 3) are reflected in Figure 17 by the longer crack length required to cause failure.

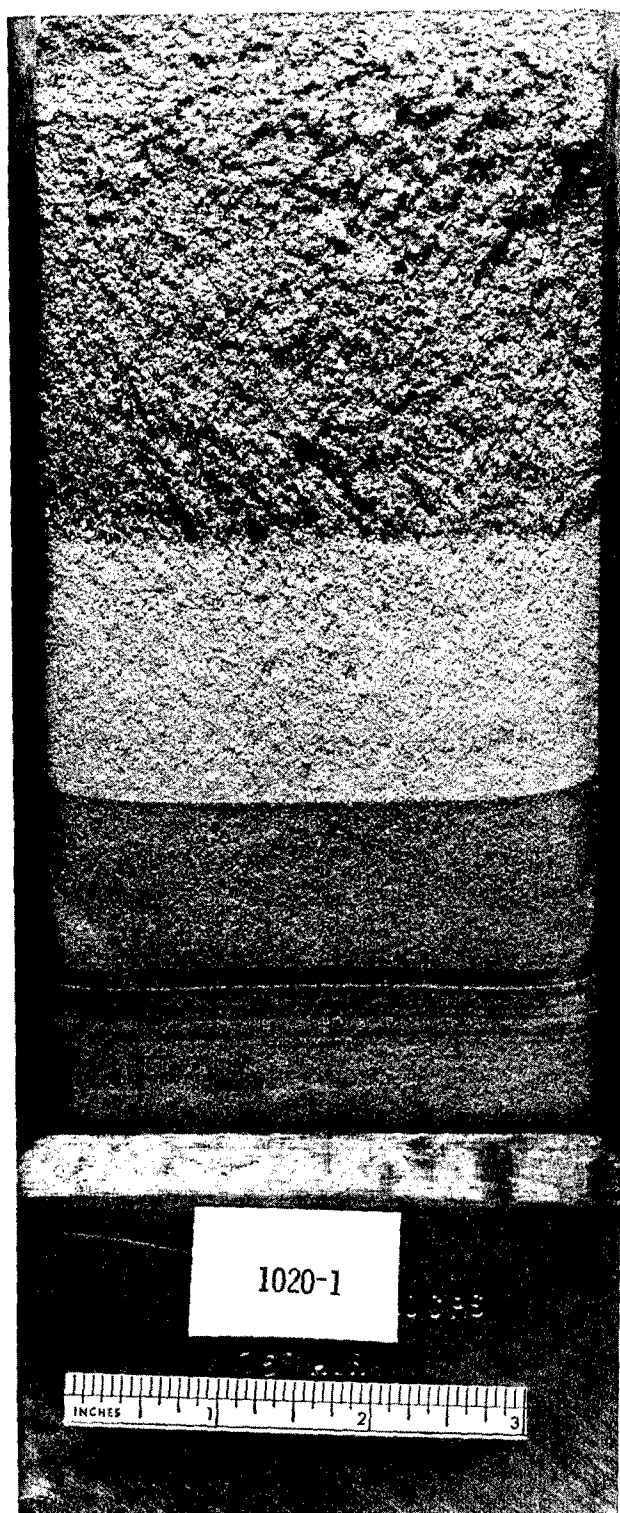
Figures 18 through 22 show the room temperature fracture appearances of the cyclic loading tests. With the exception of the 7039-T6 aluminum alloy, the crack fronts remained relatively straight throughout each test. However, as indicated in Figure 22, the fatigue crack front in the 7039-T6 aluminum alloy never became straight. As a



Sec. 7 Fig. 16—Fatigue crack growth behavior observed for various ferrous alloys



Sec. 7 Fig. 17—Comparison of the fatigue crack growth behavior observed for AISI 1020, 1144 and 4140 steels



Sec. 7 Fig. 18-Room temperature fatigue fracture appearance of AISI 1020 steel
(4T WOL Specimen)



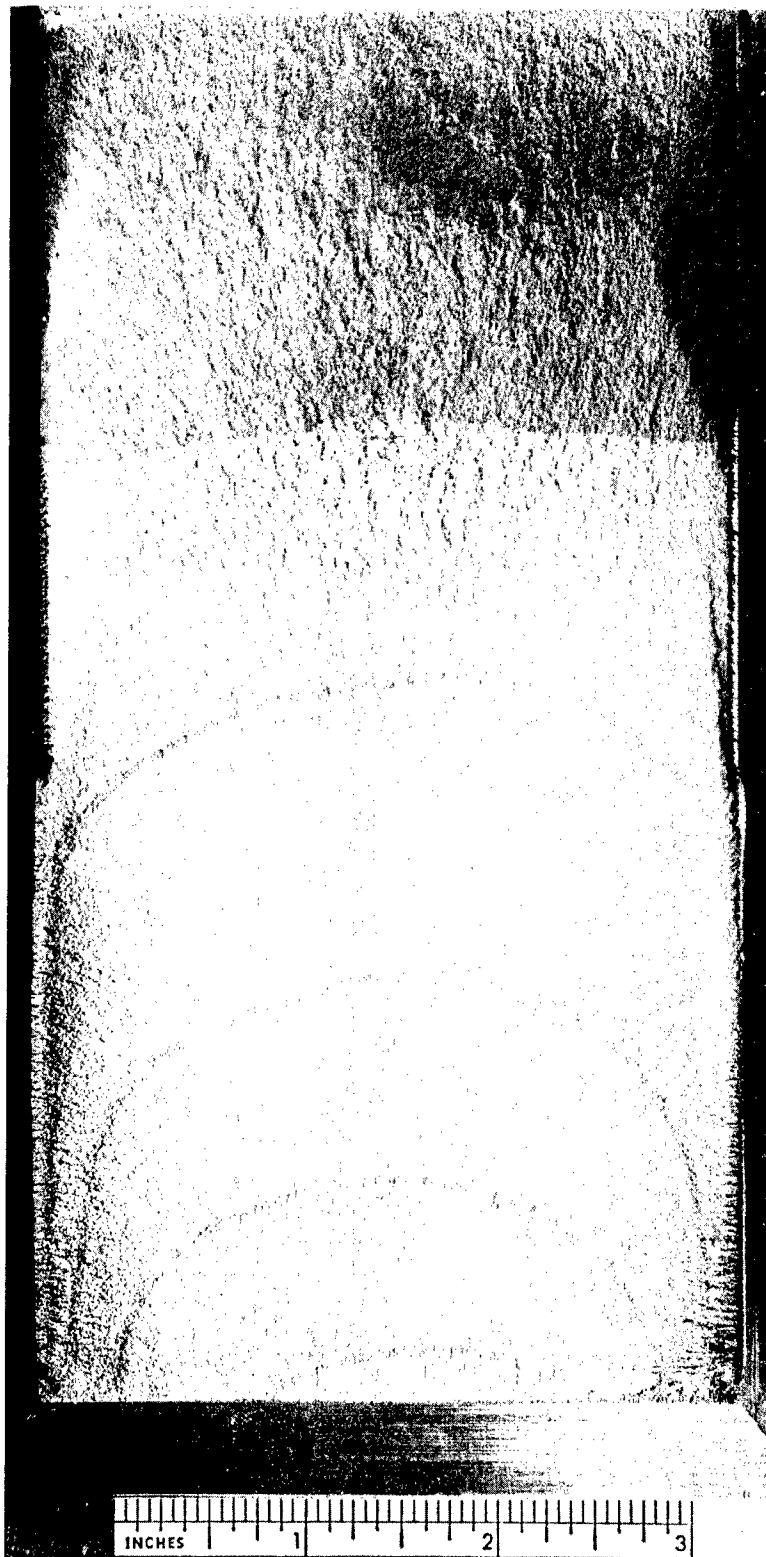
Sec. 7 Fig. 19—Room temperature fatigue fracture appearance of AISI 1045 steel
(4T WOL Specimen)



Sec. 7 Fig. 20—Room temperature fatigue fracture appearance of AISI 1144 steel
(4T WOL Specimen)



Sec. 7 Fig. 21—Room temperature fatigue fracture appearance of AISI 4140 steel
(4T WOL Specimen)



7039-1
75°F

Sec. 7 Fig. 22—Room temperature fatigue fracture appearance of 7039-T6 aluminum
(4T WOL Specimen)

result, the 7039-T6 test could not be properly analyzed since it was not possible to accurately compute the stress intensity factor at the tip of the irregular crack front. In addition, since the crack growth monitor only scans the center one inch length of the crack front, the crack length measurements were not sufficiently accurate. For the above reasons, the data generated with the "4T" WOL 7039-T6 aluminum specimen were not considered valid.

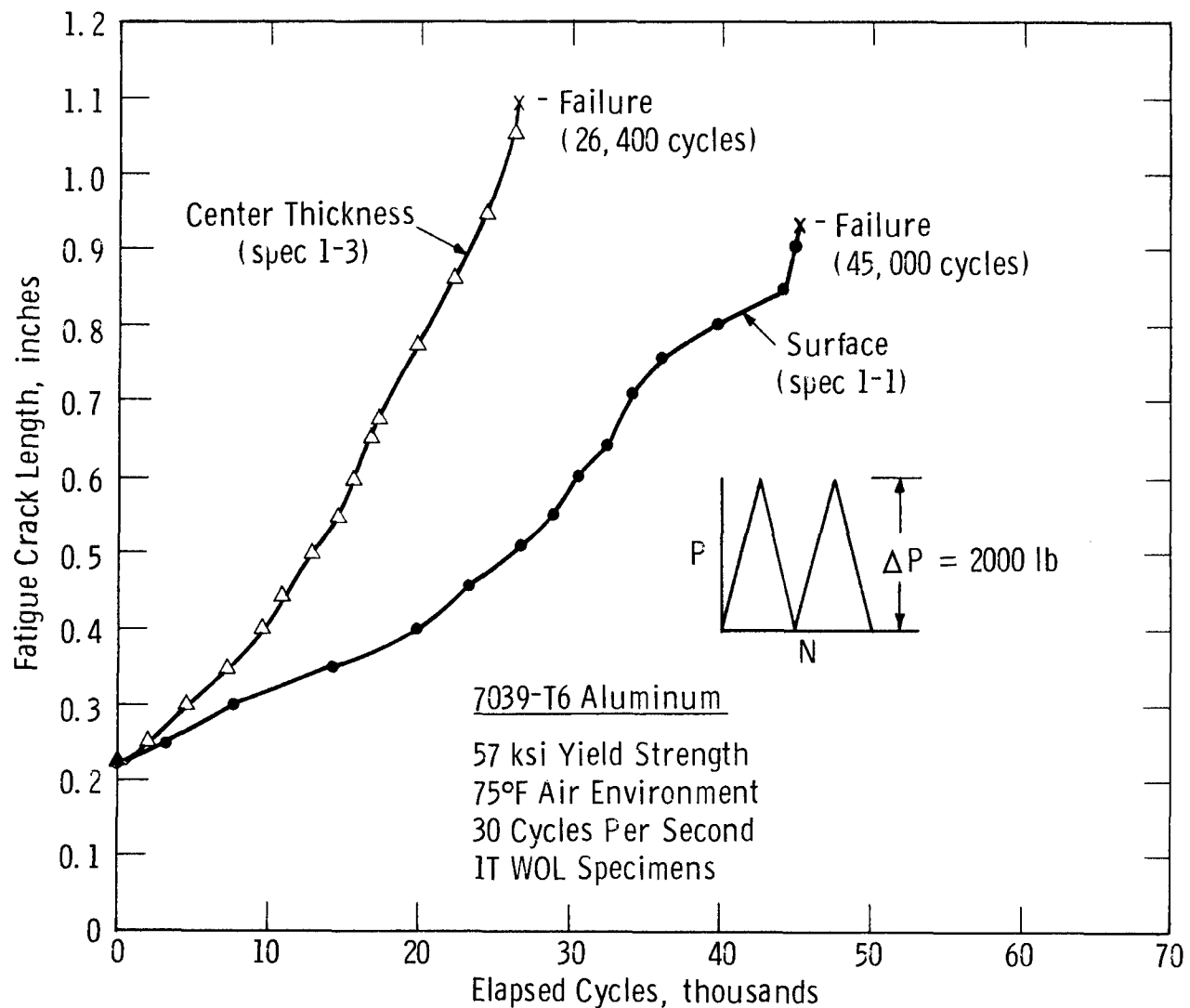
The concave nature of the fatigue crack front developed in the 7039-T6 aluminum alloy is indicative of a variation in mechanical properties through-the-thickness of the as received plate. From the appearance of the crack front (Figure 22), it is apparent that the resistance to fatigue crack propagation is much less near the center of the plate than near the surface. To further substantiate this observation, "1T" WOL specimens were prepared from the surface and center-thickness locations of the broken "4T" specimen. The crack length versus elapsed cycles data generated with these specimens are presented in Figure 23. Note that the fatigue resistance of the material near the surface of the 4 inch-thick forging is greater than that of the center-thickness material. In addition, the precracks developed in the 1 inch-thick specimens were perfectly straight.

In order to express the fatigue crack growth data in terms of a quantitative design parameter, the crack length versus elapsed cycles data were converted to the form of the change in stress intensity factor per cycle, ΔK , versus the crack growth rate, da/dN .

The fatigue crack growth rates were established by means of a computerized curve fitting analysis of the crack length versus number of elapsed cycles data.⁽¹⁰⁾ The mathematical model used to analyze the data has the general polynominal form of $a = b_0 + b_1 N^{x_0} + b_2 N^{x_1}$ where "a" is the crack length, N is the number of elapsed cycles, b_0 , b_1 etc. are constants and x_0 , x_1 etc. are exponents of increasing value.

The ΔK parameter associated with a specific crack growth rate was determined from the following expression:

Curve 587293-A



Sec. 7 Fig. 23—Effect of test specimen location on the fatigue behavior observed for 7039-T6 aluminum

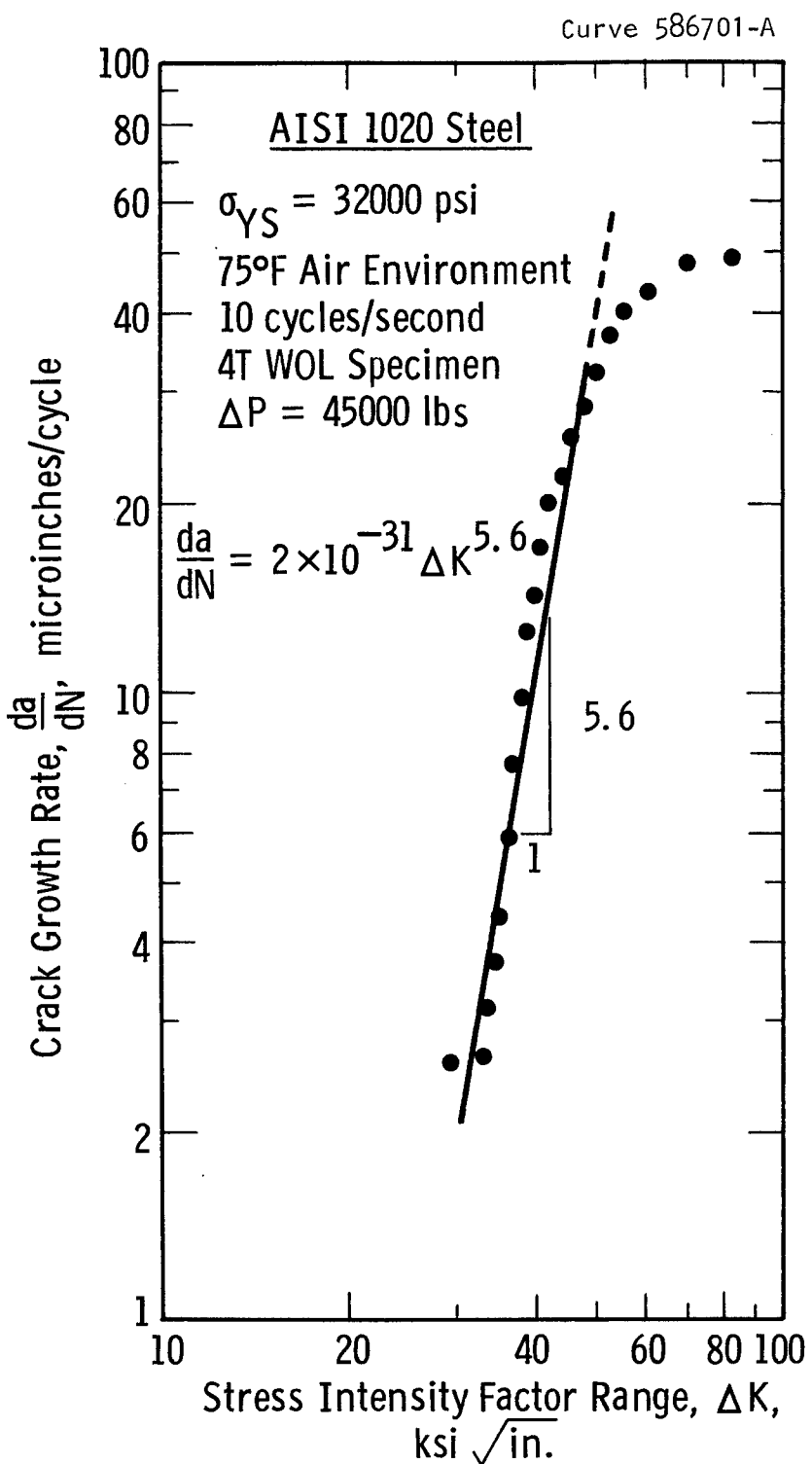
$$\Delta K = K_{\max} - K_{\min} = Y \frac{P_{\max} \sqrt{a}}{BW} - Y \frac{P_{\min} \sqrt{a}}{BW}$$

where "a" is the crack length corresponding to a particular crack growth rate, P_{\max} and P_{\min} are the maximum and minimum loads per cycle, B is the specimen thickness measured at the roots of the side notches, W is the specimen width (Figure 7) and Y is a compliance constant which depends upon crack length. Since the specimens were cycled from essentially zero load to P_{\max} , ΔK is equivalent to K_{\max} . Figures 24 to 28 present the crack growth rate versus stress intensity factor range for the five alloys investigated. Note that with the exception of a few data points at the low and high values of ΔK , the ferrous alloys exhibit a linear relationship between $\log da/dN$ versus $\log \Delta K$. The rate of change of $\log da/dN$ with $\log \Delta K$ for each steel investigated is expressed in terms of the slope given on the appropriate curve. Figure 29 presents a comparison of the $\frac{da}{dN}$ versus ΔK relationship obtained for the ferrous alloys. Note that the slopes vary from 4 for the 1045 steel to 10 for the 4140 steel.

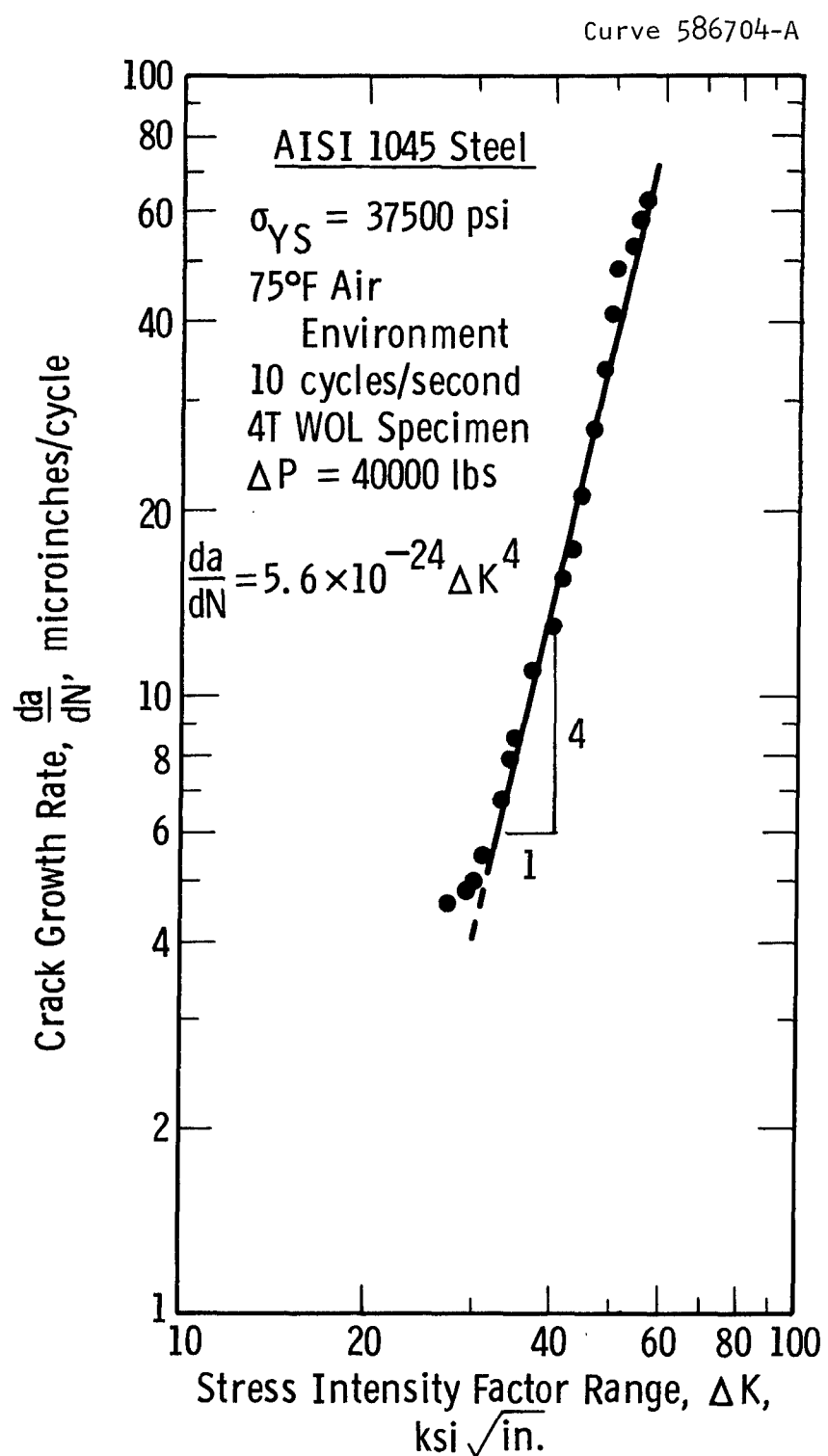
Since a straight line relationship between $\log da/dN$ versus $\log \Delta K$ was obtained for the ferrous alloys, these data can be expressed in terms of the generalized fatigue crack growth rate law developed by Paris.⁽¹¹⁾ This fatigue crack growth rate law has the form of

$$\frac{da}{dN} = C_o \Delta K^n$$

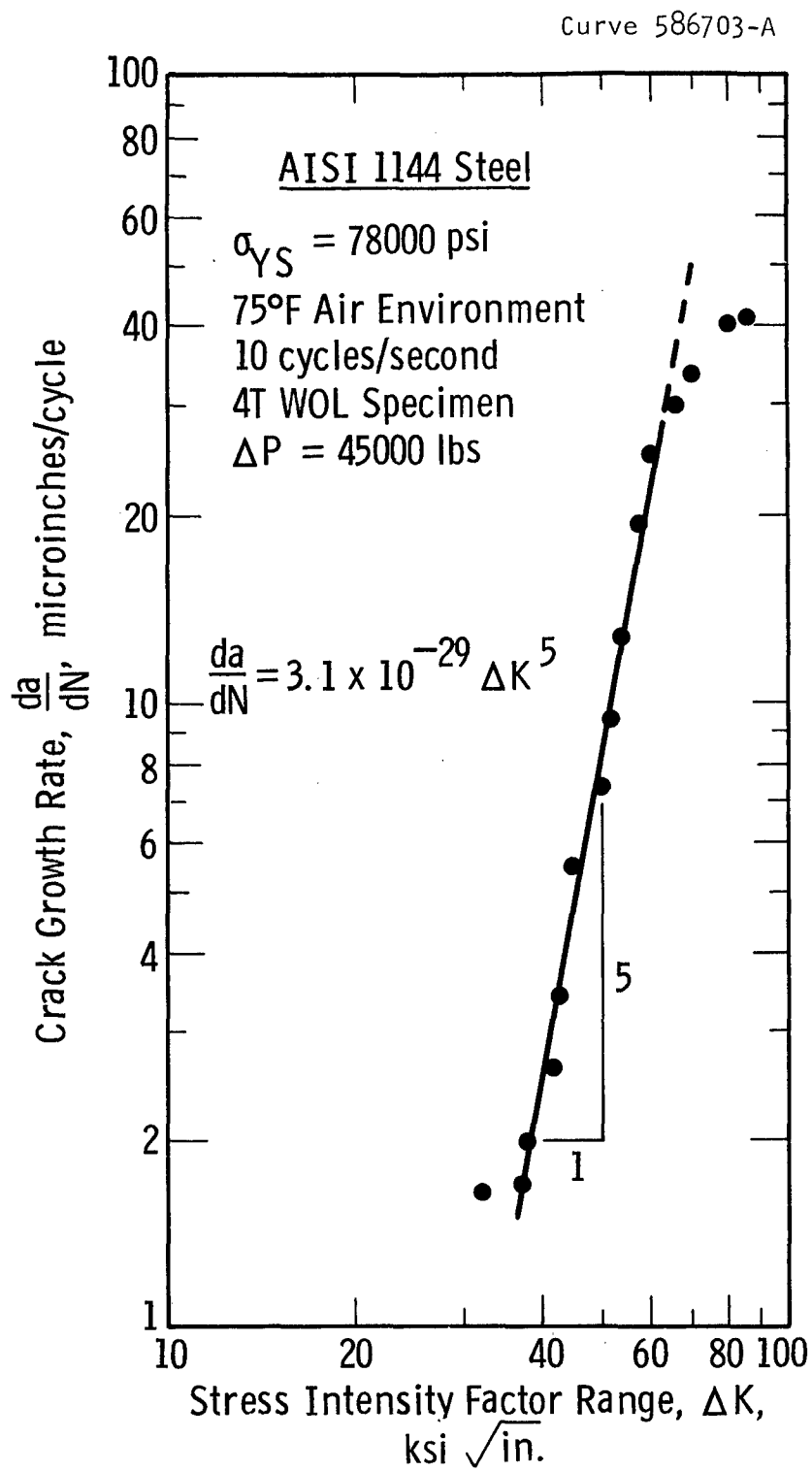
where n is the slope of the $\log \frac{da}{dN}$ versus $\log \Delta K$ curve and C_o is an empirical constant determined from the data. The values of the C_o parameters for the steel alloys are given on the appropriate crack growth rate curves and summarized in Figure 29. From a knowledge of the slope and C_o parameters it is possible to make life predictions under cyclic loading conditions. The use of such data in design will be demonstrated in an example problem.



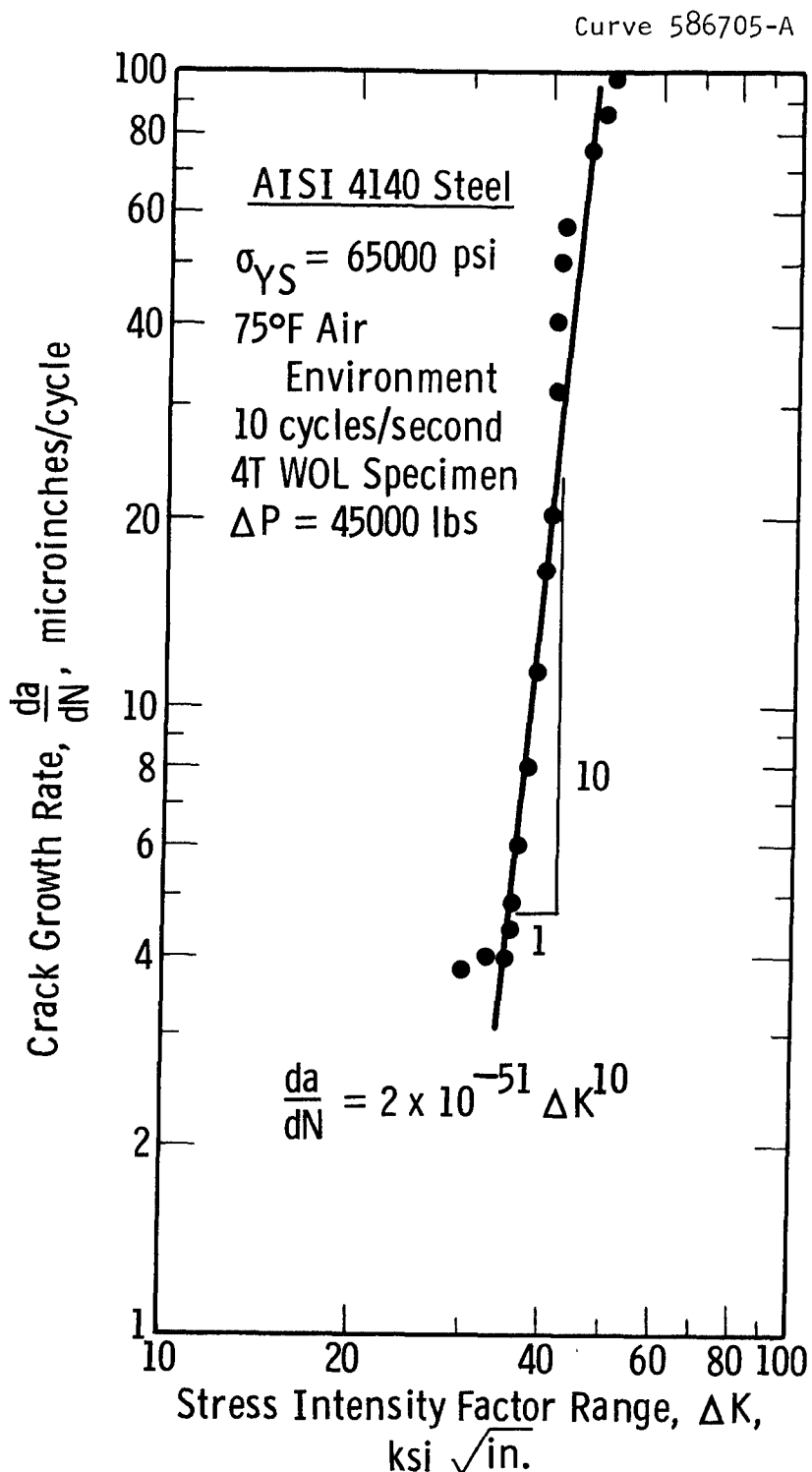
Sec. 7 Fig. 24—Fatigue crack growth rate versus stress intensity factor range for AISI 1020 steel



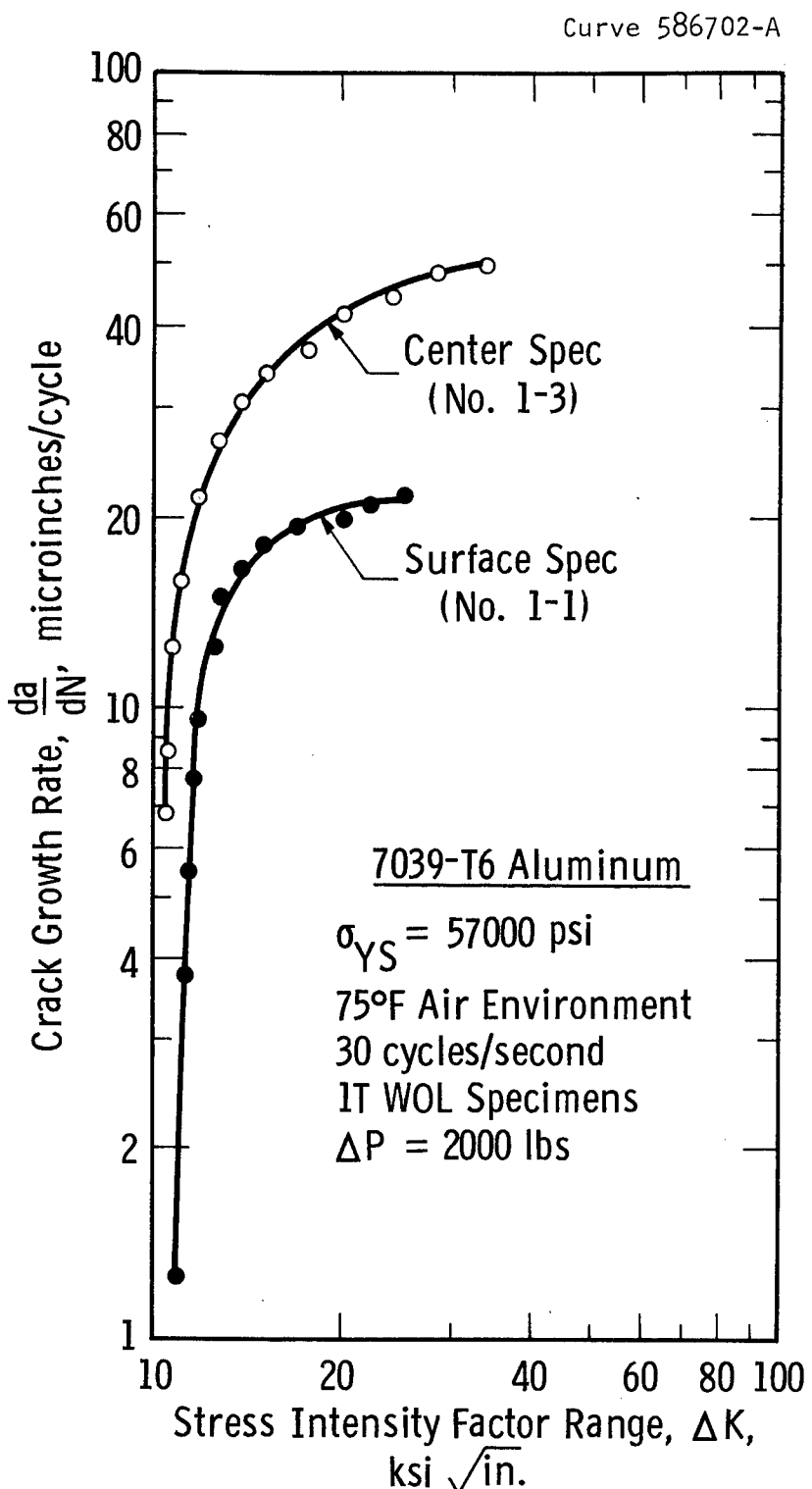
Sec. 7 Fig. 25—Fatigue crack growth rate versus stress intensity factor range for AISI 1045 steel



Sec. 7 Fig. 26—Fatigue crack growth rate versus stress intensity factor range for AISI 1144 steel

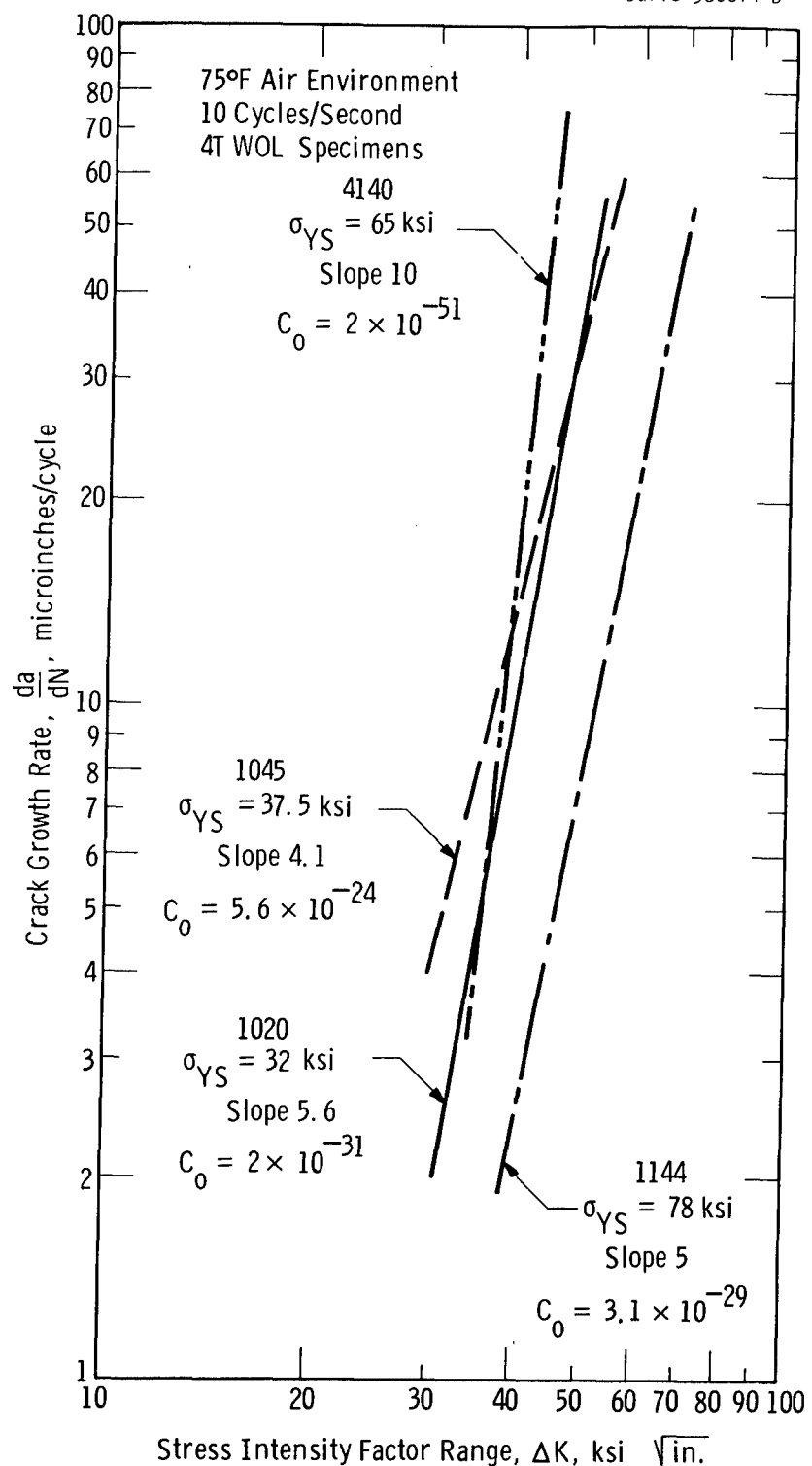


Sec. 7 Fig. 27 —Fatigue crack growth rate versus stress intensity factor range for AISI 4140 steel



Sec. 7 Fig. 28 –Fatigue crack growth rate versus stress intensity factor range for 7039-T6 aluminum

Curve 586614-B



Sec. 7 Fig. 29—Comparison of $\frac{da}{dN}$ vs ΔK for AISI 1020, 1045, 1144 and 4140 steels

The crack growth rate data established for the 7039-T6 aluminum alloy (Figure 28) are linear over a very narrow ΔK range (11 to 13 ksi $\sqrt{\text{in.}}$). Beyond this range the curve bends rapidly consequently, these data do not conform to the generalized crack growth rate law and cannot be interpreted as such. A numerical integration procedure must be used to employ these data in design calculations. The details of such a technique are available in the literature. (11)

Note that the rate of crack growth at a given ΔK level is substantially greater in the center-thickness aluminum specimen than in the surface specimen.

7.10 DISCUSSION

7.10.1 TEST MATERIALS

The results of the material characterization study indicate that with the exception of the AISI 4140 steel, no significant variations in through-the-thickness tensile properties were encountered (Figure 3). Similar results were obtained for the through-the-thickness impact tests (Figure 4). However, no significant variation in impact data was encountered for the 4140 steel which did show a variation in tensile properties. The slight variations in through-the-thickness properties are to be expected for these alloys when supplied in 4 inch thick sections. The results of the microstructure examination (Figures 5 and 6) confirm the results of the tensile and impact testing. Specifically, no significant variation in microstructure was observed between the near surface and center-thickness portions of the "as-received" material.

Although the through-the-thickness properties of the ferrous alloys involved in this investigation were quite uniform, the Charpy impact properties (summarized in Figure 2) were all on the low side of the expected range. Existing Charpy impact data indicate that for the ferrous alloys studied in this investigation impact energies in excess of 15 ft-lbs. (12-14) are feasible when section sizes permit the development of more optimum microstructures (Martensitic, Bainitic, etc.) by the quench and temper operation.

For the case of the AISI 1144 steel forgings, the low room temperature impact properties (5 ft-lbs.) are consistent with the low reduction in area and elongation values reported in Table 3 (6.9 and 5.2 per cent for the reduction in area and elongation, respectively). In the case of both 1144 and 4140 steels, the low impact properties obtained are considered representative of that expected for the metallurgical structures produced. Examination of typical hardenability data for such steels clearly shows that for the section sizes involved the hardening heat treatments employed could not produce any more favorable microstructure.

7.10.2 TOUGHNESS TESTING

With the exception of the 1020 carbon steel, valid plane strain fracture toughness data were obtained within the temperature range of interest for each alloy investigated. Consequently, these results indicate that brittle fracture of low-strength alloys is in fact a possibility under the proper loading conditions and, existing linear elastic fracture mechanics concepts can be used to measure the brittle fracture potential of such alloys.

The actual K_{Ic} numbers presented in Table 3 were judged valid on the basis of the primary requirement that the specimen thickness, B , be equal to or greater than 2.5 times the ratio of apparent toughness to yield strength quantity squared. However, an additional requirement that is of particular concern to the testing conducted in this investigation involves the straightness of the fatigue precrack. The currently accepted criterion for precrack straightness requires that the crack length (as measured from the center-line of loading) at the center and quarter-thickness locations be within 5 per cent of the numerical average of these crack lengths.⁽⁸⁾ In addition, the crack length at the surface

of the specimen should be within 10-per cent of this average. Examination of the fractured test specimen shown in Figures 11 to 15 clearly indicate that the 1020 and 1045 steels satisfy the precrack straightness criteria. However, the 4140 steel and 7039-T6 aluminum alloy fail to satisfy the 10-per cent surface crack criterion and the 1144 steel, although it satisfies the crack straightness criteria, is of such an irregular nature that the applicability of the straightness criteria is questionable. The requirement that the surface crack length be within 10-per cent of the average crack length based upon center and quarter thickness measurements is an arbitrary criterion for which no substantiating experimental data exist. If we assume that this is too stringent a requirement in view of the small portion of the actual crack front influenced by the surface of the specimen, the K_{Ic} data reported for the 4140 steel and 7039-T6 aluminum can be considered a valid measure of the materials inherent toughness. On the other hand, if we assume that the shorter portion of the crack front near the specimen surfaces serves to retard fracture, then the reported K_{Ic} value for the 4140 steel and 7039-T6 aluminum must be considered overestimates of the actual toughness. We believe that the first assumption is more realistic however, this problem can only be resolved by conducting additional tests with specimens having straight crack fronts.

With regard to the irregular precrack fronts encountered in the 1144 alloy steel, additional testing is also required to substantiate the applicability of the existing straightness criteria to such a precrack.

It was noted earlier, that an irregular fatigue precrack front is generally characteristic of a material which exhibits a significant variation in through-the-thickness properties. Note, however, that this is not the case for the 1144 steel or for that matter, the other alloys studied. Apparently, the parameter which controls the shape of the precrack is not always reflected in the conventional through-the-thickness properties.

The results of the fracture toughness testing portion of this investigation show that 4 inch thick sections of the 1144 and

4140 steels and the 7039-T6 aluminum satisfy plane strain conditions at room temperature. Expressed in another way, the results show that in the presence of a defect, 4 inch thick sections of these alloys are subject to brittle failure at room temperature. Since many applications which use these alloys involve section sizes less than 4 inches thick, it becomes necessary to establish the section size above which brittle fracture is possible and fracture mechanics concepts are applicable. This minimum section size can be determined by solving the specimen size criterion formula [$B = 2.5 \left(\frac{K_Q}{\sigma_{YS}} \right)^2$] for B when K_Q equals the material's K_{Ic} . For the case of the 1020 and 1045 steels, which do not exhibit plane strain conditions at room temperature, the minimum section size required to develop plane strain loading can be estimated by using the apparent toughness, K_Q in the above equation.

Using the K_Q value to predict the section size necessary for the development of plane strain conditions provides only a very rough estimate and must be qualified as such. The minimum section sizes necessary to develop plane strain conditions at room temperature for the alloys investigated are given below:

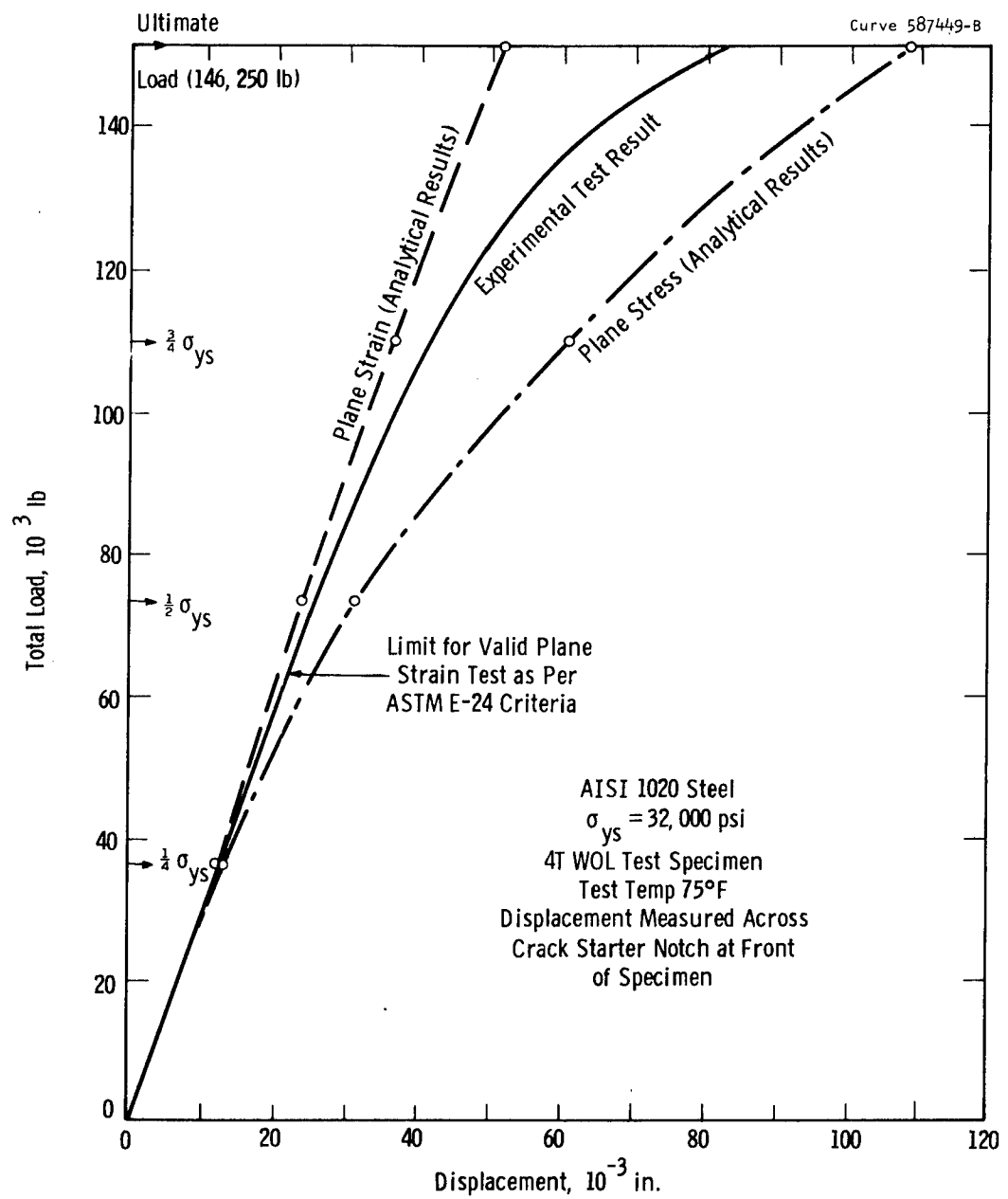
Material	Relative Toughness $\frac{K_{Ic}}{\sigma_{YS}}$	Minimum Thickness for Plane Strain, in.
1020 steel	1.72*	7.50*
1045 steel	1.70*	7.25*
1144 steel	0.77	1.48
4140 steel	0.83	1.72
7039-T6 aluminum	0.33	0.27

* Approximate values based upon K_Q

The thickness values presented above also represent the minimum thickness of the respective alloys for which existing linear elastic fracture mechanics design concepts are applicable. For applications involving these materials in section sizes less than the minimum for plane strain conditions, significant plastic yielding

accompanies failure in the presence of a flaw and elastic-plastic analyses are required to establish adequate failure criteria. Presently, such elastic-plastic fracture criteria do not exist. As a first approach to the development of an elastic-plastic fracture analysis design concept, the Stress Analysis Section of the Mechanics Department at the Westinghouse Research Laboratories has developed a finite element computer program which can predict the displacement in the vicinity of a crack-like defect under known loading conditions. (15, 16, 17, 18) Since the displacements in turn, are directly related to the stresses, this program provides a technique for analyzing crack tip stress conditions and may eventually lead to a practical design concept. In order to confirm the analytical displacement predictions, the 1020 specimen tested at room temperature was instrumented for displacement measurements on each side near the crack tip as well as across the crack-starter notch. The analytical technique accurately predicted the range of displacements for both plane stress and plane strain conditions across the crack-starter notch as shown in Figure 30, but not those in the vicinity of the crack tip. It was later found that as the result of experimental error, the displacement measurements in the vicinity of the crack tip were not correct. Therefore, the results of the experiment were inconclusive relative to crack tip displacements. Similar experiments involving other low-strength alloys yield very promising results and will be reported shortly. (10)

The limit of allowable deviation from linearity of load-displacement behavior for valid plane strain fracture toughness testing (as per current ASTM E-24 recommendations, references 2 and 8) is identified on the experimental curve in Figure 30. Note that up to this point, the experimental curve deviates little from the load-displacement behavior predicted for plane strain conditions. This observation provides additional evidence that the existing criteria for plane strain fracture toughness testing are realistic.



Sec. 7 Fig. 30-Analytical and experimental load-displacement curves for AISI 1020 steel

7.10.3 CYCLIC LOADING (FATIGUE) TESTS

The presentation of fatigue crack growth data in terms of crack length versus number of elapsed cycles can provide a valuable basis for the comparison of fatigue properties and the effect of various test parameters. For example, Figure 17 clearly indicates the variation in fatigue cracking resistance of 4140, 1020 and 1144 steels and Figure 23 demonstrates the superior fatigue cracking resistance of the material near the surface of the 7039-T6 aluminum forging as compared to the material in the center. However, since specimen size and geometry and applied load as well as other parameters influence the crack length versus elapsed cycles behavior, such data are suitable for comparison only if all data to be compared are generated under identical loading conditions. Consequently, crack length versus elapsed cycles data are of a qualitative nature and cannot be applied directly to engineering design considerations involving loading conditions other than those under which the data were generated. Since the stress intensity concept of fracture mechanics incorporates the applied stress and flaw size (crack length) into a single-term parameter which is independent of specimen size and geometry, the stress intensity approach to fatigue provides a quantitative design technique. Specifically, fatigue data presented in terms of the rate of crack growth, da/dN , versus the change in crack tip stress intensity, ΔK , yield design data applicable to a wide variety of different loading conditions.⁽¹¹⁾ In addition, da/dN versus ΔK data provide a unique parameter which can be used to compare fatigue crack growth data generated under various laboratory conditions.

The deviation from a linear relationship between $\log da/dN$ versus $\log \Delta K$ observed for each alloy at high or low or both levels of ΔK has been observed for several other structural alloys.⁽¹⁹⁾ This behavior is attributed to intermittent rather than continuous crack growth. At the higher levels of ΔK the intermittent crack growth is related to the high degree of plastic yielding which tends to retard crack growth. Electron microscopic examination of fatigue fractures developed at high ΔK levels indicate the presence of a

considerable amount of dimpled rupture and the distinct absence of well formed striations. This observation indicates that at high ΔK levels, the crack propagates in bursts but occasionally grows in regular steps which result in the formation of striations. At present, the intermittent crack growth observed at the lower ΔK levels cannot be explained.

Although significant from an academic point of view, the deviation from a straight line relationship at the higher ΔK levels is not of practical importance since the ΔK levels approach the K_{Ic} of the material and structures would not knowingly be permitted to operate at such high K levels. In addition, the projected slope yields a faster growth rate than actually observed resulting in a conservative estimate of growth rate.

At the lower values of ΔK , it appears that a lower limit of crack growth rate exists. This behavior can be confirmed only by conducting additional crack growth rate testing at lower values of ΔK than those involved in this investigation. Since the crack growth rates observed at the lower ΔK levels exceed the rates projected by the linear slope it is important that the lower limit of crack growth rate be taken into account. Particularly, since component life data predicted from the generalized crack growth rate law at the lower ΔK levels will be an overestimate of actual performance.

Comparison of the crack growth rate data established for the ferrous alloys studied in this investigation (Figure 29) indicates that the da/dN versus ΔK relationship is independent of material yield strength. Specifically, the materials with the higher yield strengths, 1144 ($\sigma_{YS} = 78$ ksi) and 4140 ($\sigma_{YS} = 65$ ksi) steels, exhibit the slowest and fastest crack growth behavior, respectively. The lowest strength steel (AISI 1020, $\sigma_{YS} = 32$ ksi) yields an intermediate growth rate. Although these results clearly demonstrate the independent nature of fatigue behavior with respect to material yield strength, it has been shown that for a given alloy heat treated to various strength levels,

the higher strength levels yield the lower growth rates. Therefore, it is apparent that additional factors aside from yield strength alone determine the fatigue properties of structural alloys.

Correlation of the rate of fatigue crack growth with the relative toughness of the alloys also indicates that the fatigue properties are independent of toughness.

7.11 ACCURACY OF RESULTS

The inherent fracture toughness characteristics as well as the fatigue crack growth properties of a given alloy are known to be strongly dependent upon the metallurgical history of the material.⁽⁹⁾ Specifically, the chemistry, melting practice, microstructure, fabrication technique and heat treatment are among the more significant factors which ultimately determine the fracture resistance properties of an alloy. Consequently, the limited amount of data generated in this investigation cannot arbitrarily be applied to similar heats of the same alloys. Considerably more data for a statistically accurate sampling of the respective materials are required to adequately characterize these materials and ultimately provide information suitable for design. However, the results of this investigation do clearly demonstrate that existing fracture mechanics concepts are applicable to relatively low-strength, high to intermediate-toughness materials and they provide a here-to-fore nonexistent basis for the level of fracture resistance that we can expect for some commonly used structural alloys.

7.12 EXAMPLE PROBLEMS

In order to demonstrate the use of fracture mechanics concepts in design, two hypothetical problems have been selected and the pertinent considerations and computations described in detail. The first example involves a four point loaded beam in pure bending and the second, a thin-walled pressure vessel. In the first example, the problem is to select the most desirable of two materials for the proposed operational requirements. Material selection will be limited to the AISI 1144 and 4140

quenched and tempered steels involved in the experimental portion of this investigation. The second example involves a 1144 steel pressure vessel in which a crack has been detected and it is necessary to calculate the remaining useful life. Both problems assume room temperature loading conditions in an inert environment. The pertinent room temperature properties for the two steels involved in the examples are given below:

Material	Yield Strength, psi	Tensile Strength, psi	K_{Ic} psi $\sqrt{\text{in}}$	Fatigue Crack Growth Data
AISI 1144 steel	78,000	122,000	62,000	Fig. 26
AISI 4140 steel	65,000	101,000	56,000	Fig. 27

It will be assumed that both steels are supplied to a guaranteed minimum yield strength of 60,000 psi and this value will be used for all design considerations. The solutions to both problems involve four general areas of consideration:

- a) initial design
- b) computation of critical flaw size
- c) calculation of cyclic life
- d) development of inspection criteria and safety factors

The first example also includes a material selection consideration. Each of the above considerations are described in detail.

7.12.1 EXAMPLE PROBLEM NO. 1 - BEAM IN BENDING

a. Operational Requirements

The following requirements are involved in this hypothetical example:

1. Supply a beam of rectangular cross-section to be loaded under four point bending (pure bending) to a maximum load of 26,800 lbs.
2. Dimensional requirements dictate that the beam be 4" high with a major and minor span of 8 feet and 6 feet, respectively.

3. The beam is to be subjected to zero to maximum load cyclic loading at 75°F in an inert environment.

4. The minimum cyclic life requirement is 100,000 cycles.

5. The maximum applied nominal stress is not to exceed 1/2 the material yield strength. For this example, the maximum applied stress requirement is equivalent for both materials i.e., 30,000 psi.

b. Initial Design Considerations

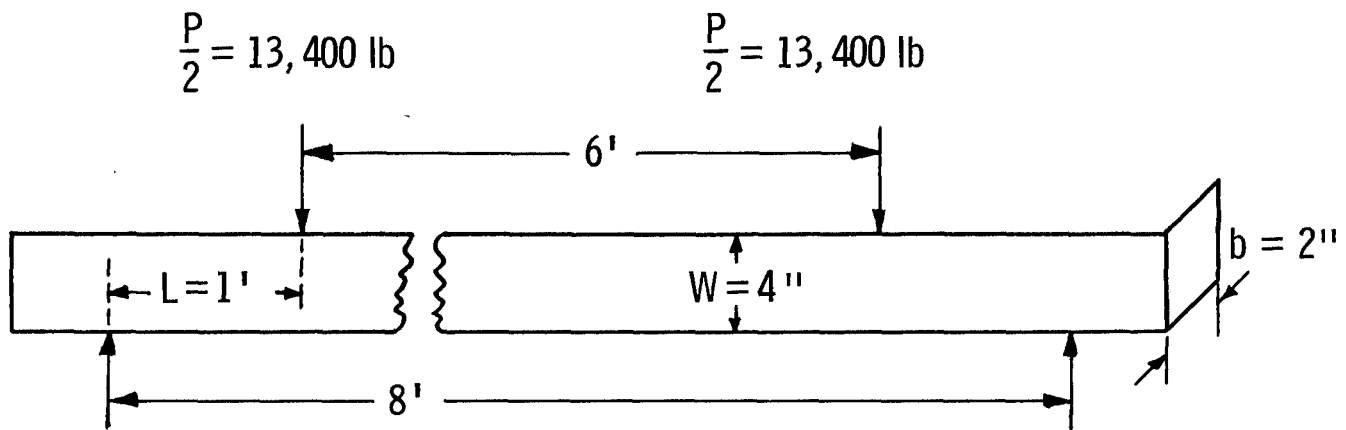
The application described above essentially involves a simple beam in pure bending and can be analyzed accordingly with the bending moment and flexure equations. The bending moment M is equal to half the applied load times the moment arm L or $M = \frac{PL}{2}$. For the proposed problem, P equals 26,800 lbs. and L equals 12" (half the difference between the major and minor spans) resulting in a bending moment of 161,000 in-lbs. In order to satisfy the maximum nominal stress requirement of 30,000 psi, we can compute the beam thickness b from the flexure equation $\sigma = \frac{M}{z}$ where σ is the maximum outer fiber tension stress, M is the bending moment (161,000 in-lbs.) and z is the rectangular section modulus ($z = \frac{bw^2}{6}$, w equals the beam height, 4 in.). Solving for b yields a beam thickness requirement of 2 in. Figure 31 illustrates the loading conditions and pertinent initial design equations.

c. Calculation of Critical Flaw Size

Since it is generally realistic to assume that all structures contain discontinuities of some type it is necessary to establish the critical defect size which will result in failure. For the problem at hand, we will limit our consideration of defect sizes to edge cracks between the minor span where the tensile stresses are at the maximum. For the case of pure bending, the outer fiber tensile stresses are essentially constant within the minor span, as a result, our considerations will be applicable to edge cracks at any location within the minor span.

In order to compute the critical flaw size in terms of fracture mechanics, we must first establish if linear elastic fracture mechanics

Dwg. 857A562



$$\text{Bending Moment, } M = \frac{PL}{2} = 161,000 \text{ in.-lb}$$

$$\text{Outer Fiber Tension Stress, } \sigma = \frac{M}{Z} = 30,000 \text{ psi}$$

$$\text{Rectangular Section Modulus, } Z = \frac{bW^2}{6}$$

Sec. 7 Fig. 31—Loading conditions for example problem No. 1

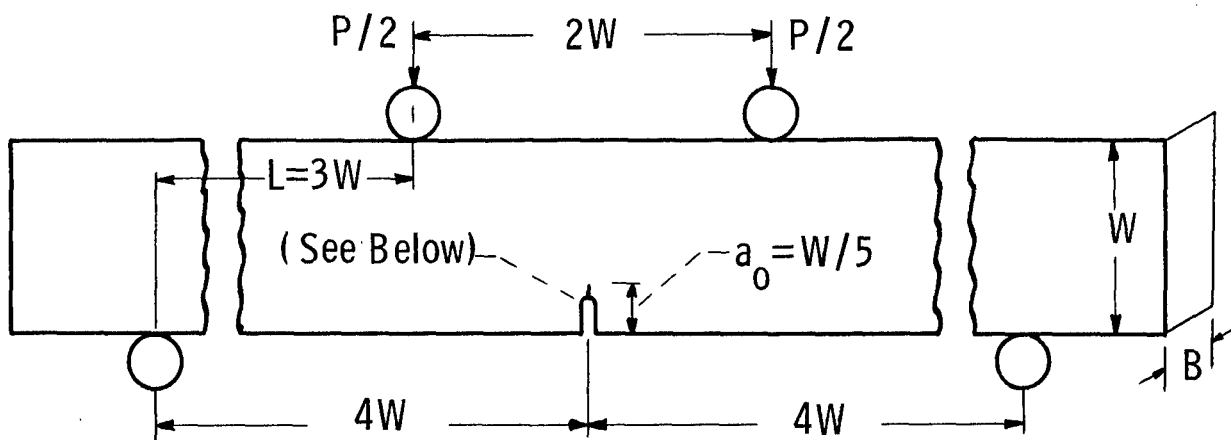
concepts are applicable to the loading conditions of interest. To do this we must know the K_{Ic} and yield strength for the material at the minimum operating temperature. We then solve the specimen size criteria formula [$B = 2.5 (K_{Ic}/\sigma_{YS})^2$] for the minimum thickness for which plane strain conditions prevail. The minimum thickness for plane strain conditions at room temperature for the 1144 and 4140 steels are 1.48 and 1.72 inches, respectively. Since our problem involves a 2 inch thick beam, fracture mechanics concepts are applicable and we can proceed.

Once it has been established that fracture mechanics concepts are applicable to the problem, we must then have available an adequate stress analysis of the loading conditions and an accurate stress intensity expression which relates flaw size and applied stress to the stress intensity factor.

An adequate stress analysis is available from our initial design considerations and valid K_{Ic} data were obtained from the experimental portion of this investigation. In addition, an accurate stress intensity expression is available for the loading conditions of interest. Figure 32 presents the appropriate expression along with an illustration of the conditions for which the expression is applicable. This expression was developed specifically for use with the four-point loaded notched-bend fracture toughness specimen and consequently, a graphical solution of the complex polynominal portion of the equation is readily available in the literature.^(1,9) Figure 33 presents the graphical solution for the case of pure bending (four point loading) as well as for two conditions of three point loading. Using the graph in Figure 33 the stress intensity expression becomes:

$$K_I = \frac{6Ma}{BW^2} Y^{1/2}$$

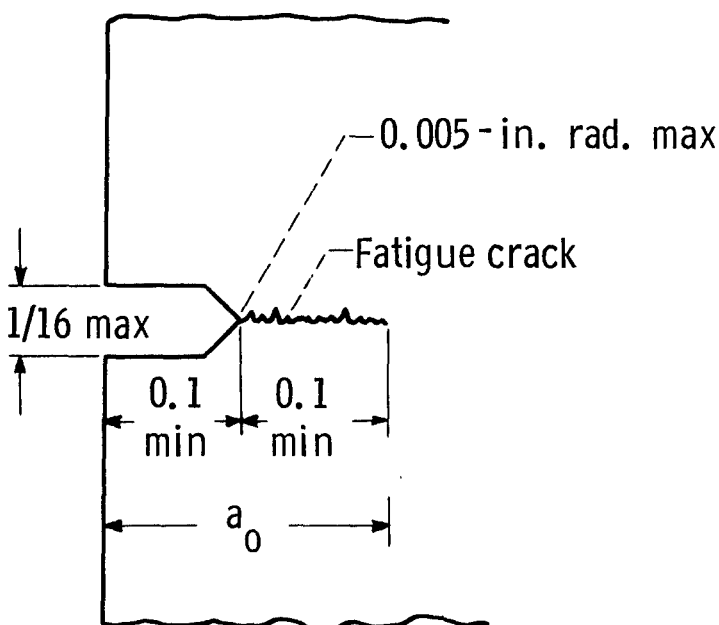
where Y is a function of a/W . This commonly used form of the K -expression is fine for use with test specimens where the crack size, "a" is a known parameter and K_I is to be determined. However, for the case of a



$$K_I = \frac{6M}{B} \frac{a^{1/2}}{W^2} \left[1.99 - 2.47 \left(\frac{a}{W} \right) + 12.97 \left(\frac{a}{W} \right)^2 - 23.17 \left(\frac{a}{W} \right)^3 + 24.80 \left(\frac{a}{W} \right)^4 \right]$$

for $\frac{a}{W} = 0$ to 0.6

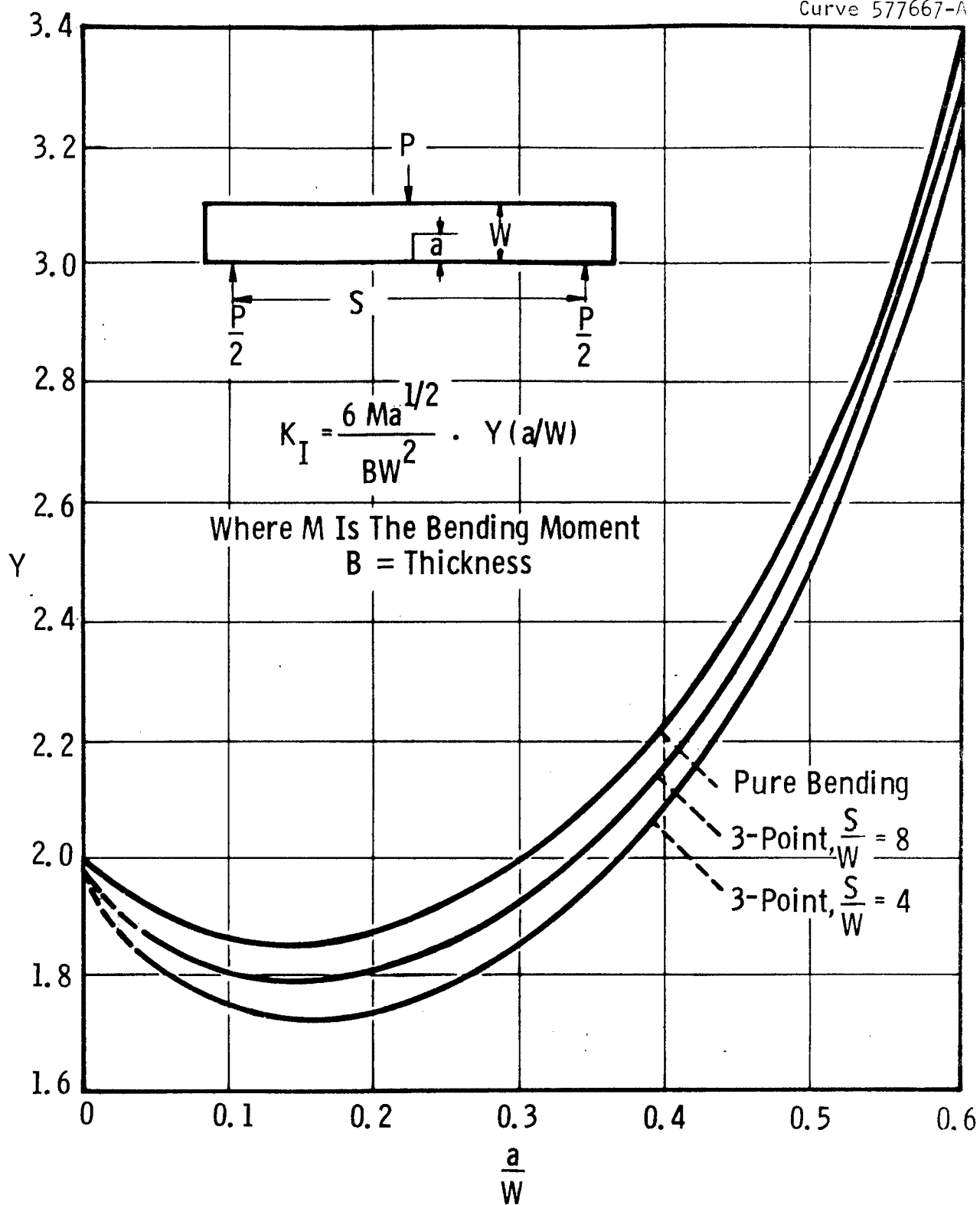
$$\text{where } M = \frac{PL}{2}$$



Fatigue crack starter for edge-notched plate specimens

Sec. 7 Fig. 32—Notch bend specimen (four-point loaded)

Curve 577667-A



Sec. 7 Fig. 33 - K calibrations for bend specimens

design application where "a" is the unknown, the expression must be modified such that we can graphically solve for a/W and ultimately, "a". A more desirable form for use in the example problem is

$$X = \frac{K_I b W^{3/2}}{6M}$$

where X is a function of a/W . The graphical solution in Figure 33 was converted to the above form by letting X equal $Y (a/W)^{1/2}$ and plotting X against a/W . This form of the graphical solution is presented in Figure 34. For additional accuracy the graphical solutions can readily be replaced by relatively simple computer programs.

Using the expression:

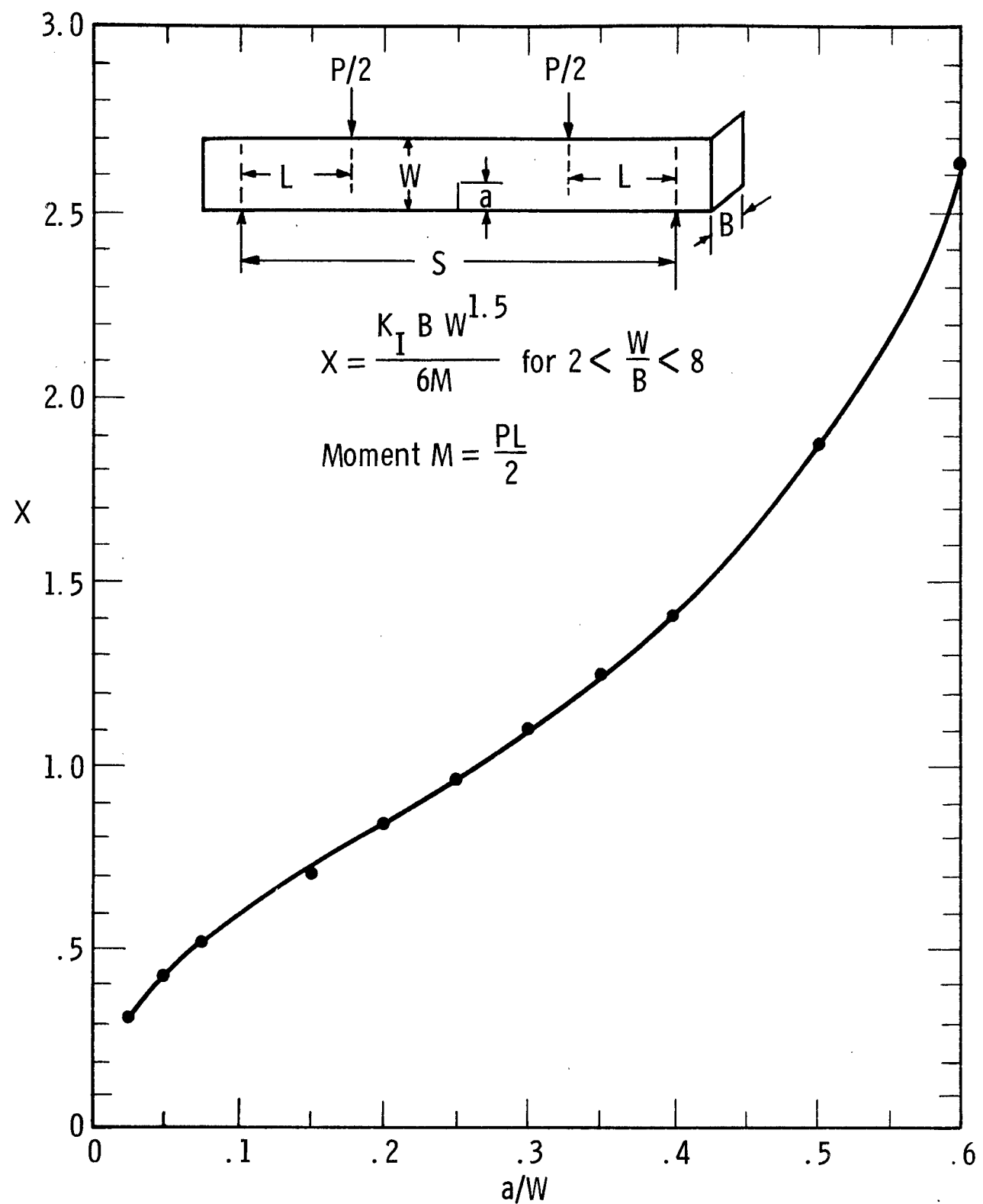
$$X = \frac{K_I b W^{3/2}}{6M}$$

(where $b = 2"$, $W = 4"$, $M = 160,000$ in-lbs and K_I is 62 ksi $\sqrt{\text{in}}$ and 56 ksi $\sqrt{\text{in}}$; the K_{Ic} values for AISI 1144 and 4140 steels, respectively) and the graphical solution in Figure 34, the critical flaw depths are found to be 1.2 in. for the 1144 steel and 1.06 in. for the 4140 steel. These flaw sizes represent the critical defect sizes which will cause failure as the result of a single application of load under the loading conditions described for the example problem.

d. Calculation of Cyclic Life

Assuming the initial presence or early development of a defect in a cyclically loaded structure, it is obvious that knowledge of the critical flaw size alone does not permit an estimate of the useful life of the structure. The component life is dependent upon the rate at which an existing defect will grow to the critical flaw size under the prescribed loading conditions. Consequently, we must compute the maximum initial allowable defect size (edge crack depth)

Curve 587292-A



Sec. 7 Fig. 34—K calibration for 4 point loaded notched bend specimen

that will not grow to the critical size for failure during the required life of the structure (100,000 cycles). In order to make these calculations we must have fatigue crack growth rate data expressed in terms of the stress intensity factor as well as the other data needed to compute the critical flaw sizes. The fatigue crack growth rate data for AISI 1144 and 4140 steels are presented in Figures 26 and 27, respectively. These data clearly illustrate the dependence of the rate of crack growth on the change in stress intensity per cycle, ΔK . Since the ΔK parameter increases as the crack length increases, it is apparent that to compute the number of cycles to failure for a given initial flaw size one must integrate the crack growth rate data over ΔK values representing the ΔK level at the start of life (that corresponding to the initial flaw size) to the ΔK level at failure, $\Delta K = K_{Ic}$.

Interpreted in another way, our goal at this point in the problem is to establish the crack length versus number of elapsed cycles curve for the component geometry and loading conditions of the example problem from crack growth rate data established with entirely different loading conditions. The ability to do just this is the primary advantage of the fracture mechanics approach to fatigue.

Since we are interested in calculating the maximum initial allowable flaw size for the prescribed loading conditions, we must select a lower limit of initial flaw size and corresponding ΔK value with which to begin the integration. This lower limit of flaw size is generally selected as the minimum flaw size which can reliably be detected with existing nondestructive inspection techniques. For this example, let us assume that the minimum detectable flaw size is an edge crack 0.125 in. deep. In addition, let us incorporate an inspection safety factor of 2 at this point yielding a minimum detectable flaw size of 0.250 in. The stress intensity factor corresponding to this flaw size then becomes the lower limit for the integration procedure. Solving the stress intensity expression for "a" equal to 0.250 in. yields a K_I value of 29 ksi $\sqrt{\text{in}}$. Since the loading conditions involve zero to maximum cyclic load, $K_I = \Delta K$.

Although the required integration procedure can readily be adapted to a short computer program, for example purposes, we will proceed with a numerical integration technique.

Since the crack growth rate data (Figures 26 and 27) indicate a constant growth rate at the lower ΔK levels which substantially exceeds that predicted by extrapolating the linear portion of the curve, the faster growth rate must be used to establish a conservative prediction of life. At ΔK levels of 37 ksi $\sqrt{\text{in.}}$ and 35 ksi $\sqrt{\text{in.}}$ for the AISI 1144 and 4140 steels, respectively, the growth rate data fall on the linear portion of the curve and can be analyzed accordingly. Consequently, the growth rate encountered between $\Delta K = 29 \text{ ksi } \sqrt{\text{in.}}$ and $\Delta K = 37 \text{ ksi } \sqrt{\text{in.}}$ for the 1144 steel and $\Delta K = 35 \text{ ksi } \sqrt{\text{in.}}$ is assumed to be constant. For this portion of the integration, the crack growth rate for the AISI 1144 steel is 1.7 microinches per cycle and 3.8 microinches per cycle for the 4140 steel. By computing the crack length at which the growth rate begins to follow the linear portion of the da/dN versus ΔK curves (the crack length corresponding to ΔK values of 37 ksi $\sqrt{\text{in.}}$ and 35 ksi $\sqrt{\text{in.}}$ for the 1144 and 4140 steels, respectively) and by dividing the difference between this crack length and the initial crack length by the growth rate, the number of elapsed cycles can be computed. For the case of the 1144 steel, 110,000 cycles at a growth rate of 1.7 microinches/cycle are required for a 0.250 in. deep crack to grow to 0.440 in. deep, the crack length corresponding to a ΔK value of 37 ksi $\sqrt{\text{in.}}$. Following the same reasoning for the 4140 steel, 39,000 cycles are required for a 0.250 deep crack to grow to .400 in. deep, a ΔK value of 35 ksi $\sqrt{\text{in.}}$. From this point on the crack growth rate can be assumed to follow a linear relationship on the log-log plots. To integrate over this portion of the crack growth rate curve, it becomes necessary to select a convenient elapsed cycles interval and to assume that the growth rate remains constant over this interval. The increase in crack length during this interval of growth is then added to the crack length at the beginning of the interval and a new ΔK value computed. The crack growth rate associated with the new

ΔK value is read off of the appropriate da/dN vs ΔK curve and the increase in crack length over the cyclic interval at the higher growth rate computed and again a new ΔK value established. This process is repeated until the ΔK value reaches K_{Ic} and at this point failure is eminent. The total number of elapsed cycles required to go from the crack length at the start of life to the critical flaw size is then the number of cycles to failure.

To further illustrate the procedure involved, portions of the actual results of the numerical integration for both alloys are presented below. For each step in the integration procedure the increase in crack length is computed, added to the previous crack length and a new a/W value determined. The X value corresponding to the new a/W is read off the curve in Figure 34 and the stress intensity equation:

$$X = \frac{K_I b W^{3/2}}{6M}$$

used to compute the new ΔK level for the next interval of growth.

RESULTS OF NUMERICAL INTEGRATION

<u>AISI 1144 Steel</u>			<u>AISI 4140 Steel</u>			
a , crack depth, in.	K_I ksiv/in	$\frac{da}{dN}$ $\mu\text{-in/cycle}$ From Fig. 26	N Number of Elapsed Cycles	a , crack depth, in.	K_I ksiv/in	$\frac{da}{dN}$ $\mu\text{-in/cycle}$ From Fig. 27
0.250	29	1.7	0 39,000 44,000 50,000 54,000 58,000 60,000 61,000 61,500 110,000	0.250 0.400 0.420 0.453 0.506 0.621 0.747 1.06	29 35 36 37.8 40.3 44.3 48.6 56	3.8 3.8 5.0 9.0 20.0 56.0 140.0 Failure
0.440	37	1.7				

AISI 1144 Steel

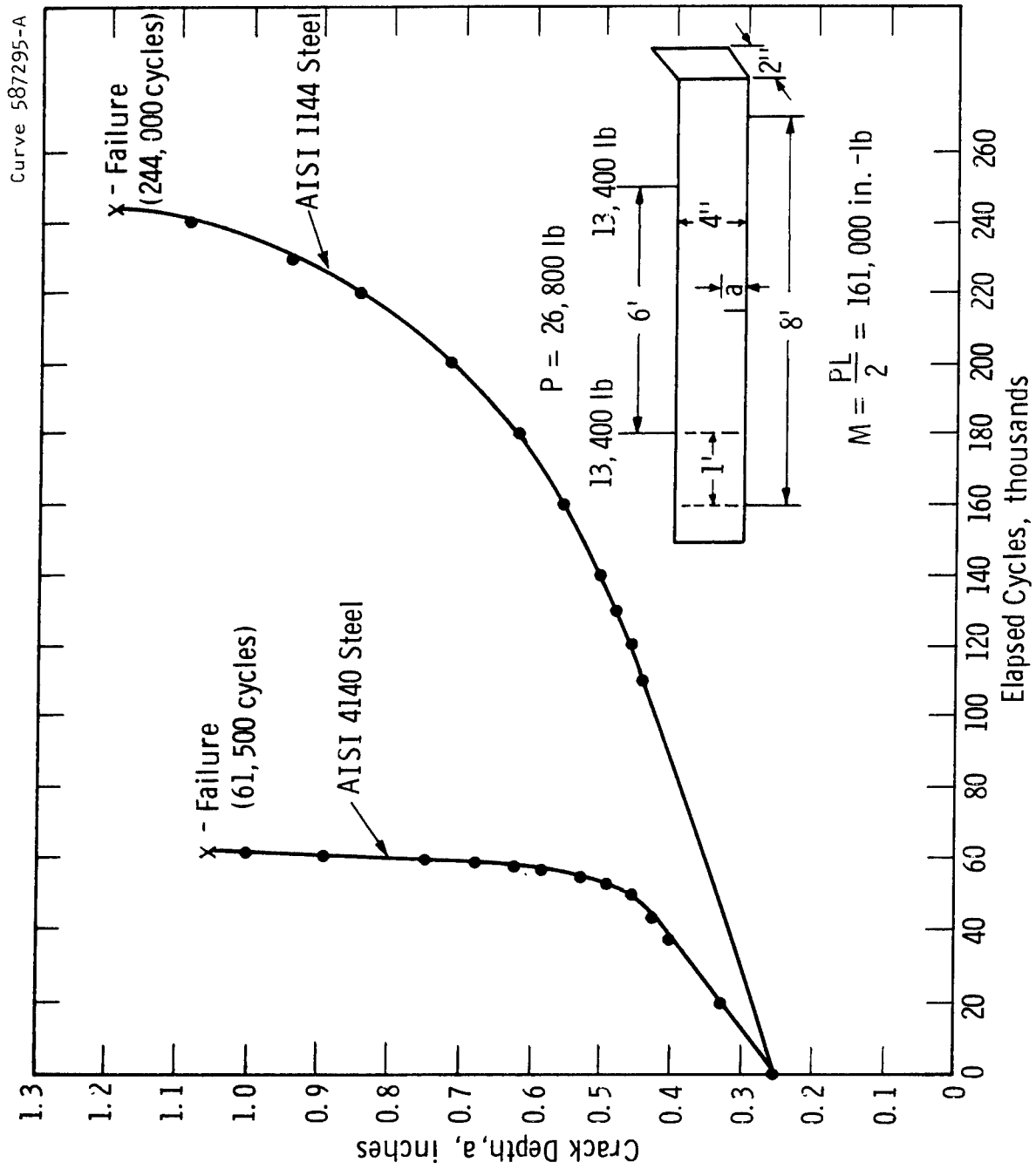
a, crack depth, in.	K _I ksi $\sqrt{\text{in}}$	$\frac{da}{dN}$ $\mu\text{-in}/\text{cycle}$ From Fig. 26	N Number of Elapsed Cycles
0.500	39.6	2.4	140,000
0.619	44.4	4.4	180,000
0.713	47.4	6.0	200,000
0.848	51.6	9.5	220,000
0.943	56	15.0	230,000
1.200	62	25.0	244,000 - Failure

Note that at 61,500 cycles, failure has occurred in the 4140 steel whereas the crack in the 1144 steel is still growing at the initial rate. The results of the numerical integration are presented in graphical form in Figure 35. Presented in this manner, the results clearly demonstrate the fatigue crack growth behavior of the two steels considered in the example problem. However, for design purposes it is more convenient to present the data in terms of the crack depth versus the cycles to failure rather than crack depth versus elapsed cycles. The data shown in Figure 35 can easily be converted to crack depth versus cycles to failure by subtracting the elapsed cycles at a given crack depth from the total number of cycles required to cause failure. These results are presented in Figure 36.

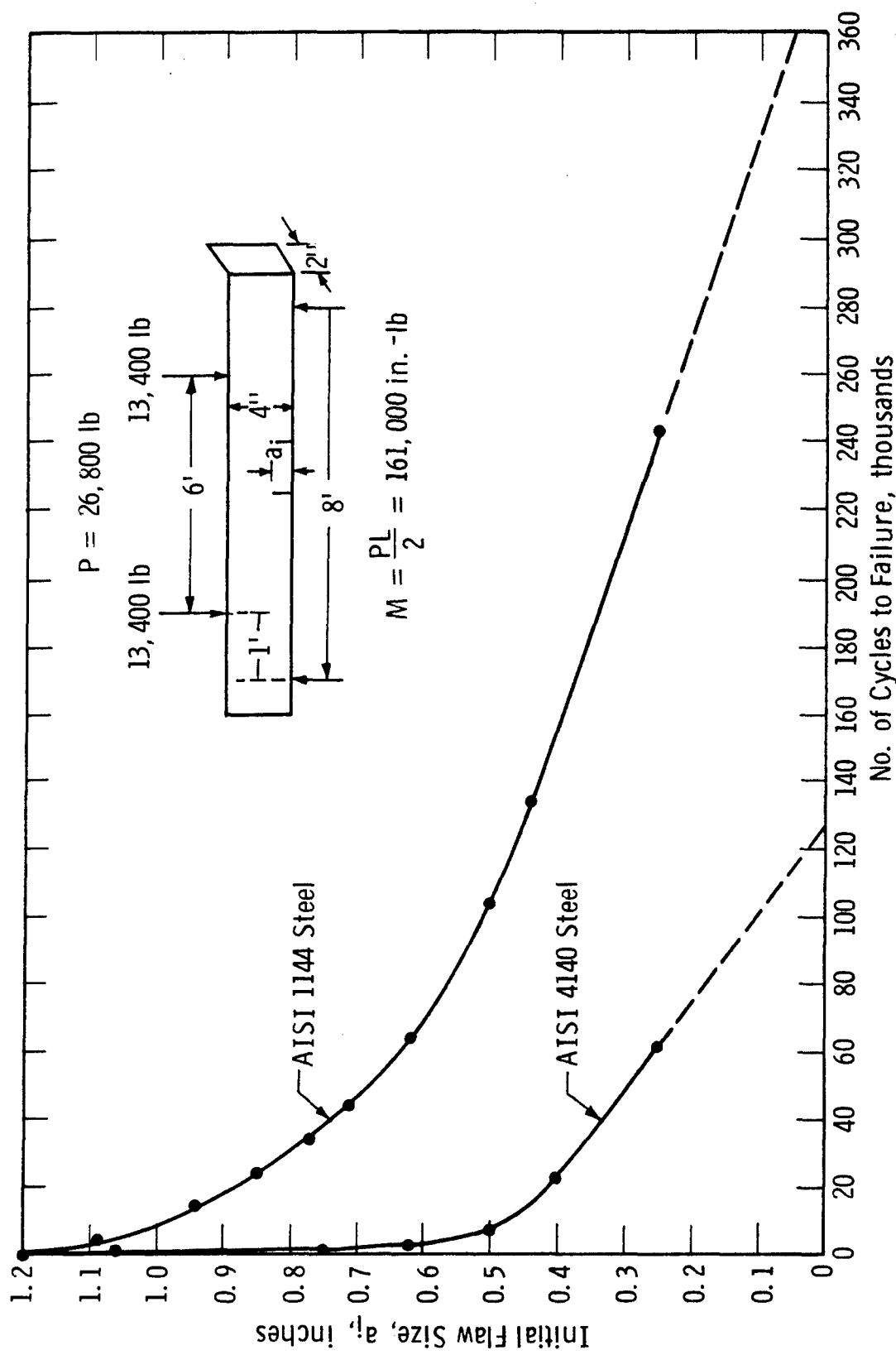
In order to satisfy the minimum cyclic life requirement of 100,000 cycles, Figure 36 indicates that the maximum initial allowable crack depth must not exceed 0.100 in. for the 4140 steel or 0.510 in. for the 1144 steel.

Material Selection

In our previous discussion, it was decided to establish a minimum detectable crack depth criterion of 0.250 in. Since the maximum initial allowable flaw depth established for the 4140 steel (0.100 in.) is less than the minimum size which can reliably be detected based upon



Sec. 7 Fig. 35—Crack growth behavior computed for example problem



Sec. 7 Fig. 36—Initial flaw size versus cycles to failure for example problem

the above nondestructive inspection criterion, the 4140 steel is not acceptable for the proposed application. The presence of a 0.250 in. deep edge crack in the 4140 steel beam would result in a cyclic life of only 61,500 cycles. The maximum initial allowable flaw depth for the 1144 steel (0.510 in.) is well above the 0.250 in. deep minimum detectable depth and consequently, the 1144 steel is well suited for the proposed application.

e. Development of Inspection Criteria and Safety Factors

The development of adequate nondestructive inspection criteria and design safety factors for a structure assumed to contain a defect are closely related. Specifically, design safety factors can be established on the basis of applied stress or cyclic life which in turn, influence the defect size which must be detectable. In addition, a safety factor can be incorporated in a design situation on the basis of the inspection level such as was the case for this example problem.

If we select a safety factor of two on the cyclic life for the 1144 steel beam, the maximum initial allowable flaw size is 0.33 in. and we must establish an inspection level capable of detecting this flaw size. However, if we also incorporate a safety factor of two into the inspection level sensitivity such that defects 0.152 in. deep can be detected, the cyclic life of the structure becomes 300,000 cycles, a total safety factor of 3 on cyclic life.

Earlier in our discussion, we established the minimum detectable flaw depth to be 0.125 in. and proceeded to incorporate a safety factor of two into the consideration. However, if we establish our inspection sensitivity to the minimum flaw size which can reliably be detected and inspect to this level, those structures which pass the inspection will yield a total cyclic life of at least 320,000 cycles and our design safety factor will be 3.2. If a larger safety factor is desired, a material with crack growth properties and/or a K_{Ic} toughness superior to 1144 steel must be used or the design stress reduced accordingly.

7.12.2 EXAMPLE PROBLEM NO. 2 - THIN-WALLED PRESSURE VESSEL

a. Operational Requirements

An 88 inch diameter, 100 inch long, 4 inch thick wall pressure vessel made of 1144 steel has been subjected to an in-service inspection and a 0.400 inch deep, 4 inch long semi-elliptical surface crack detected at mid-length on the inside of the vessel. The major axis of the defect (length) is oriented in the axial direction of the vessel. The pressure vessel is used to contain a hydrostatic system at a maximum pressure of 3000 psi and is subjected to zero to maximum pressure cyclic loading at room temperature in an inert environment. Determine the remaining useful life of the structure.

b. Initial Design Considerations

The application described above can be analyzed in accordance with thin-walled pressure vessel design concepts. Specifically, the maximum circumferential (hoop) stress can be computed from the following equation

$$\sigma = \frac{PD}{2t}$$

where P is the internal pressure (3000 psi), D is the internal diameter of the pressure vessel (80 in.) and t is the wall thickness. Solving this equation for σ yields a maximum applied circumferential stress of 30,000 psi.

c. Calculation of Critical Flaw Size

In our previous example it was shown that the minimum thickness for plane strain conditions with the 1144 steel being considered is 1.48 inches. Therefore, linear elastic fracture mechanics concepts are applicable to this example and we can proceed with the calculation of the critical flaw size. The appropriate stress intensity expression for the loading conditions described above is:⁽⁹⁾

$$K_I^2 = \frac{1.21 a \pi \sigma^2}{\phi^2 - 0.212 \left(\frac{\sigma}{\sigma_{YS}} \right)^2}$$

where:

K_I = stress intensity factor, ksi $\sqrt{\text{in}}$
 ϕ = flaw shape parameter
 σ = applied tensile stress, ksi
 σ_{YS} = 0.2% yield strength, ksi
 a = crack depth, inches

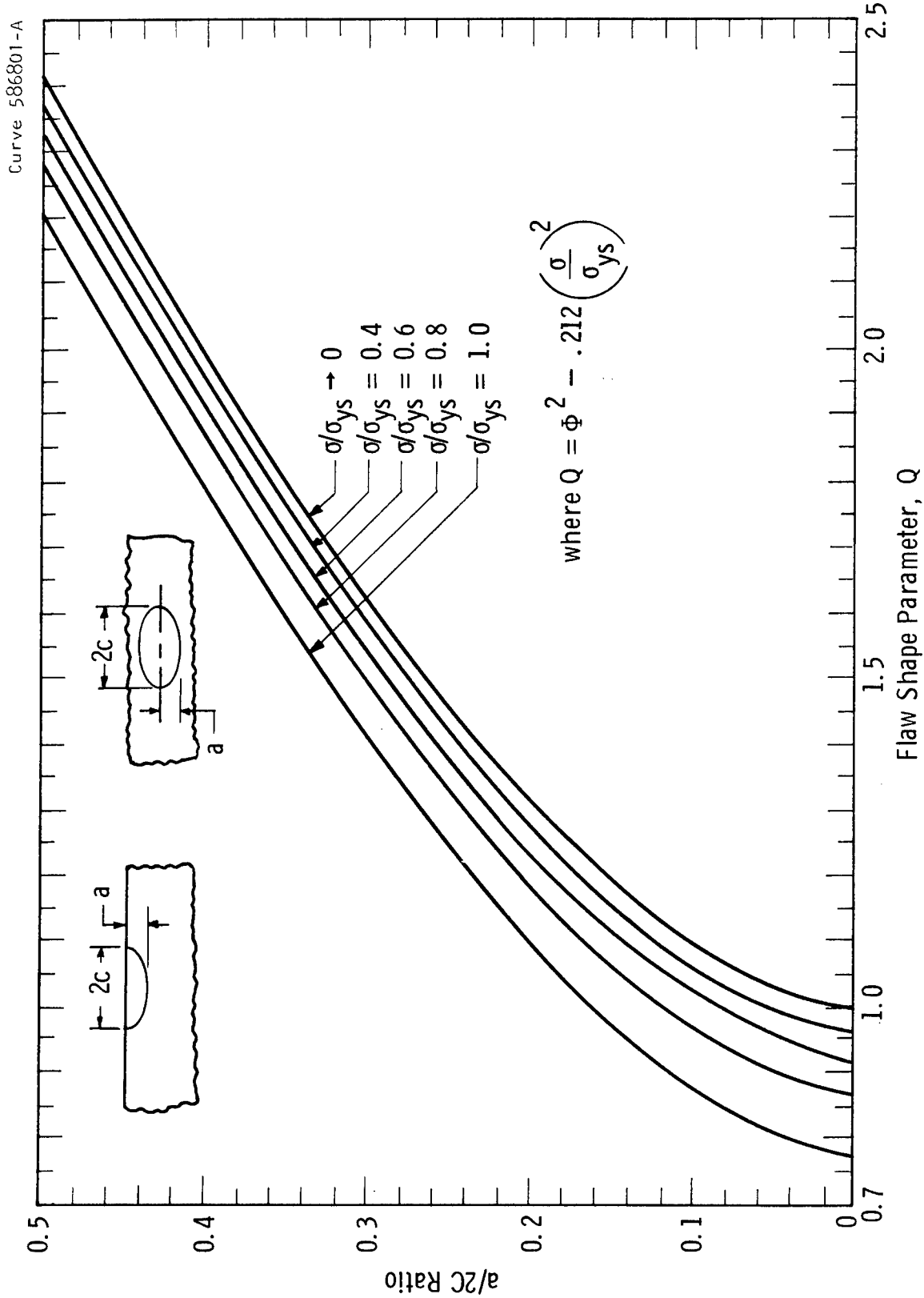
Rearranging the above expression and setting K_I equal to K_{Ic} yields the following critical flaw size expression for a semi-elliptical surface crack subjected to tension stresses perpendicular to the major plane of the flaw:

$$a_{cr} = \frac{K_{Ic}^2 [\phi^2 - 0.212 (\frac{\sigma}{\sigma_{YS}})^2]}{1.21 \pi \sigma^2}$$

In order to facilitate the use of this expression and specifically, to simplify the calculation of the flaw shape parameter, a graphical solution of ϕ^2 is available where the flaw shape parameter is expressed as a Q factor and $Q = \phi^2 - 0.212 (\sigma/\sigma_{YS})^2$. This solution is presented in Figure 37. For the flaw length to depth ratio of 10 considered in this example $a/2c = .1$ and $Q = 1.03$. Solving the above expression for the conditions specified in this example problem ($\sigma = 30$ ksi, $K_{Ic} = 62 \sqrt{\text{in}}$, $Q = 1$) yields a critical flaw size 1.1 inches deep by 11 inches long. This flaw size represents the critical defect size which will cause failure as the result of a single application of load for the conditions described in this problem.

d. Calculation of Cyclic Life

Once the critical flaw size has been determined we can proceed to the calculation of the remaining cyclic life. Specifically, we must determine the number of cycles required for the existing flaw



Sec. 7 Fig. 37—Flaw shape parameter curves for surface and internal cracks

(.40" deep by 4.0" long) to grow to the critical flaw size of 1.1" deep x 11" long. To do this, we must have available suitable fatigue crack growth rate data expressed in terms of fracture mechanics parameters. These data are available for the 1144 steel being considered and are given in Figure 26 where da/dN is the crack growth rate and ΔK is the change in stress intensity factor per cycle. The parameters identified as n and C_o represent the slope of the $\log da/dN$ versus $\log \Delta K$ curve and the intercept constant, respectively. These parameters are considered empirical material constants which describe the fatigue crack growth rate properties of the material in terms of the generalized fatigue crack growth rate law: $da/dN = C_o \Delta K^n$. From a knowledge of these parameters, as well as the critical defect size, it is possible to compute the number of elapsed cycles required for the existing flaw to grow to failure. However, as was pointed out in the experimental portion of this investigation and in the first example problem, the fatigue crack growth rate of the 1144 steel does not follow the generalized growth rate law at ΔK levels below 37 ksi $\sqrt{\text{in}}$. At ΔK levels below 37 ksi $\sqrt{\text{in}}$, the rate of crack growth appears to be constant. Therefore, we must determine the ΔK level associated with the existing flaw size to determine if the growth rate law is applicable over the range of ΔK levels to failure. This can be done by solving the stress intensity expression for K_I when "a" equals the existing flaw size (0.400 in.). The corresponding ΔK level is 37 ksi $\sqrt{\text{in}}$. and we can proceed to compute the remaining cyclic life based on the generalized crack growth rate law.

A convenient cyclic life expression based on fracture mechanics concepts has been developed by Wilson⁽⁹⁾ and will be used for this problem. The general form of the equation is presented below.

$$N = \frac{2}{(n-2)C_o M^{n/2} \Delta\sigma^n} \left[\frac{1}{a_i \frac{n-2}{2}} - \frac{1}{a_{cr} \frac{n-2}{2}} \right] \quad \text{for } n \neq 2$$

$$N = \frac{1}{C_o M \Delta\sigma^2} \ln \frac{a_{cr}}{a_i} \quad \text{for } n = 2$$

where

N = number of cycles to grow to critical flaw size

a_i = initial crack size, in.

n = slope of $\log da/dN$ vs $\log \Delta K$ curve

C_0 = empirical intercept constant

a_{cr} = critical flaw size, in.

$\Delta\sigma$ = applied cyclic load range, ksi

M = component geometry and flaw shape parameter

The above expression is applicable to those loading situations where the relationship between applied load, flaw size and stress intensity factor has the form of $K_I = \sigma \sqrt{Ma}$. In addition, it is assumed that the cyclic stress range ($\Delta\sigma$) remain constant throughout the component life and that the mean stress does not influence the results.

The first step in the use of the cyclic life expression is to establish the component geometry and flaw shape parameter M . For the problem under consideration (an elliptical surface flaw subjected to tension stresses normal to the major plane of the crack), $K_I^2 = 1.21 \pi \sigma^2 (a/Q)$ where $Q = 1.03$. Converting the equation to the generalized form of $K = \sigma \sqrt{Ma}$ and solving for M yields $M = 3.8$. We now have all the necessary parameters to solve the cyclic life expression. Substituting the appropriate values into the life expression ($\Delta\sigma = 30,000$ psi, $n = 5$, $C_0 = 3.1 \times 10^{-29}$, $M = 3.8$, $a_i = 0.400$ in., $a_{cr} = 1.10$ in.) and solving for N yields 99,600 cycles. Therefore, 99,600 cycles are required for a 0.400 inch deep crack to grow to 1.100 inch deep at the prescribed loading conditions. From this information it is now possible to conclude that the remaining useful life of the pressure vessel is 99,600 cycles and appropriate steps can be taken to remove the vessel from service prior to approaching unsafe operation.

7.12.3 DISCUSSION OF EXAMPLE PROBLEMS

The two example problems presented here do not demonstrate all of the considerations that can be and are employed in the fracture mechanics approach to design. Specifically, no attempt was made to

evaluate the case of a component operating in a hostile environment where stress corrosion crack growth may occur and no consideration was given to possible proof testing situations commonly encountered in pressure vessel fabrication. However, the basic aspects of calculating the critical flaw size and useful life data have been demonstrated and these techniques need only be modified slightly to incorporate other variables into the design considerations.

One additional consideration obviously lacking in the example problems is the possible variation in material throughout the structure. Particularly, the variation in properties due to welding. If a structure contains a weld, adequate K_{Ic} and crack growth rate data for both the weld metal and heat affected zone must be available to adequately evaluate the structure. Again, the same design concepts demonstrated in the example problems apply.

Section 7.13 References

1. W. F. Brown, Jr. and J. Srawley, "Plane Strain Crack Toughness Testing of High Strength Metallic Materials," ASTM Special Technical Publication No. 410, 1966.
2. J. E. Srawley, M. H. Jones, W. F. Brown, Jr., "Determination of Plane Strain Fracture Toughness," Materials Research and Standards, June 1967, p. 262.
3. E. T. Wessel, "State of the Art of the WOL Specimen for K_{Ic} Fracture Toughness Testing," Engineering Fracture Mechanics, Vol. 1, 1968, pp. 77-103.
4. H. D. Greenberg, E. T. Wessel, and W. H. Pyle, "Fracture Toughness of Turbine-Generator Rotor forgings," presented at the National Symposium on Fracture Mechanics at Lehigh University, Bethlehem, Pa. June 17-19, 1968.
5. W. G. Clark, Jr., "Ultrasonic Detection of Crack Extension in the WOL Type Fracture Toughness Specimen," Materials Evaluation, August 1967, p. 185.
6. W. G. Clark, Jr., and L. J. Ceschini, "An Ultrasonic Crack Growth Monitor," Westinghouse Research Laboratories Scientific Paper No. 68-7D7-BFPWR-P1, April 1968. To be published.
7. "Proposed Recommended Practice for Plane-Strain Fracture Toughness Testing of High-Strength Metallic Materials Using a Fatigue-Cracked Bend Specimen," Part 31, ASTM Standards 1968, p. 1018.
8. "Method of Test for Plane-Strain Fracture Toughness of Metallic Materials," Tentative Draft distributed at ASTM Committee E-24 Meetings, Atlanta, Ga., Sept. 30, 1968.
9. E. T. Wessel, W. G. Clark, Jr. and W. K. Wilson, "Engineering Methods for the Design and Selection of Material Against Fracture," U. S. Army Tank-Automotive Center Report. Contract No. DA-30-064-AMC-602(T), AD NO. 801005, June 24, 1966.
10. A. J. Federowicz and B. A. Powell, "A Computer Program to Obtain A Min-Max Regression Model by Linear Programming," Westinghouse Research Laboratories Report 68-1C3-COMP-R2, July 15, 1968.
11. P. C. Paris, "The Fracture Mechanics Approach to Fatigue," Proc. Tenth Sagamore Army Materials Research Conference, August, 1963, Syracuse University Press, 1964.

12. "Properties and Selection of Metals," Metals Handbook, 8th Edition Vol. 1, 1961, p. 225.
13. W. S. Pellini, F. A. Brant and E. E. Layne, "Performance of Cast and Rolled Steels in Relation to the Problem of Brittle Fracture," Preprint No. 53-3 American Foundrymen's Society Annual Meeting, 1953.
14. "Materials Selection Issue," Materials Engineering Vol. 66, No. 5 Oct. 1967, p. 65.
15. I. S. Tuba, "A Method of Elastic-Plastic Plane Stress and Strain Analysis," Journal of Strain Analysis, Vol. 1, No. 2, 1966, p. 115-120.
16. I. S. Tuba, "An Analytic Method for Elastic-Plastic Solutions," International Journal of Solids and Structures, Vol. 3, 1967, p. 543-564.
17. S. E. Gabrielse and C. Visser, "A Finite Element Computer Program for Plane-Stress and Plane-Strain Elastic-Plastic Problems," Westinghouse Research Report 67-1D7-GENCO-R3.
18. D. P. Wei and I. S. Tuba, "A Computer Program for the Elastic and Elastic-Plastic Analysis of Compact-Tension Fracture Test Specimen," Westinghouse Research Report 68-1D7-FMPWR-R1.
19. R. C. Bates and W. G. Clark, Jr., "Fractography and Fracture Mechanics," Westinghouse Research Laboratories Scientific Paper 68-1D7-RDAFC-P1, September 4, 1968. Presented at the ASM National Metal Congress, Detroit, October 1968.

TECHNICAL REPORT DISTRIBUTION LIST

<u>Address</u>	<u>No. of Copies</u>
Commanding General, U.S. Army Tank-Automotive Command, Warren, Michigan 48090	
ATTN: AMSTA-CL, Chief Scientist/Technical Director of Laboratories.....3	
AMSTA-R, Director, Development & Engineering Directorate.....1	
AMSTA-RI, International Division.....1	
AMSTA-RR, Systems Concept Division.....1	
AMSTA-RS, Engineering Control Systems Division.....1	
AMSTA-RE, Vehicle Systems Division.....1	
AMSTA-B, Vehicular Components & Materials Laboratory.....1	
AMSTA-BS, Laboratory Support Division.....2	
AMSTA-M, Maintenance Directorate.....1	
AMSTA-Q, Quality Assurance Directorate.....1	
AMSTA-W, Commodity Management Office.....1	
AMCPM-CV-D, Combat Vehicle Project Office.....1	
AMCPM-GPV, General Purpose Vehicles Project Manager Office.....1	
AMCPM-M60, M60, M60A1, M48A3 Project Manager Office.....1	
AMCPM-GG, M561/XM705 Project Manager Office.....1	
AMCPM-MBT-EA, US/FRG MBT Engineering Project Manager Office.....1	
Commanding General U.S. Army Materiel Command	
ATTN: AMCRD-GV	
Washington, D. C. 20315	1
Commanding General U.S. Army Weapons Command	
ATTN: AMSWE-RDR	
Rock Island, Illinois 61202	1
Commanding General U.S. Army Test & Evaluation Command	
ATTN: AMSTE-TA	
AMSTE-BB	
Aberdeen Proving Ground, Maryland 21005	1
Commanding General Engineering Research & Development Laboratory	
Fort Belvoir, Virginia 22060	1
Commanding General U.S. Army Combat Developments Command	
Ft. Belvoir, Virginia 22060	1

<u>Address</u>	<u>No. of Copies</u>
Commanding General U.S. Army Combat Developments Command Combat Arms Group ATTN: Materiel Division Fort Leavenworth, Kansas 66027	1
Commanding General U.S. Army Combat Developments Command Combat Service Support Group ATTN: Materiel Division Ft. Lee, Virginia 23801	1
Commanding Officer Watervliet Arsenal Watervliet, New York 12189	1
Commanding Officer Frankford Arsenal ATTN: SMUFA-L7000, Technical Library Bridge & Tacony Streets Philadelphia, Pennsylvania 19137	1
Commanding Officer Rock Island Arsenal Rock Island, Illinois 61202	1
Commanding Officer Picatinny Arsenal Dover, New Jersey 07801	1
Commanding Officer U.S. Army Materials & Mechanics Research Center Watertown, Massachusetts 02172	1
Commanding Officer Aberdeen Proving Ground ATTN: Technical Library Aberdeen Proving Ground, Maryland 21005	1
Commanding Officer Yuma Proving Ground Yuma, Arizona 85364	1
Commanding Officer U.S. Army Combat Developments Command Armor Agency ATTN: Materiel Division Ft. Knox, Kentucky 40121	1

<u>Address</u>	<u>No. of Copies</u>
Commanding Officer U.S. Army Aviation Materiel Laboratories Fort Eustis, Virginia 23604	1
Commanding Officer U.S. Army Ballistic Research Laboratories Aberdeen Proving Ground, Maryland 21005	1
Commanding Officer U.S. Army Natick Laboratories ATTN: Technical Library Natick, Massachusetts 01762	1
Commanding Officer Harry Diamond Laboratories ATTN: AMXDO, Library Connecticut Avenue & Van Ness Street, N.W. Washington, D. C. 20438	1
Commander U.S. Naval Ship R&D Center Washington, D. C. 20007	1
Director Naval Research Laboratory ATTN: Technical Information Center Anacostia Station Washington, D. C. 20390	1
Commandant U.S. Marine Corps ATTN: Code A0411 Washington, D. C. 20380	1
Commander Air Force Materials Laboratory Wright-Patterson Air Force Base, Ohio 45433	1
Headquarters Defense Documentation Center for Scientific & Technical Information ATTN: Document Service Computer Center Cameron Station Alexandria, Virginia 22314	20
Defense Materials Information Center Battelle Memorial Institute 505 King Avenue Columbus, Ohio 43201	1



UNCLASSIFIED

Security Classification

DOCUMENT CONTROL DATA - R & D

(Security classification of title, body of abstract and indexing annotation must be entered when the overall report is classified)

1. ORIGINATING ACTIVITY (Corporate author) Westinghouse Research Laboratories Pittsburgh, Pennsylvania		2a. REPORT SECURITY CLASSIFICATION UNCLASSIFIED
		2b. GROUP
3. REPORT TITLE FRACTURE MECHANICS TECHNOLOGY FOR COMBINED LOADING AND LOW-TO-INTERMEDIATE STRENGTH METALS		
4. DESCRIPTIVE NOTES (Type of report and inclusive dates) Technical Report, Final, Nov. 1968		
5. AUTHOR(S) (First name, middle initial, last name) William K. Wilson, William G. Clark, Jr., Edward T. Wessel		
6. REPORT DATE November 18, 1968	7a. TOTAL NO. OF PAGES 245	7b. NO. OF REFS 60
8a. CONTRACT OR GRANT NO. DAAE 07-67-C-4021	9a. ORIGINATOR'S REPORT NUMBER(S) TACOM Technical Report No. 10276 (final)	
b. PROJECT NO. 1G024401A105	9b. OTHER REPORT NO(S) (Any other numbers that may be assigned <i>this report</i>) Westinghouse Research Report 68-9D7-BTLFR-R1	
c.		
d.		
10. DISTRIBUTION STATEMENT Distribution of this document is unlimited.		
11. SUPPLEMENTARY NOTES	12. SPONSORING MILITARY ACTIVITY Department of the Army, United States Army Tank Automotive Command, Vehicular Components and Materials Laboratory, Warren, Michigan 48090	
13. ABSTRACT The feasibility of extending the usefulness of fracture mechanics technology was explored in two areas (1) situations of crack instability under combined crack-tip loading conditions (2) characterization of the fracture behavior of low-to-intermediate strength materials. Calibrations of the crack-tip stress intensity factors were developed for modes I-II and modes I-III types of combined loading. Experimental determinations of the critical crack-tip conditions for fracture were obtained for various ratios of K_I/K_{II} and K_I/K_{III} loading using 7178-T651 and 7075-T651 aluminum alloys. The development of an engineering fracture criteria for combined mode loading appears feasible.		
Fracture mechanics tests for K_{Ic} fracture toughness and fatigue crack growth rates (da/dN versus ΔK) were conducted for several low strength materials; AISI 1020, 1045, 1144 and 4140 steels and 7039-T6 aluminum. For the conditions studied existing linear-elastic fracture mechanics technology was found to be directly applicable to all of the materials, except AISI 1020 steel. Example problems are used to demonstrate the engineering application of the technology. Existing elastic plastic analysis were applied to the AISI 1020 steel non plane-strain test data. The development of a fracture criteria applicable to non plane-strain fracture conditions appears feasible.		

UNCLASSIFIED

Security Classification

14. KEY WORDS	LINK A		LINK B		LINK C	
	ROLE	WT	ROLE	WT	ROLE	WT
Fracture						
Brittle						
Toughness						
Crack Growth						
Defects						
Mechanics						
Stress Analysis						
Stress Intensity Factors						
Ferrous Alloys						
Aluminum Alloys						
Inspection						
Design						
Testing						
Combined loading						
Life expectancy						
Linear-elastic						
Fracture-mechanics						
Fatigue						
Computer programs						
Cracks						
Crack-tip displacements						
Fracture modes						